

**DOT/FAA/AR-03/71**

Office of Aviation Research  
Washington, D.C. 20591

# **Detection of Stress Buildup in Airframes**

August 2004

Final Report

This document is available to the U.S. public  
through the National Technical Information  
Service (NTIS), Springfield, Virginia 22161.



U.S. Department of Transportation  
**Federal Aviation Administration**

## **NOTICE**

This document is disseminated under the sponsorship of the U.S. Department of Transportation in the interest of information exchange. The United States Government assumes no liability for the contents or use thereof. The United States Government does not endorse products or manufacturers. Trade or manufacturer's names appear herein solely because they are considered essential to the objective of this report. This document does not constitute FAA certification policy. Consult your local FAA aircraft certification office as to its use.

This report is available at the Federal Aviation Administration William J. Hughes Technical Center's Full-Text Technical Reports page: [actlibrary.tc.faa.gov](http://actlibrary.tc.faa.gov) in Adobe Acrobat portable document format (PDF).

1. Report No. <b>DOT/FAA/AR-03/71</b>		2. Government Accession No.		3. Recipient's Catalog No.	
4. Title and Subtitle <b>DETECTION OF STRESS BUILDUP IN AIRFRAMES</b>				5. Report Date <b>August 2004</b>	
				6. Performing Organization Code	
7. Author(s) <b>Dr. P.A. Stampe, Dr. R. J. Kennedy, and Dr. W.P. Tucker</b>				8. Performing Organization Report No.	
9. Performing Organization Name and Address <b>Department of Physics Florida A&amp;M University Tallahassee, FL 32307</b>				10. Work Unit No. (TRAIS)	
				11. Contract or Grant No.	
12. Sponsoring Agency Name and Address <b>U.S. Department of Transportation Federal Aviation Administration Office of Aviation Research Washington, DC 20591</b>				13. Type of Report and Period Covered <b>Final Report</b>	
				14. Sponsoring Agency Code <b>ANM-100</b>	
15. Supplementary Notes <b>The FAA William J. Hughes Technical Center Technical Monitor were Drs. John Bakuckas and Felix Abali.</b>					
16. Abstract <p>This exploratory study investigates the role of texture development during fatigue cycling on crack initiation in airframes. The presence of texture in metals is known to relate to fatigue and the initiation of cracks. It has not been conclusively demonstrated, however, that texture will develop in a material simply due to cyclic fatigue. In this study, the development of texture during fatigue cycling of rolled aluminum 2024-T3 sheet was monitored using x-ray diffraction techniques. The texture development was calculated as a function of number of fatigue cycles (1) to determine whether texture changes as a material is fatigued and (2) to correlate the development of texture to crack formation.</p> <p>X-ray diffraction measurements show that the rolling direction initially lies normal to the preferred plane on which grains are oriented. In Millers indices, the rolling direction and the normal plane are denoted as [100] and (100) respectively. Upon fatigue cycling, an initially rapid development of texture is found to occur. Prior to cracking, the grains rotate such that the [100] direction lies along the stress axis. The rate of texture development is dependent on the direction of the strain axis with respect to the rolling direction of the aluminum and the number of cycles to failure. After crack initiation, the texture development slows down and changes gradually until the point of failure. This demonstrates that texture development does indeed occur with fatigue and plays a role in the development of cracks in the aluminum sheet. A more detailed study is required to develop a diagnostic test for proximity to crack initiation.</p>					
17. Key Words <b>X-ray diffraction, Pole figures, Inverse pole figures, Orientation, Rolling direction, Distribution functions, Texture, Crack initiation, Fatigue cycles</b>				18. Distribution Statement <b>This document is available to the public through the National Technical Information Service (NTIS) Springfield, Virginia 22161.</b>	
19. Security Classif. (of this report) <b>Unclassified</b>		20. Security Classif. (of this page) <b>Unclassified</b>		21. No. of Pages <b>198</b>	
				22. Price	

## TABLE OF CONTENTS

	Page
EXECUTIVE SUMMARY	vii
1. INTRODUCTION	1
2. EXPERIMENTAL DETAILS	1
2.1 Specimen Description	1
2.2 Experimental Procedure	3
2.2.1 Tensile Testing of Specimens to Determine Yield Strength	3
2.2.2 Fatigue Cycling	4
2.2.3 X-ray Texture Measurements	4
2.2.4 Microscopy	5
3. RESULTS: FATIGUE UNTIL FAILURE	5
3.1 Test Matrix	5
3.2 Texture Evolution	6
3.2.1 Pole Figure Analysis	6
3.2.2 Orientation Distribution Function	18
3.2.3 Inverse Pole Figures	19
3.2.4 $\theta/2\theta$ Scans of Specimens' Surfaces	23
3.3 Scanning Electron Microscope Surface Imaging	24
4. FATIGUE UNTIL CRACK FORMATION	25
4.1 Test Matrix	25
4.2 Texture Evolution and Crack Initiation	26
4.2.1 Pole Figures	26
4.2.2 Inverse Pole Figures	31
4.2.3 $\theta/2\theta$ Scans of Specimens' Surfaces	35
4.3 Scanning Electron Microscope Surface Imaging	35
5. DISCUSSION OF RESULTS	37
6. CONCLUSION AND SUMMARY	37
7. SUGGESTIONS FOR FUTURE RESEARCH	38



## APPENDICES

- A—Specimen Layout and Testing Procedure  
 B—Direct and Inverse Pole Figure Data as a Function of Fatigue  
 C—Scanning Electron Microscope Surface Investigation as a Function of Fatigue  
 D—Literature Review

## LIST OF FIGURES

Figure		Page
1	Tensile Stress-Strain Curve for Specimen B1	3
2	Schematic Diagram of Inverse Pole Figures for a (100)<110> Rolled Metal Plate	5
3	The Dependence of the Number of Cycles to Failure on Specimen Orientation	6
4	(a) The {111} and (b) {200} Pole Figures for an Ideal (100)-Oriented Single Crystal of Aluminum	7
5	The {111} Pole Figure of Sample A2 Prior to Fatigue Cycling	8
6	The {200} Poles for the Same Unstressed Sample A2 as in Figure 5	9
7	The Ideal Theoretical Pole Plot for the (a) (111), (b) (200), (c) (220), and (d) (311) Poles of the First Orientation	10
8	Three Cubes of Aluminum Tipped 18° From Normal Along the Transverse Direction and Twisted 15° Both Clockwise and Anticlockwise About the Transverse Direction	10
9	The Ideal Theoretical Pole Plot for the (a) (111), (b) (200), (c) (220), and (d) (311) Poles of the Second Orientation	11
10	The Ideal Theoretical Pole Plot for the (a) (111), (b) (200), (c) (220), and (d) (311) Poles of the Third Orientation	12
11	The (111) Reflections of Specimen A2 as a Function of Number of Fatigue Cycles	14
12	The (200) Reflections of Specimen A2 as a Function of Number of Fatigue Cycles	15

13	The (220) Reflections of Specimen A2 as a Function of Number of Fatigue Cycles	16
14	The (311) Reflections of Specimen A2 as a Function of Number of Fatigue Cycles	17
15	A Constant $\theta=9.0^\circ$ Slice of the Orientation Distribution Function for Specimen A2 as a Function of Fatigue Cycling	18
16	Inverse Pole Figures Showing the Distribution of Crystallographic Axes With Respect to an Axis Normal to the Surface of Specimen A2	20
17	Inverse Pole Figures Showing the Distribution of Crystallographic Axes With Respect to an Axis Parallel to the Strain Axis of the Specimen A2	21
18	Inverse Pole Figures Showing the Distribution of Crystallographic Axes With Respect to the Transverse Axis of Specimen A2	22
19	$\theta/2\theta$ Scan Through the (111) and (200) Poles of Specimen A2 Prior to Fatigue Cycling	23
20	The Ratio of the Intensity of the (200) Reflection to the (111) Orientation	24
21	Fatigue Cracks in the Gage Region of an Aluminum Specimen After Failure	25
22	Pole Figures Showing the Evolution of Texture of the (111) Poles of Sample G1	27
23	Pole Figures Showing the Evolution of Texture of the (200) Poles of Sample G1	28
24	Pole Figures Showing the Evolution of Texture of the (220) Poles of Sample G1	29
25	Pole Figures Showing the Evolution of Texture of the (311) Poles of Sample G1	30
26	Evolution of the Inverse Pole Figure Calculated Along the Normal Direction for Specimen G1	32
27	Evolution of the Inverse Pole Figure Calculated Along the Stress Direction for Specimen G1	33
28	Evolution of the Inverse Pole Figure Calculated Along the Transverse Direction for Specimen G1	34
29	The Ratio of the Intensity of the (200) Reflection to the (111) Orientation	35
30	SEM Images of Sample H4 as a Function of the Number of Fatigue Cycles	36

## LIST OF TABLES

Table		Page
1	Specimen Test Matrix	2
2	Tensile Stress Data for Samples Cut Parallel and Perpendicular to the Plate's Rolling Direction	3
3	Test Matrix for Groups A-C Specimens: Cycles per Step	6
4	Text Matrix Indicating the Number of Fatigue Cycles per Step and the Subsequent Examination Technique	26

## EXECUTIVE SUMMARY

This exploratory study investigates the role of texture development (preferred grain orientation) on crack initiation during fatigue cycling. The presence of texture in metals is known to relate/correlate to fatigue and the initiation of cracks. It has not been conclusively demonstrated, however, that texture will develop in a material simply due to cyclic stress. In this study, the development of texture during fatigue cycling of rolled aluminum 2024-T3 sheet was monitored using x-ray diffraction techniques (pole figures, inverse pole figures, and orientation distribution functions). The texture development was measured as a function of number of fatigue cycles to (1) determine whether texture develops as a material is fatigued and (2) to correlate the development of texture to crack formation.

X-ray diffraction measurements show that initially the rolling direction lies normal to the preferred plane on which grains are oriented. In Millers indices, the rolling direction and the normal plane are denoted as  $[100]$  and  $(100)$  respectively. Upon fatigue cycling, an initially rapid development of texture is found to occur. Prior to cracking, the grains rotate such that the  $[100]$  direction lies along the stress axis. This texture development appears dependent of the direction of the stress axis with respect to the rolling direction of the aluminum sheet, although the rate of texture change and the number of cycles to failure is dependent on specimen orientation. After crack initiation begins, the texture development slows and changes little until the point of failure. This shows that texture development does indeed occur with fatigue and plays a role in the development of cracks in the aluminum sheet. A more detailed study is required to develop a diagnostic test for proximity to crack initiation.

## 1. INTRODUCTION.

Fatigue is caused by repetitive stresses that lead to gradual microscopic changes in the material, which lead to the formation of dislocations and eventually the initiation of microcracks. These microcracks then propagate through the material on successive stress cycles and coalesce into larger cracks, eventually causing failure of the structure. This phenomenon is a cause for concern in the aerospace industry, since the failure of aircraft parts during flight can have catastrophic consequences. It is thus pertinent to establish a nondestructive preventative maintenance method for testing a material's likelihood for crack initiation.

The propagation of cracks through materials has been shown to depend on a number of factors, including the crystalline texture of the material. This texture is known to be sensitive to thermal and mechanical processing during part preparation [1]. It has been suggested that texture may also evolve during cyclic fatigue of a material [2]. Since texture is readily measured by x-ray diffraction, it should be relatively straightforward to determine whether texture development could be used as a benchmark to test for the proximity of a material to crack initiation.

The aim of this project was two-fold. Firstly, to determine whether the texture of a polycrystalline metal is affected by cyclic fatigue. This possibility was investigated in depth in a literature review (see appendix D). Secondly, if the texture does change with fatigue, does it track with the number of cycles? If so, then the texture evolution, combined with microscopic surface examination, would determine whether the threshold for crack initiation can be detected by means of texture measurements.

Two test procedures were used in this investigation. In the first procedure, the specimens were fatigued for a large number of cycles per step (20,000) until fatigue failure occurred. After each step, x-ray texture measurements were performed, and the orientation distribution function of the material was calculated. Surface cracks were investigated using a scanning electron microscope (SEM) to determine the main direction and pattern of crack growth in these specimens. In the second procedure, incremental steps were taken between 0 and 20,000 cycles to approach the onset of crack initiation more gradually. At each step, x-ray texture and SEM measurements were taken. After each procedure was completed, the texture and SEM data were evaluated. This will be described in more detail in sections 4 and 5.

## 2. EXPERIMENTAL DETAILS.

### 2.1 SPECIMEN DESCRIPTION.

All specimens used in this study were machined from 0.090" thick 2024-T3 aluminum plate provided by the Federal Aviation Administration (FAA). Fatigue specimens of suitable size to be mounted on the stage of the x-ray diffractometer were machined, following the pattern shown in figure A-1 of appendix A. Although it is normal to include a stress concentrator, such as a hole or notch in the gage region of fatigue specimens, this was not done in this study. This allowed for crack initiation throughout the gage region, thus increasing the possibility of observing cracking through the relatively bulk technique of x-ray diffraction. Furthermore, it allowed the onset of crack initiation to be approached gradually, increasing the possibility of observing texture evolution prior to crack initiation.

The preparation of metal plate through rolling is known to induce preferred grain orientations. To account for any effects of pre-existing texture on the results, specimens were machined at various angles to the rolling direction of the aluminum plate. Several specimens were made with their applied strain axes lying at 0°, 45°, and 90° to the rolling direction, as shown in figures A-2 and A-3 of appendix A. To increase the statistical significance of the data, more than one specimen was cut along each direction. Each specimen was given an identification code that corresponded to its orientation and fatigue pattern.

Table 1 lists the specimens used in this study by their identification code and purpose. Groups A (except sample A1), B (except sample B1), and C were used in the fatigue-to-failure tests, while groups G, H, and I were used in the incremental fatigue tests. This set of data is also included in table A-1 of appendix A for convenience. SEM studies were carried out on three of the specimens in the incremental fatigue tests (G4, H4, and I4) to measure the onset and progression of fatigue cracks. As will be discussed in greater detail, cracks initiated prior to 20,000 cycles, while approximately 100,000 cycles were required for failure.

TABLE 1. SPECIMEN TEST MATRIX

Sample ID	Specimen Orientation (0°)	Type of Test
A1	0	stress-strain
A2	0	fatigue to failure
A3	0	fatigue to failure
A4	0	fatigue to failure
B1	90	stress-strain
B2	90	<sup>†</sup> specimen damaged
B3	90	fatigue to failure
B4	90	fatigue to failure
B5	90	fatigue to failure
C1	45	fatigue to failure
C2	45	fatigue to failure
C3	45	fatigue to failure
G1	0	fatigue 22,000 cycles
G2	0	fatigue 22,000 cycles
G3	0	fatigue 22,000 cycles
G4	0	fatigue 22,000 cycles and SEM
H1	90	fatigue 22,000 cycles
H2	90	fatigue 22,000 cycles
H3	90	fatigue 22,000 cycles
H4	90	fatigue 22,000 cycles and SEM
I1	45	fatigue 22,000 cycles
I2	45	fatigue 22,000 cycles
I3	45	fatigue 22,000 cycles
I4	45	fatigue 22,000 cycles and SEM

<sup>†</sup>The grip region of specimen B2 was damaged during the first fatigue step and was excluded from the data set and replaced with specimen B5.

## 2.2 EXPERIMENTAL PROCEDURE.

### 2.2.1 Tensile Testing of Specimens to Determine Yield Strength.

The mechanical properties of a specimen cut from a rolled plate can be orientation-dependent due to rolling-induced texture in the plate. Thus, to determine the mean yield strength of the specimens, tensile testing was performed on samples cut parallel (A1) and perpendicular (B1) to the rolling direction. No yield strength testing was carried out on samples cut at 45° to the rolling direction, because it was assumed that their properties would be intermediate to those of A1 and B1. The yield strength values were used to determine the fatigue parameters used in this experiment. The results are summarized in table 2, with the results from sample B1 shown in figure 1.

TABLE 2. TENSILE TEST DATA FOR SAMPLES CUT PARALLEL AND PERPENDICULAR TO THE PLATE'S ROLLING DIRECTION

Specimen	Specimen Orientation	Shear Modulus (GPa)	Yield Strength (MPa)	Tensile Strength (MPa)	Elongation (%)	Area Reduction (%)
A1	0°	65	360	471	15.7	24.6
B1	90°	67	312	451	17.7	23.5

The maximum stress for the fatigue cycling measurements reported herein was chosen to be at the upper end of the elastic region, at 300 MPa. Samples were fatigued from 30-300 MPa per cycle, resulting in  $R = 0.1$ . This relatively large stress was chosen to reduce the total number of cycles to failure. A more detailed study would use a much lower maximum stress to obtain more data points.

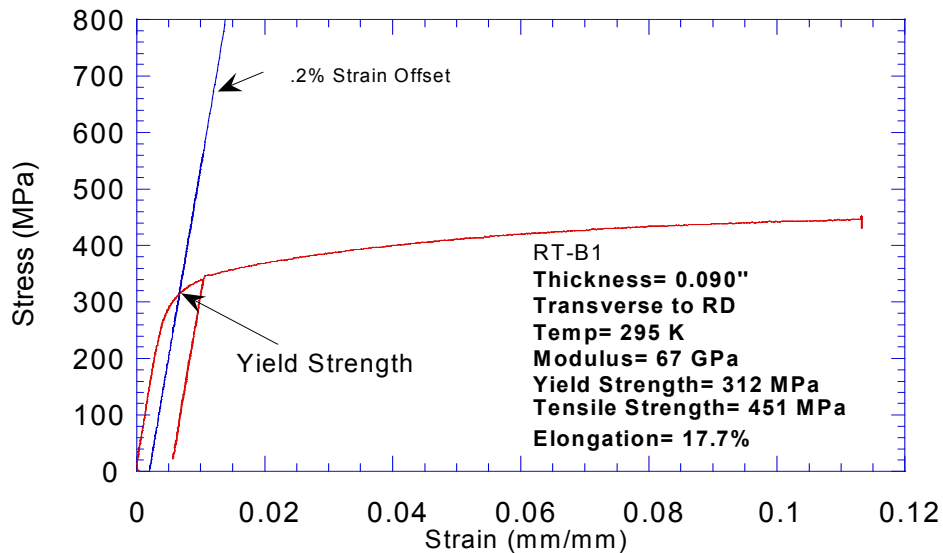


FIGURE 1. TENSILE STRESS-STRAIN CURVE FOR SPECIMEN B1

### 2.2.2 Fatigue Cycling.

Specimens were fatigued using a Fatigue Dynamics LFE 500 machine with a MS6000 Direct Stress attachment. Maximum and minimum stresses during the fatigue process were monitored using a computer during the fatigue cycling process. Samples of groups A (except sample A1), B (except sample B1), and C were fatigued in steps of 20,000 cycles at a frequency of 20 Hz until failure (approximately 100,000 cycles). Detailed x-ray measurements were performed between each successive step as described in section 3.

Sample groups G, H, and I were fatigued in steps of 2,000 cycles at a frequency of 4 Hz to a maximum of 22,000 cycles. The same maximum and minimum stresses were used as specimens A-C (except samples A1 and B1). After each step, detailed x-ray texture measurements were performed on three specimens from each group, while the surface of the fourth specimen was examined with an SEM for signs of crack initiation.

### 2.2.3 X-ray Texture Measurements.

Detailed x-ray texture measurements were carried out on a Philips Materials Research Diffractometer. This is a four-circle x-ray diffractometer capable of pole figure measurements. All measurements were performed using  $\text{CuK}\alpha$  radiation. The diameter of the x-ray spot on the sample surface was set to 2 mm to find an average texture over a number of grains. The center of each specimen was clearly marked and aligned with a pre-existing grid on the stage of the x-ray diffractometer. Thus, the texture in the center of the gage region of the specimen was measured, ensuring reproducibility of the alignment between successive fatigue steps.

At each step, pole figures were taken for the aluminum's (111), (200), (220), and (311) x-ray reflections for accurate calculation of the orientation distribution function (ODF). To improve accuracy, the pole figures were taken with a step size of 3 degrees rather than the customary 5 degrees. Following data collection, the pole figures were corrected, and the ODF was calculated. Since a number of the pole figures appear asymmetric, even after correction, the ODF was calculated for triclinic symmetry rather than for orthorhombic symmetry. This way, more of the measured texture information was retained to avoid the production of spurious texture elements. From each ODF, a series of inverse pole figures were generated. An inverse pole figure (IPF) plots the probability of a certain crystallite orientation lying along a fixed direction in the specimen. Since only 1/24 of the IPF is unique for a material with cubic symmetry, typically only a small triangular section, corresponding to the smallest symmetry unit, is plotted. As shown in figure 2, each corner of the IPF corresponds to a certain crystallite orientation. Figure 2(a) shows the normal IPF for a specimen with (100)<110> symmetry, while figures 2(b) and 2(c) show the corresponding rolling and transverse pole figures. The nomenclature  $(hkl)\langle uvw \rangle$  is commonly used for a rolled material, where  $(hkl)$  are the Miller indices of the lattice planes parallel to the surface of the rolled specimen, and  $\langle uvw \rangle$  is the lattice vector lying along the rolling direction.

From the location of the poles or regions of higher intensity in an inverse pole figure, one can deduce the preferred orientation, or texture, present in the specimen. This information can also be obtained from the orientation distribution function, which is a more complete representation



of the texture. Both types of data will be presented in this analysis as well as the interpretation based on the original pole figures.

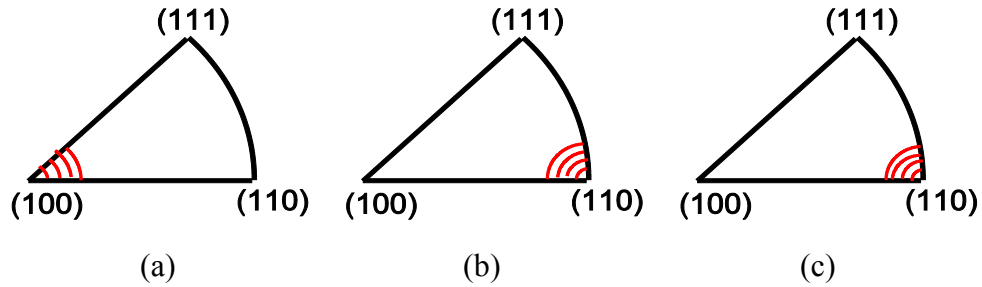


FIGURE 2. SCHEMATIC DIAGRAM OF INVERSE POLE FIGURES FOR A (100)<110> ROLLED METAL PLATE (a) ALONG THE DIRECTION NORMAL TO THE SHEET, (b) ALONG THE ROLLING DIRECTION, AND (c) ALONG THE TRANSVERSE DIRECTION

The evolution of the intensity of the (111), (200), and (220) reflections as a function of distance from the center of the gage region (parallel to the strain direction) was also measured with simple  $\theta/2\theta$  scans as a first principles method of determining the evolution of preferred orientation with strain.

#### 2.2.4 Microscopy.

Scanning electron microscopy was performed at the National High Magnetic Field Laboratory. The gage region of each specimen was examined using an Electroscan Model E-3 Environmental Scanning Electron Microscope (ESEM). The ESEM is a conventional SEM with a variable specimen environment. The microscope operates up to 30 kV, with magnifications from 50x to 200,000x, resolution of 4 nm and LaB<sub>6</sub> electron source gun. The ESEM is equipped with a high-resolution imaging archive system, a Princeton Gamma-Tech energy dispersive x-ray and imaging analysis system, and a backscattered electron detector.

### 3. RESULTS: FATIGUE UNTIL FAILURE.

#### 3.1 TEST MATRIX.

Table 3 details the test matrix for each specimen in the measurement set. Each sample fractured after a different number of fatigue cycles, with the C samples having the shortest lifetime. The lifetime of each sample is shown explicitly in figure 3. The shorter lifetimes of B3-B5 are not surprising since this orientation had a slightly lower yield strength than the samples with the stress axis parallel to the rolling direction.

TABLE 3. TEST MATRIX FOR GROUPS A-C SPECIMENS: CYCLES PER STEP

Specimen	Step 1	Step 2	Step 3	Step 4	Step 5	Step 6	Step 7
A2	22000	20000	20000	20000	20000	20000	14200*
A3	22000	20000	20000	20000	20000	20000	8000*
A4	22000	20000	20000	20000	20000	20000	700*
B3	22000	20000	20000	20000	19700*		
B4	22000	20000	20000	20000	15000*		
B5	22000	20000	20000	20000	13900*		
C1	22000	20000	20000	17300*			
C2	22000	20000	20000	20000	8900*		
C3	22000	20000	20000	20000	13000*		

\* = number of cycles at failure

Maximum Stress: 300 MPa, Minimum Stress: 30 MPa, Cycling Frequency: 20 Hz

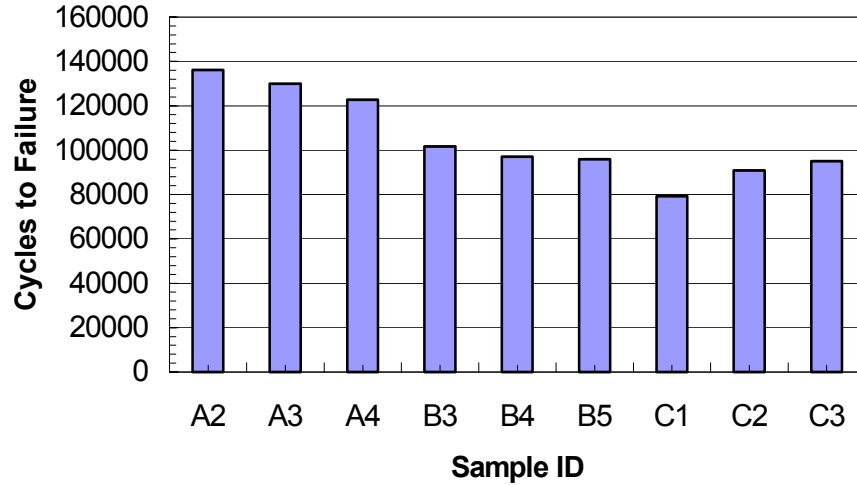


FIGURE 3. THE DEPENDENCE OF THE NUMBER OF CYCLES TO FAILURE ON SPECIMEN ORIENTATION

## 3.2 TEXTURE EVOLUTION.

### 3.2.1 Pole Figure Analysis.

Before the effect that the strain has on the orientation of the crystallites of the aluminum sample can be understood, it is necessary to understand the orientation of the crystallites in unstressed aluminum. A similar understanding of the orientation in stressed aluminum then gives an understanding of the effect of the applied strain.

Figure 4(a) shows an ideal  $\{111\}$  pole figure for a (100)-oriented single crystal of aluminum, i.e., one for which the  $[100]$  direction is normal to the sample. Only angles of either  $70^\circ$  or  $109^\circ$  are possible between the various  $\{111\}$  poles. For example, the angles between the  $(111)$  and  $(11\bar{1})$

poles and between the  $(111)$  and  $(1\bar{1}1)$  poles are both  $70^\circ$ , while the angle between the  $(111)$  and  $(1\bar{1}\bar{1})$  poles is  $109^\circ$ . Figure 4(b) shows the corresponding  $\{200\}$  pole figure. Since this crystal is  $\{100\}$  oriented, the  $(200)$  pole is in the center. For a cubic material like aluminum, the angle between the  $\{200\}$  poles is fixed at  $90^\circ$ , thus, the other  $\{200\}$  poles are  $90^\circ$  away from the center at the edge of the  $(200)$  pole figure. It should also be noted that since the angle between the  $\{111\}$  and  $\{100\}$  planes can be shown to be  $54.7^\circ$ , i.e., each of the  $\{111\}$  poles is  $54.7^\circ$  from the center of the  $\{111\}$  pole figure for this particular orientation of aluminum. In the pole figures below, the concentric circles denote tilt ( $\psi$ ) angles of  $30^\circ$ ,  $60^\circ$ , and  $90^\circ$  from the normal direction. The angle of rotation about the normal direction ( $\phi$ ) varies from  $0^\circ$  to  $360^\circ$  around the circumference of the figure. The  $\phi = 0$  location is taken to be at the  $(002)$  pole on the right of figure 4(b) and increases counterclockwise. In all the pole figures shown, the  $\phi = 0$  location indicates the strain axis, while  $\phi = 90$  the transverse direction.

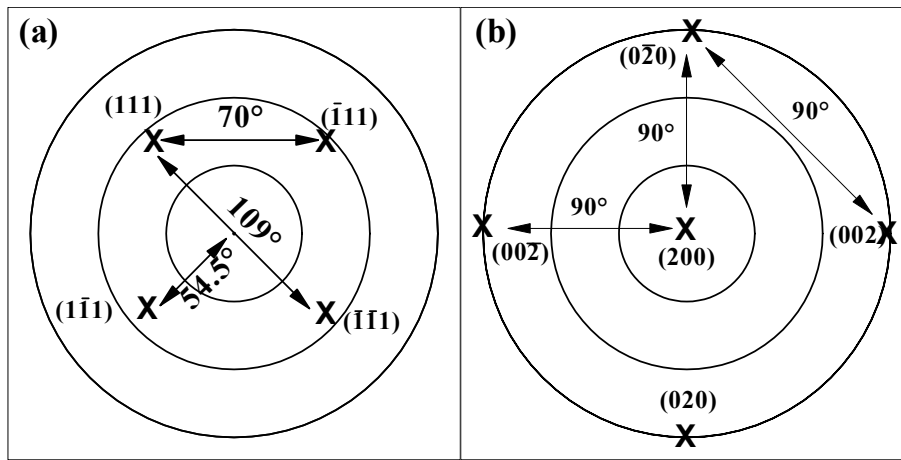


FIGURE 4. (a) THE  $\{111\}$  AND (b)  $\{200\}$  POLE FIGURES FOR AN IDEAL  $(100)$ -ORIENTED SINGLE CRYSTAL OF ALUMINUM

Similar pole figures can be generated to show the positions of the  $\{110\}$  and  $\{311\}$  poles, and similar restrictions on the possible angles between the planes, both within the one pole figure and between pole figures can be found. For a  $\{110\}$  pole figure, the only possible angles between  $\{110\}$  poles for a cubic material such as aluminum are  $60^\circ$  and  $90^\circ$ ; for a  $\{311\}$  pole figure, the possible angles are  $0^\circ$ ,  $35.1^\circ$ ,  $50.5^\circ$ ,  $63^\circ$ , and  $84.8^\circ$ .

If the orientation of the crystal changes so that the  $[100]$  direction is no longer normal, the position of all of the poles alters. However, the angles between the planes remain the same. For example, on the  $\{111\}$  pole plot (figure 4(a)), although the position of the  $\{111\}$  poles alters, the angle between the  $\{111\}$  poles always remains either  $70^\circ$  or  $109^\circ$ , and the angles between the  $\{111\}$  and  $\{100\}$  planes remains  $54.7^\circ$ .

Figure 4 shows the pole figure for a single crystallite of aluminum. In a practical sample there are numerous such crystallites that may or may not be similarly oriented. Should the crystallites be extremely highly oriented along the same direction, measured pole figures will be similar to figure 4. However, as disorder develops in the orientation of the various crystallites, a

broadening of the poles in the pole figure will result. Normally, there exists an additional number of other orientations of the crystallites besides the one shown in figure 4. Typically, these different orientations will be at significantly different angles to each other, and since each orientation will have its own set of poles in each pole figure, many regions of increased intensity will result. For example, the  $\{111\}$  pole figure from a single crystal will have four regions of increased intensity. If there are two crystallites, there are likely to be eight regions of increased intensity, etc. However, less than eight poles may result for poles that coincide. In a sample made from a large number of crystallites that were randomly oriented to each other, no regions of increased relative intensity would occur. Rather, a uniform intensity would be observed over the whole pole figure.

Since all of the specimens were cut from the same sheet of material, the initial texture is the same for all specimens. Figure 5 shows the  $\{111\}$  pole figure of the unstressed sample A2. Five regions of strong intensity are observed. Regions 1 and 2 have been further divided into regions A, B, C, D, and E, as labeled in figure 5. Each region in figure 5 corresponds to the  $\{111\}$  poles from different crystallites. The angles between regions 1 and 2 and regions 1 and 3 are approximately  $70^\circ$  and  $109^\circ$  respectively. Thus, if the poles in region 1 are assumed  $(111)$ , then those in region 2 are either  $(11\bar{1})$  or  $(1\bar{1}1)$ , and those in region 3 are  $(1\bar{1}\bar{1})$ .

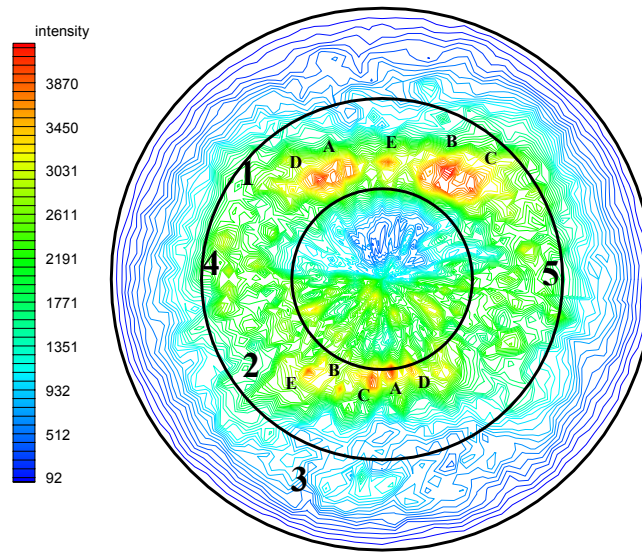


FIGURE 5. THE  $\{111\}$  POLE FIGURE OF SAMPLE A2 PRIOR TO FATIGUE CYCLING

Figure 6 shows the measured  $\{200\}$  poles for the same sample. Most of the intensity from the  $\{200\}$  poles is located in one region, labeled 1, with several less intense regions (2 to 5) scattered with no obvious connection between them.

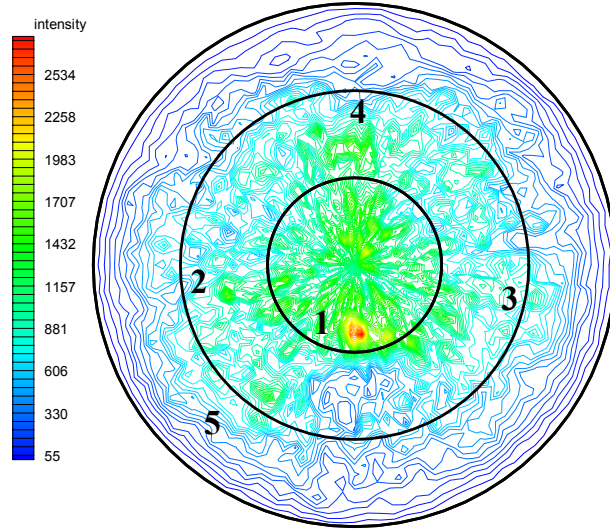


FIGURE 6. THE  $\{200\}$  POLES FOR THE SAME UNSTRESSED SAMPLE A2 AS IN FIGURE 5

Analysis of the (111) and (200) pole figures suggest that there are three major orientations of crystallites in the unstressed aluminum sample together with broadening effects for each orientation.

- The first orientation  $[(611)\langle 110 \rangle]$  has the (100) planes tilted at approximately  $18^\circ$  to the normal along the transverse direction with a  $\pm 2^\circ$  spread along the rolling direction. In plane, the  $\langle 011 \rangle$  directions are parallel to the rolling direction with a  $\pm 15^\circ$  spread about the rolling direction. This means that for this orientation, the  $[611]$  direction is approximately normal to the sample surface. The analysis is given below.

Lines (similar to figure 4), from poles in figure 5 whose angles are  $109^\circ$ , drawn from region 1 (A, B, C, D, E) towards region 3 and passing through the point corresponding to the  $\{200\}$  poles of figure 6 terminate in region 3 at points consisting of higher intensity compared to the background. This indicates that those points in regions 1 and 3 belong together, and they come from crystallites all of whose orientations have their corresponding (100) plane at point 1 in figure 6. If points in region 1 are assumed (111), then those in region 3 are  $(1\bar{1}\bar{1})$ .

The  $(11\bar{1})$  and  $(1\bar{1}1)$  poles of the crystallites for the  $[(611)\langle 110 \rangle]$  orientation are at positions 4 and 5, respectively, in figure 5. Similar to the  $(1\bar{1}\bar{1})$  poles at position 3, these poles are spread out with similar intensity to those of region 3. This suggests that the poles at position 1 are strong because they coincide with the second and third orientations (see figure 7). That is, the (111) poles of the  $[(611)\langle 110 \rangle]$  orientations of crystallites happen to coincide with the (111) poles of a second and third orientations of crystallites at position 1. It is either the  $(11\bar{1})$  or the  $(1\bar{1}1)$  poles of the second and third orientation/crystallites that produce the intensity at positions 2 (A, B, C, and D).

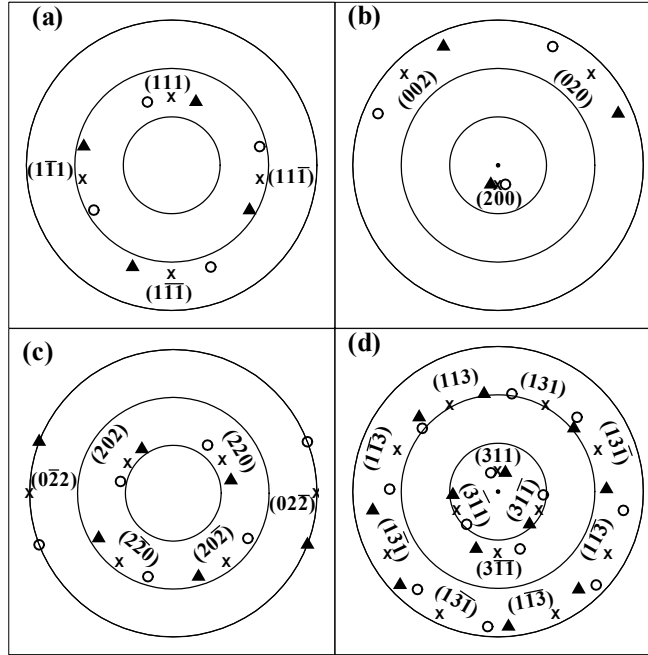


FIGURE 7. THE IDEAL THEORETICAL POLE PLOT FOR THE (a) (111), (b) (200), (c) (220), AND (d) (311) POLES OF THE FIRST ORIENTATION

The calculated pole figures for this orientation are shown in figure 7(a)-(d). From figure 7(b) it can be seen that the (100) planes are tilted by  $18^\circ$  to the normal direction (ND) along the transverse direction (TD), and have a  $\pm 2^\circ$  spread along the rolling direction (RD). The (010), and (001) planes are at  $45^\circ$  and  $135^\circ$  to both the RD and TD, respectively, each with a  $\pm 0^\circ$  spread in  $\phi$ . Equivalently, figure 7(c) shows that the (011) planes are parallel to the RD with a spread of  $\pm 20^\circ$  in  $\phi$ . Further analysis shows that the [611] directions are approximately normal to the sample surface. Figure 8 shows a schematic view of this orientation.

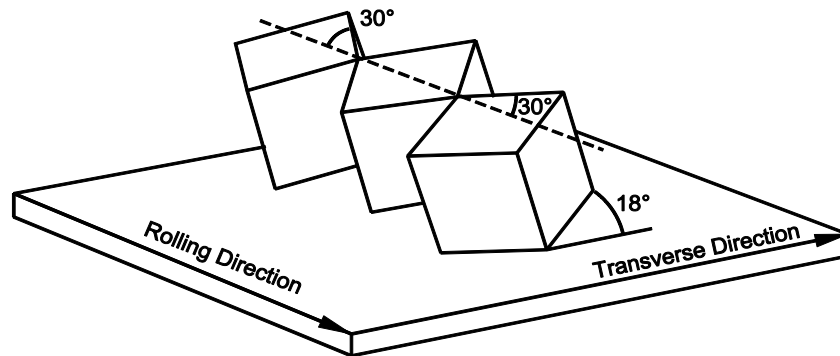


FIGURE 8. THREE CUBES OF ALUMINUM TIPPED  $18^\circ$  FROM NORMAL ALONG THE TRANSVERSE DIRECTION AND TWISTED  $15^\circ$  BOTH CLOCKWISE AND ANTICLOCKWISE ABOUT THE TRANSVERSE DIRECTION

- The second orientation (see figure 9(a)-(d)) is approximately (110) plane. For this orientation, the (111) pole occurs at position 1A of figure 5. From the  $(11\bar{1})$  pole at position 2A, the position of the  $(1\bar{1}1)$  and the  $(1\bar{1}\bar{1})$  poles are at  $\psi$  values just greater than  $85^\circ$ . This is a region that is difficult for the x-ray diffractometer to measure due to physical constraints, and thus, these poles are not visible. The  $\{200\}$  pole figure has the  $(00\bar{2})$  pole at  $\psi$  of  $83^\circ$  and  $\phi$  of  $270^\circ$ ; the (200) pole is at  $\psi$  of  $45^\circ$  and a  $\phi$  of  $173^\circ$ ; the (020) pole is at  $\psi$  of  $45^\circ$  and  $\phi$  of  $7^\circ$ ; both with a  $\pm 20^\circ$  spread in  $\phi$ .

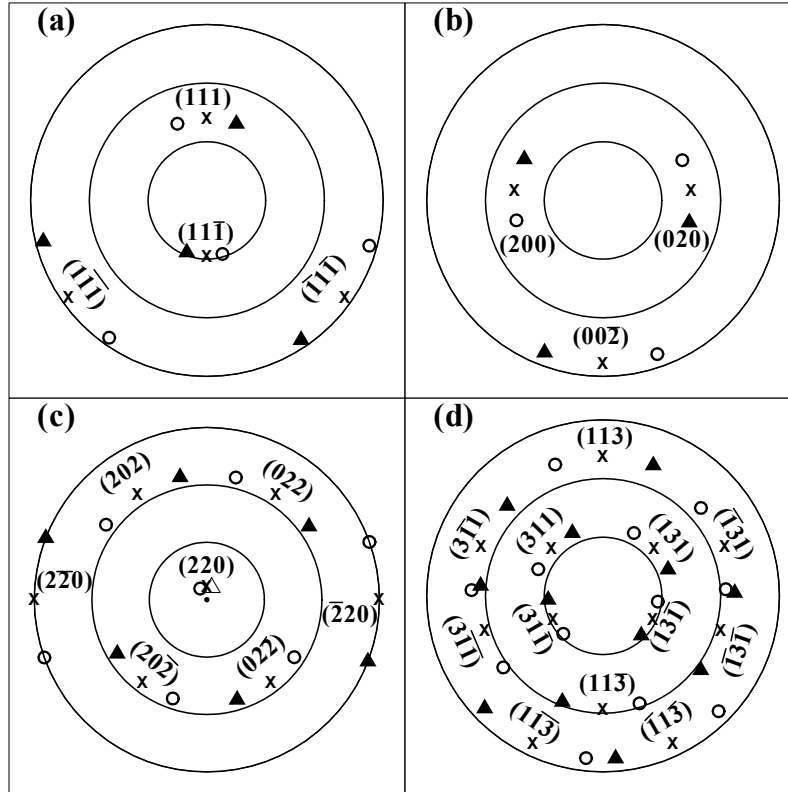


FIGURE 9. THE IDEAL THEORETICAL POLE PLOT FOR THE (a) (111), (b) (200), (c) (220), AND (d) (311) POLES OF THE SECOND ORIENTATION

Thus, the center of the crystallites of the second orientation is essentially (110) oriented, except that it is rotated  $7^\circ$  from the ND toward the TD with a spread of  $\pm 2^\circ$  in  $\psi$ . The  $\langle 001 \rangle$  direction is at  $45^\circ$  to both the normal and rolling directions and is also canted  $7^\circ$  towards the transverse direction with a  $\phi$  spread of  $\pm 20^\circ$ . Furthermore, the  $(\bar{1}10)$  planes are along the rolling direction with a spread of  $\pm 20^\circ$  in  $\phi$ . Further analysis shows that the  $[66\bar{1}]$  directions are approximately normal to the sample surface. Thus, the second orientation is  $(66\bar{1})\langle \bar{1}10 \rangle$ .

- For the third orientation (see figure 10(a)-(d)), the (111) pole occurs at position 1A of figure 5. From the  $(11\bar{1})$  pole at position 2B, the position of the  $(1\bar{1}1)$  and  $(1\bar{1}\bar{1})$  poles are at  $\psi$  values, a little greater than  $75^\circ$ . As for the second orientation, this is a region





In conclusion, the initial texture of the aluminum tested in this study has the  $\langle 110 \rangle$  direction preferentially along the rolling direction of the material, with a variety of planes normal to the surface of the material.

Figures 11-14 show the change in specimen A2 as it is fatigued. Figures 11(a), 12(a), 13(a), and 14(a) show the measured (111), (200), (220) and (311) pole figures for the virgin specimen. The evolution of the texture can be seen in the changes from parts (a) to (h) of figures 11-14. The broad distribution of texture shown in figures 11(a) and 13(a) is reduced in figures 11(b) and 13(b) respectively, as the crystallites rotate in plane to align preferentially with the [100] direction along the strain axis. Figure 14(a) shows a relatively small peak that is spread into line of intensity along the stress axis as a function of fatigue cycles. In figure 12, the (200) poles are pulled towards the center of the pole figure, rather than being localized near  $\psi = 30$  degrees. This means that the (100) planes of the aluminum are being pulled parallel to the sample surface. Corresponding changes take place in the (111), (220), and (311) pole figures. The crystallites orient themselves with a primarily (100) orientation, and also align themselves in the plane, as can be seen by the evolution of four regions of high relative intensity in the (111) and (220) pole figures. From the orientation of these (111) and (220) poles, the in-plane orientation can be determined to have  $\langle 100 \rangle$  directions along the stress and transverse directions. The same evolution of the pole figures is seen in samples A3 and A4.

The measured pole figures for samples B3-B5 are similar to those of samples A2-A4, except that the features have been rotated by  $90^\circ$  as expected, since they were cut with their stress axes at  $90^\circ$  to the rolling direction. The evolution of the pole figures is similar to that of specimens A2-A4, with the (100) planes rotating to lie parallel to the specimen surface, and the  $\langle 100 \rangle$  directions along the stress and transverse directions (see appendix B).

The samples that were cut with their stress axis at  $45^\circ$  to the rolling direction show a remarkable lack of texture evolution. There is a slight smearing out of the regions of higher intensity in the pole figures for specimens C1-C3 (appendix B), but there is no sign of the development of (100) texture that is visible in the other specimens. Curiously, these samples fractured at the lowest number of cycles. This suggests that the stress direction already lay along the weakest direction in the crystallites, and perhaps cracking was initiated prior to texture change in this special direction. With the initial orientation as described above, the sample would have been cut at  $45^\circ$  to the  $\langle 110 \rangle$  directions and, thus, approximately along the [100] direction. Samples A2-A4 and B3-B5 fracture after the [100] direction has rotated along the strain axis. This suggests that for samples C1-C3 the presence of (100) texture already along the stress direction is the cause of the fatigue cracking at lower fatigue cycles.

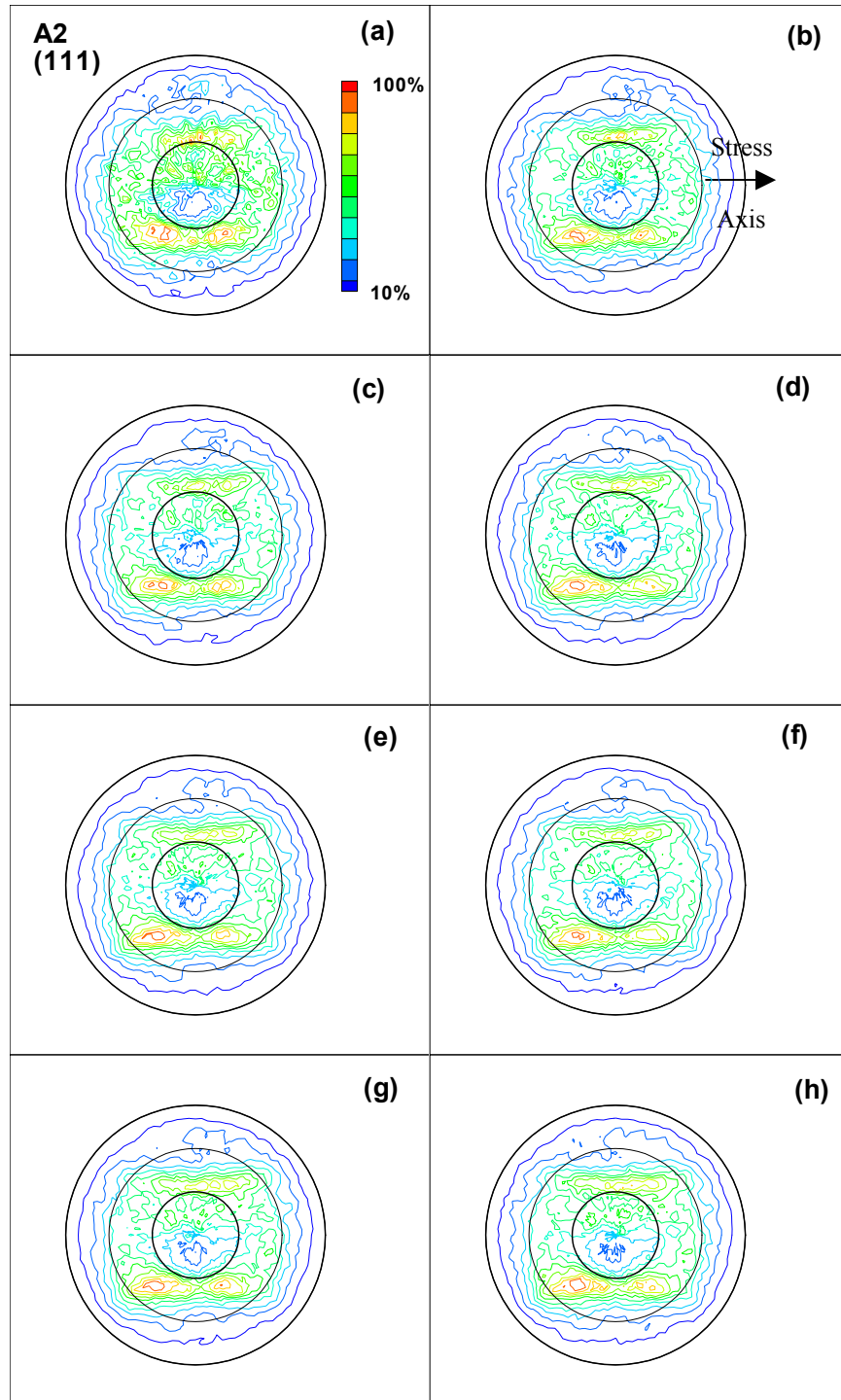


FIGURE 11. THE (111) REFLECTIONS OF SPECIMEN A2 AS A FUNCTION OF NUMBER OF FATIGUE CYCLES (a) VIRGIN SAMPLE, (b) 22,000 CYCLES, (c) 42,000 CYCLES, (d) 62,000 CYCLES, (e) 82,000 CYCLES, (f) 102,000 CYCLES, (g) 122,000 CYCLES, AND (h) AFTER FRACTURE

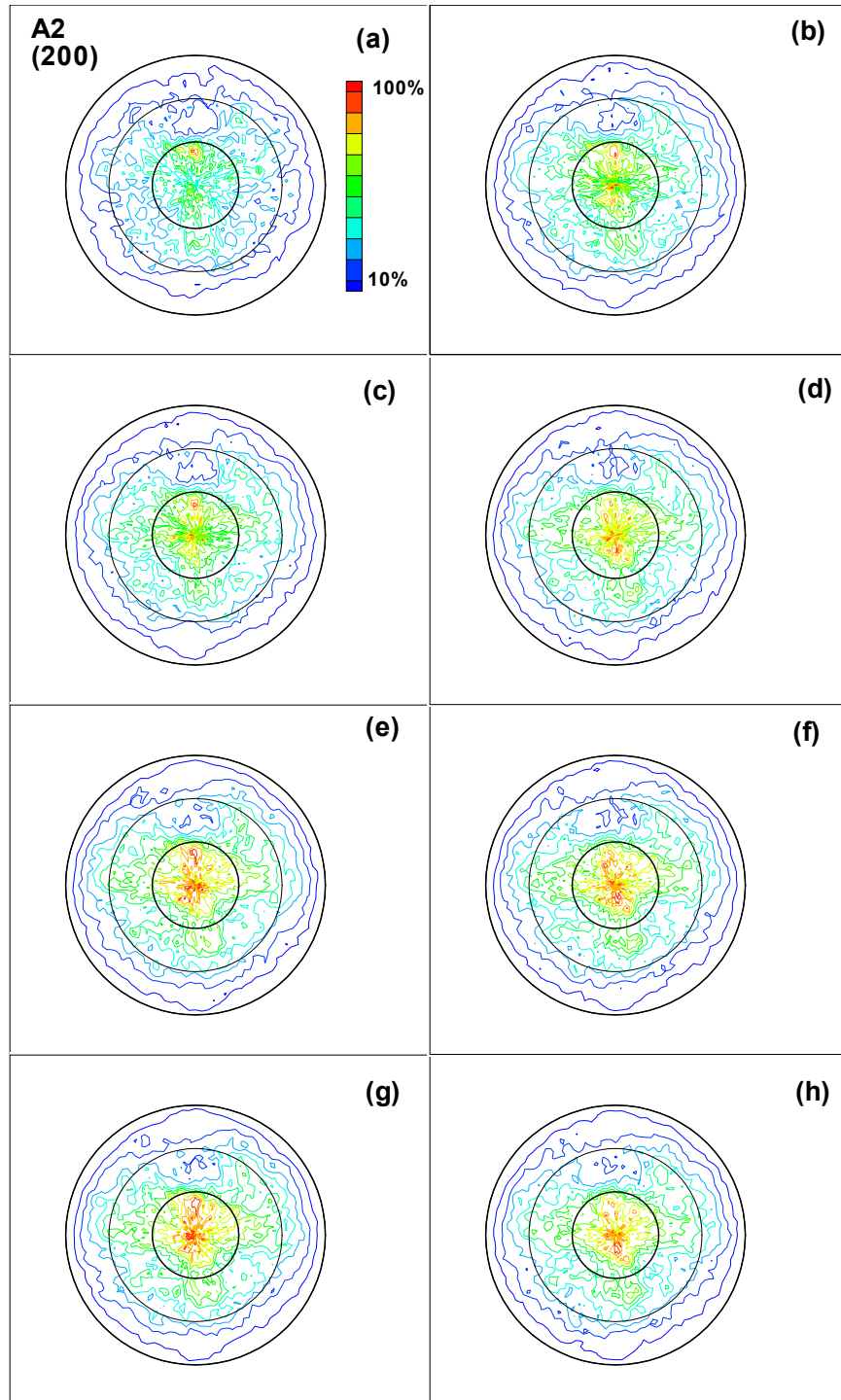


FIGURE 12. THE (200) REFLECTIONS OF SPECIMEN A2 AS A FUNCTION OF NUMBER OF FATIGUE CYCLES (a) VIRGIN SAMPLE, (b) 22,000 CYCLES, (c) 42,000 CYCLES, (d) 62,000 CYCLES, (e) 82,000 CYCLES, (f) 102,000 CYCLES, (g) 122,000 CYCLES, AND (h) AFTER FRACTURE

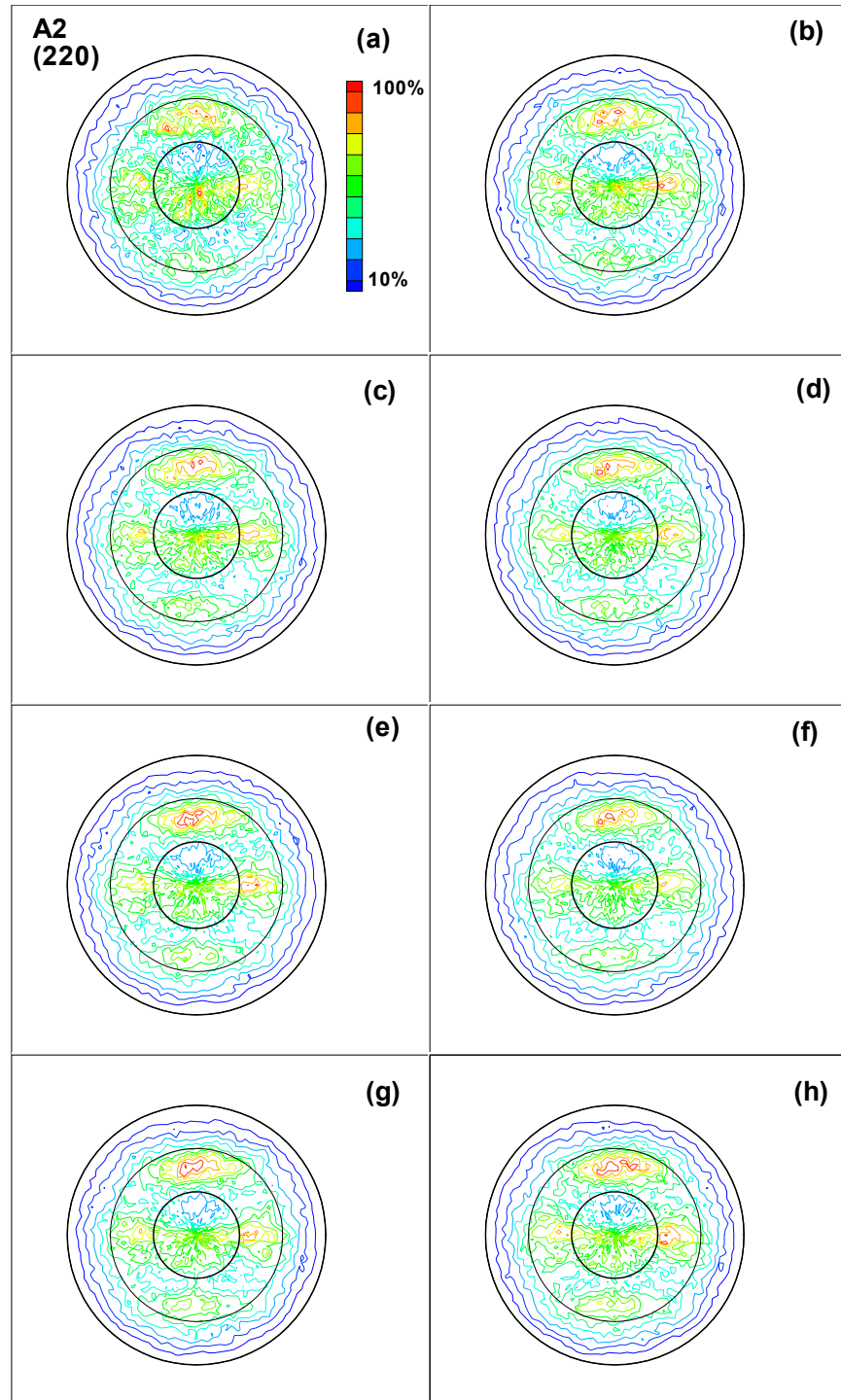


FIGURE 13. THE (220) REFLECTIONS OF SPECIMEN A2 AS A FUNCTION OF NUMBER OF FATIGUE CYCLES (a) VIRGIN SAMPLE, (b) 22,000 CYCLES, (c) 42,000 CYCLES, (d) 62,000 CYCLES, (e) 82,000 CYCLES, (f) 102,000 CYCLES, (g) 122,000 CYCLES, AND (h) AFTER FRACTURE

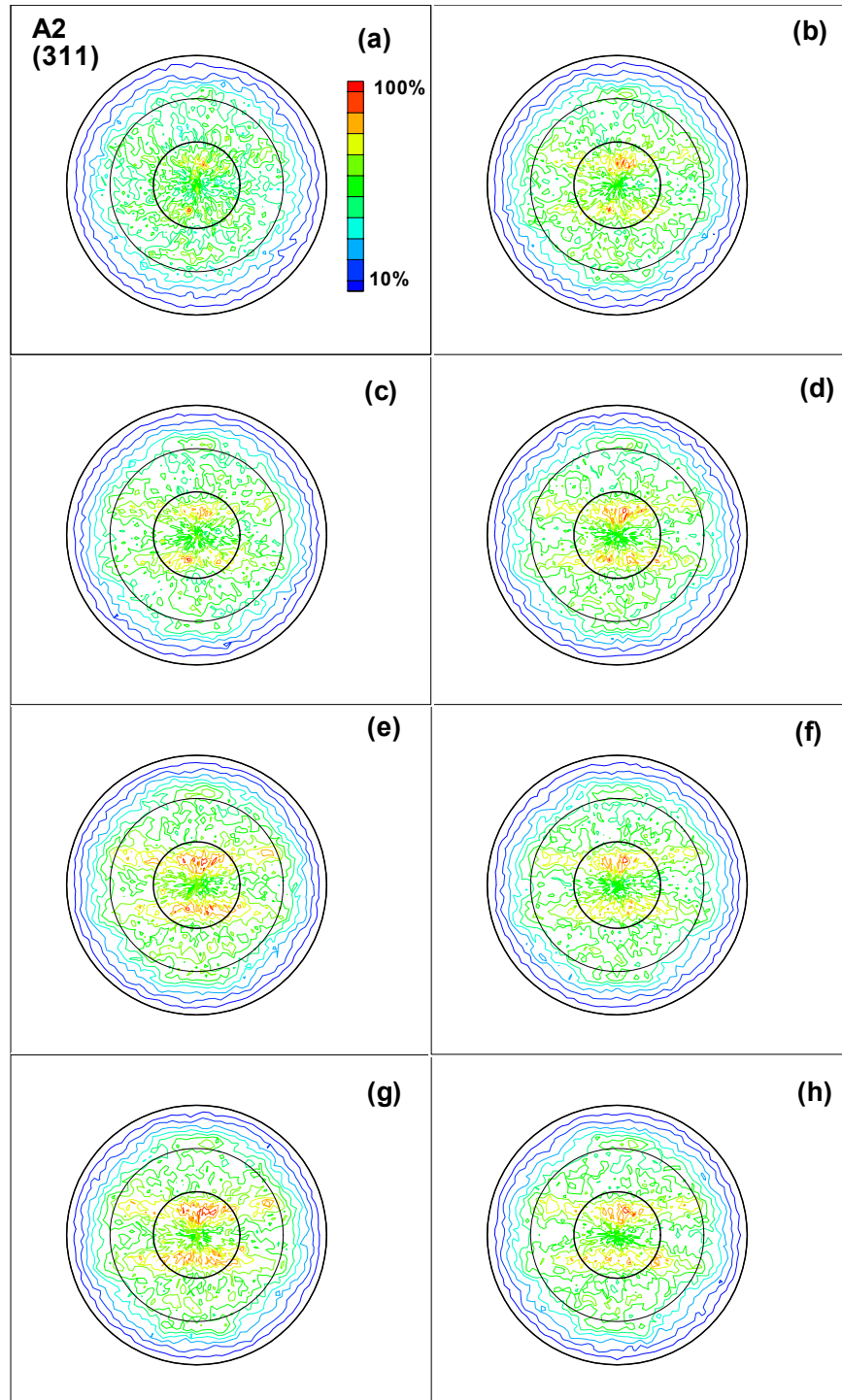


FIGURE 14. THE (311) REFLECTIONS OF SPECIMEN A2 AS A FUNCTION OF NUMBER OF FATIGUE CYCLES (a) VIRGIN SAMPLE, (b) 22,000 CYCLES, (c) 42,000 CYCLES, (d) 62,000 CYCLES, (e) 82,000 CYCLES, (f) 102,000 CYCLES, (g) 122,000 CYCLES, AND (h) AFTER FRACTURE

### 3.2.2 Orientation Distribution Function.

The evolution of the ODF for this same sample (A2) is plotted in figure 15. Several constant  $\theta$  sections are plotted (in Roe units) for varying amounts of fatigue. The streaks of intensity in the virgin specimen along the  $\psi$  axis indicate a fixed plane parallel to the surface of the specimen, but a random distribution of directions in plane. As the number of cycles increase, these streaks shrink into spots along the  $\psi$  axis, indicating the evolution of a preferred orientation along the stress axis. The location of the spots is at  $\psi$  values of  $0^\circ$ ,  $90^\circ$ ,  $180^\circ$ , and  $360^\circ$  and are highly symmetric, which again indicates the presence of preferred orientation, and is consistent with the broad regions in the pole figures breaking down into smaller, more intense regions. There is no sign in the ODF's calculated for this material of the typical orientations found in a face-centered cubic material. Thus, an attempt was not made to analyze the texture directly from the ODF. Instead, the texture evolution was looked at in inverse pole figures calculated from the ODF at each step in the fatigue process.

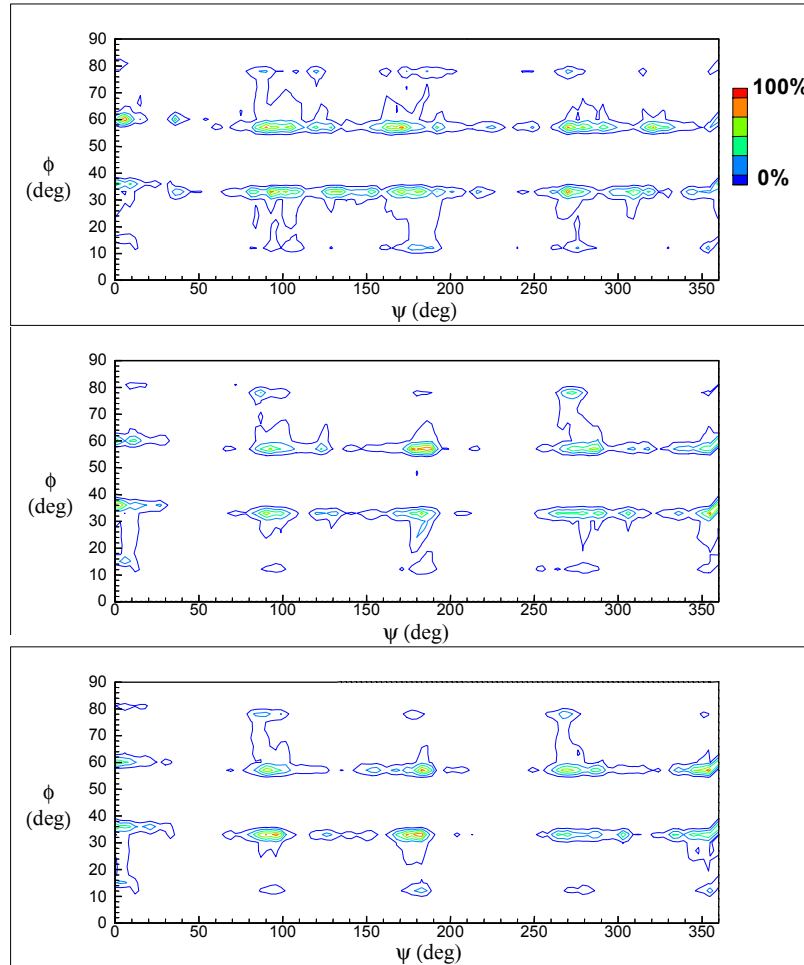


FIGURE 15. A CONSTANT  $\theta = 9.0^\circ$  SLICE OF THE ORIENTATION DISTRIBUTION FUNCTION FOR SPECIMEN A2 AS A FUNCTION OF FATIGUE CYCLING, (TOP) VIRGIN SPECIMEN, (MIDDLE) AFTER 22,000 CYCLES, AND (BOTTOM) AFTER FRACTURE

### 3.2.3 Inverse Pole Figures.

Although, in broad terms the inverse pole figures agree with the pole figures described in section 2, there is more disagreement. This is attributed to the assumptions made while converting pole figure data to inverse pole figures. Note the distinction between pole figures and inverse pole figures. Pole figures are recorded directly from the x-ray diffractometer and have had no mathematical manipulations performed on them. They are measurements of intensity as a function of the angles  $\phi$  and  $\psi$ . The inverse pole figures assume that the sample, in this case aluminum, has cubic symmetry and that the information within 1/24 of the stereographic projection is identical to all other similar regions. This is not true especially for a uniaxial material which has been strained. In making this assumption, a considerable amount of information has to be discarded; in particular, just the information that is most likely to show the changes to the aluminum induced by a stress. Principally, the difficulty arises in the assumed four-fold symmetry of the data, which clearly is not present in the pole figures of figures 11-14. To calculate the ODF and the inverse pole figures, corrections are made to symmetrize the measured pole figures. Thus, in this case, the inverse pole figures do not reflect the entire change seen with complete accuracy. However, there are some similarities that can be observed that would be easier to interpret inverse pole figures than direct pole figures. An interpretation of the inverse pole figures for samples A-C is given below.

Figures 16-18 show IPF calculated from the ODF for specimen A2. Figure 16 shows IPF calculated along the z direction, which corresponds to the direction normal to the specimen. In figure 16, the distribution of planes parallel to the surface of the specimen shows little variation. The only significant change observed is a decrease in the intensity near the (110) corner, corresponding to a rotation of the (916) planes out of the sample surface. Generally, from the pole figure analysis, one would expect to see a large increase in the intensity at the (100) corner of the figure, but it is not observed. In fact, very little change is in the normal IPF for any of the specimens (appendix B). In the inverse pole figure there are two spots of higher intensity. The first weak spot along the line joining (100) to (111) corresponds roughly to the first orientation in the virgin specimen, i.e., (611). The second weak spot, close to the (110) corner, corresponds to a (916) orientation, very different from any of the orientations derived from the direct pole figures. The only observable change with fatigue is that this second spot gradually disappears as the number of cycles increases.

Figure 17 shows inverse pole figures taken along the strain axis in the plane of the specimen. The intensity throughout the IPF for the virgin specimen moves toward the (100) corner and away from both the (110) and (111) corners, which is consistent with the rotation of the (100) planes along the strain direction. The intensity centered along the line leading from (110) to (111) disappears before 22,000 cycles. Figure 18 shows inverse pole figures along an axis perpendicular to the strain direction, the transverse direction. There is a little change in the pole density as a function of fatigue. An interpretation of the pole figure measurements, in figures 17 and 18 one would expect to see a large intensity around the (110) corner initially moving slowly toward the (100) direction. This initial orientation is not seen; however, there is a broad intensity contour roughly midway along the line joining (110) to (111), corresponding roughly to a (212) plane. The offset at the location of this peak may be due to the broadening of the pole figure measurements caused by the distribution of crystallite orientations. Other than this, there is a relatively high intensity distributed throughout the IPF. There is a clear change in these figures,



consistent with the rotation of grains in plane. The (212) peaks vanish between 0 and 22,000 cycles, and most of the intensity in the IPF shifts to the (100) corner. This is consistent with the pole figure analysis. There is less change observed along the transverse direction, indicating that the applied stress is the driving mechanism for the reorientation of the crystallites. In the transverse direction, the initially strong intensity near the center of the IPF (roughly a (123) orientation) becomes broader.

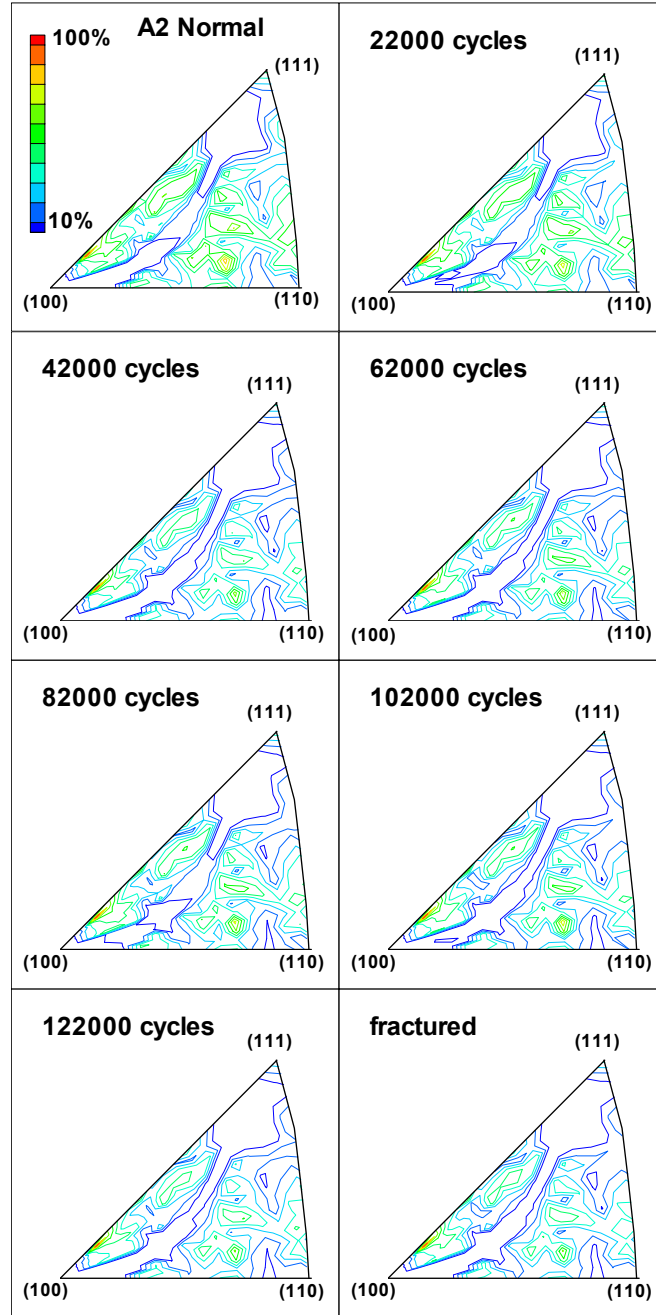


FIGURE 16. INVERSE POLE FIGURES SHOWING THE DISTRIBUTION OF CRYSTALLOGRAPHIC AXES WITH RESPECT TO AN AXIS NORMAL TO THE SURFACE OF SPECIMEN A2



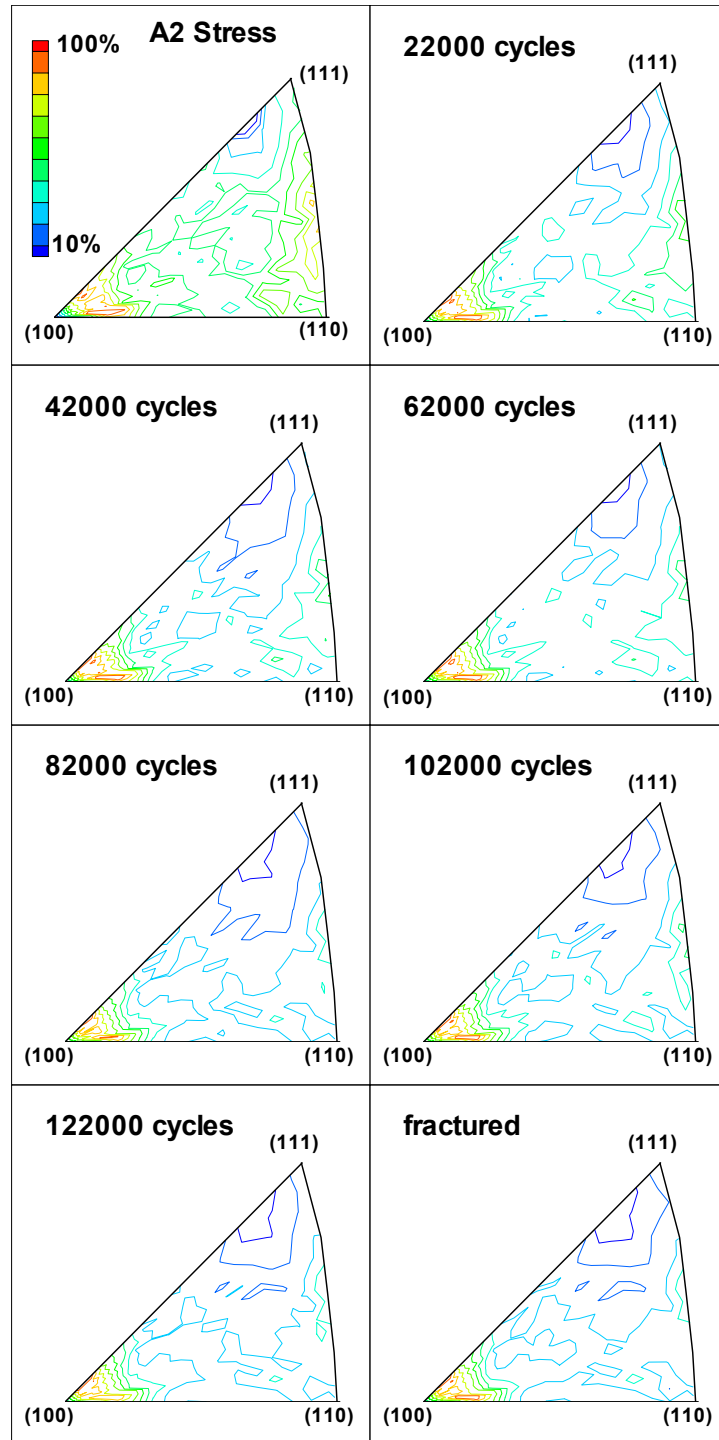


FIGURE 17. INVERSE POLE FIGURES SHOWING THE DISTRIBUTION OF CRYSTALLOGRAPHIC AXES WITH RESPECT TO AN AXIS PARALLEL TO THE STRAIN AXIS OF SPECIMEN A2

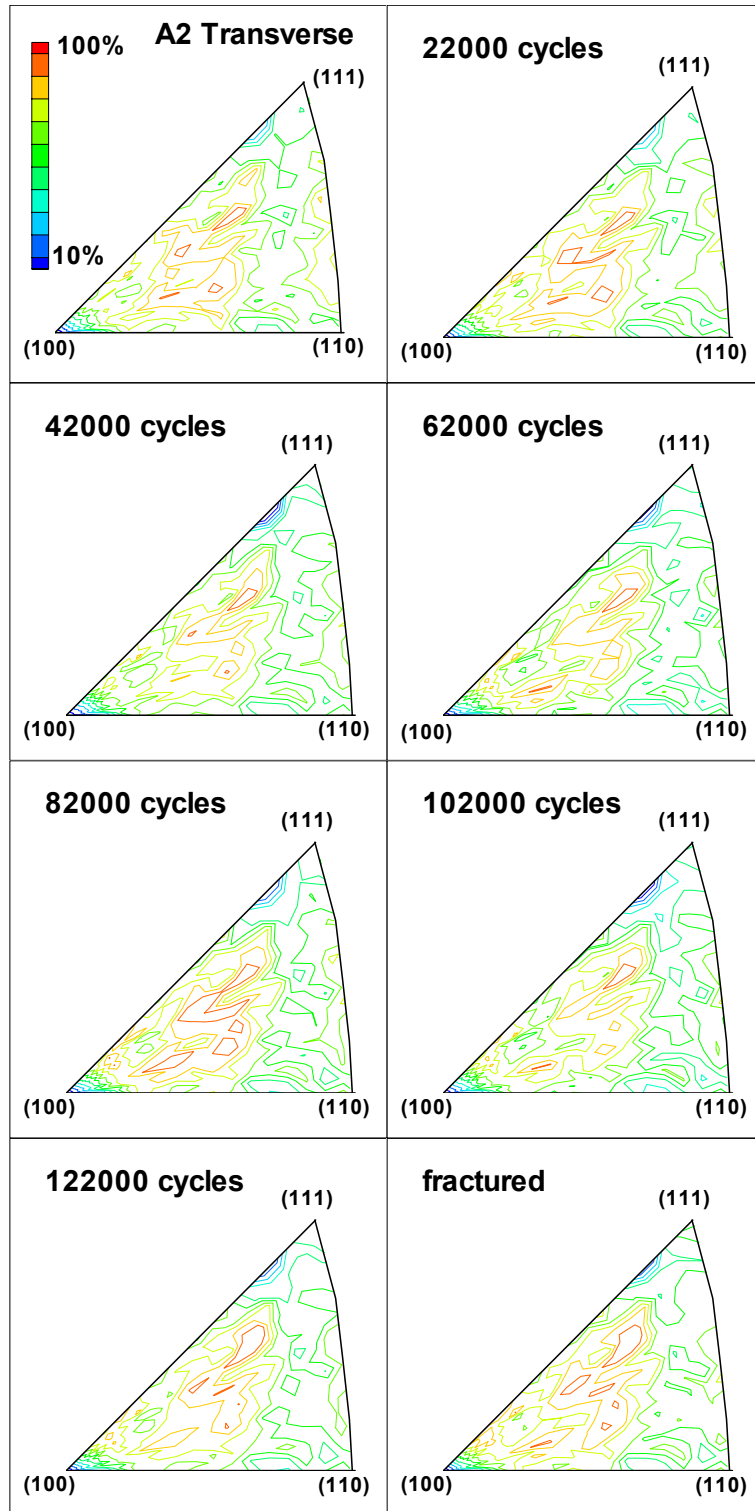


FIGURE 18. INVERSE POLE FIGURES SHOWING THE DISTRIBUTION OF CRYSTALLOGRAPHIC AXES WITH RESPECT TO THE TRANSVERSE AXIS OF SPECIMEN A2

A similar trend is observed for the specimens cut with the strain axis normal to the rolling direction (figures B-21 through B-42 of appendix B). There is little change in the normal IPF's, while the stress and transverse IPF's show clear reorientation of the  $\langle 100 \rangle$  directions to lie along the strain and transverse directions. The (123) orientation in the center of the strain IPF disappears by 22,000 cycles, and the crystallites align with (100) along the strain direction. The (212) orientation present at the edge of the transverse IPF again vanishes with cycling. It should be noted that for these samples, the transverse direction is along the rolling direction of the metal.

The specimens with the strain axis at  $45^\circ$  to the rolling direction show little change in any of the IPFs (figures B-43 through B-63 of appendix B). There is a slight amount of increase in the amount of (100) orientation along the strain direction, but significantly less than that observed for the samples cut along and perpendicular to the rolling direction.

#### 3.2.4 $\theta/2\theta$ Scans of Specimens' Surfaces.

A simple approximate method for obtaining a measurement of the amount of preferred orientation in a material is to do a powder scan, or  $\theta/2\theta$  scan of the surface of the material. The resulting data show which planes are parallel to the surface of the material. The relative intensity of the peaks indicates the relative amount of one orientation compared to another.  $\theta/2\theta$  scans were taken at the center of each specimen along the length of the gage region at each step in the fatigue process, and the ratio of the intensity of the (200) reflection to the (111) orientation was obtained. Figure 19 shows a sample curve, obtained for specimen A2 before it was stressed. As the material is cycled, the relative intensity of the two peaks changes. Figure 20 shows the results for different number of stress cycles, averaged over each set of three specimens. The curve labeled A is the data from specimens A2, A3, and A4. The curve labeled B is the data from specimens B3, B4, and B5, and the curve labeled C is data averaged from specimens C1, C2, and C3. There is a clear change in the intensity of the (111) peaks compared to the (200) peaks for curves A and B.

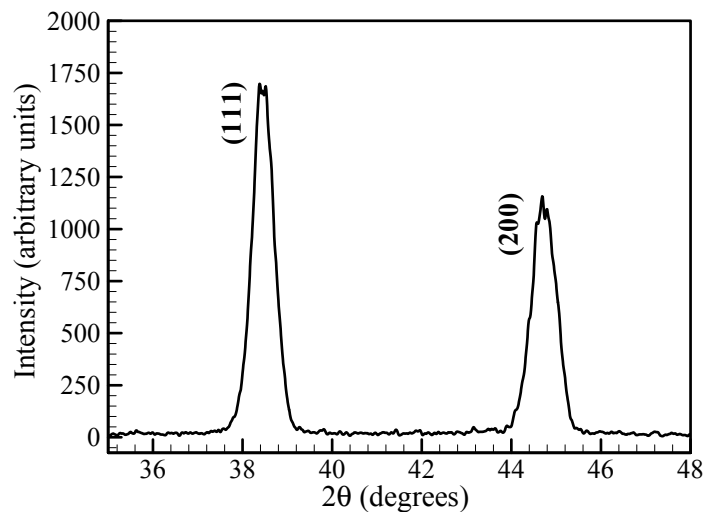


FIGURE 19.  $\theta/2\theta$  SCAN THROUGH THE (111) AND (200) POLES OF SPECIMEN A2 PRIOR TO FATIGUE CYCLING

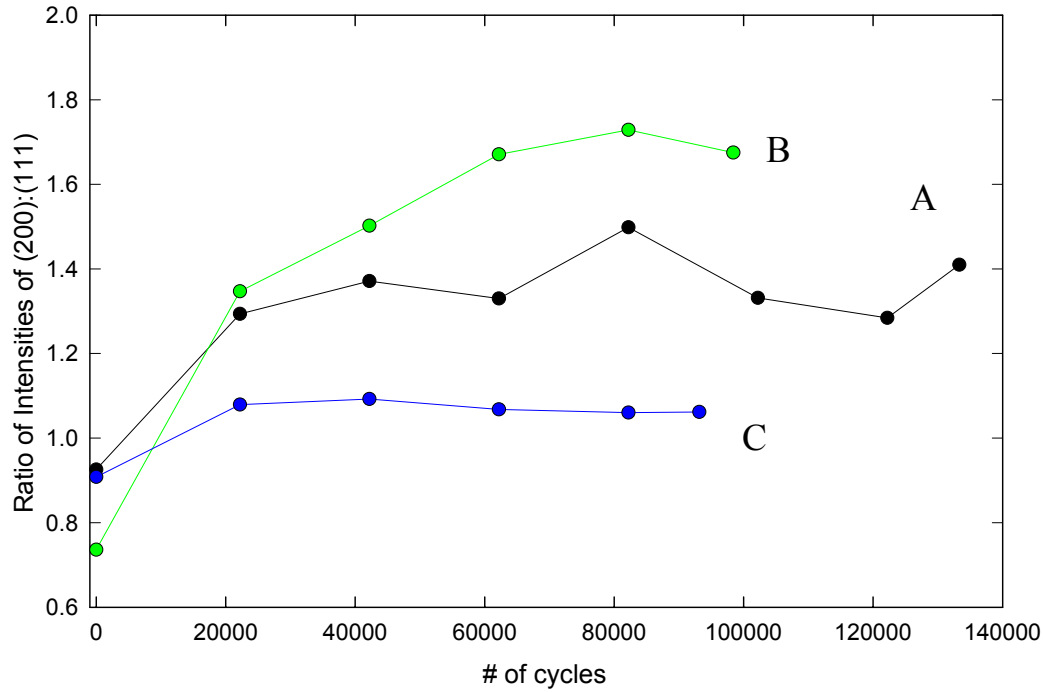


FIGURE 20. THE RATIO OF THE INTENSITY OF THE (200) REFLECTION TO THE (111) ORIENTATION

The increase of intensity of the (100)-oriented phase in comparison to the (111)-oriented component implies an increase in the amount of (100)-oriented planes parallel to the sample surface. This is in direct agreement with the pole figure information in section 4.2.1. Note that the amount of change in the relative intensity of the two peaks is the highest in the samples cut with the strain direction perpendicular to the rolling direction. The weakest change, in fact almost no change in error, occurs in the specimens cut at  $45^\circ$  to the strain direction and again, this is consistent with the information obtained from the pole figure measurements. These were the weakest samples, i.e., which fractured at a lower number of cycles than those cut parallel and perpendicular to the rolling direction.

### 3.3 SCANNING ELECTRON MICROSCOPE SURFACE IMAGING.

The surfaces of specimens A-C were visibly observed to change with cycling. After the first step of 22,000 cycles, the surfaces appeared granular to the eye and, when examined microscopically, were beginning to crack. After failure, the samples were placed in the ESEM and the surfaces were examined both in and around the gage region. Cracking occurred primarily perpendicular to the axis of the applied stress, as shown in figure 21. However, numerous offshoots of the cracks propagating at  $45^\circ$  to the strain axis were observed along the  $[110]$  directions, which are the expected preferred slip directions in a face-centered cubic material such as aluminum.

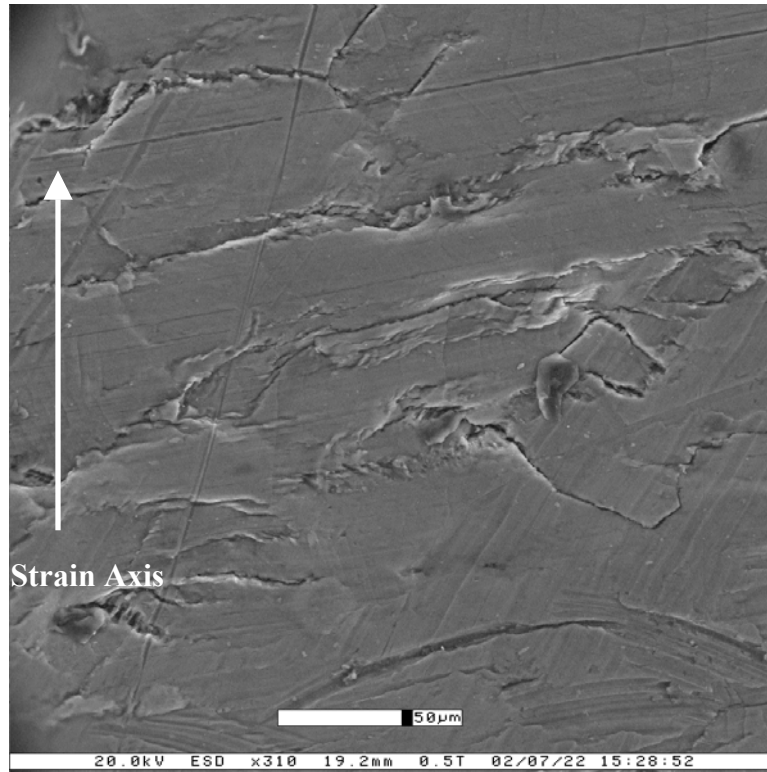


FIGURE 21. FATIGUE CRACKS IN THE GAGE REGION OF AN ALUMINUM SPECIMEN AFTER FAILURE

#### 4. FATIGUE UNTIL CRACK FORMATION.

##### 4.1 TEST MATRIX.

Table 4 details the test matrix in the measurement set for each specimen. Since considerable change in texture as well as the presence of cracking were observed in specimens A-C prior to 20,000 cycles, samples G-I were stressed in steps of 2,000 cycles, from zero to a maximum of 22,000 cycles. This filled the region between the unstressed sample and step 1 of samples A-C, for finer determination of the onset of crack formation.

TABLE 4. TEXT MATRIX INDICATING THE NUMBER OF FATIGUE CYCLES PER STEP AND THE SUBSEQUENT EXAMINATION TECHNIQUE

Sample ID	Initial Exam	Step 1	Step 2	Step 3	Step 4	Step 5	Step 6	Step 7	Step 8	Step 9	Step 10	Step 11
G1	X-ray ODF	2000 ODF	2000 ODF	2000 ODF	2000 ODF	2000 ODF	2000 ODF	2000 ODF	2000 ODF	2000 ODF	2000 ODF	2000 ODF
G2	X-ray	2000 ODF	2000 ODF	2000 ODF	2000 ODF	2000 ODF	2000 ODF	2000 ODF	2000 ODF	2000 ODF	2000 ODF	2000 ODF
G3	X-ray	2000 ODF	2000 ODF	2000 ODF	2000 ODF	2000 ODF	2000 ODF	2000 ODF	2000 ODF	2000 ODF	2000 ODF	2000 ODF
G4	SEM	2000 SEM	2000 SEM	2000 SEM	2000 SEM	2000 SEM	2000 SEM	2000 SEM	2000 SEM	2000 SEM	2000 SEM	2000 SEM
H1	X-ray	2000 ODF	2000 ODF	2000 ODF	2000 ODF	2000 ODF	2000 ODF	2000 ODF	2000 ODF	2000 ODF	2000 ODF	2000 ODF
H2	X-ray	2000 ODF	2000 ODF	2000 ODF	2000 ODF	2000 ODF	2000 ODF	2000 ODF	2000 ODF	2000 ODF	2000 ODF	2000 ODF
H3	X-ray	2000 ODF	2000 ODF	2000 ODF	2000 ODF	2000 ODF	2000 ODF	2000 ODF	2000 ODF	2000 ODF	2000 ODF	2000 ODF
H4	SEM	2000 SEM	2000 SEM	2000 SEM	2000 SEM	2000 SEM	2000 SEM	2000 SEM	2000 SEM	2000 SEM	2000 SEM	2000 SEM
I1	X-ray	2000 ODF	2000 ODF	2000 ODF	2000 ODF	2000 ODF	2000 ODF	2000 ODF	2000 ODF	2000 ODF	2000 ODF	2000 ODF
I2	X-ray	2000 ODF	2000 ODF	2000 ODF	2000 ODF	2000 ODF	2000 ODF	2000 ODF	2000 ODF	2000 ODF	2000 ODF	2000 ODF
I3	X-ray	2000 ODF	2000 ODF	2000 ODF	2000 ODF	2000 ODF	2000 ODF	2000 ODF	2000 ODF	2000 ODF	2000 ODF	2000 ODF
I4	SEM	2000 SEM	2000 SEM	2000 SEM	2000 SEM	2000 SEM	2000 SEM	2000 SEM	2000 SEM	2000 SEM	2000 SEM	2000 SEM

Maximum Stress: 300 MPa

Minimum Stress: 30 MPa

Cycling Frequency: 4.5 Hz

## 4.2 TEXTURE EVOLUTION AND CRACK INITIATION.

### 4.2.1 Pole Figures.

Since specimens G-I were cut from the same material as specimens A-C, the original texture as determined from the pole figure measurements is the same. Any small variations in texture of the virgin specimens are due to surface irregularities. The evolution of the texture is also the same for the pole figures of specimens G-I and A-C. Since the step sizes are smaller, the changes between adjacent pole figures are small and initially difficult to observe. The pole figures for specimen G1 are shown in figures 22 through 25. The pole figures for the other samples are in appendix B.

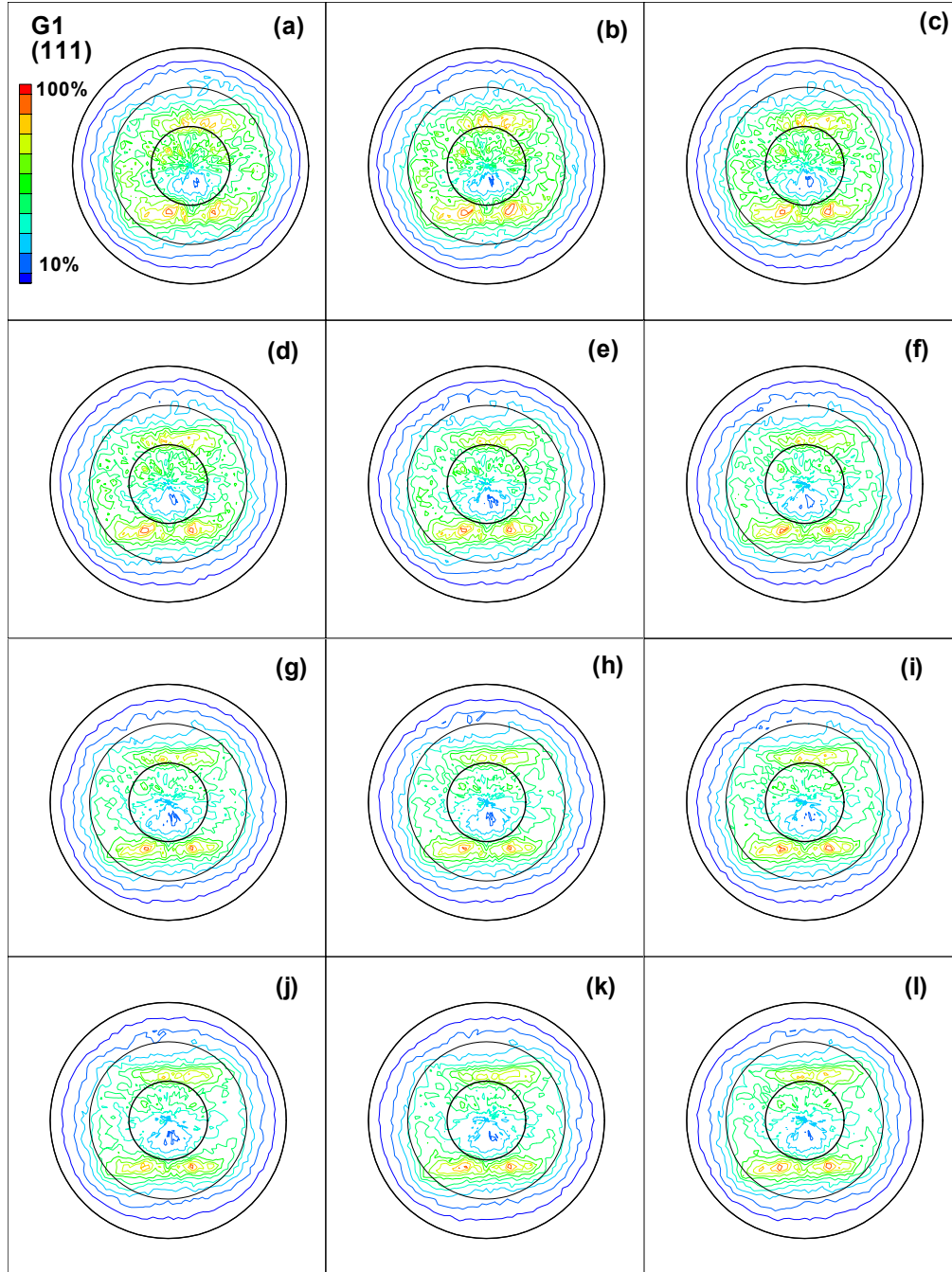


FIGURE 22. POLE FIGURES SHOWING THE EVOLUTION OF TEXTURE OF THE (111) POLES OF SAMPLE G1 (The pole figures were taken (a) on the virgin sample, and then after (b) 2,000, (c) 4,000, (d) 6,000, (e) 8,000, (f) 10,000, (g) 12,000, (h) 14,000, (i) 16,000, (j) 18,000, (k) 20,000, and (l) 22,000 fatigue cycles.)

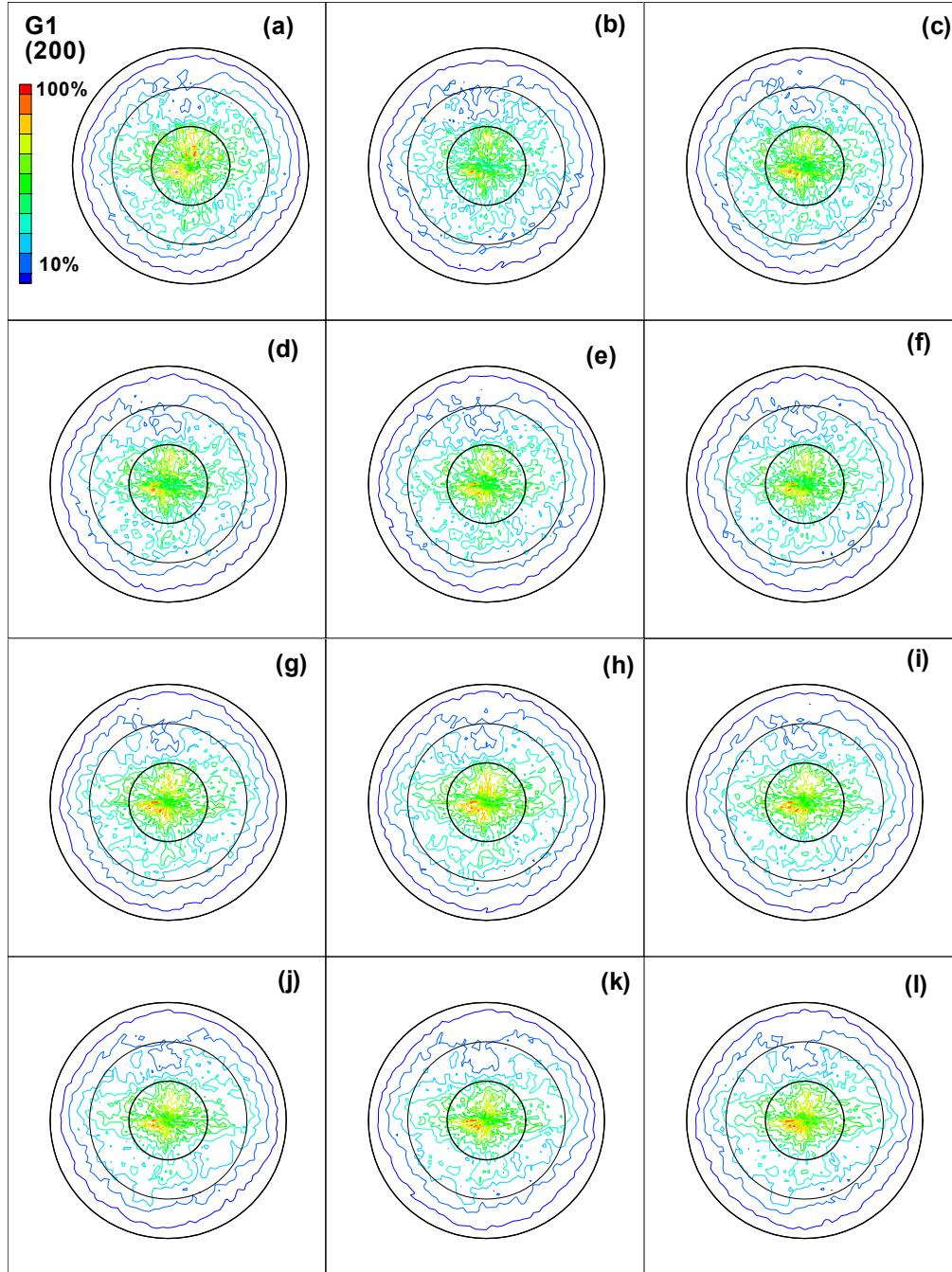


FIGURE 23. POLE FIGURES SHOWING THE EVOLUTION OF TEXTURE OF THE (200) POLES OF SAMPLE G1 (The pole figures were taken (a) on the virgin sample, and then after (b) 2,000, (c) 4,000, (d) 6,000, (e) 8,000, (f) 10,000, (g) 12,000, (h) 14,000, (i) 16,000, (j) 18,000, (k) 20,000, and (l) 22,000 fatigue cycles.)



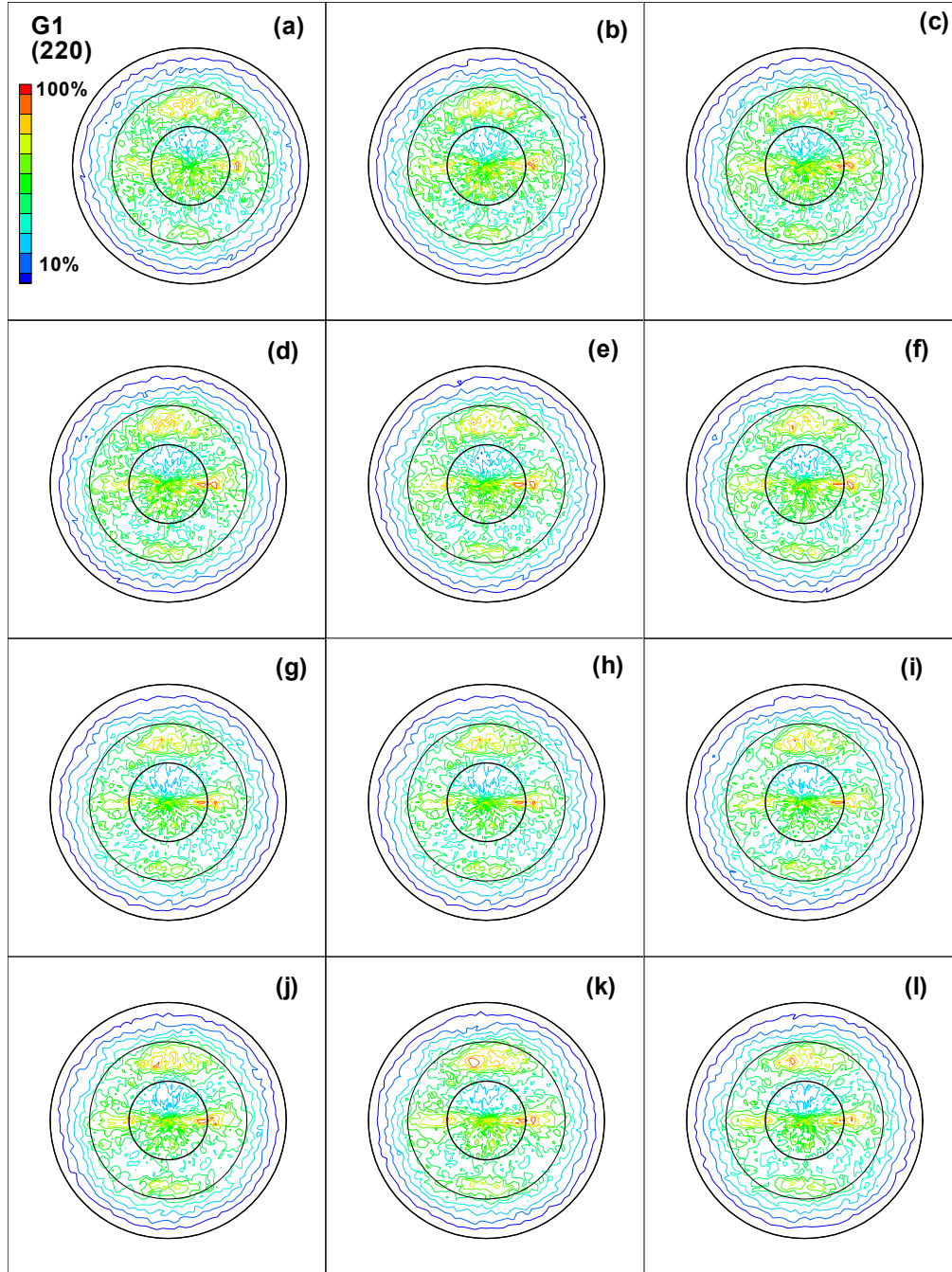


FIGURE 24. POLE FIGURES SHOWING THE EVOLUTION OF TEXTURE OF THE (220) POLES OF SAMPLE G1 (The pole figures were taken (a) on the virgin sample, and then after (b) 2,000, (c) 4,000, (d) 6,000, (e) 8,000, (f) 10,000, (g) 12,000, (h) 14,000, (i) 16,000, (j) 18,000, (k) 20,000, and (l) 22,000 fatigue cycles.)

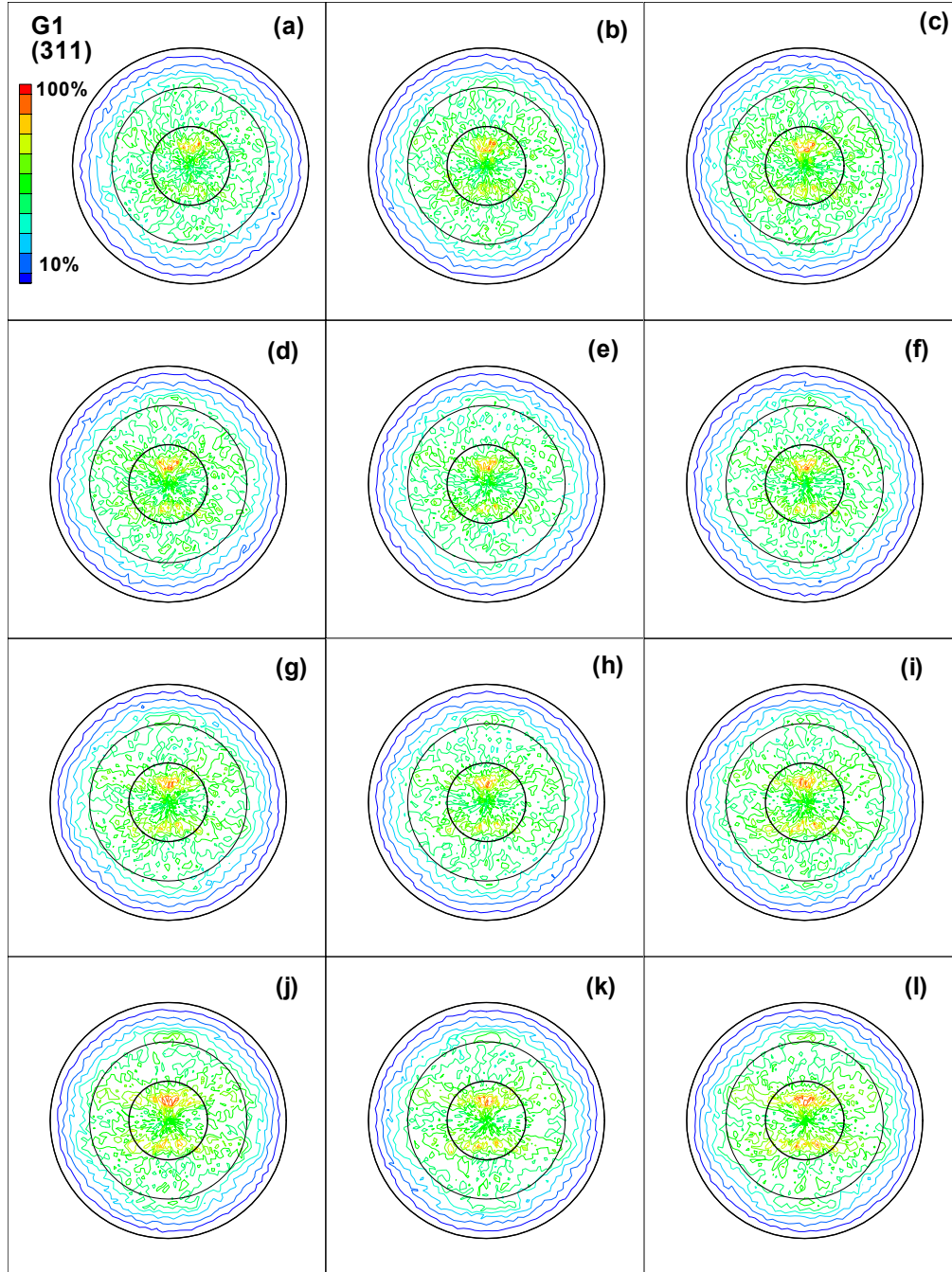


FIGURE 25. POLE FIGURES SHOWING THE EVOLUTION OF TEXTURE OF THE (311) POLES OF SAMPLE G1 (The pole figures were taken (a) on the virgin sample, and then after (b) 2,000, (c) 4,000, (d) 6,000, (e) 8,000, (f) 10,000, (g) 12,000, (h) 14,000, (i) 16,000, (j) 18,000, (k) 20,000, and (l) 22,000 fatigue cycles.)

The (200) poles are again pulled into the center of the pole figures, while the material reorients such that the [100] direction is parallel to the strain axis. This is indicated by a slight reorganization of the broad intensity in the (111)-(311) pole figures. The changes are almost too small to track in the pole figures, and can be better represented by changes in the inverse pole figures, which appear to be more sensitive.

#### 4.2.2 Inverse Pole Figures.

The IPF for sample G1 are shown in figures 26-28. As would be expected from the data of the (A) samples, the change in the normal IPF is minimal. However, in the stress direction, it is possible to see the gradual reduction of the intensity near the center of the IPF as the material becomes (100)-oriented. In the transverse IPF, shown in figure 28, a broadening occurs in the high-intensity center region of the figure, similar to what happened in the (A) samples.

The (H) samples behave similar to the (B) samples (see figures in appendix B). Again, in the stress direction, gradual changes can be seen as a function of the number of cycles. The (212) orientation, out at the edge of the IPF, disappears around 9,000 cycles, while the high-intensity region at the center of the IPF disappears at a higher number of cycles. By 22,000 cycles, only (100) orientation is observed in the IPF. In the transverse IPF, the change is less pronounced, with only a gradual increase of intensity toward the (100) orientation.

The (I) samples, like the (C) samples, show little change in the inverse pole figures (see figures in appendix B). In the stress direction, the intensity in the center of the IPF gradually faded away and was replaced by intensity at (100). The intensity in the center of the inverse pole figure vanished about 14,000 cycles.

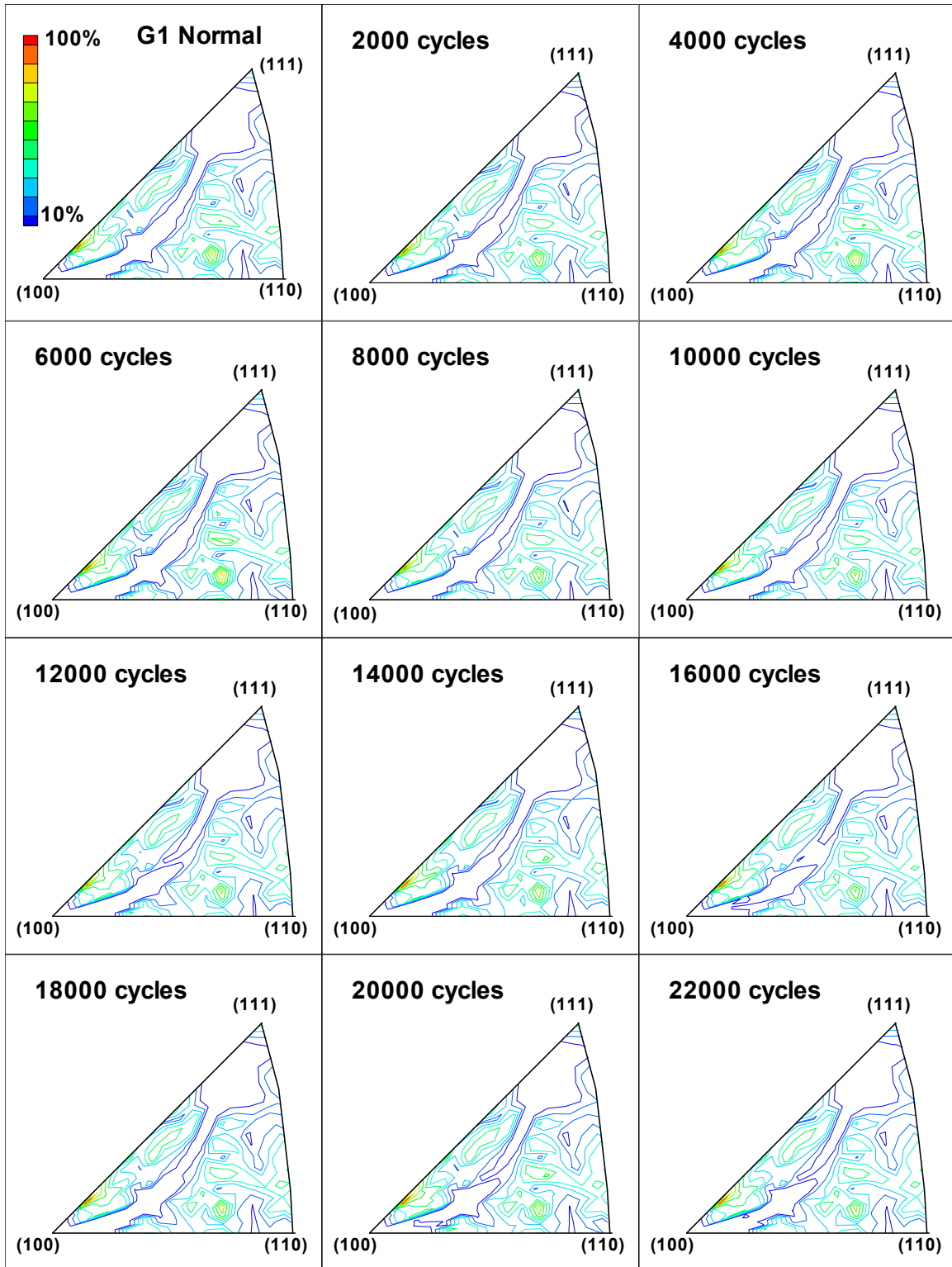


FIGURE 26. EVOLUTION OF THE INVERSE POLE FIGURE CALCULATED ALONG THE NORMAL DIRECTION FOR SPECIMEN G1

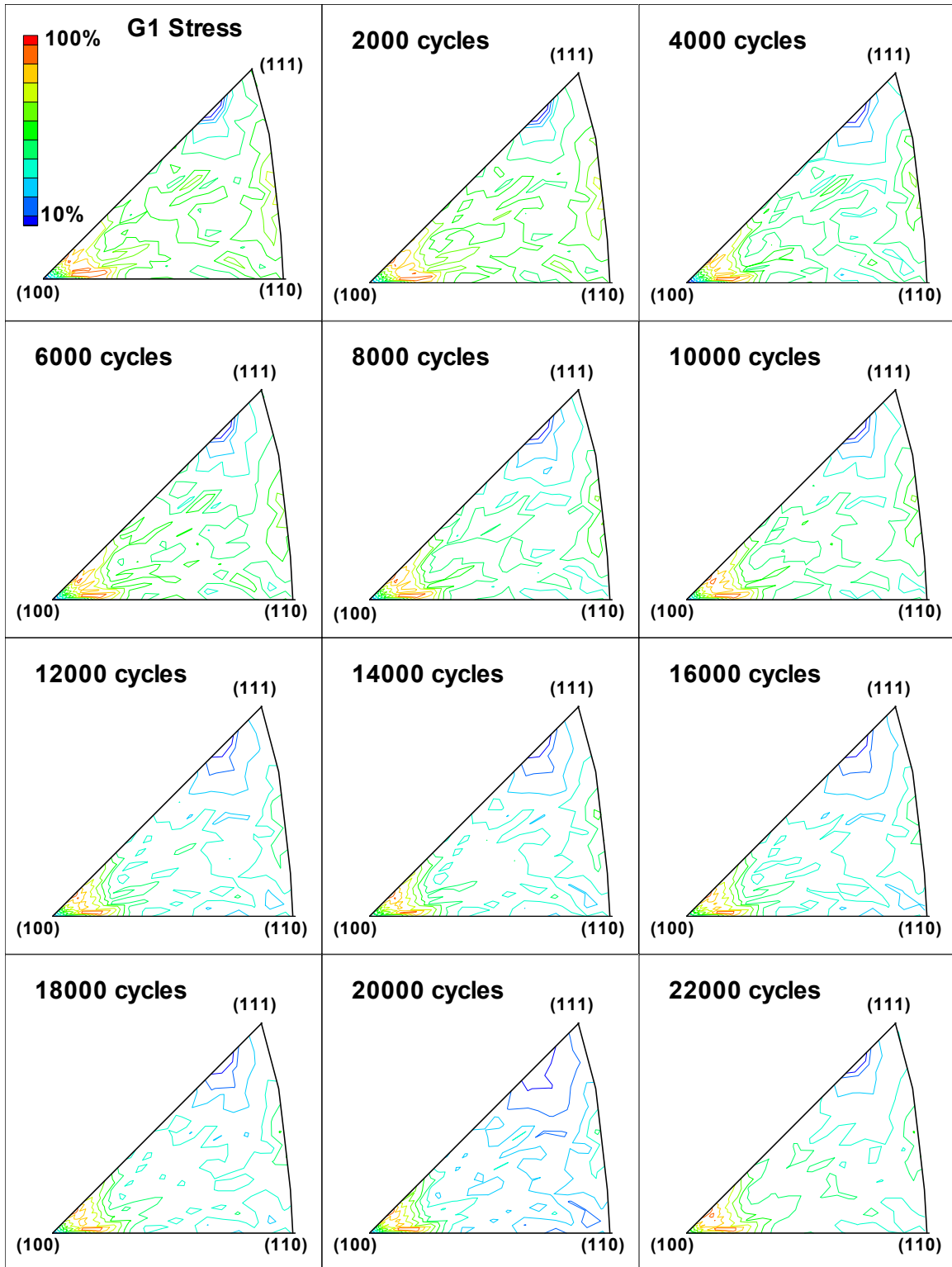


FIGURE 27. EVOLUTION OF THE INVERSE POLE FIGURE CALCULATED ALONG THE STRESS DIRECTION FOR SPECIMEN G1

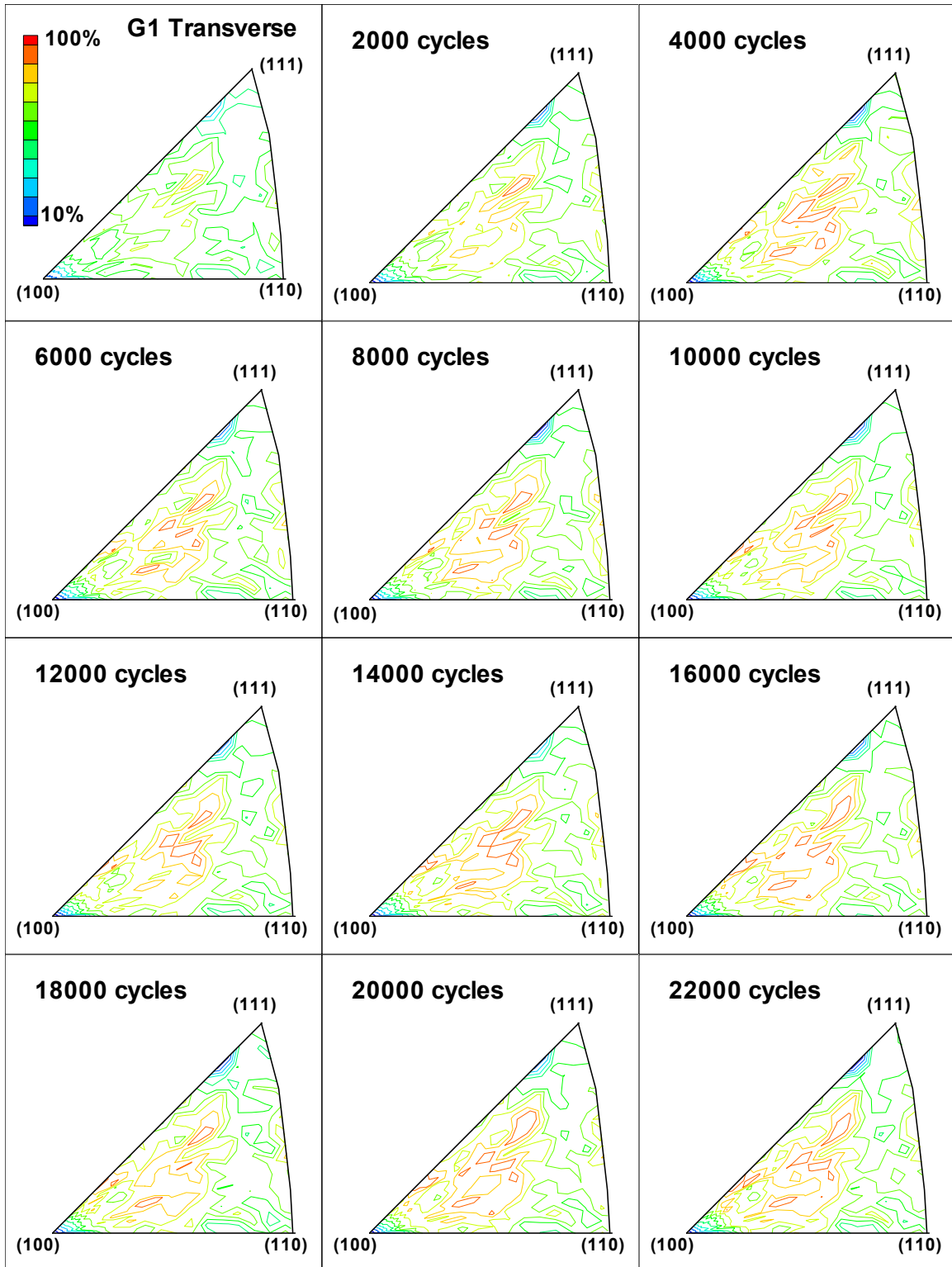


FIGURE 28. EVOLUTION OF THE INVERSE POLE FIGURE CALCULATED ALONG THE TRANSVERSE DIRECTION FOR SPECIMEN G1

#### 4.2.3 $\theta/2\theta$ Scans of Specimens' Surfaces.

Figure 29 shows the ratio of the intensities of (200) to (111) peaks from the  $\theta/2\theta$  scans. The curves labeled G and H represent the averaged data from specimens G1-G3 and H1-H3 respectively. There is a clear change in the intensity of the (111) peaks compared to the (200) peaks for curve H. The change is smaller for curve G with an increase in intensity rates from 0.85 to 1.15. The curve from samples I1-I3 shows little change within error. These results are consistent with the results observed for specimens A-C, with the greatest change occurring for the (H) samples cut with the strain axis perpendicular to the rolling direction, and the least for the I specimens cut with the strain axis at  $45^\circ$  to the rolling direction.

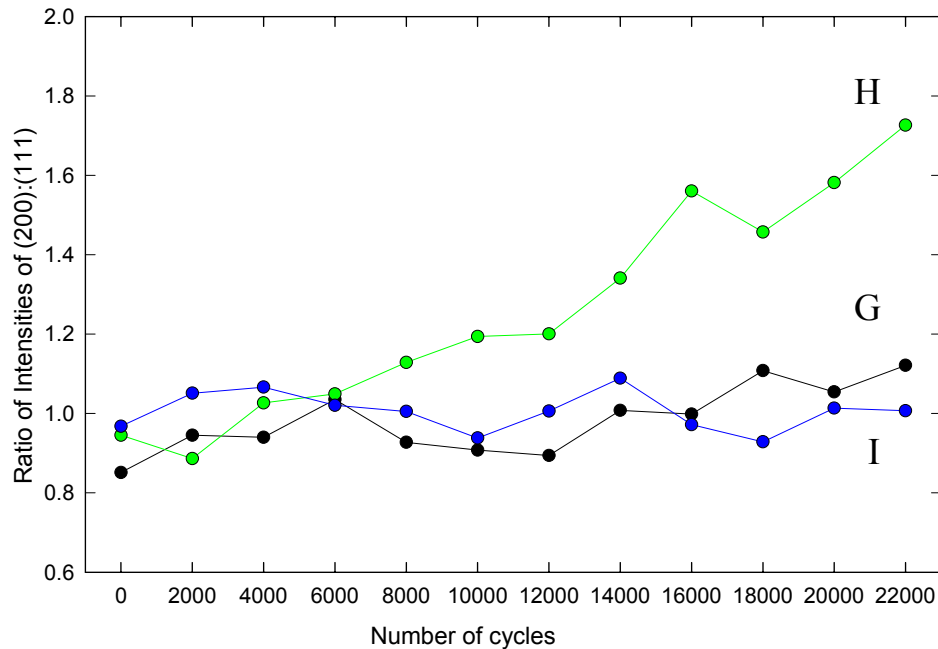


FIGURE 29. THE RATIO OF THE INTENSITY OF THE (200) REFLECTION TO THE (111) ORIENTATION

#### 4.3 SCANNING ELECTRON MICROSCOPE SURFACE IMAGING.

From the inverse pole figure measurements, it appeared that measurable changes in texture were occurring between 6,000 and 12,000 fatigue cycles, especially in samples H1-H3. Figure 30 is a montage of SEM images taken on specimen H4 between 0 and 10,000 fatigue cycles. The scale bar on each figure is 50  $\mu\text{m}$ . The vertical lines are small surface features due to machining of the material. A few small cracks were visible after 4,000 cycles, and a high density of cracks about 6,000 cycles. By 10,000 cycles there were many cracks, both perpendicular and at  $45^\circ$  to the stress axis. This corroborates the inverse pole figure results showing the primary texture changes before 10,000 cycles. Appendix C contains composite images for all three orientations as a function of fatigue cycling. Similar crack initiation can be seen in all materials.



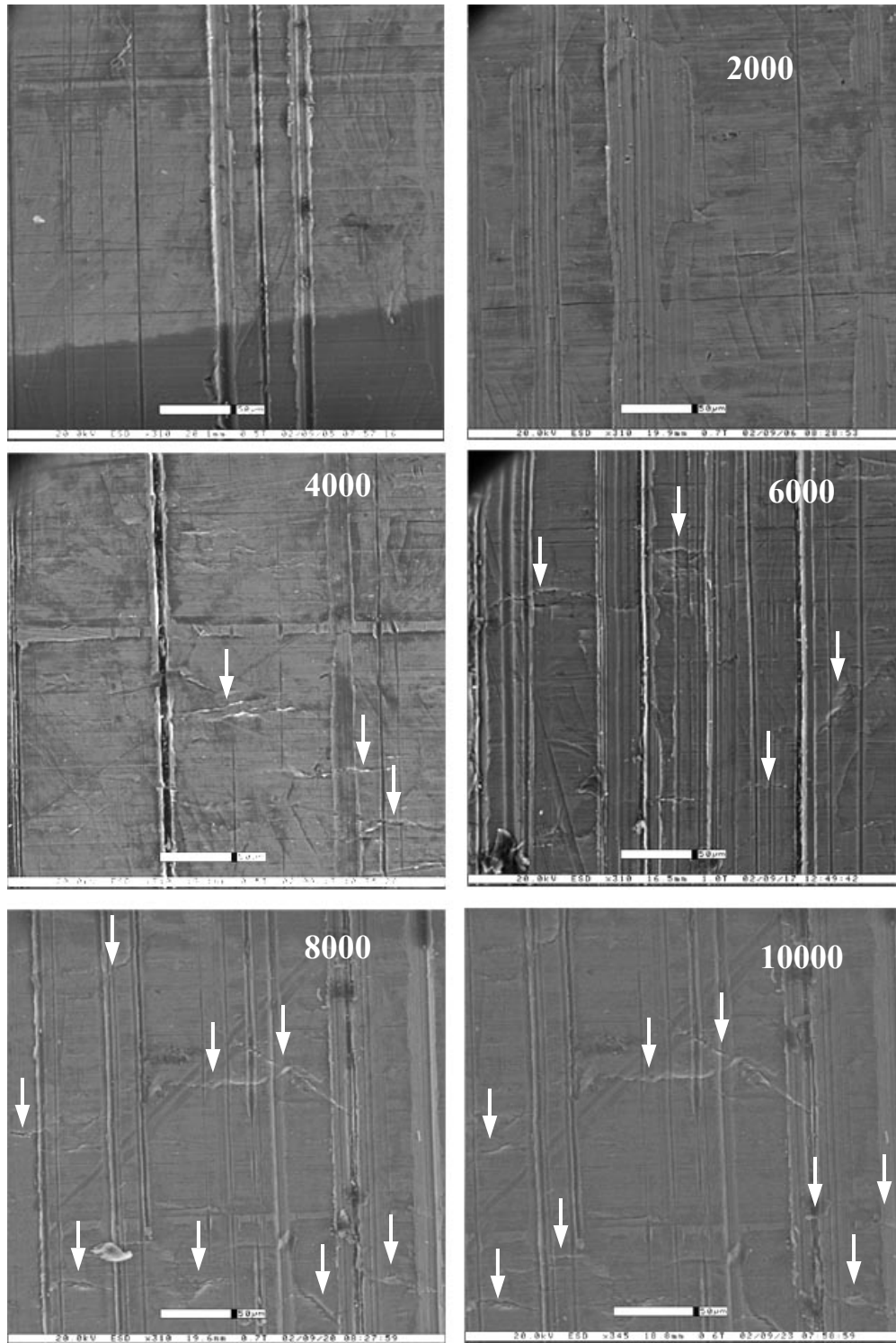


FIGURE 30. SEM IMAGES OF SAMPLE H4 AS A FUNCTION OF THE NUMBER OF FATIGUE CYCLES



## 5. DISCUSSION OF RESULTS.

Both the direct and inverse pole figures show a significant change in the texture of the aluminum as a function of fatigue cycling. As the material is stressed, the (100) planes rotate to lie parallel to the surface of the specimen, while the [100] directions rotate to lie along the stress direction. In the samples cut with the stress direction at 45° to the rolling direction, the [100] direction in the majority of the crystallites present already lies close to the stress direction. Thus, there is less texture change observed in these specimens (C and I). In the first part of the experiment, where large 20,000 cycle steps were taken in fatigue, it was found that most of the changes in the texture, as seen by the IPFs, occur before 20,000 cycles. Surface examination of samples A-C revealed cracking prior to 20,000 cycles.

When smaller fatigue steps of 2000 cycles were used, the same trend in the texture evolution was observed. SEM investigation of the surfaces after each step showed that crack initiation occurred close to the time at which certain features vanished in the IPFs. Thus, the disappearance of certain texture features can be used to predict the onset of crack initiation.

$\theta/2\theta$  scans also showed systematic changes with fatigue. The intensity of the (200) reflections increased with fatigue as a result of the increased (100) texture of the material. However, along the 45° directions in the crystal, these changes were very small. It was also found that these scans were sensitive to the exact location on the material surface. Since the specimen cannot be located at exactly the same place each time it was remounted on the x-ray stage ( $\pm 1$  mm). It was necessary to average over a 5-mm surface area to obtain consistent results. Since these scans are much simpler and faster than pole figure measurements, this is attractive.

## 6. CONCLUSION AND SUMMARY.

It was shown that texture changes develop in a material due to application of a cyclic stress and that measurements of the texture by x-ray diffraction techniques can be used as a precursor of the formation of cracks prior to their onset. These measurements were performed on samples of aluminum 2024-T3 that were cut parallel, perpendicular, and at 45° to the rolling direction. It was shown that as the number of cycles increases, the orientation of the material changes from its initial [110] rolling direction of the aluminum and that prior to cracking, the aluminum grains rotate from the [100] direction to a preferable direction along the applied stress axis.

The rate of texture development is dependent on the orientation of the stress to the rolling direction of the aluminum plate. It was found that the rate of texture development is fastest along the transverse direction, followed by the rolling direction, and slowest for those samples cut at 45° to the rolling direction. This is likely a reflection of the number of grains within the material that are initially oriented so their [100] directions are parallel to the applied stress axis. An alternative proposition is that samples cut 45° to the rolling direction are weaker and that microcracking occurs for the stress levels used.

Texture changes develop rapidly prior to the formation of cracks. However, after crack formation, the texture change is slow, presumably because the stress is absorbed in crack formation rather than in grain reorientation.

From this initial study, it is believed that given sufficient development time, the amount of texture may be used as a measure of the probability of the formation of cracks in metals. By providing a predictable measure of the vulnerability of the metal structure to the onset of cracking, this technique could save the aircraft industry considerable time and money in maintenance and repair.

## 7. SUGGESTIONS FOR FUTURE RESEARCH.

This preliminary study showed some promising results. It is now clear that the texture in a material can be changed via fatigue cycling and observed by x-ray diffraction techniques. However, more detailed measurements need to be done to identify exactly what features of the texture are most important to crack initiation. Some suggestions for further research are given below.

These measurements were obtained from fatigue cycling at a stress level close to the elastic limit for the aluminum 2024-T3 plate. This may have caused crack initiation in weaker grains within the material, reducing the effect of the texture change on crack initiation. Any future work should be done using a lower stress level and with more fatigue cycles. This will have the effect of reducing the amount of crack initiation at weak grains. It will also give the texture more time to develop and make it easier to observe. Also, cracking will occur at a much slower rate so that a more detailed examination of texture can be done.

To relate the texture changes to specific problems encountered in airframes, it would be useful to introduce stress concentrators, such as rivet holes, and conduct a study of the development of texture in the vicinity of the hole.

## 8. REFERENCES.

1. Donald J. Wulpi, "*Understanding How Components Fail*," Second Edition, 1999, ASM International, Materials Park, OH.
2. M.E. Packer and R.A. Coyle, "Modification of Texture by Fatigue and Its Application to Fatigue Metering," *Metal Science* 12 (1978) 421.

## APPENDIX A—SPECIMEN LAYOUT AND TESTING PROCEDURE

All specimens used in this study were machined from 0.090" thick 2024-T3 aluminum plate using the configuration shown in figure A-1. Figures A-2 and A-3 show the different specimens orientations. Table A-1 describes all specimens used in this study, including orientation with respect to the plate's rolling direction and the type of test to be conducted.

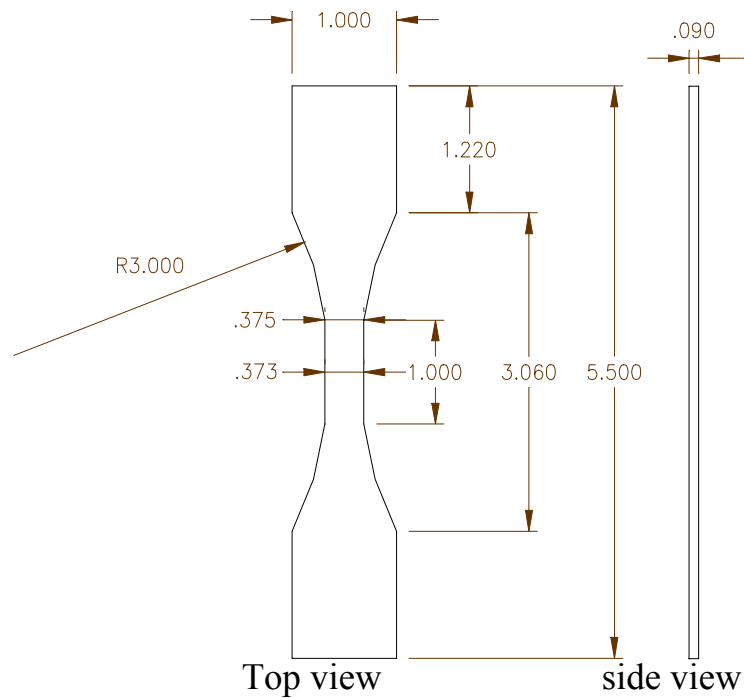


FIGURE A-1. SPECIMEN CONFIGURATION

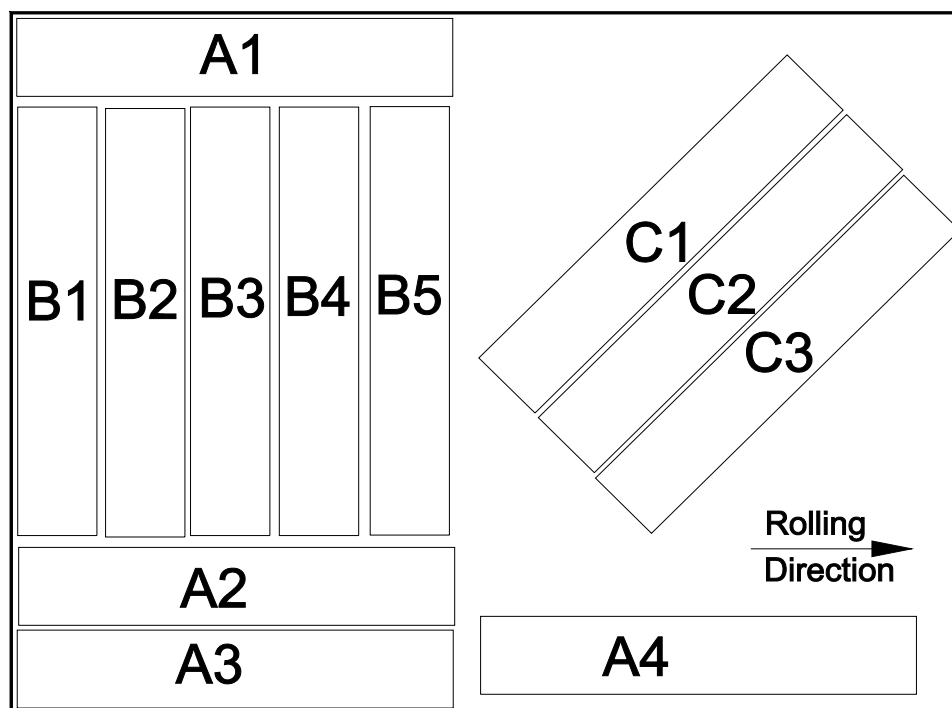


FIGURE A-2. LAYOUT OF SPECIMENS A THROUGH C ON 9" X 12" Al 2024-T3 SHEET

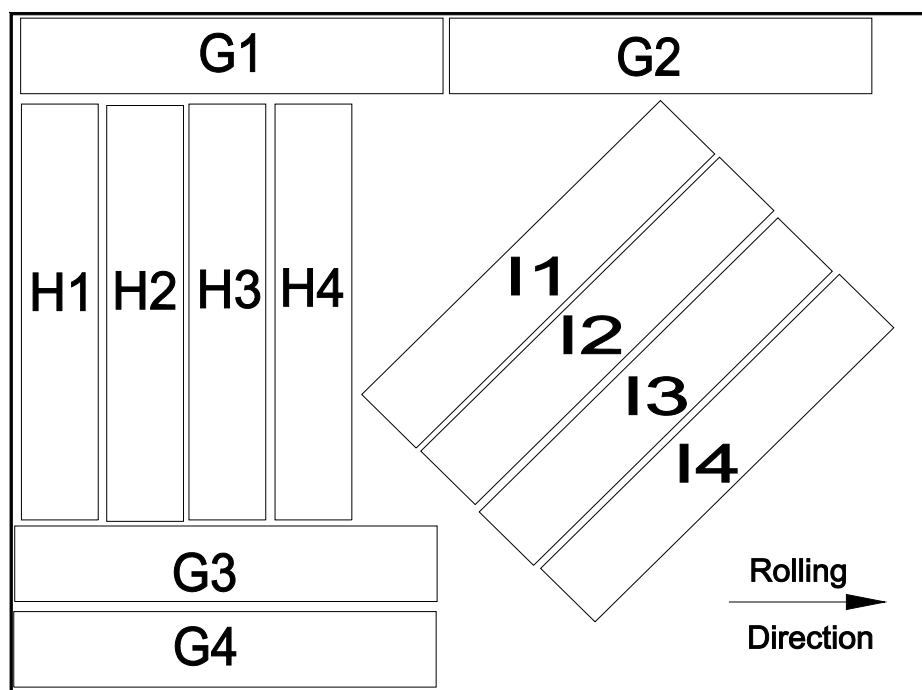


FIGURE A-3. LAYOUT OF SPECIMENS G THROUGH I ON 9" X 12" Al 2024-T3 SHEET

TABLE A-1. TEST MATRIX

Sample ID	Angle Between Strain and Grain	Type of Test
A1	0	stress-strain
A2	0	fatigue to failure
A3	0	fatigue to failure
A4	0	fatigue to failure
B1	90	stress-strain
B2	90	specimen damaged
B3	90	fatigue to failure
B4	90	fatigue to failure
B5	90	fatigue to failure
C1	45	fatigue to failure
C2	45	fatigue to failure
C3	45	fatigue to failure
G1	0	fatigue 22,000 cycles
G2	0	fatigue 22,000 cycles
G3	0	fatigue 22,000 cycles
G4	0	fatigue 22,000 cycles SEM
H1	90	fatigue 22,000 cycles
H2	90	fatigue 22,000 cycles
H3	90	fatigue 22,000 cycles
H4	90	fatigue 22,000 cycles SEM
I1	45	fatigue 22,000 cycles
I2	45	fatigue 22,000 cycles
I3	45	fatigue 22,000 cycles
I4	45	fatigue 22,000 cycles SEM

## APPENDIX B—DIRECT AND INVERSE POLE FIGURE DATA AS A FUNCTION OF FATIGUE

This appendix contains all the texture figures for the specimens measured in this study.

- The figures are ordered by specimen number.
- The direct pole figure measurements occur first. Each is a composite figure for all fatigue levels of the pole figures for a given (hkl). The (hkl) and sample number are in part (a) of each figure.
- For samples A-C, the labels (a) to (h) refer to the number of fatigue cycles, thus (a) 0 cycles, (b) 22,000, (c) 42,000, (d) 62,000, (e) 82,000, (f) 102,000, (g) 122,000, and (h) 142,000.
- For samples G-I, the steps are in increments of 2,000 cycles, thus (a) 0 cycles, (b) 2,000, (c) 4,000, (d) 6,000, (e) 8,000, (f) 10,000, (g) 12,000, (h) 14,000, (i) 16,000, (j) 18,000, (k) 20,000, and (l) 22,000.
- The inverse pole figures are also labeled by sample number and the direction along which the IPF was calculated, either normal, stress, or transverse. Each figure is labeled with the number of cycles at which it was taken.

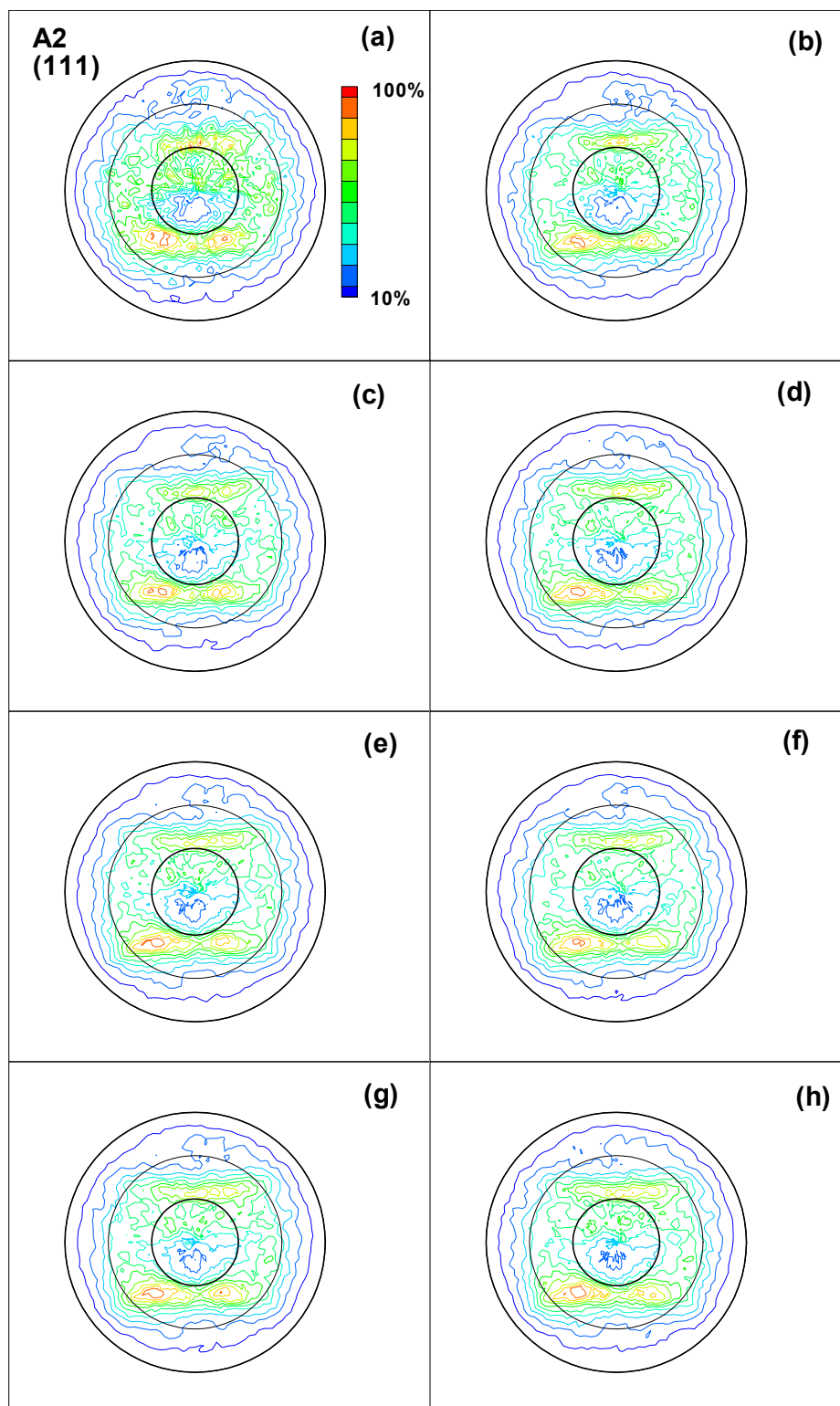


FIGURE B-1. DIRECT (111) POLE FIGURES FOR SPECIMEN A2 AFTER (a) 0, (b) 22,000, (c) 42,000, (d) 62,000, (e) 82,000, (f) 102,000, (g) 122,000 FATIGUE CYCLES, AND (h) AFTER FAILURE

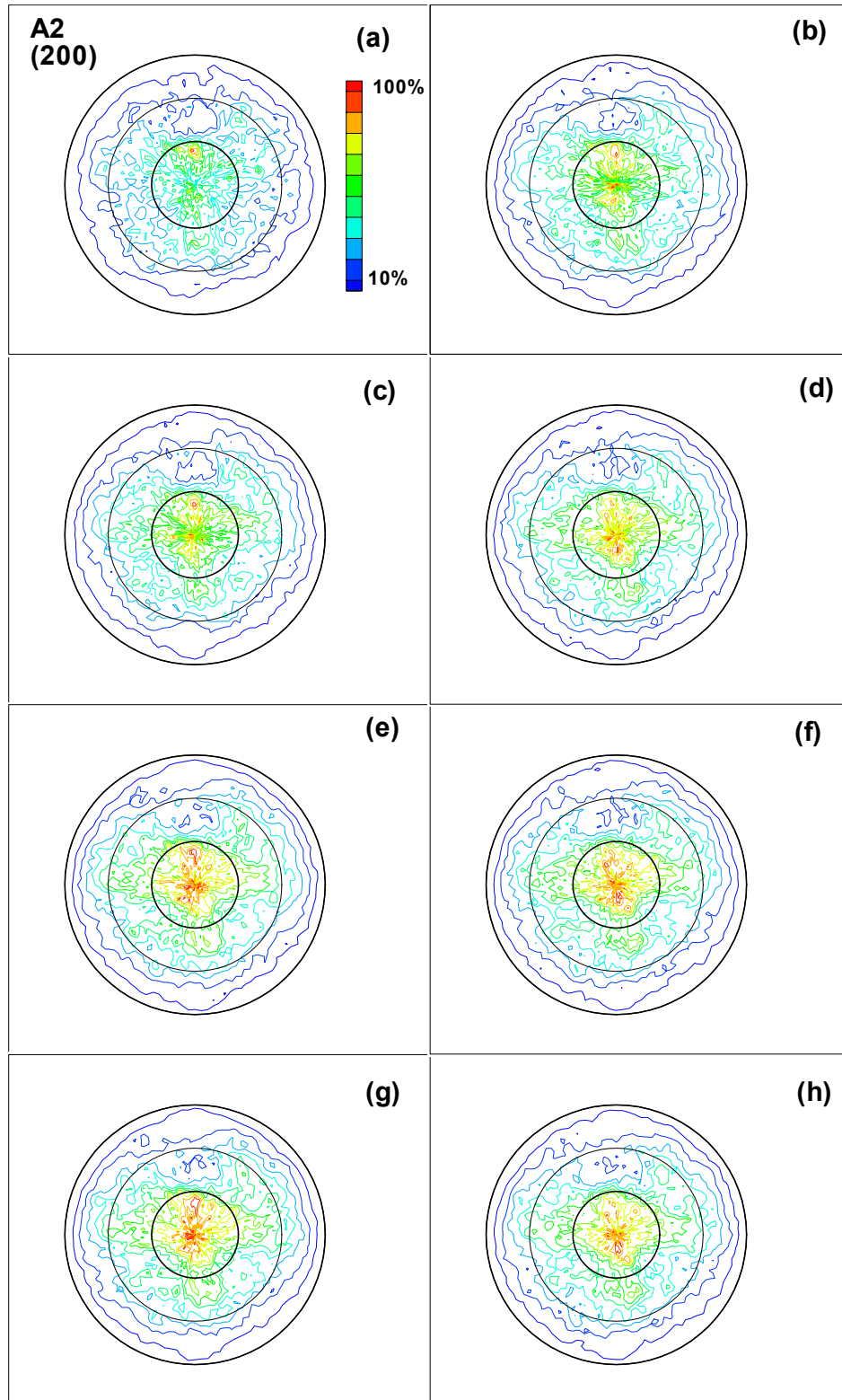


FIGURE B-2. DIRECT (200) POLE FIGURES FOR SPECIMEN A2 AFTER (a) 0, (b) 22,000, (c) 42,000, (d) 62,000, (e) 82,000, (f) 102,000, (g) 122,000 FATIGUE CYCLES, AND (h) AFTER FAILURE



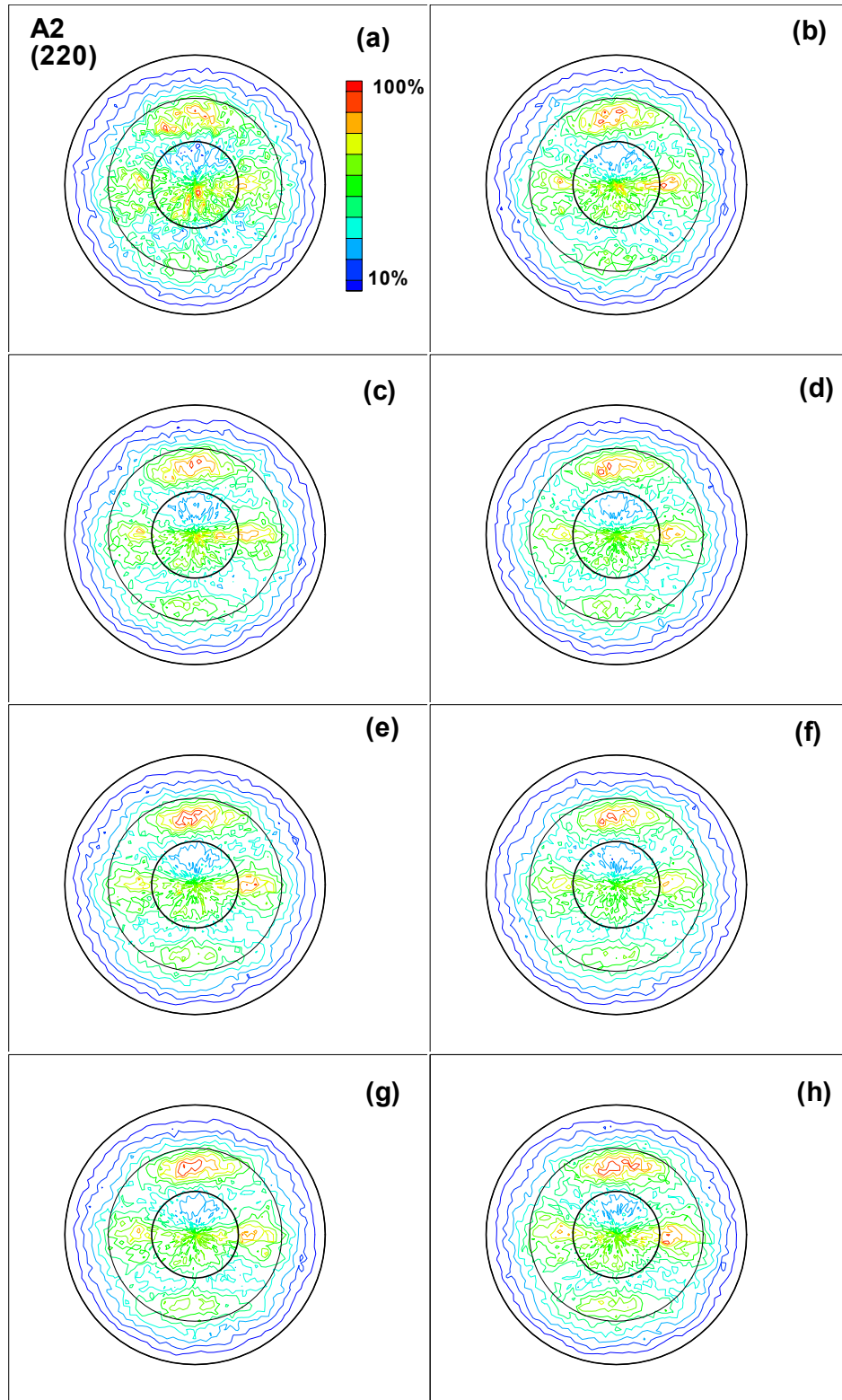


FIGURE B-3. DIRECT (220) POLE FIGURES FOR SPECIMEN A2 AFTER (a) 0, (b) 22,000, (c) 42,000, (d) 62,000, (e) 82,000, (f) 102,000, (g) 122,000 FATIGUE CYCLES, AND (h) AFTER FAILURE

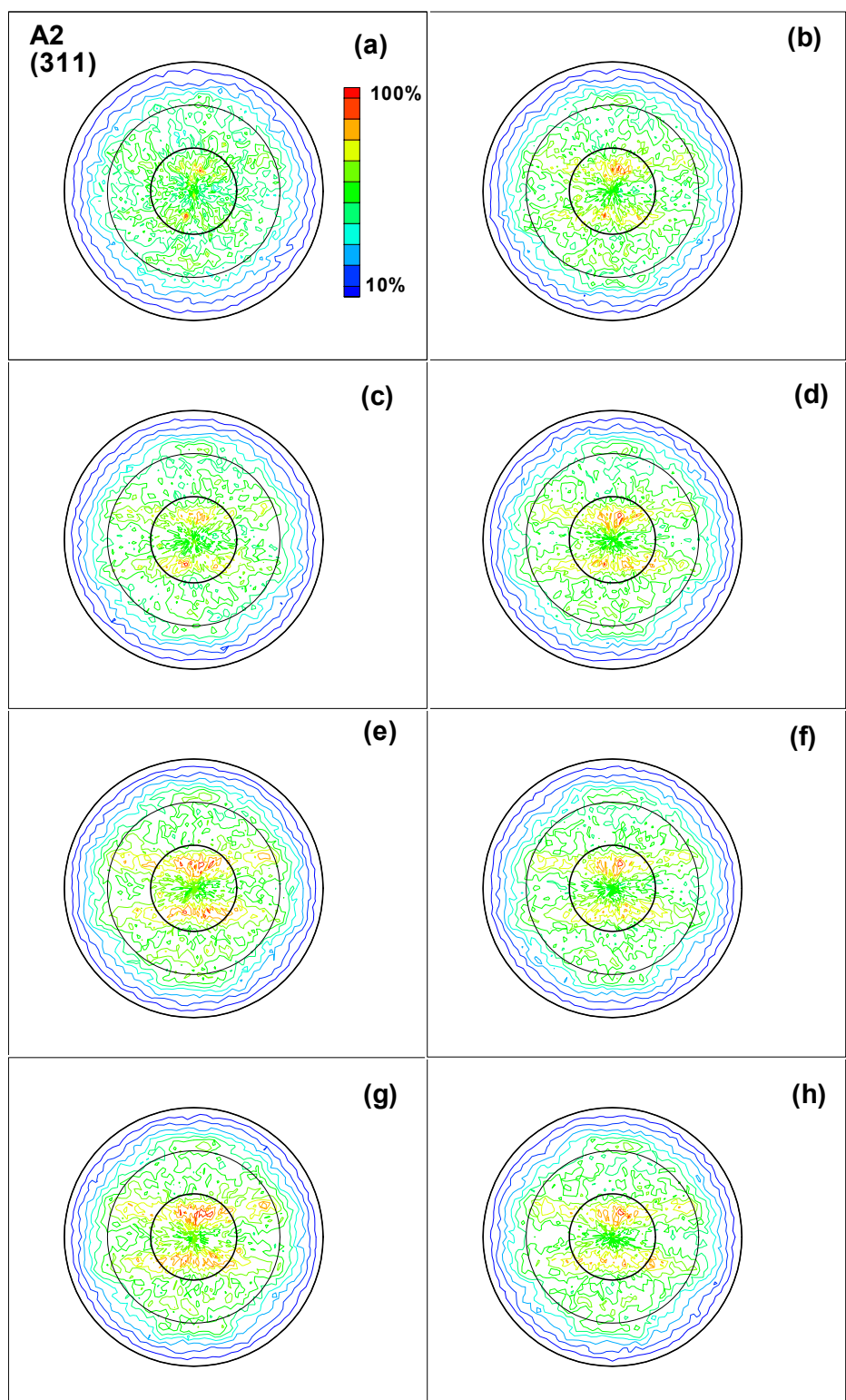


FIGURE B-4. DIRECT (311) POLE FIGURES FOR SPECIMEN A2 AFTER (a) 0, (b) 22,000, (c) 42,000, (d) 62,000, (e) 82,000, (f) 102,000, (g) 122,000 FATIGUE CYCLES, AND (h) AFTER FAILURE

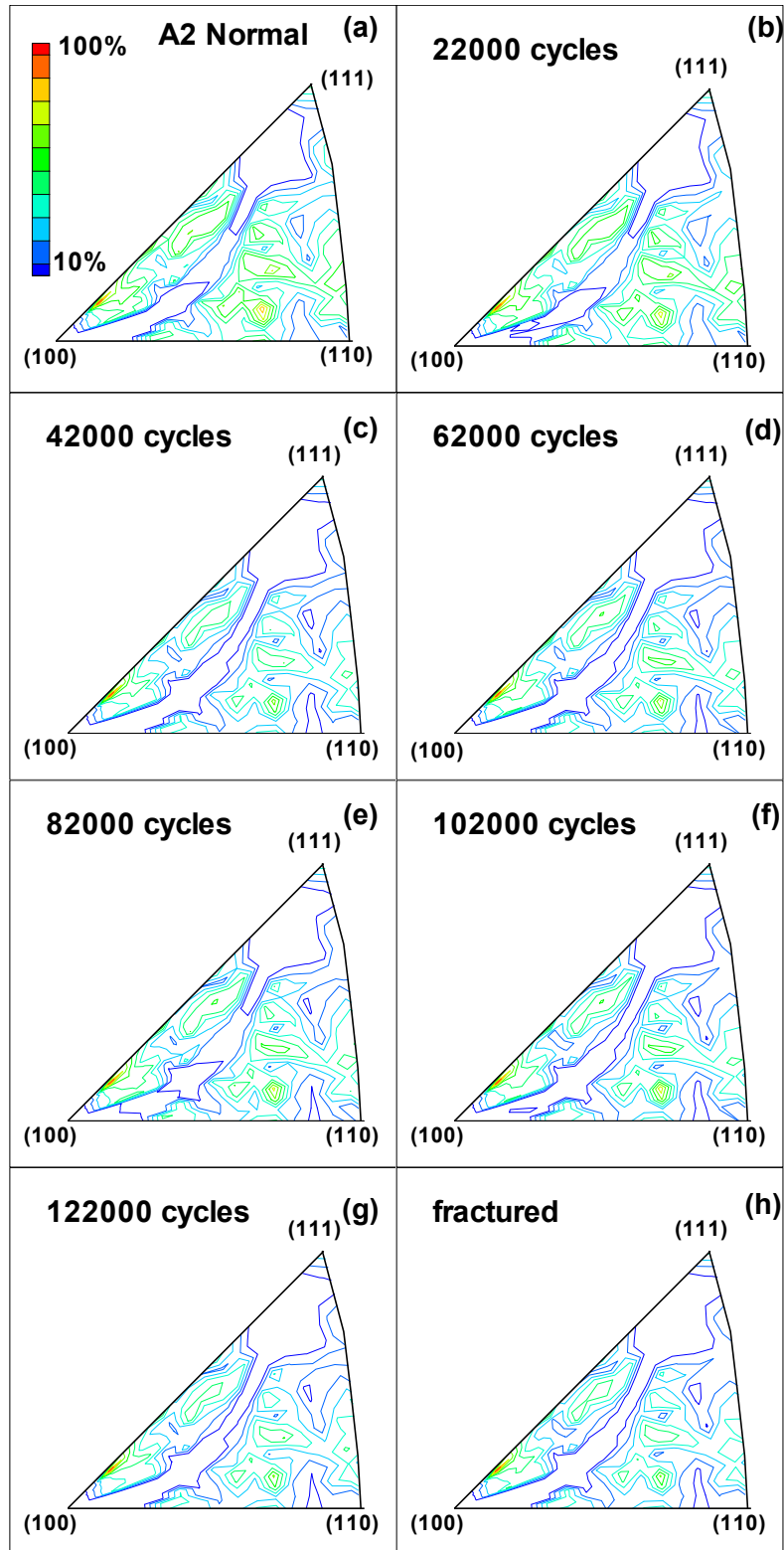


FIGURE B-5. INVERSE POLE FIGURES IN THE NORMAL DIRECTION FOR SPECIMEN A2 AFTER (a) 0, (b) 22,000, (c) 42,000, (d) 62,000, (e) 82,000, (f) 102,000, (g) 122,000 FATIGUE CYCLES, AND (h) AFTER FAILURE

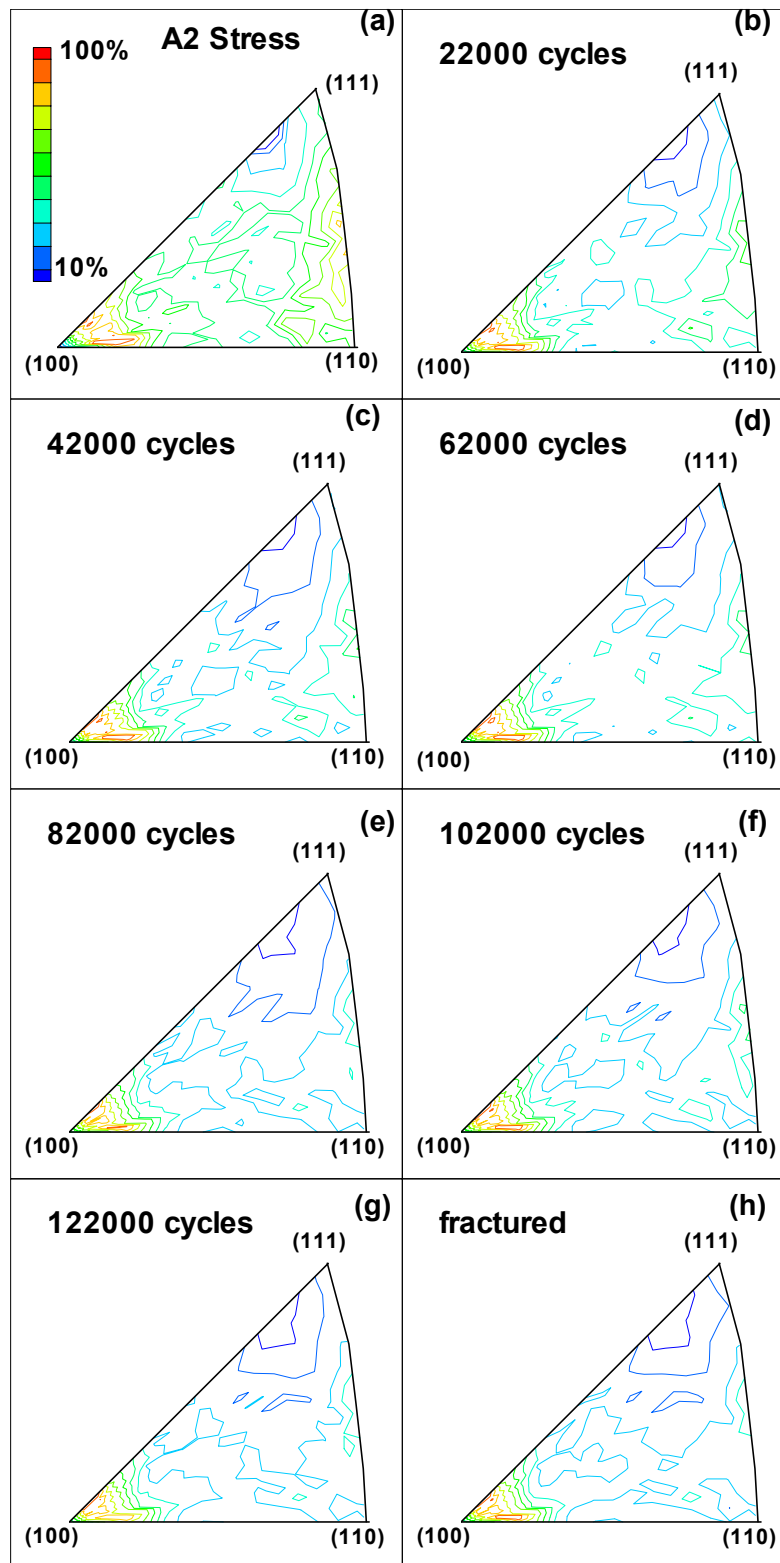


FIGURE B-6. INVERSE POLE FIGURES IN THE STRESS DIRECTION FOR SPECIMEN A2 AFTER (a) 0, (b) 22,000, (c) 42,000, (d) 62,000, (e) 82,000, (f) 102,000, (g) 122,000 FATIGUE CYCLES, AND (h) AFTER FAILURE

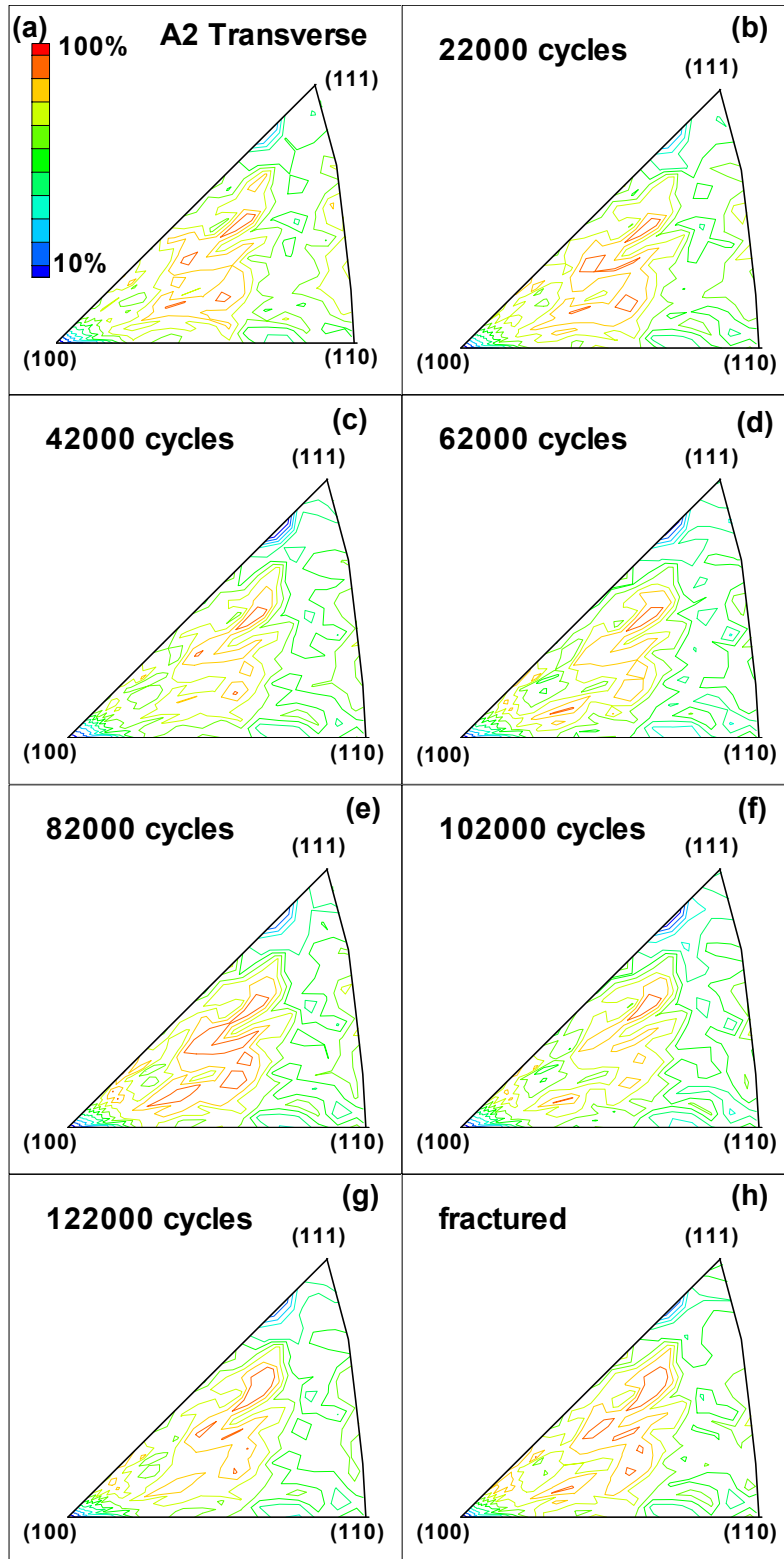


FIGURE B-7. INVERSE POLE FIGURES IN THE TRANSVERSE DIRECTION FOR SPECIMEN A2 AFTER (a) 0, (b) 22,000, (c) 42,000, (d) 62,000, (e) 82,000, (f) 102,000, (g) 122,000 FATIGUE CYCLES, AND (h) AFTER FAILURE

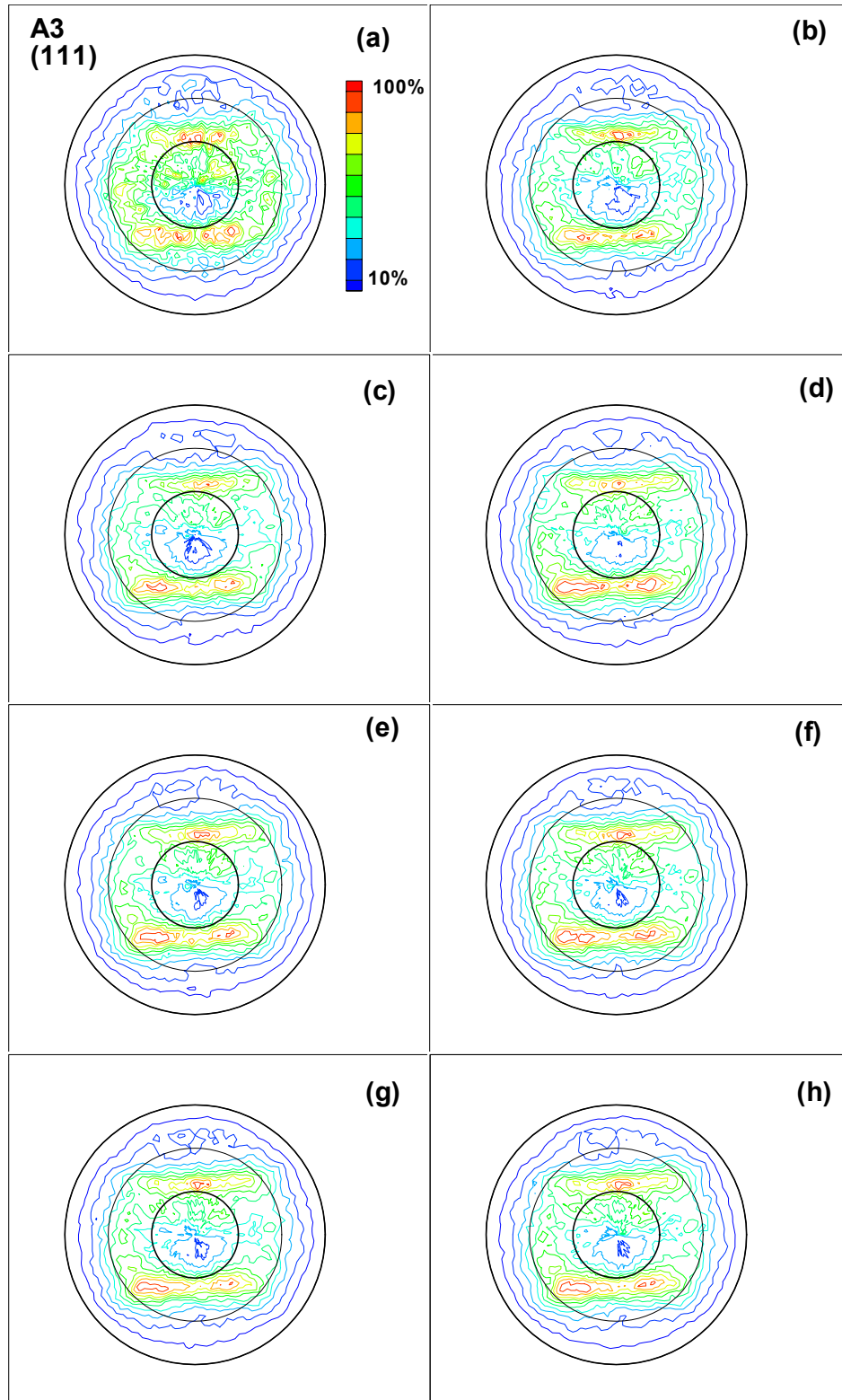


FIGURE B-8. DIRECT (111) POLE FIGURES FOR SPECIMEN A3 AFTER (a) 0, (b) 22,000, (c) 42,000, (d) 62,000, (e) 82,000, (f) 102,000, (g) 122,000 FATIGUE CYCLES, AND (h) AFTER FAILURE

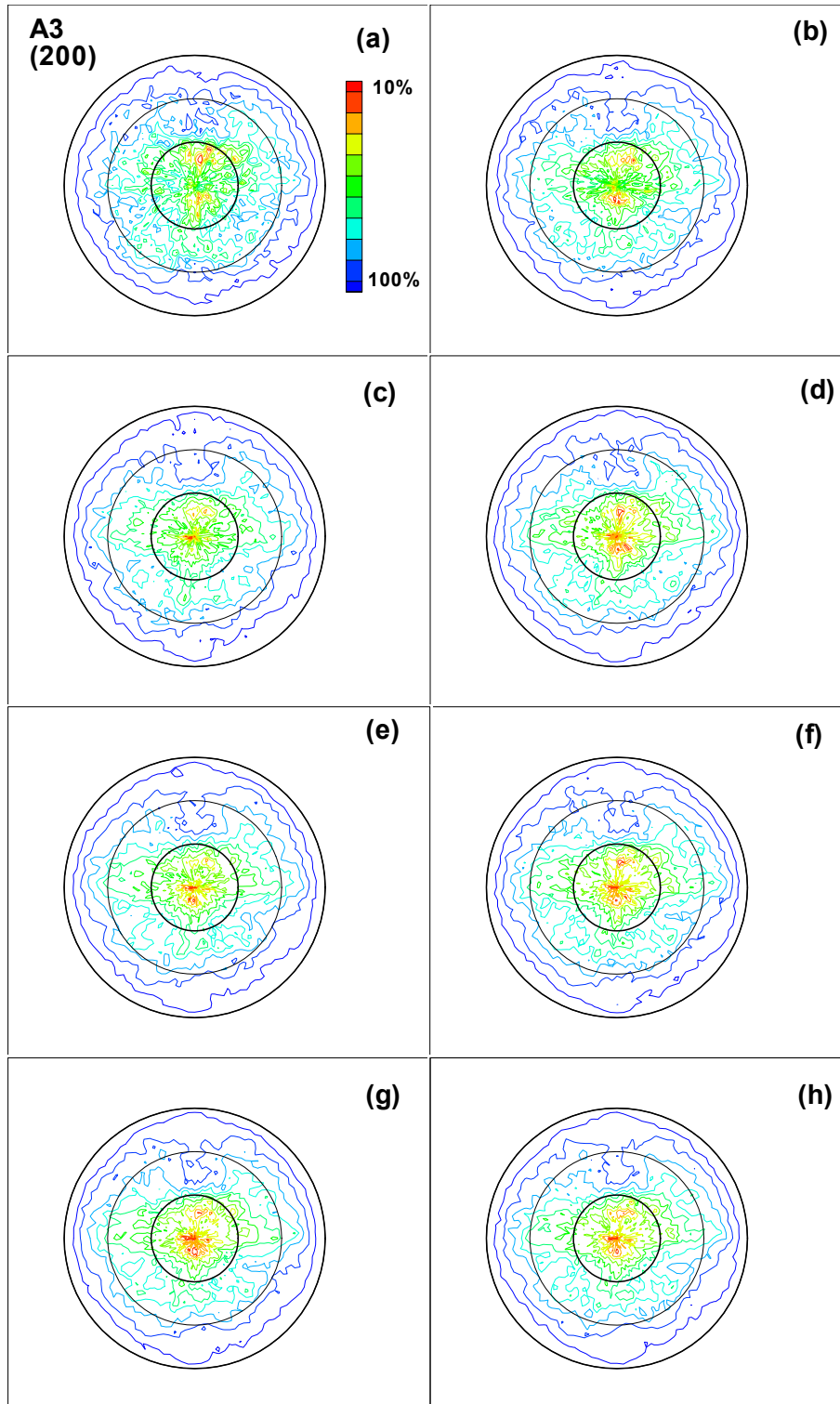


FIGURE B-9. DIRECT (200) POLE FIGURES FOR SPECIMEN A3 AFTER (a) 0, (b) 22,000, (c) 42,000, (d) 62,000, (e) 82,000, (f) 102,000, (g) 122,000, AND (h) 142,000 FATIGUE CYCLES



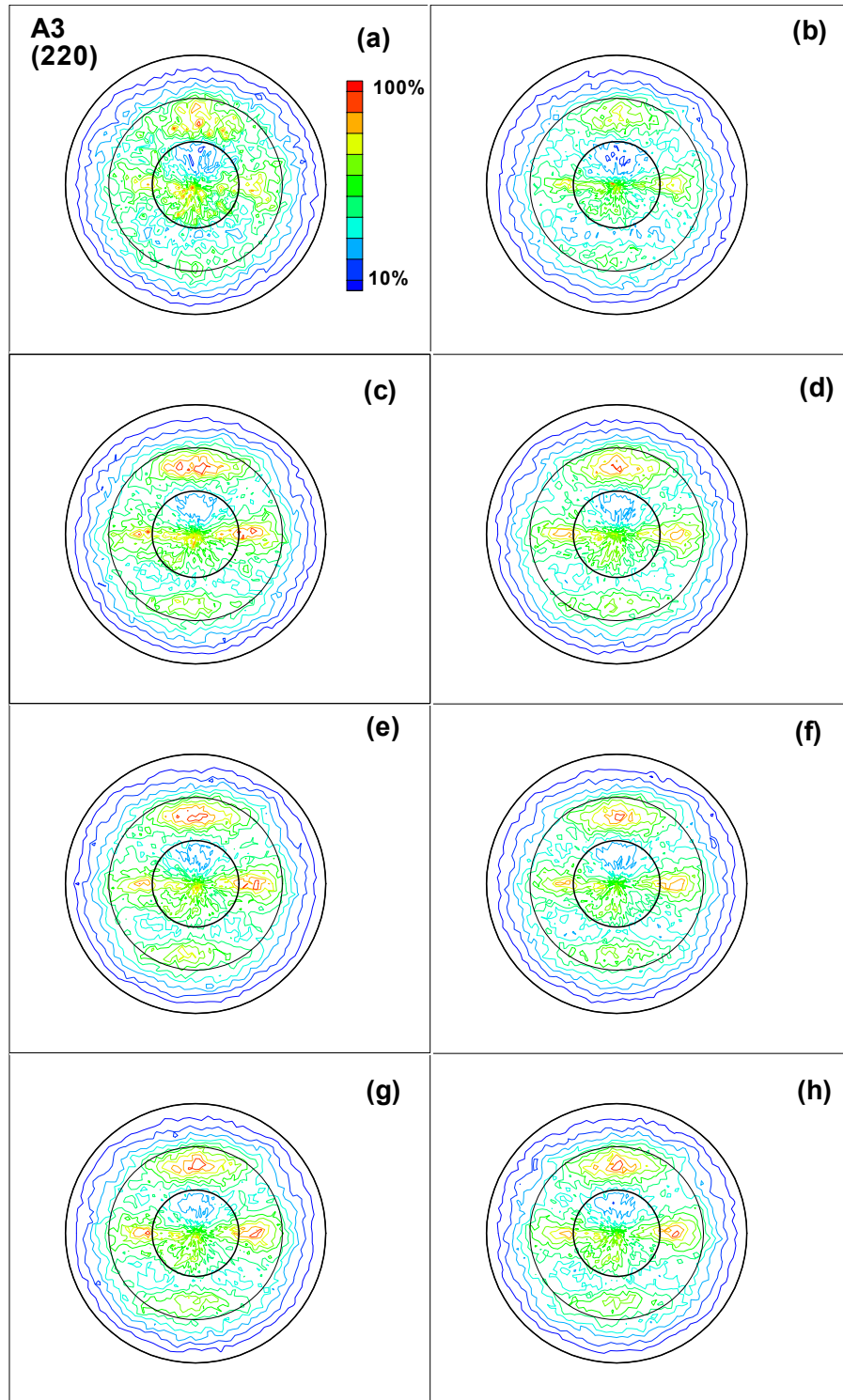


FIGURE B-10. DIRECT (220) POLE FIGURES FOR SPECIMEN A3 AFTER (a) 0, (b) 22,000, (c) 42,000, (d) 62,000, (e) 82,000, (f) 102,000, (g) 122,000 FATIGUE CYCLES, AND (h) AFTER FAILURE



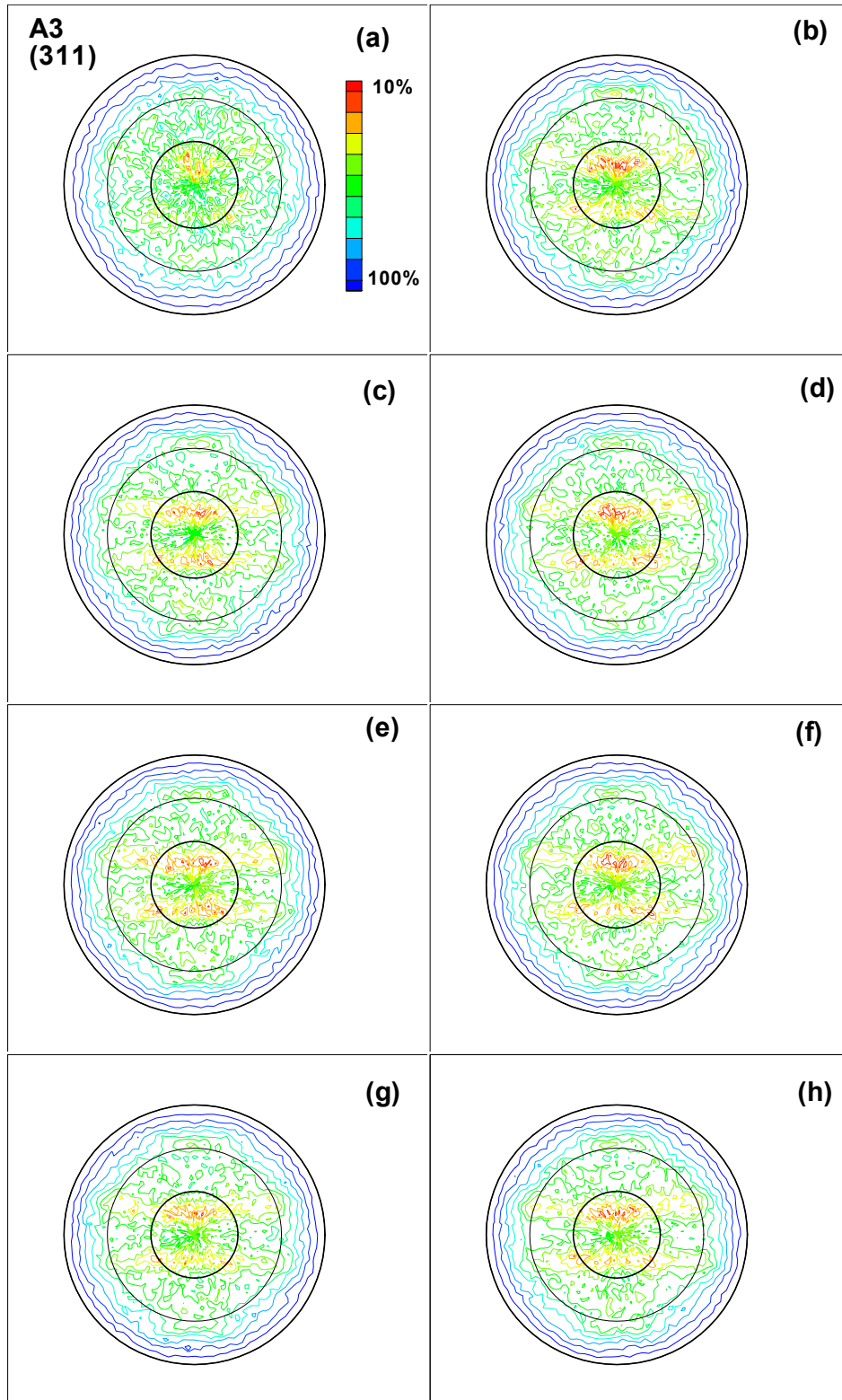


FIGURE B-11. DIRECT (311) POLE FIGURES FOR SPECIMEN A3 AFTER (a) 0, (b) 22,000, (c) 42,000, (d) 62,000, (e) 82,000, (f) 102,000, (g) 122,000 FATIGUE CYCLES, AND (h) AFTER FAILURE

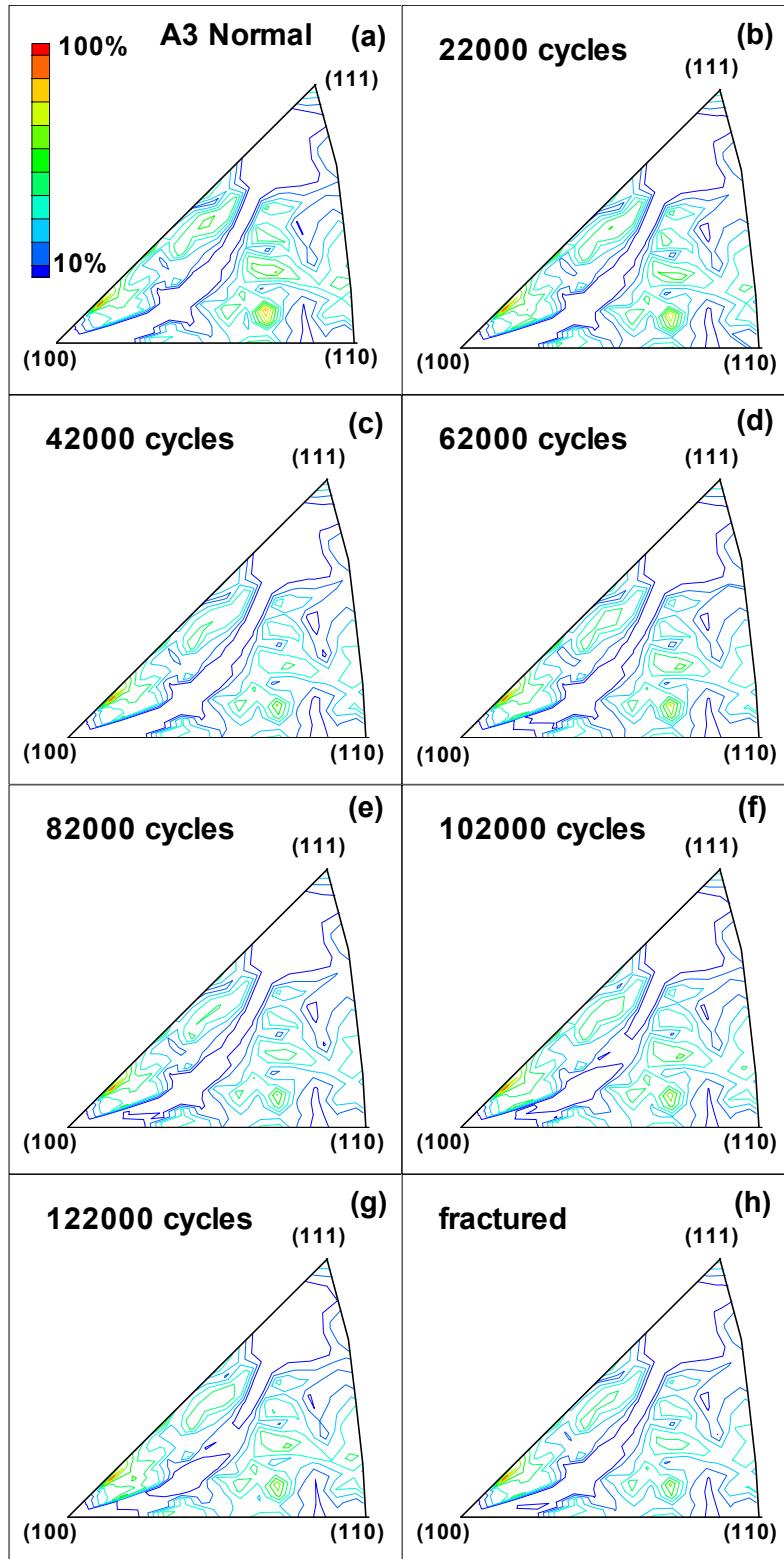


FIGURE B-12. INVERSE POLE FIGURES IN THE NORMAL DIRECTION FOR SPECIMEN A3 AFTER (a) 0, (b) 22,000, (c) 42,000, (d) 62,000, (e) 82,000, (f) 102,000, (g) 122,000 FATIGUE CYCLES, AND (h) AFTER FAILURE

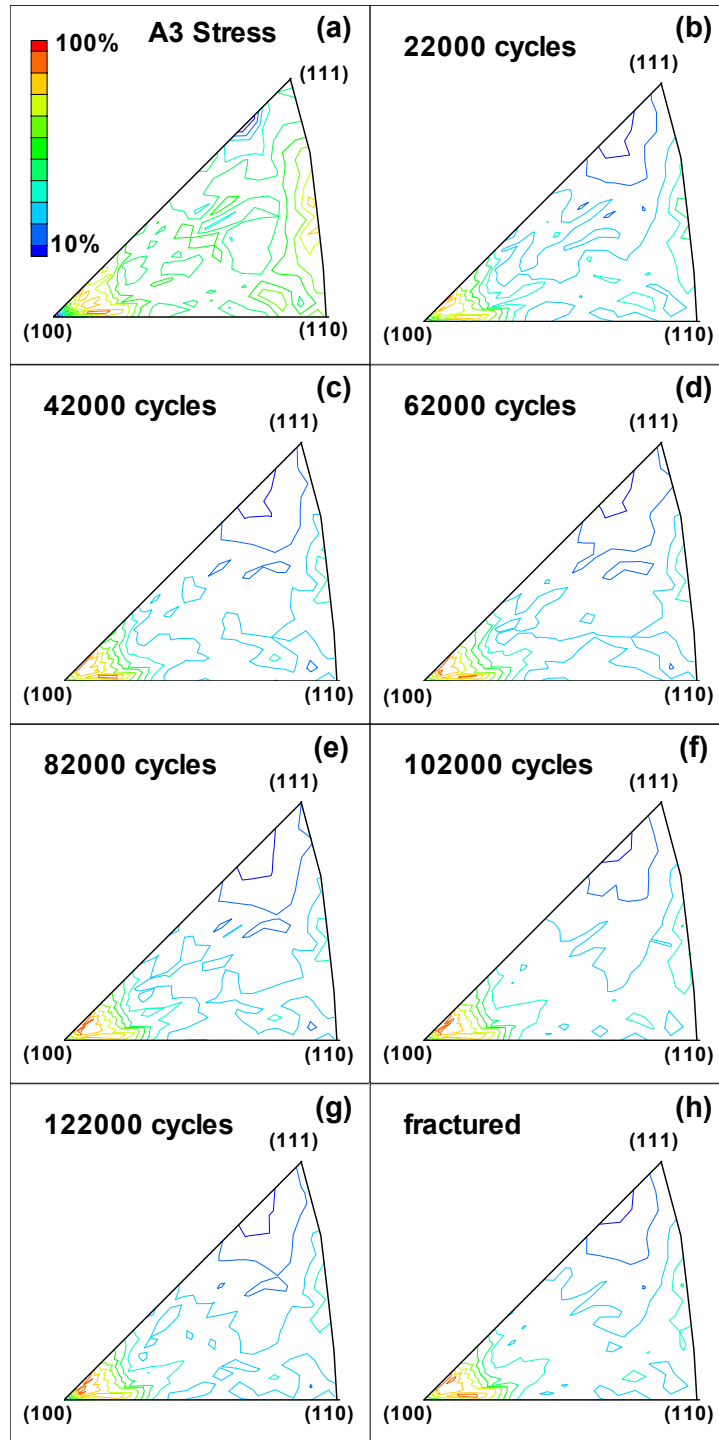


FIGURE B-13. INVERSE POLE FIGURES IN THE STRESS DIRECTION FOR SPECIMEN A3 AFTER (a) 0, (b) 22,000, (c) 42,000, (d) 62,000, (e) 82,000, (f) 102,000, (g) 122,000 FATIGUE CYCLES, AND (h) AFTER FAILURE

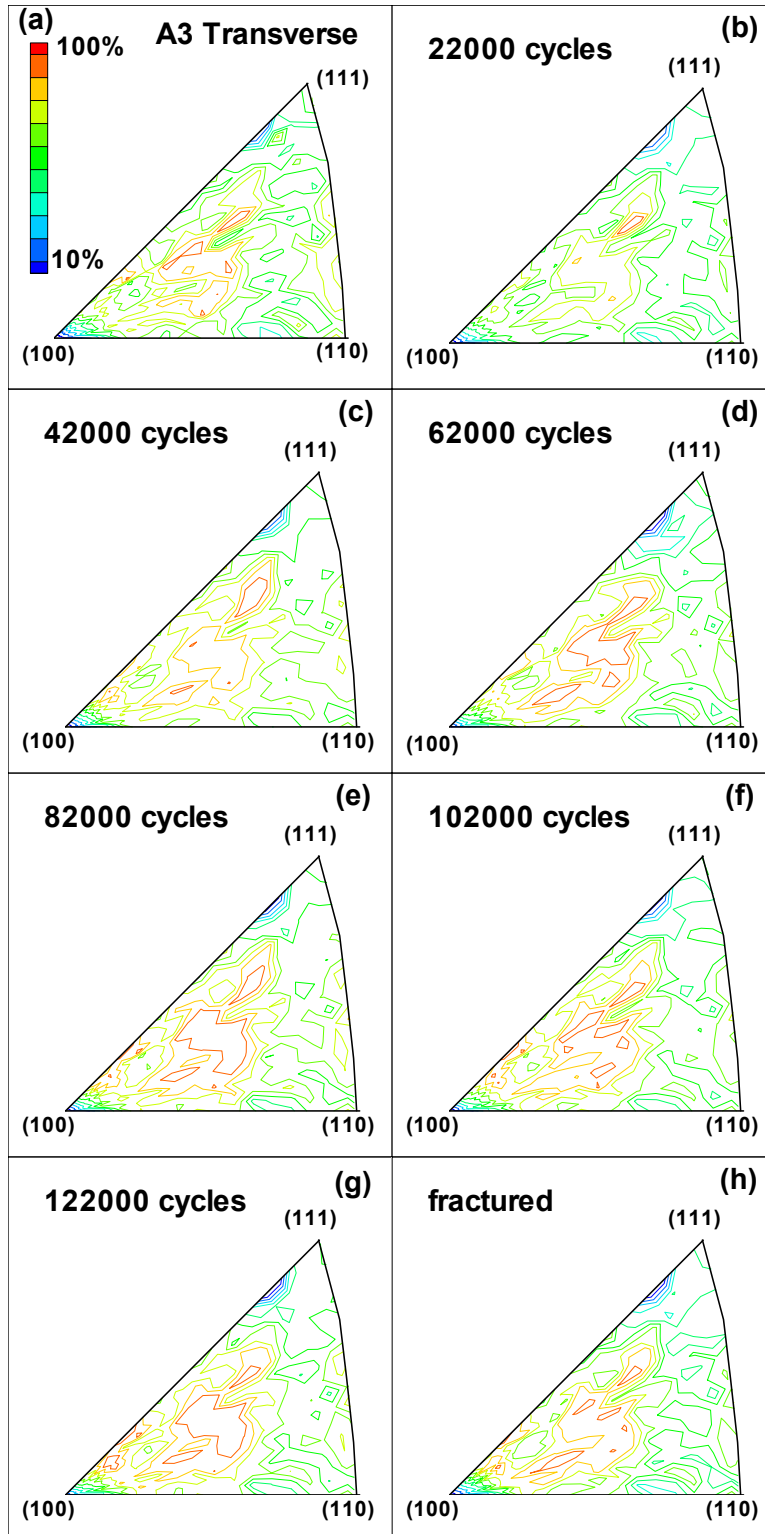


FIGURE B-14. INVERSE POLE FIGURES IN THE TRANSVERSE DIRECTION FOR SPECIMEN A3 AFTER (a) 0, (b) 22,000, (c) 42,000, (d) 62,000, (e) 82,000, (f) 102,000, (g) 122,000 FATIGUE CYCLES, AND (h) AFTER FAILURE

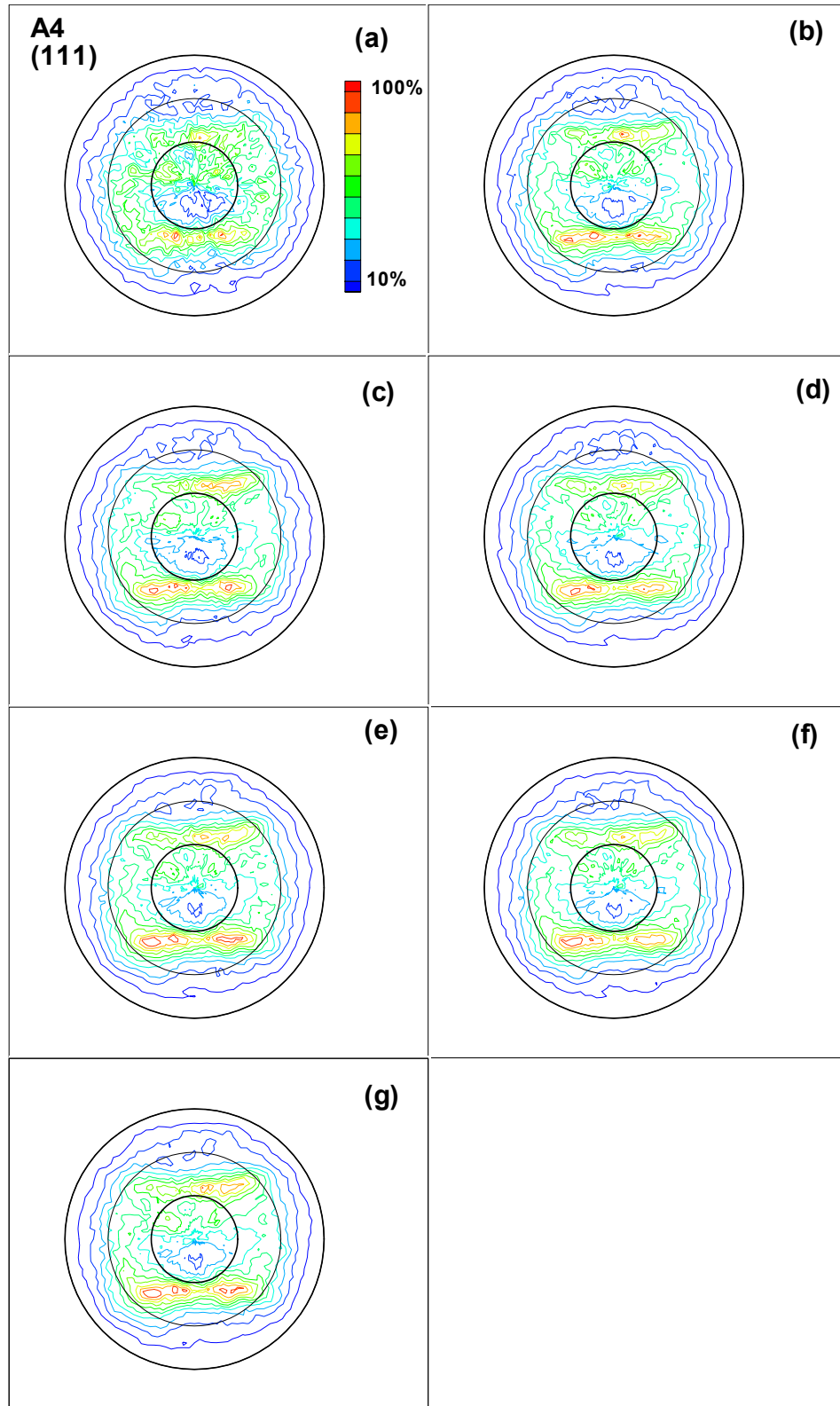


FIGURE B-15. DIRECT (111) POLE FIGURES FOR SPECIMEN A4 AFTER (a) 0, (b) 22,000, (c) 42,000, (d) 62,000, (e) 82,000, (f) 102,000, AND (g) AFTER FAILURE

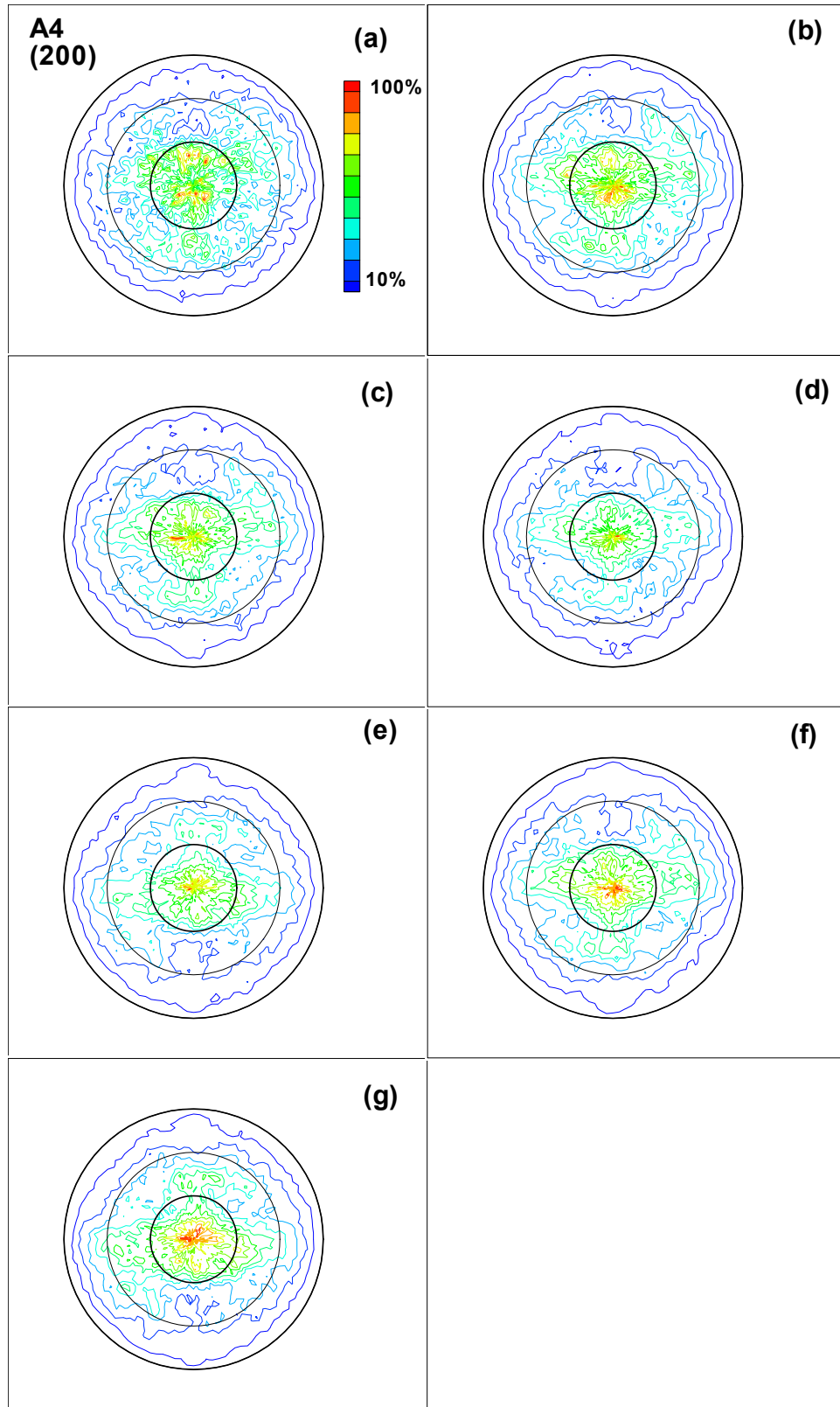


FIGURE B-16. DIRECT (200) POLE FIGURES FOR SPECIMEN A4 AFTER (a) 0, (b) 22,000, (c) 42,000, (d) 62,000, (e) 82,000, (f) 102,000, AND (g) AFTER FAILURE

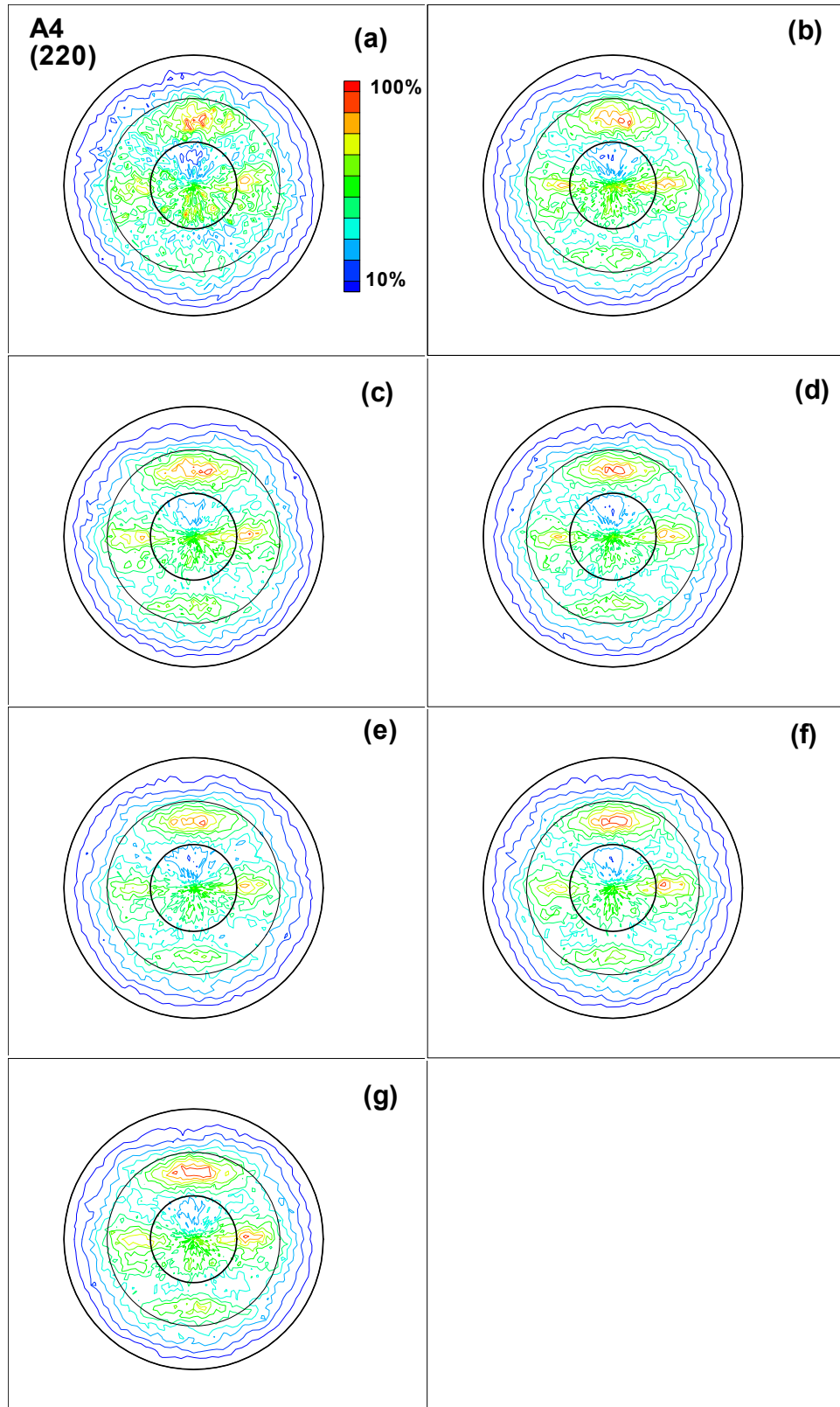


FIGURE B-17. DIRECT (220) POLE FIGURES FOR SPECIMEN A4 AFTER (a) 0, (b) 22,000, (c) 42,000, (d) 62,000, (e) 82,000, (f) 102,000, AND (g) AFTER FAILURE



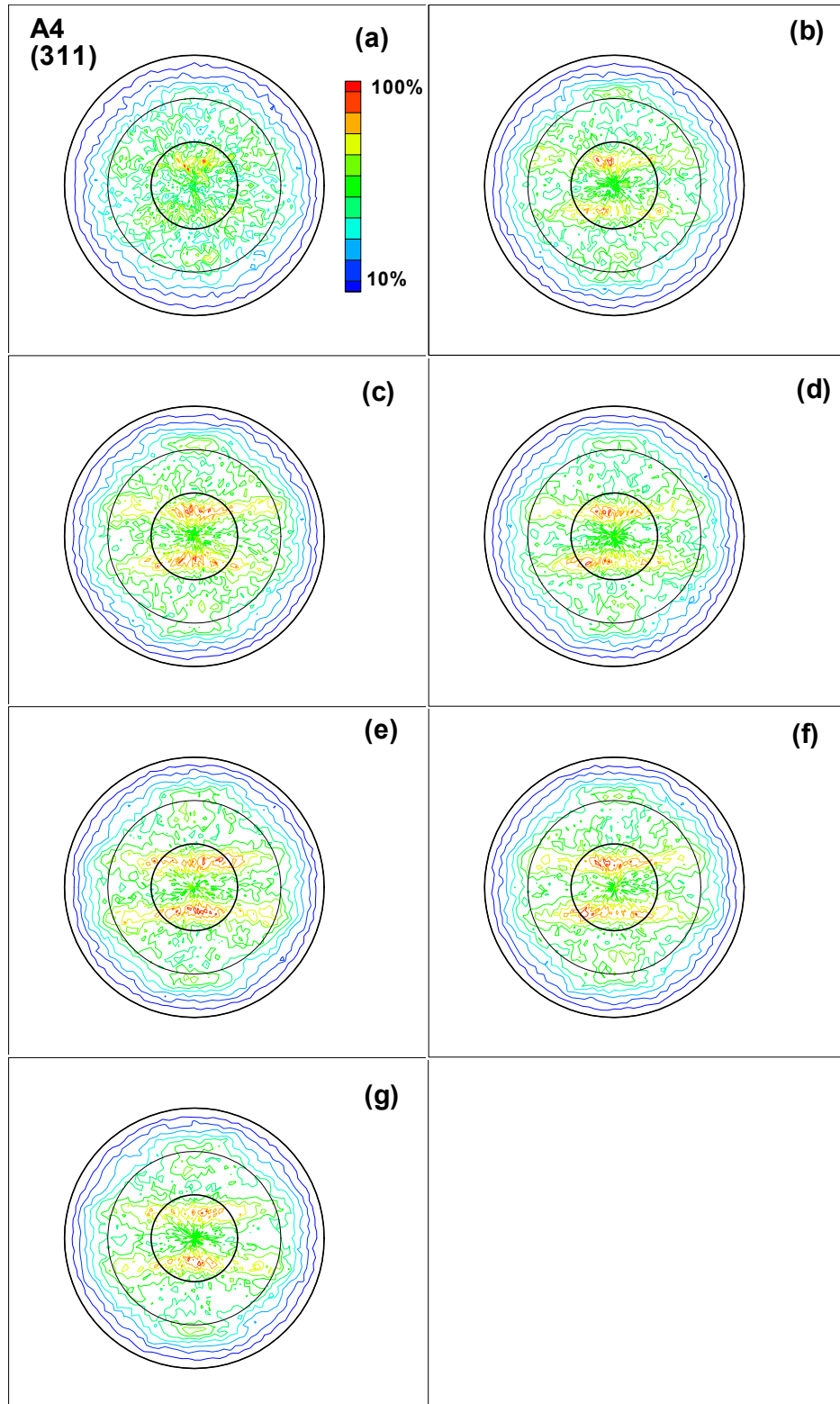


FIGURE B-18. DIRECT (311) POLE FIGURES FOR SPECIMEN A4 AFTER (a) 0, (b) 22,000, (c) 42,000, (d) 62,000, (e) 82,000, (f) 102,000, AND (g) AFTER FAILURE



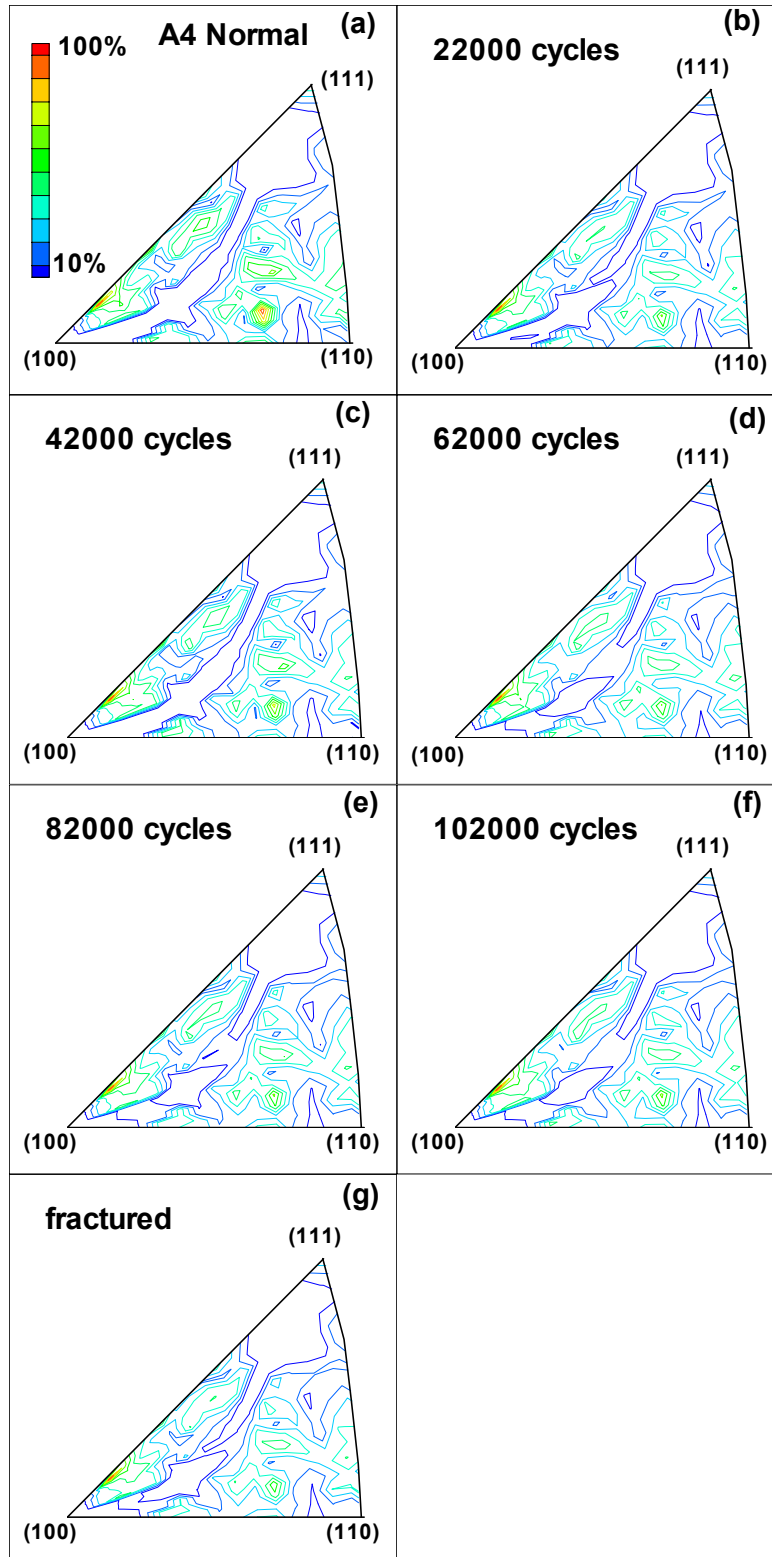


FIGURE B-19. INVERSE POLE FIGURES IN THE NORMAL DIRECTION FOR SPECIMEN A4 AFTER (a) 0, (b) 22,000, (c) 42,000, (d) 62,000, (e) 82,000, (f) 102,000, AND (g) AFTER FAILURE

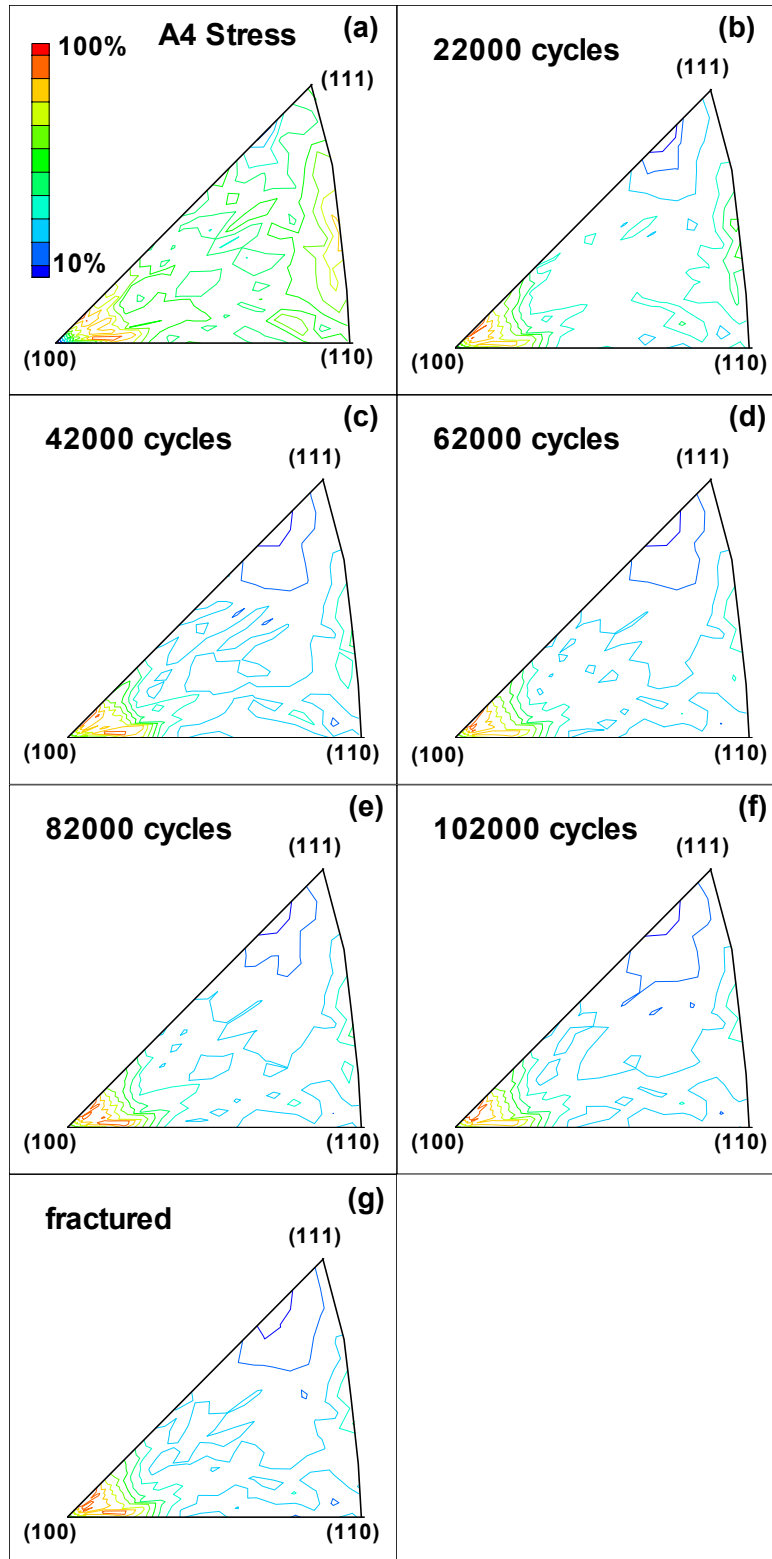


FIGURE B-20. INVERSE POLE FIGURES IN THE STRESS DIRECTION FOR SPECIMEN A4 AFTER (a) 0, (b) 22,000, (c) 42,000, (d) 62,000, (e) 82,000, (f) 102,000, AND (g) AFTER FAILURE

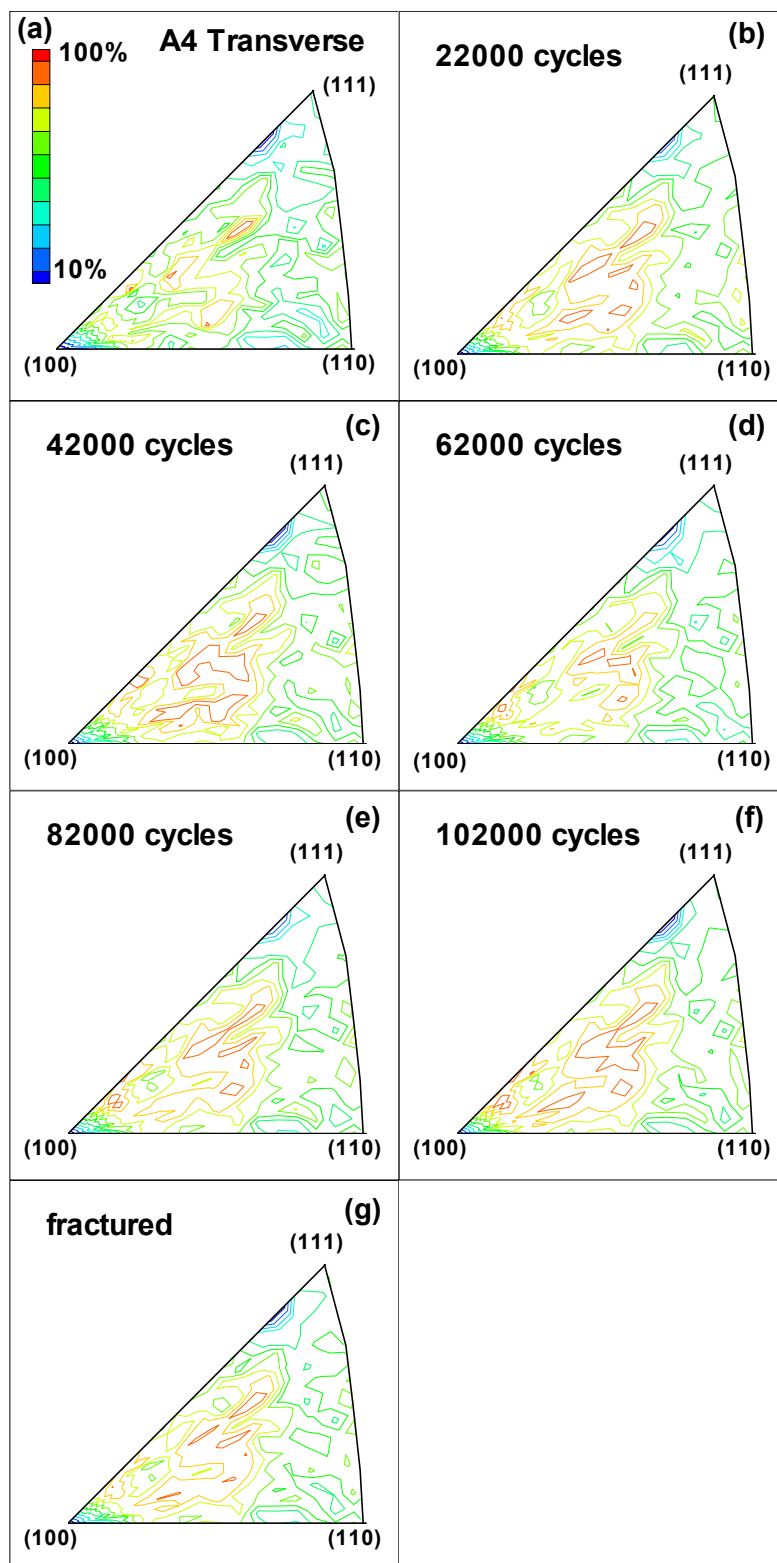


FIGURE B-21. INVERSE POLE FIGURES IN THE TRANSVERSE DIRECTION FOR SPECIMEN A4 AFTER (a) 0, (b) 22,000, (c) 42,000, (d) 62,000, (e) 82,000, (f) 102,000, AND (g) AFTER FAILURE

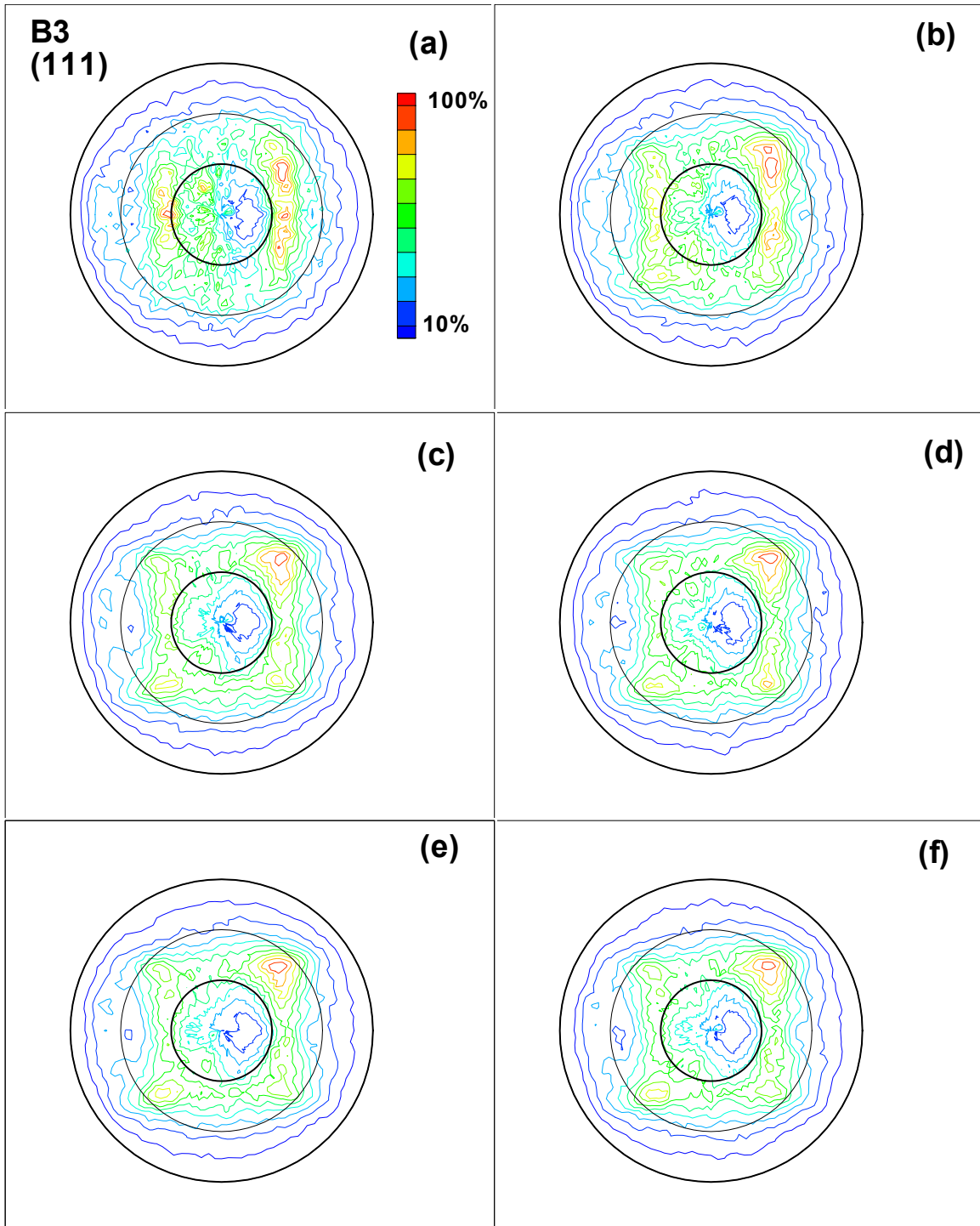


FIGURE B-22. DIRECT (111) POLE FIGURES FOR SPECIMEN B3 AFTER (a) 0, (b) 22,000, (c) 42,000, (d) 62,000, (e) 82,000 FATIGUE CYCLES, AND (f) AFTER FAILURE

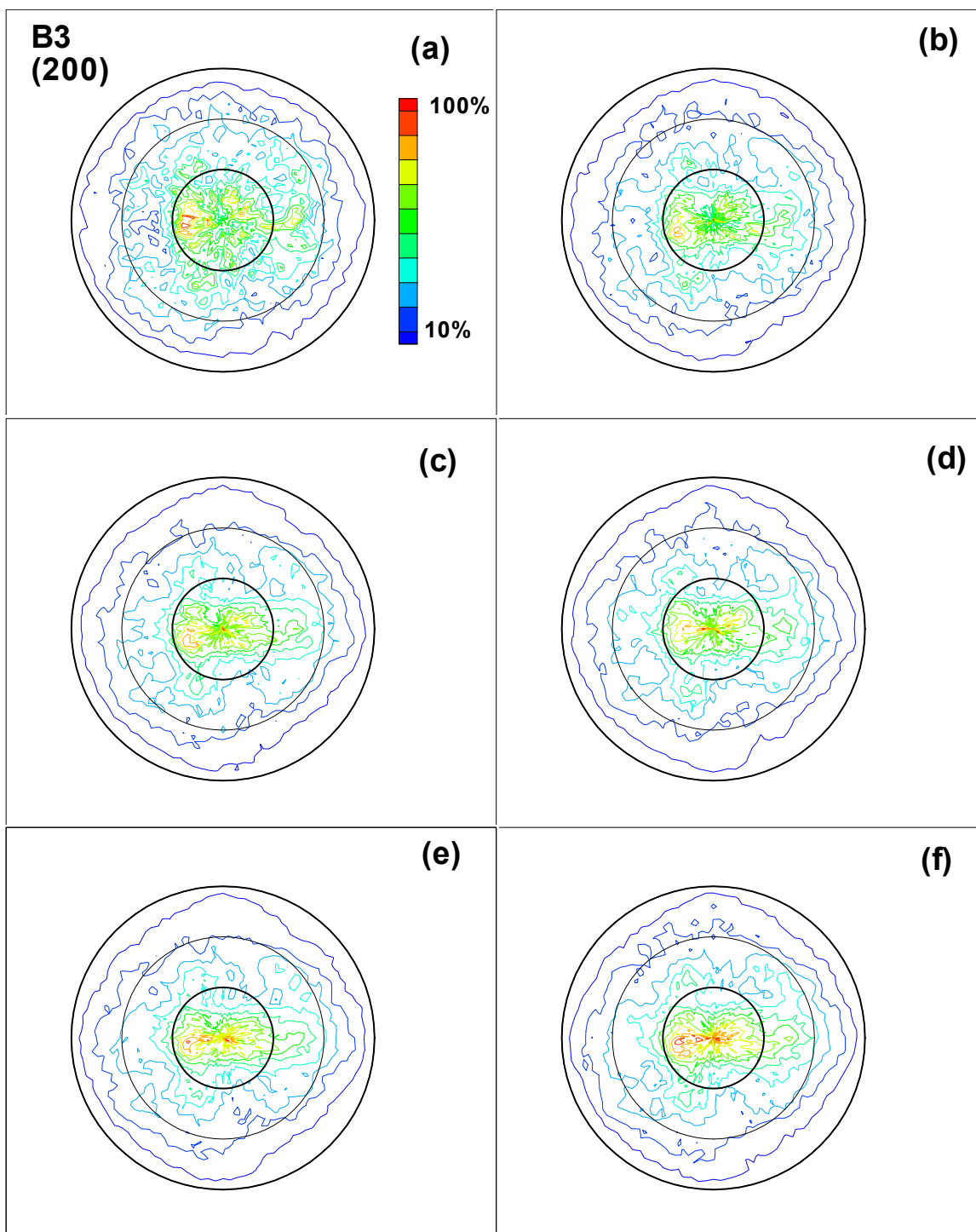


FIGURE B-23. DIRECT (200) POLE FIGURES FOR SPECIMEN B3 AFTER (a) 0, (b) 22,000, (c) 42,000, (d) 62,000, (e) 82,000 FATIGUE CYCLES, AND (f) AFTER FAILURE

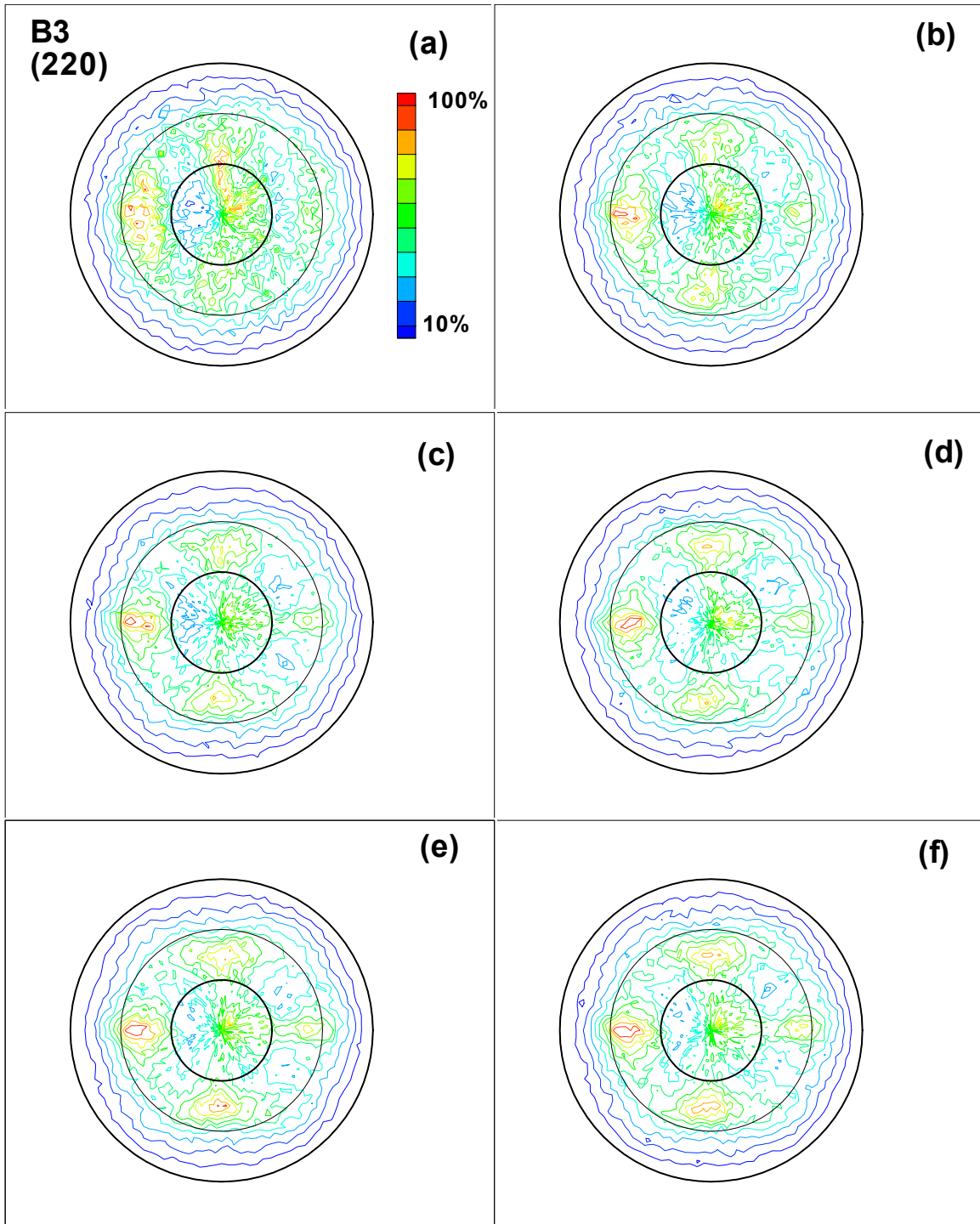


FIGURE B-24. DIRECT (220) POLE FIGURES FOR SPECIMEN B3 AFTER (a) 0, (b) 22,000, (c) 42,000, (d) 62,000, (e) 82,000 FATIGUE CYCLES, AND (f) AFTER FAILURE

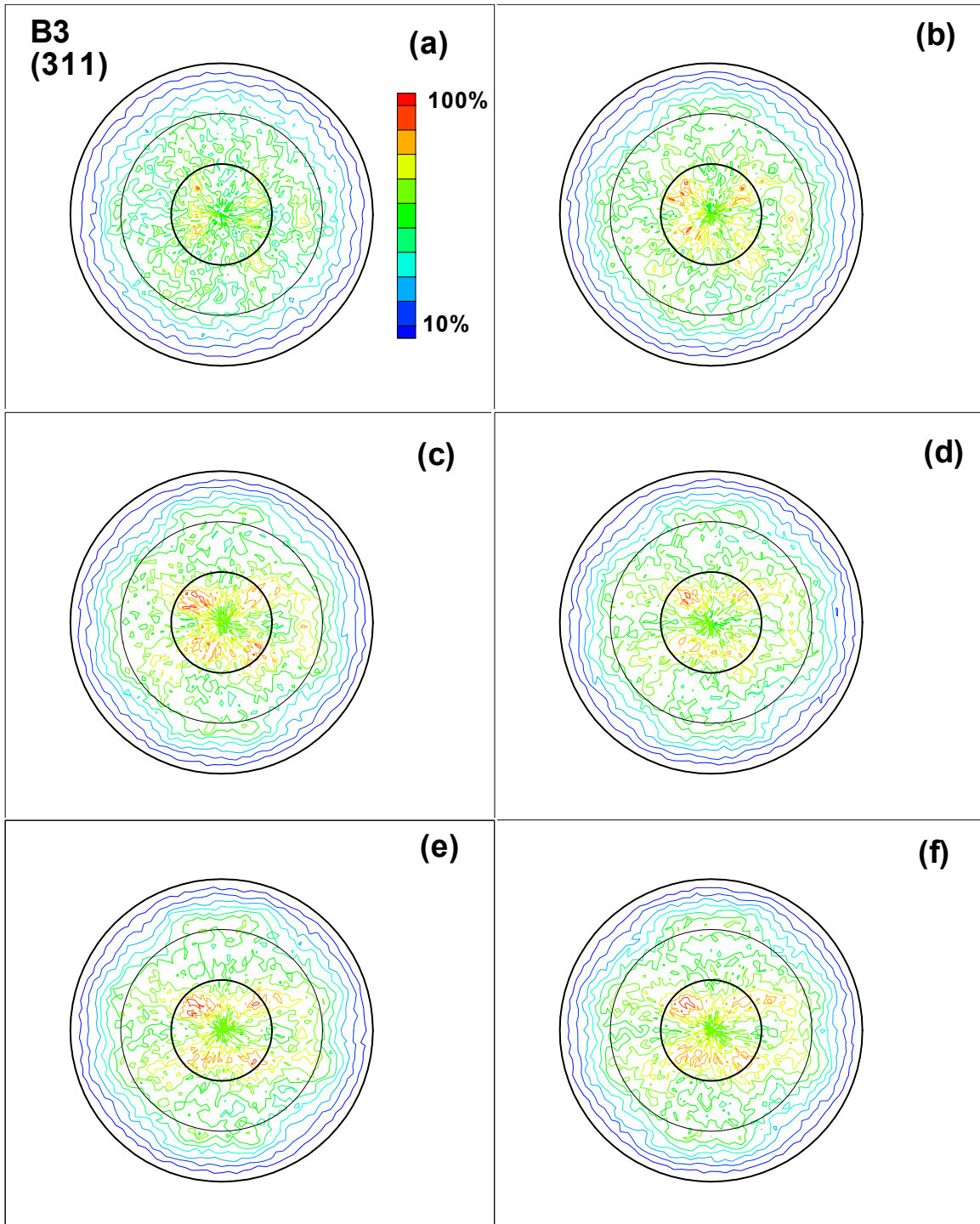


FIGURE B-25. DIRECT (311) POLE FIGURES FOR SPECIMEN B3 AFTER (a) 0, (b) 22,000, (c) 42,000, (d) 62,000, (e) 82,000 FATIGUE CYCLES, AND (f) AFTER FAILURE



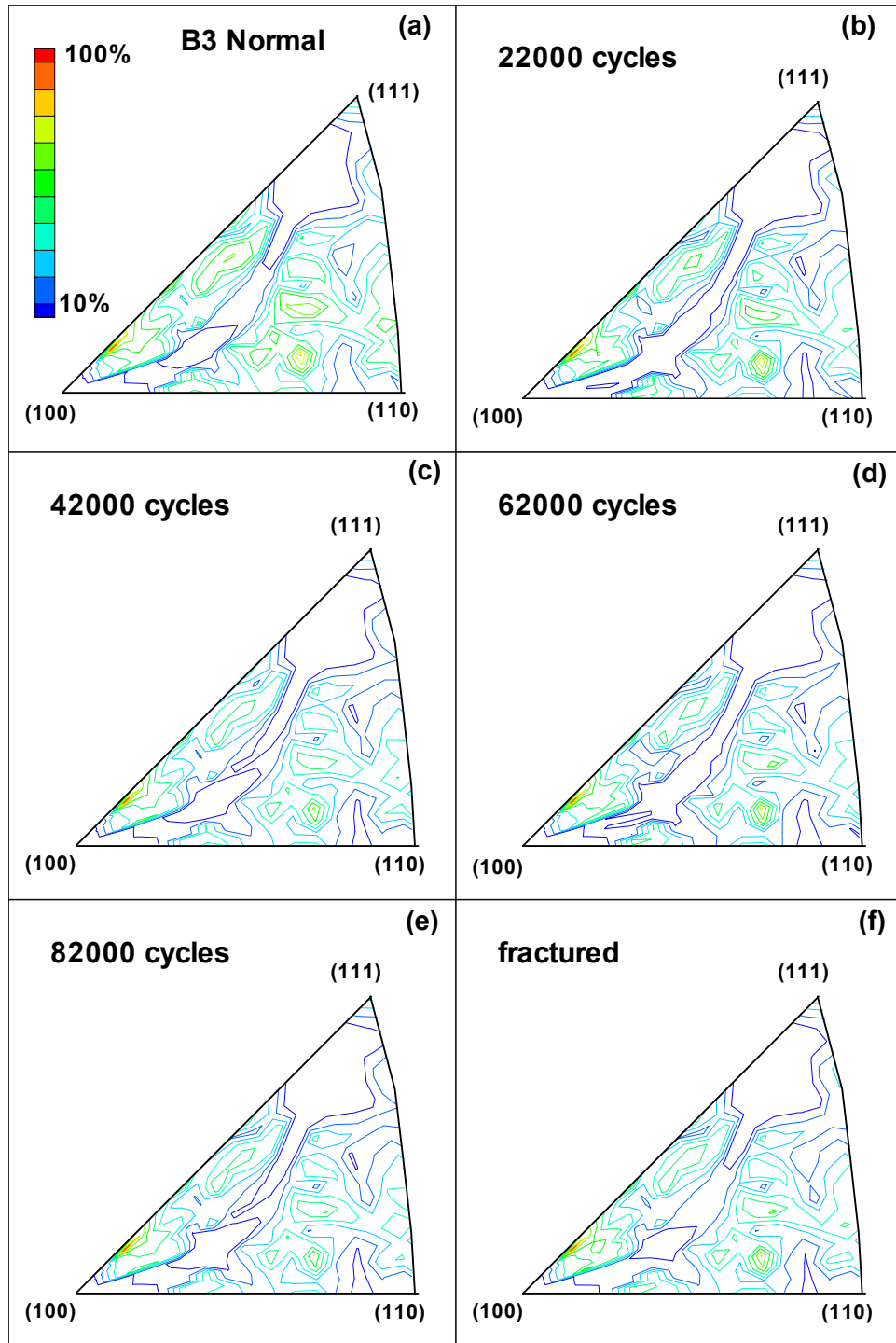


FIGURE B-26. INVERSE POLE FIGURES IN THE NORMAL DIRECTION FOR SPECIMEN B3 AFTER (a) 0, (b) 22,000, (c) 42,000, (d) 62,000, (e) 82,000 FATIGUE CYCLES, AND (f) AFTER FAILURE



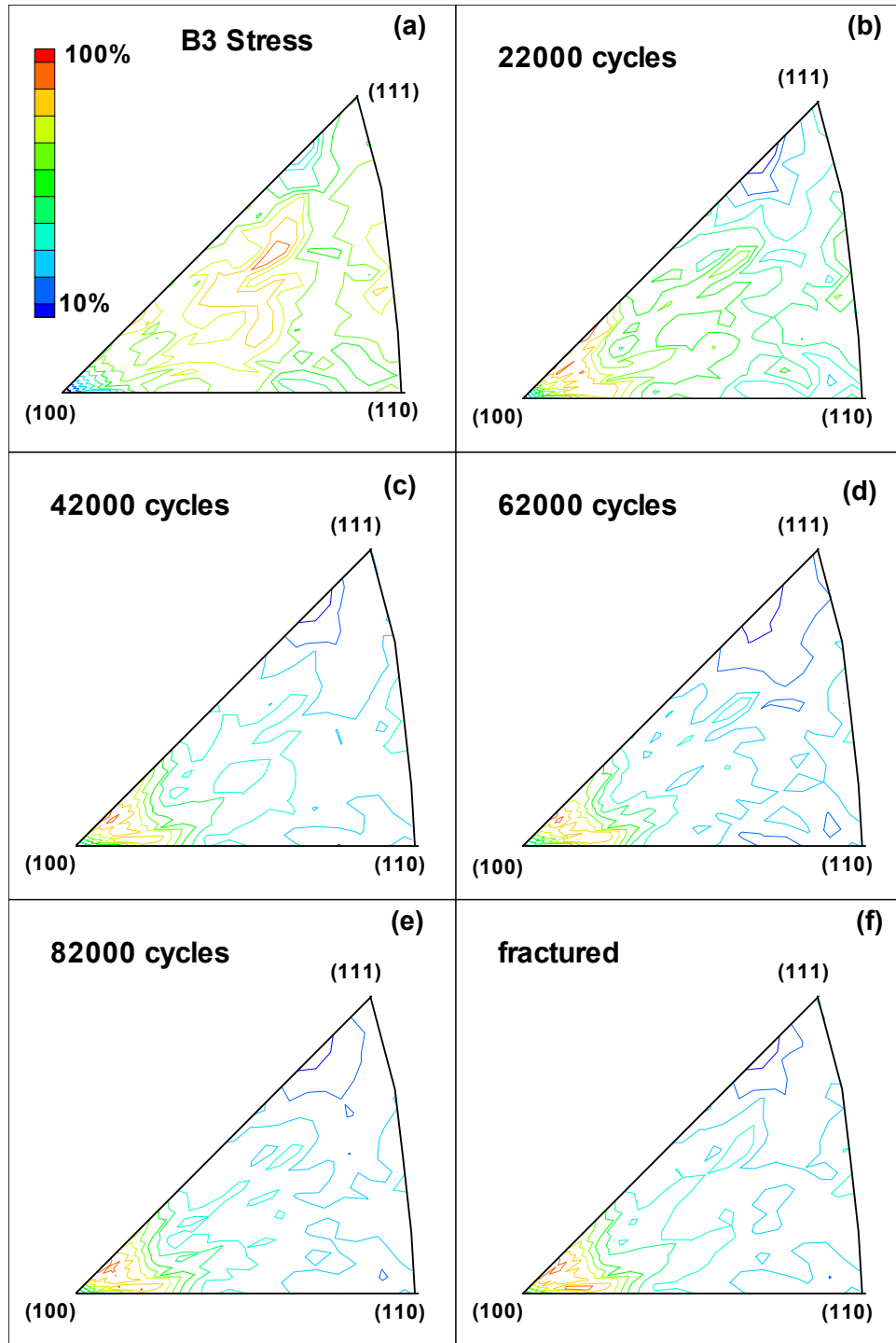


FIGURE B-27. INVERSE POLE FIGURES IN THE STRESS DIRECTION FOR SPECIMEN B3 AFTER (a) 0, (b) 22,000, (c) 42,000, (d) 62,000, (e) 82,000 FATIGUE CYCLES, AND (f) AFTER FAILURE

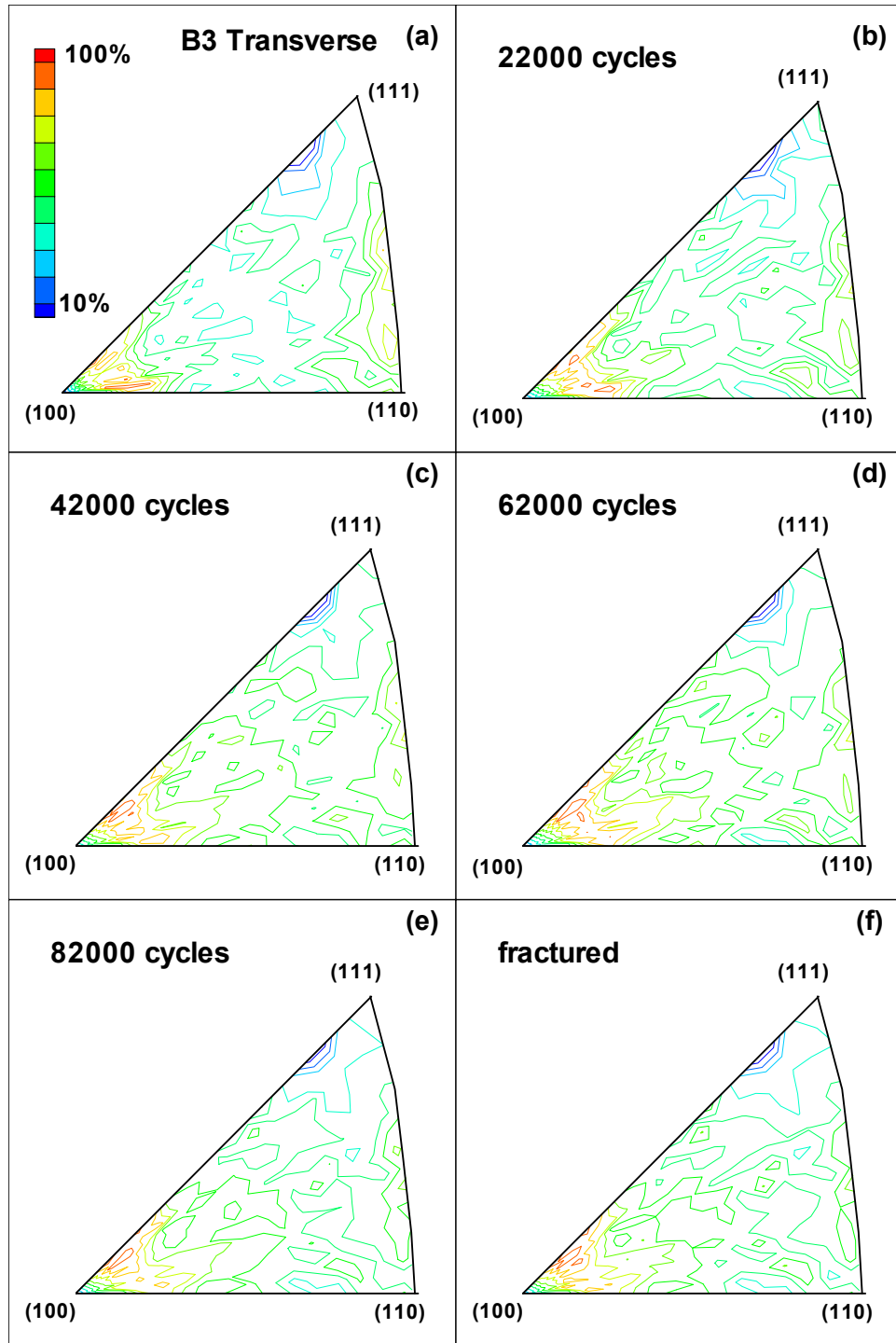


FIGURE B-28. INVERSE POLE FIGURES IN THE TRANSVERSE DIRECTION FOR SPECIMEN B3 AFTER (a) 0, (b) 22,000, (c) 42,000, (d) 62,000, (e) 82,000 FATIGUE CYCLES, AND (f) AFTER FAILURE

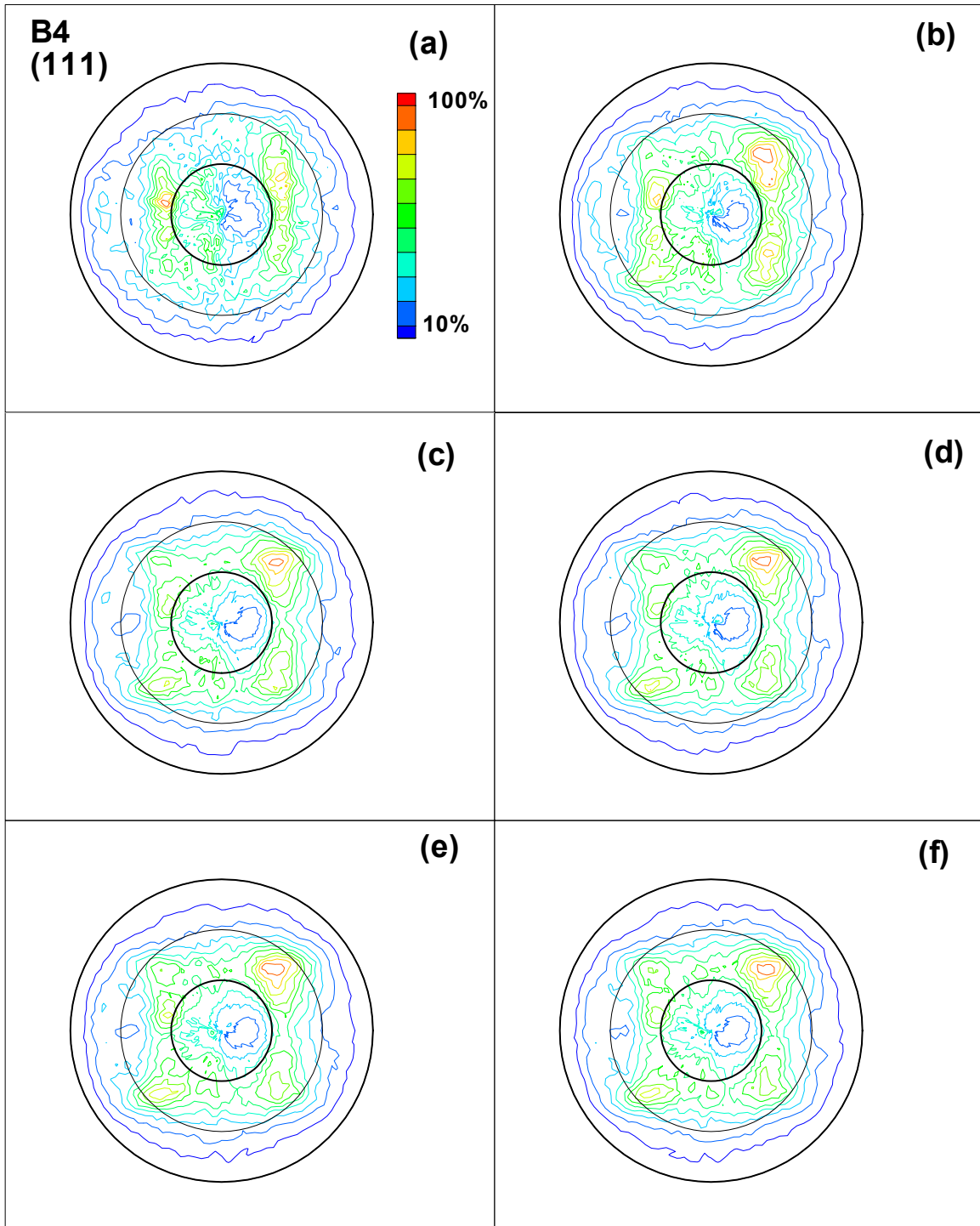


FIGURE B-29. DIRECT (111) POLE FIGURES FOR SPECIMEN B4 AFTER (a) 0, (b) 22,000, (c) 42,000, (d) 62,000, (e) 82,000 FATIGUE CYCLES, AND (f) AFTER FAILURE

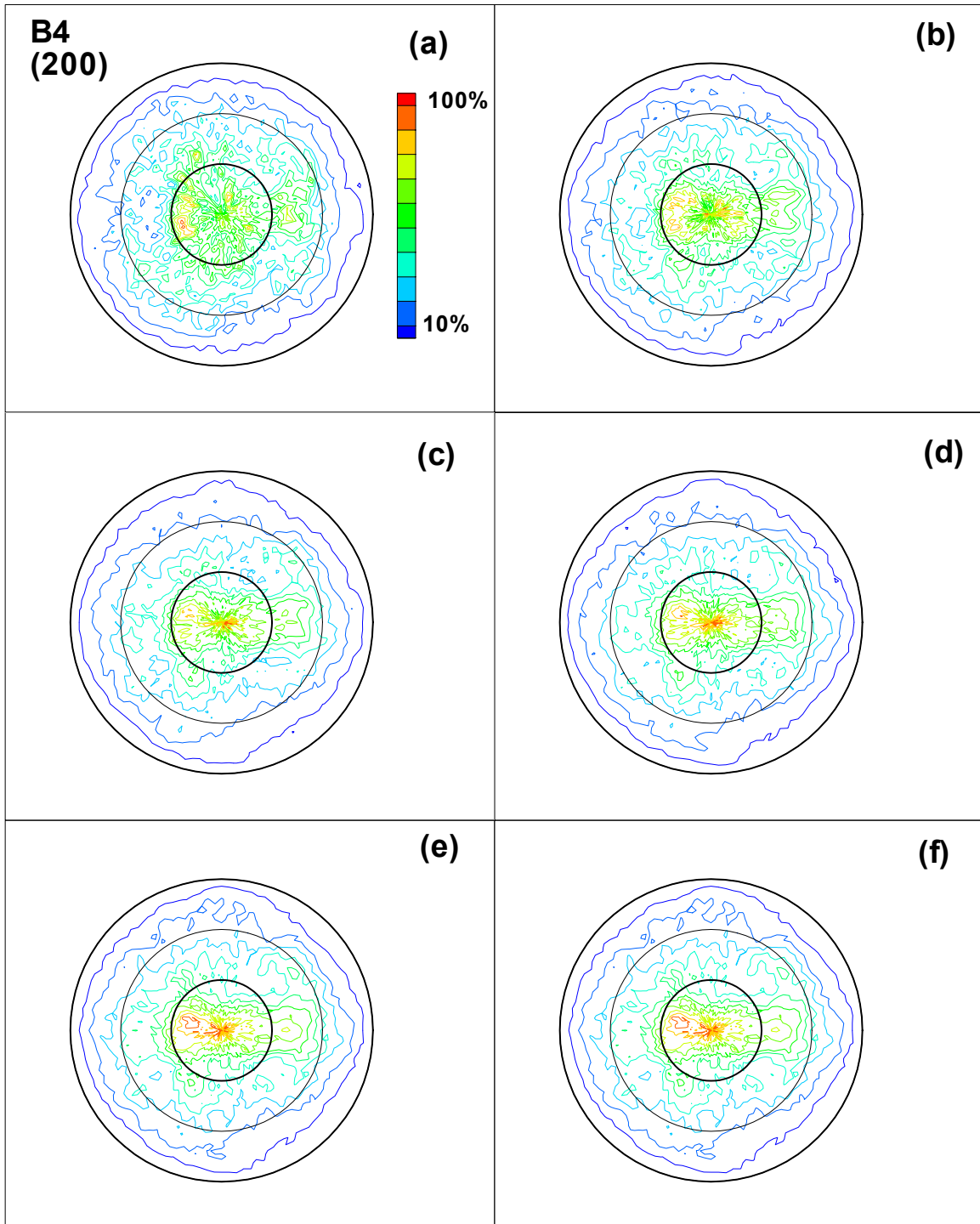


FIGURE B-30. DIRECT (200) POLE FIGURES FOR SPECIMEN B4 AFTER (a) 0, (b) 22,000, (c) 42,000, (d) 62,000, (e) 82,000 FATIGUE CYCLES, AND (f) AFTER FAILURE

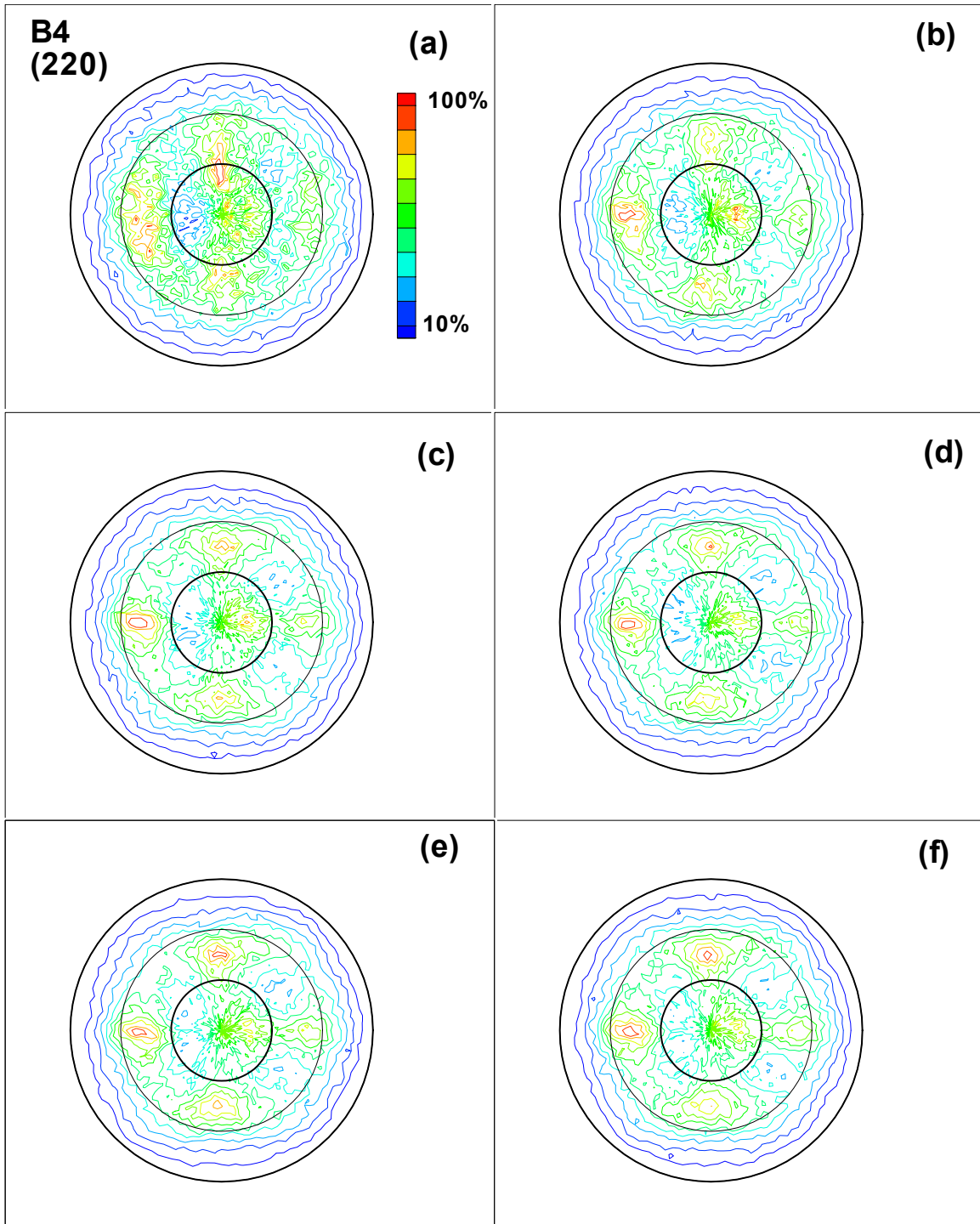
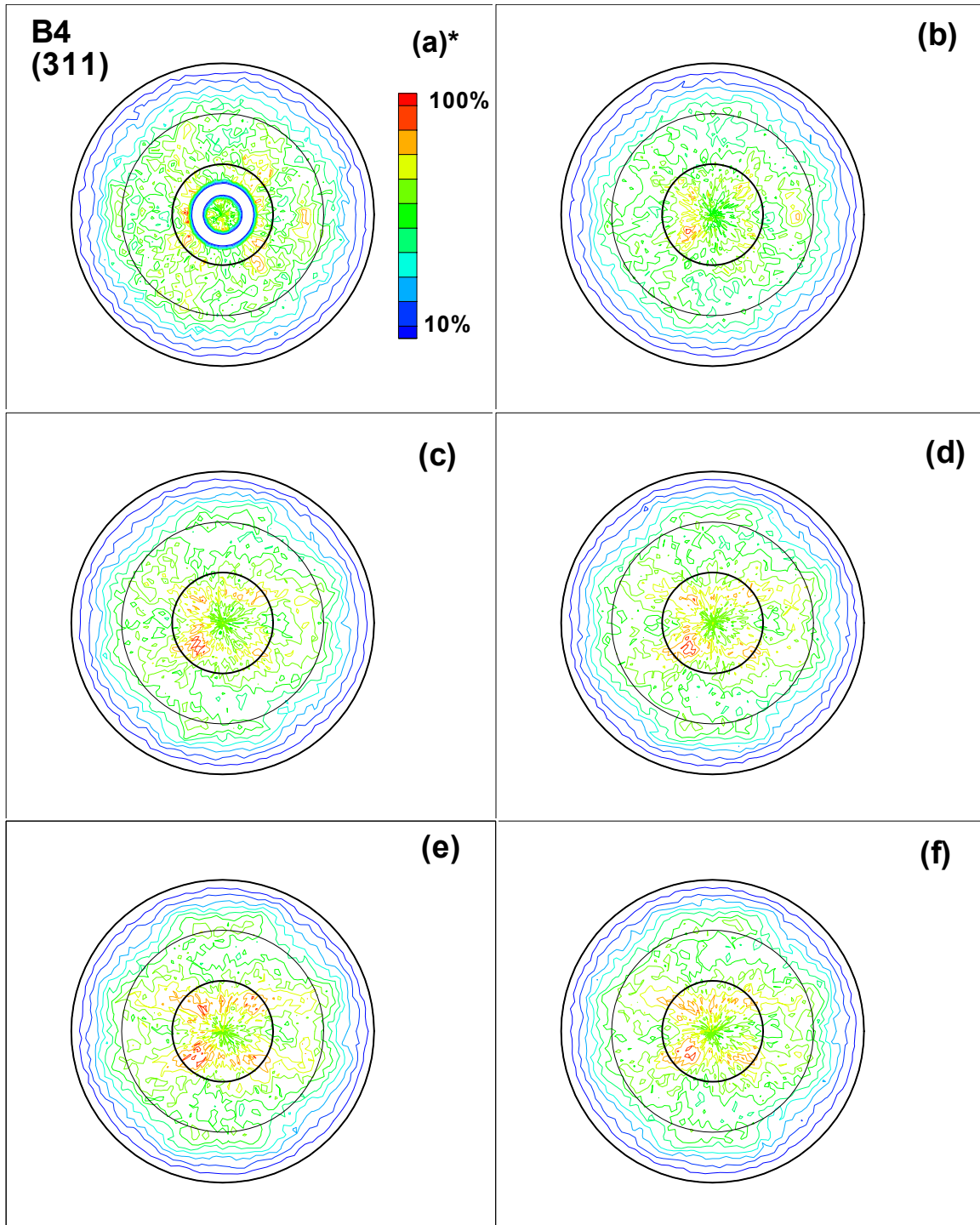


FIGURE B-31. DIRECT (220) POLE FIGURES FOR SPECIMEN B4 AFTER (a) 0, (b) 22,000, (c) 42,000, (d) 62,000, (e) 82,000 FATIGUE CYCLES, AND (f) AFTER FAILURE



\*There are clearly errors in the x-ray data in figure (a). This has a large effect on the inverse pole figures shown in figures B-33 through B-35.

FIGURE B-32. DIRECT (311) POLE FIGURES FOR SPECIMEN B4 AFTER (a) 0, (b) 22,000, (c) 42,000, (d) 62,000, (e) 82,000 FATIGUE CYCLES, AND (f) AFTER FAILURE

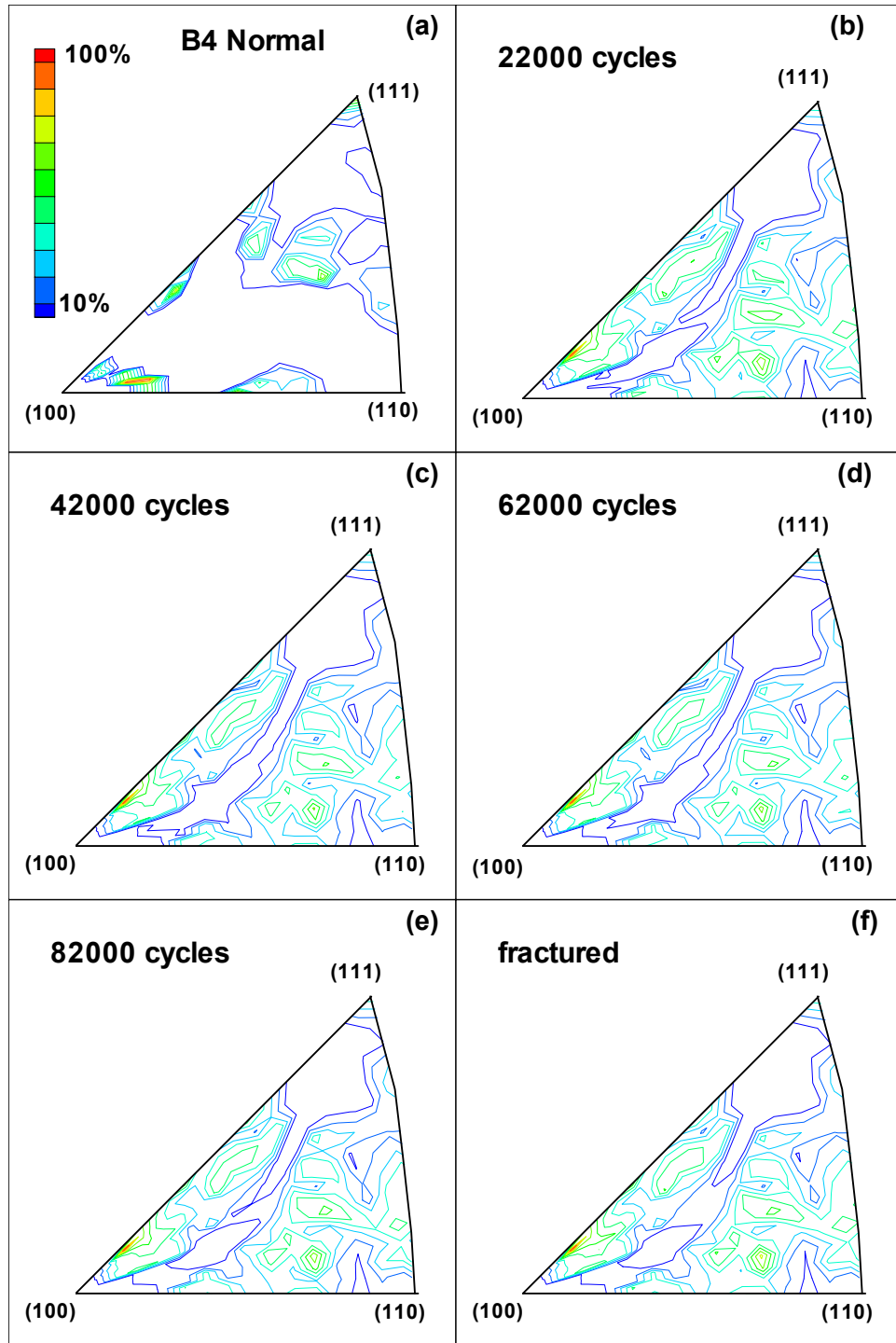


FIGURE B-33. INVERSE POLE FIGURES IN THE NORMAL DIRECTION FOR SPECIMEN B4 AFTER (a) 0, (b) 22,000, (c) 42,000, (d) 62,000, (e) 82,000 FATIGUE CYCLES, AND (f) AFTER FAILURE

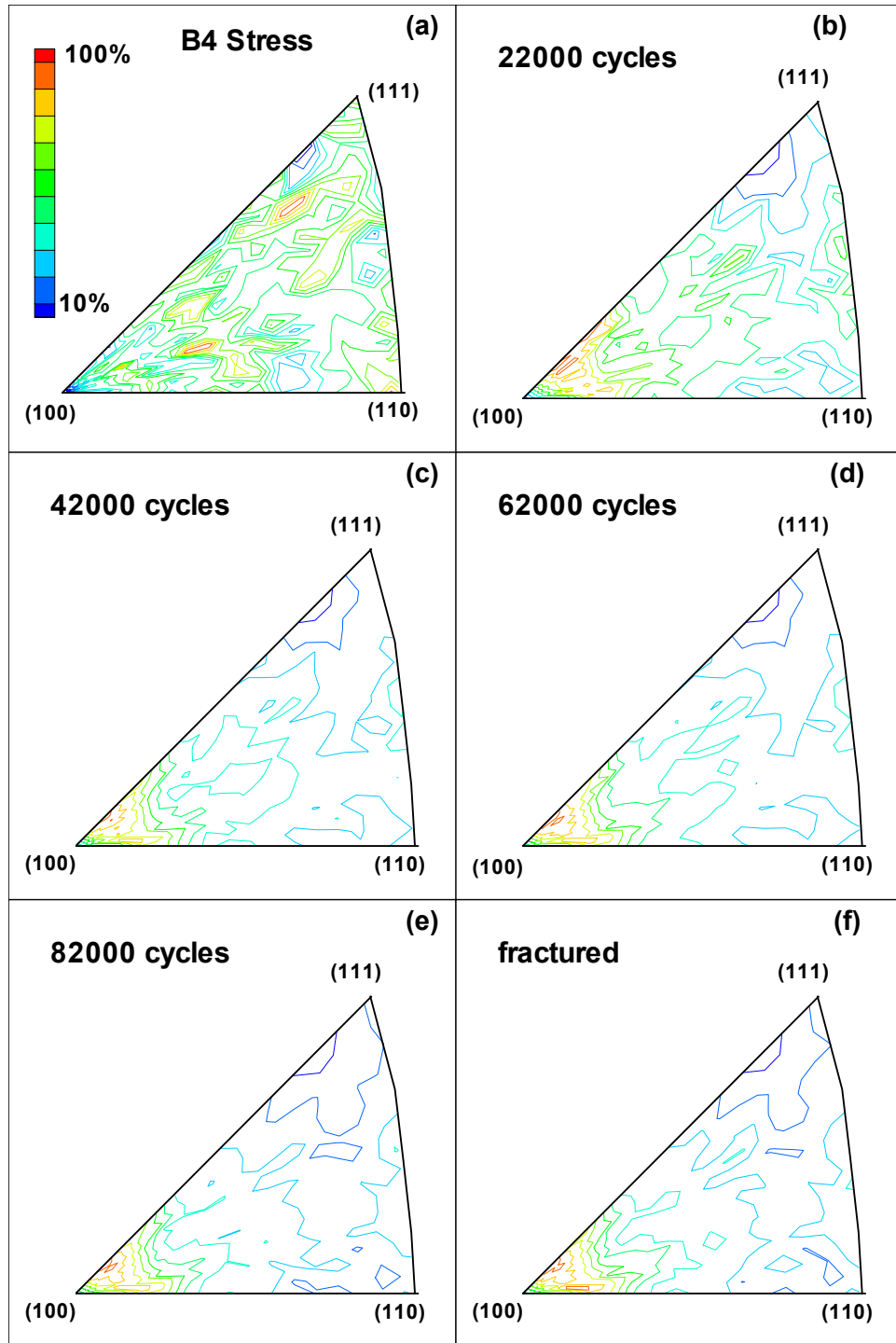


FIGURE B-34. INVERSE POLE FIGURES IN THE STRESS DIRECTION FOR SPECIMEN B4 AFTER (a) 0, (b) 22,000, (c) 42,000, (d) 62,000, (e) 82,000 FATIGUE CYCLES, AND (f) AFTER FAILURE



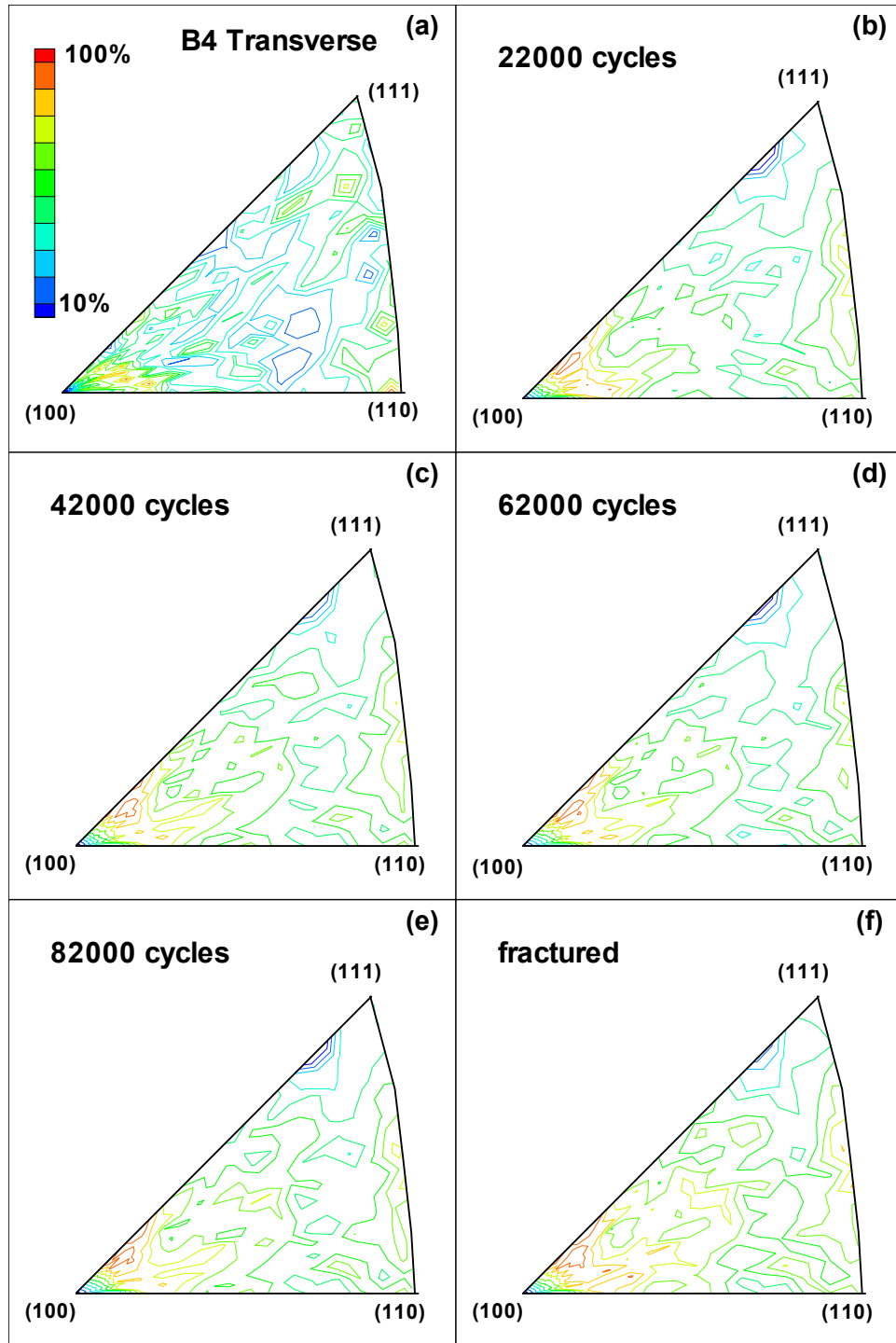


FIGURE B-35. INVERSE POLE FIGURES IN THE TRANSVERSE DIRECTION FOR SPECIMEN B4 AFTER (a) 0, (b) 22,000, (c) 42,000, (d) 62,000, (e) 82,000 FATIGUE CYCLES, AND (f) AFTER FAILURE

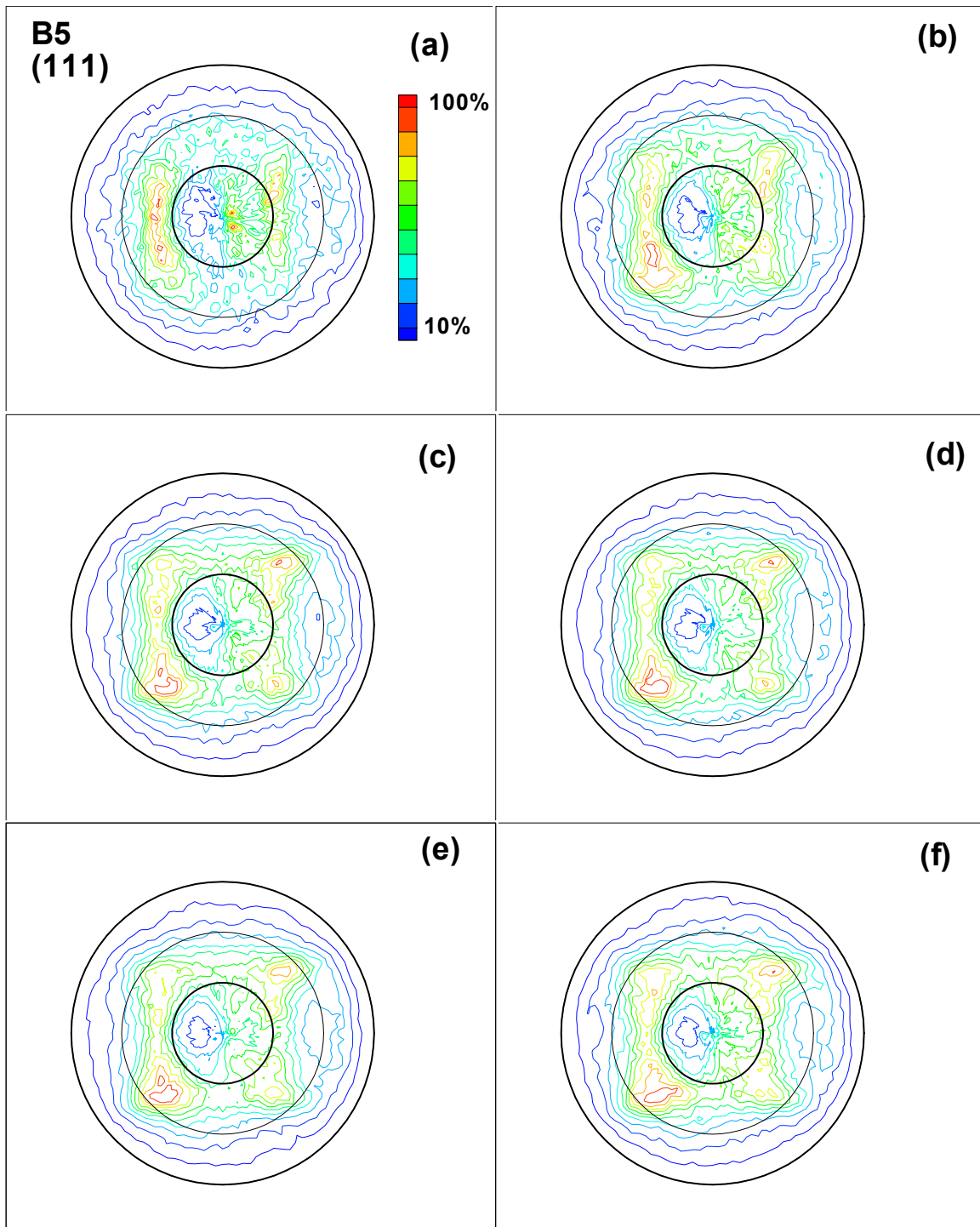


FIGURE B-36. DIRECT (111) POLE FIGURES FOR SPECIMEN B5 AFTER (a) 0, (b) 22,000, (c) 42,000, (d) 62,000, (e) 82,000 FATIGUE CYCLES, AND (f) AFTER FAILURE

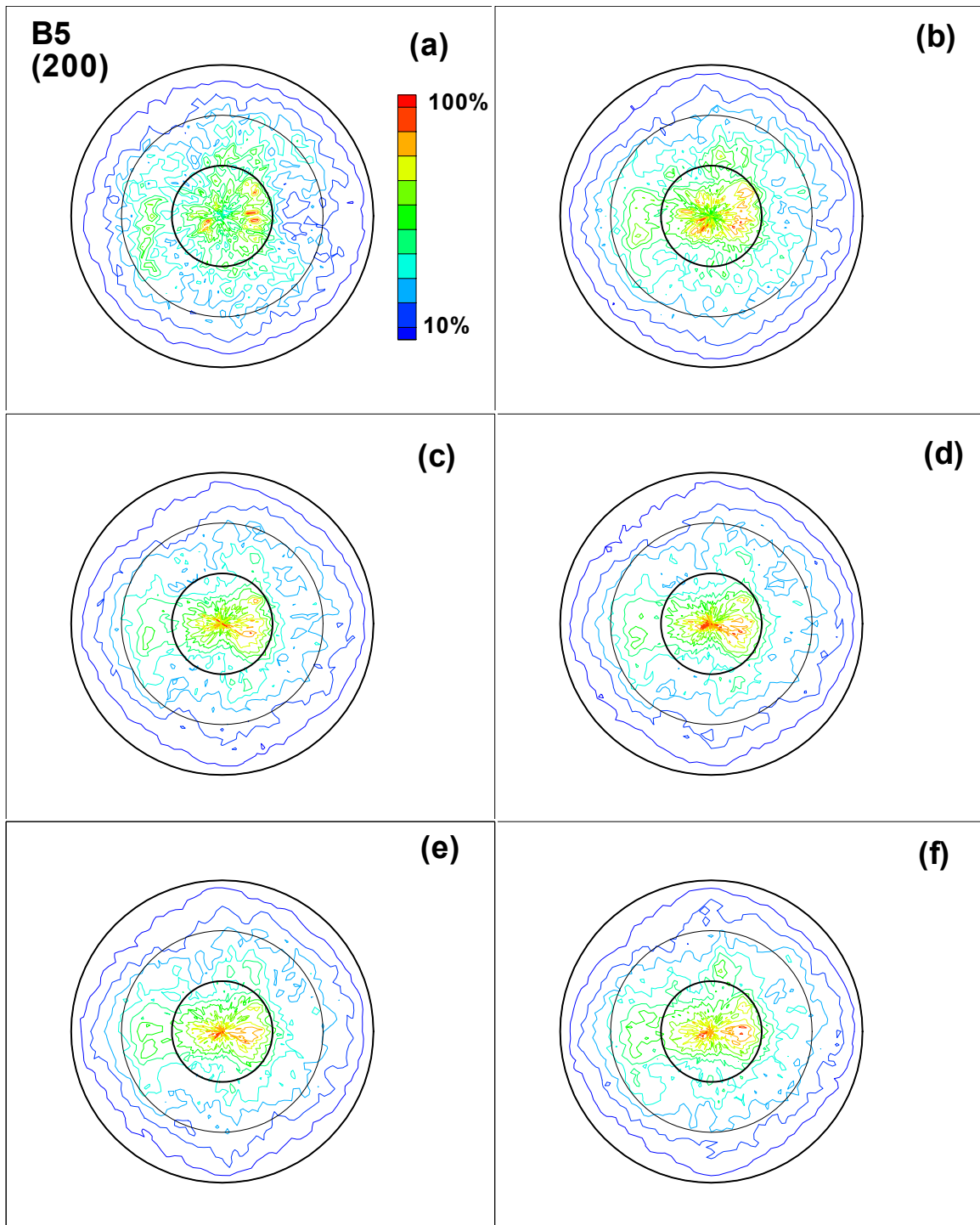


FIGURE B-37. DIRECT (200) POLE FIGURES FOR SPECIMEN B5 AFTER (a) 0, (b) 22,000, (c) 42,000, (d) 62,000, (e) 82,000 FATIGUE CYCLES, AND (f) AFTER FAILURE

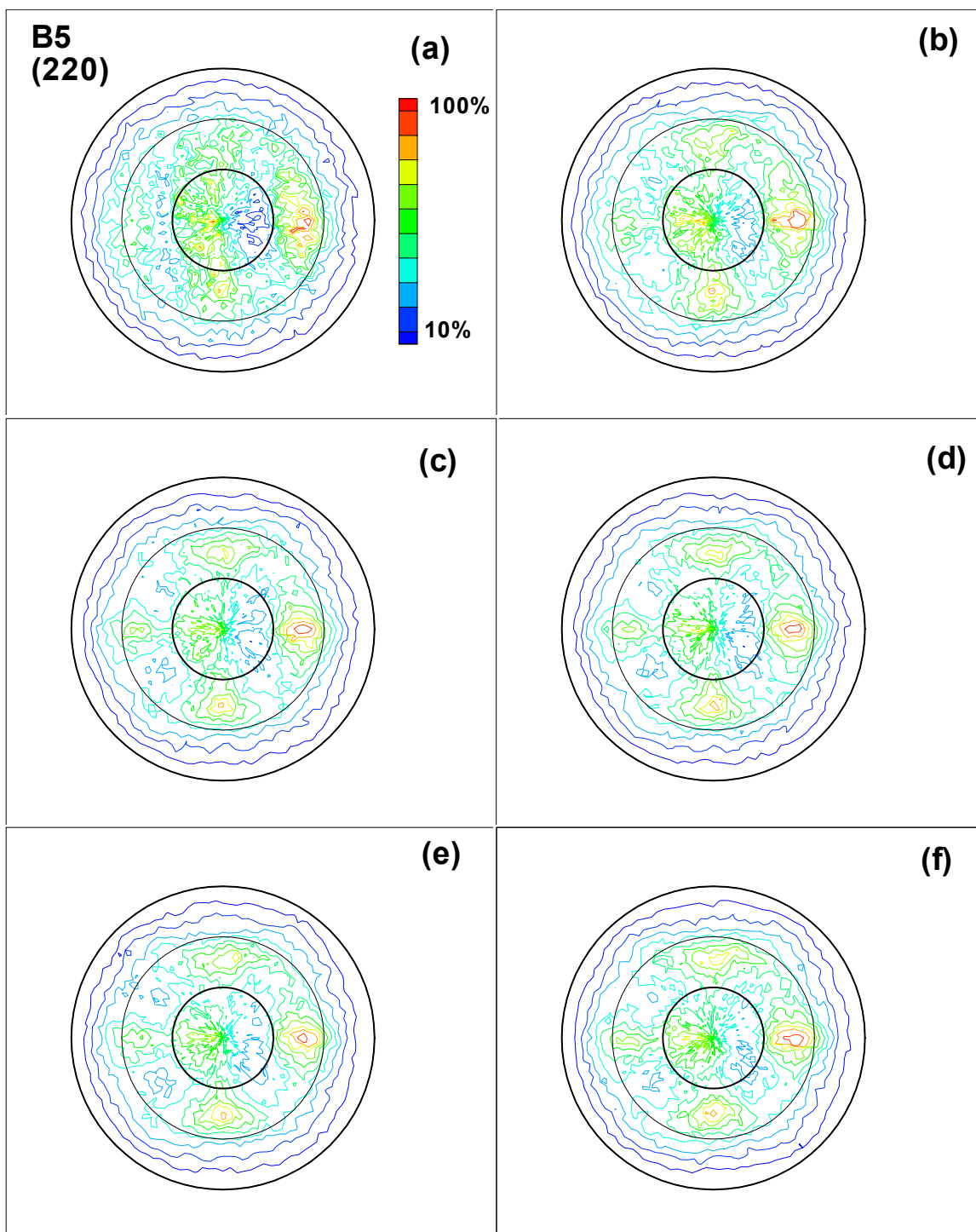


FIGURE B-38. DIRECT (220) POLE FIGURES FOR SPECIMEN B5 AFTER (a) 0, (b) 22,000, (c) 42,000, (d) 62,000, (e) 82,000 FATIGUE CYCLES, AND (f) AFTER FAILURE

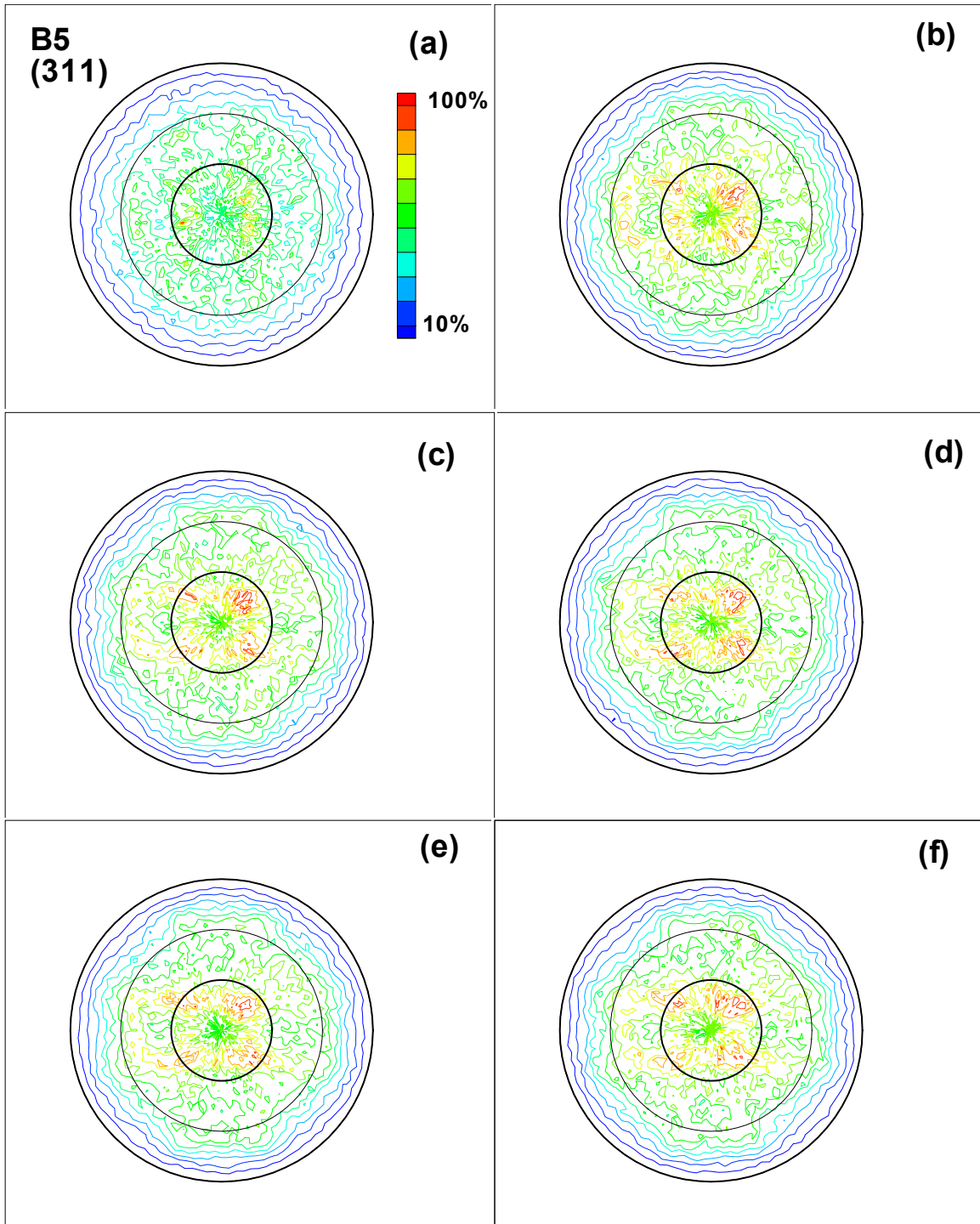


FIGURE B-39. DIRECT (311) POLE FIGURES FOR SPECIMEN B5 AFTER (a) 0, (b) 22,000, (c) 42,000, (d) 62,000, (e) 82,000 FATIGUE CYCLES, AND (f) AFTER FAILURE

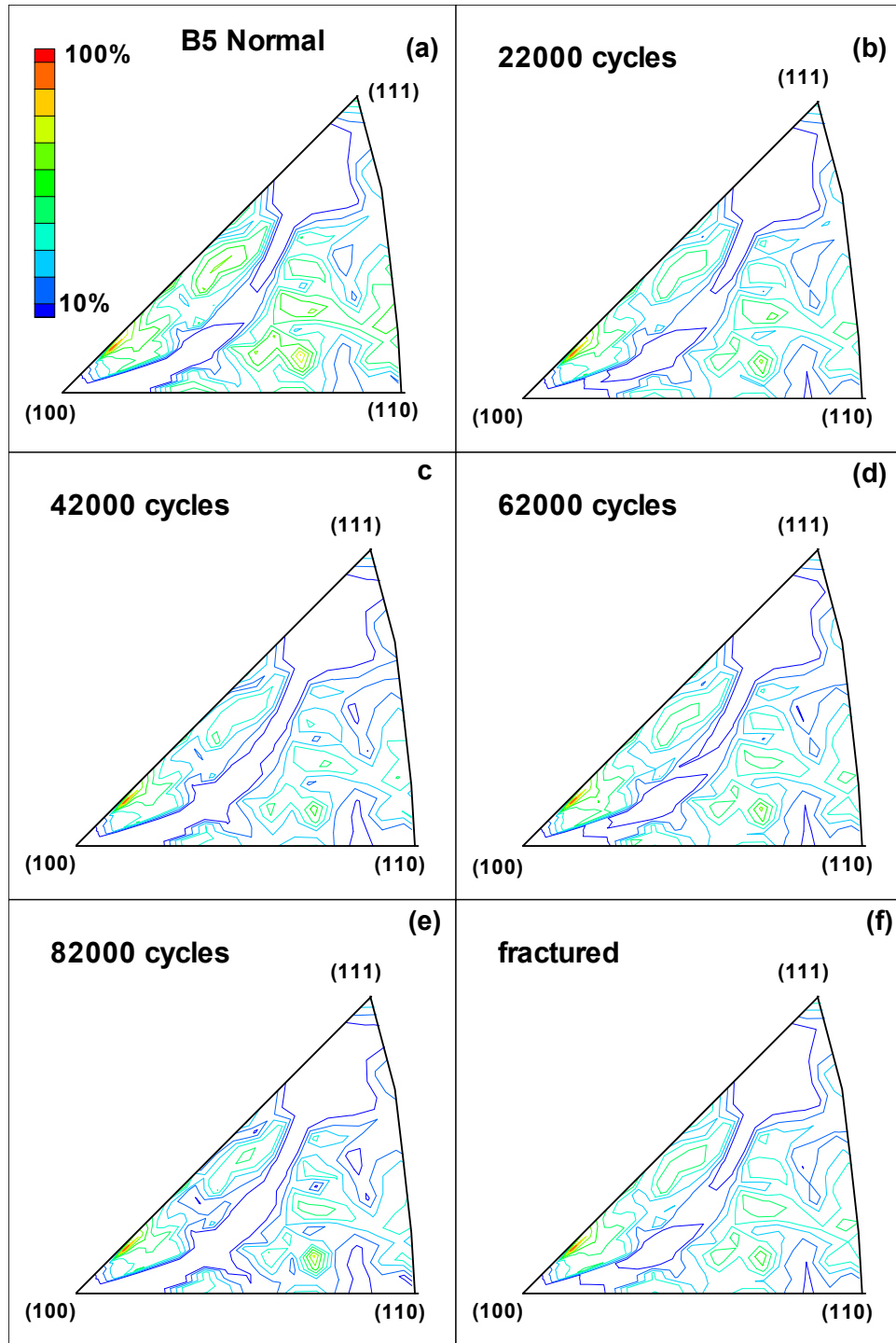


FIGURE B-40. INVERSE POLE FIGURES IN THE NORMAL DIRECTION FOR SPECIMEN B5 AFTER (a) 0, (b) 22,000, (c) 42,000, (d) 62,000, (e) 82,000 FATIGUE CYCLES, AND (f) AFTER FAILURE

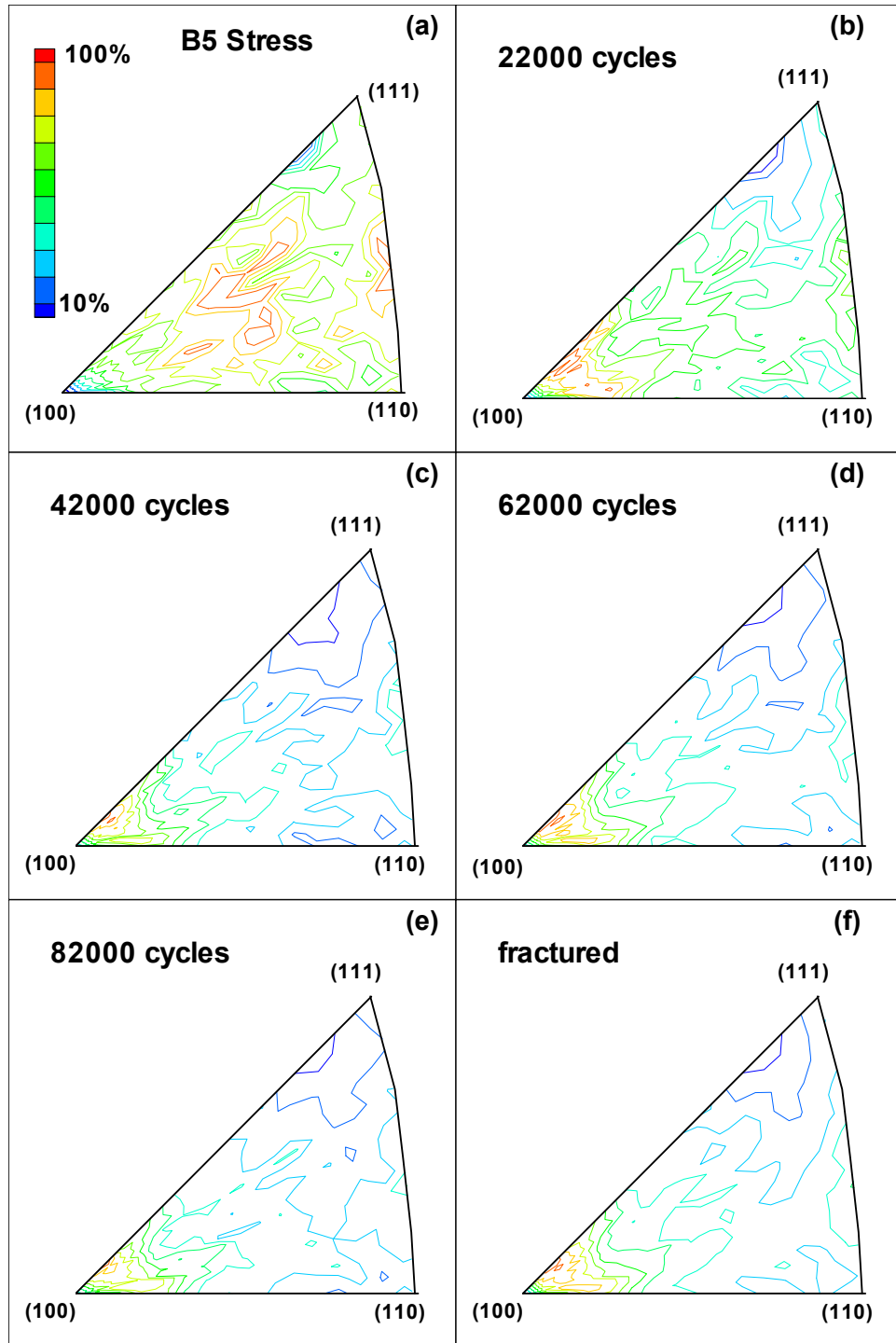


FIGURE B-41. INVERSE POLE FIGURES IN THE STRESS DIRECTION FOR SPECIMEN B5 AFTER (a) 0, (b) 22,000, (c) 42,000, (d) 62,000, (e) 82,000 FATIGUE CYCLES, AND (f) AFTER FAILURE



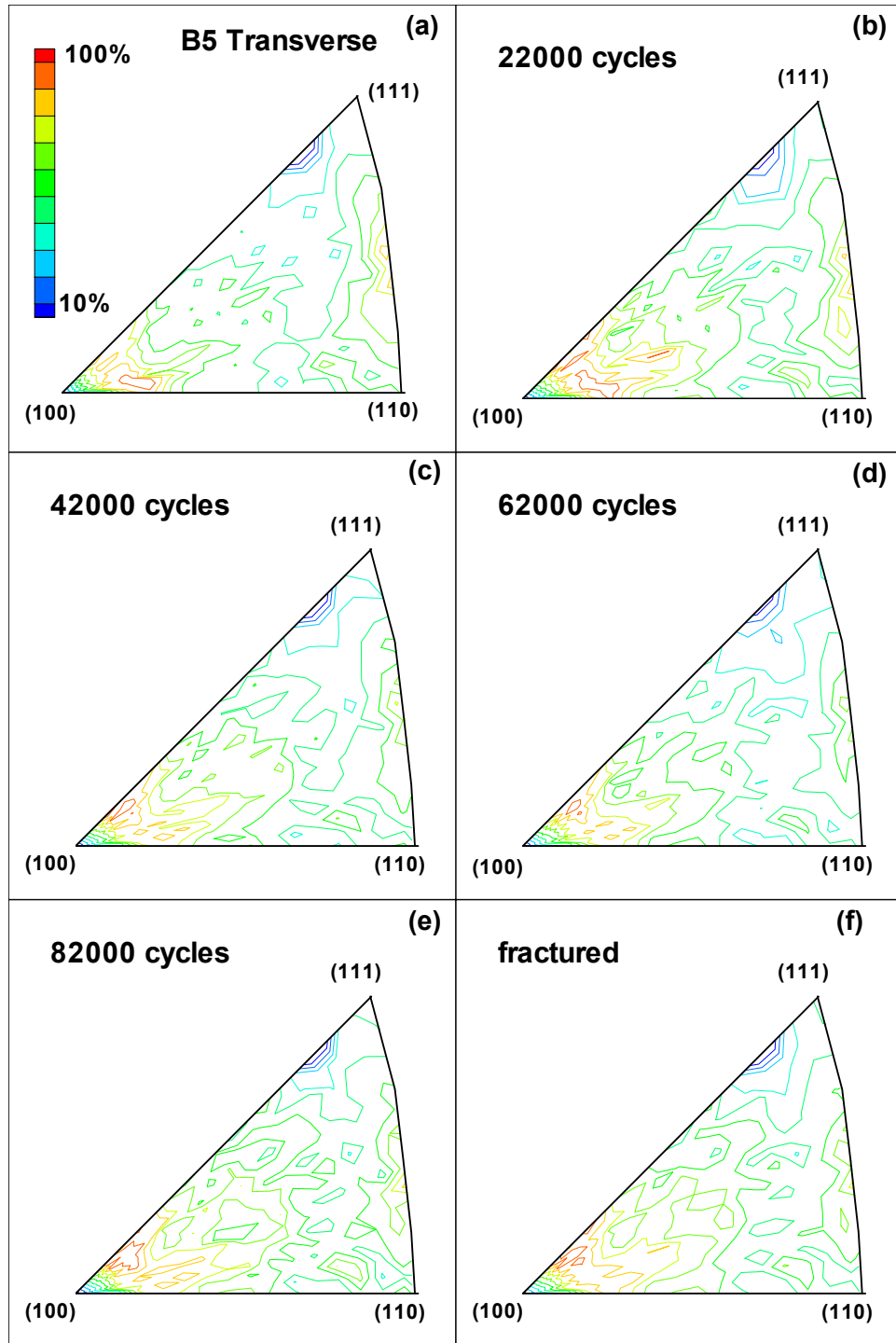


FIGURE B-42. INVERSE POLE FIGURES IN THE TRANSVERSE DIRECTION FOR SPECIMEN B5 AFTER (a) 0, (b) 22,000, (c) 42,000, (d) 62,000, (e) 82,000 FATIGUE CYCLES, AND (f) AFTER FAILURE



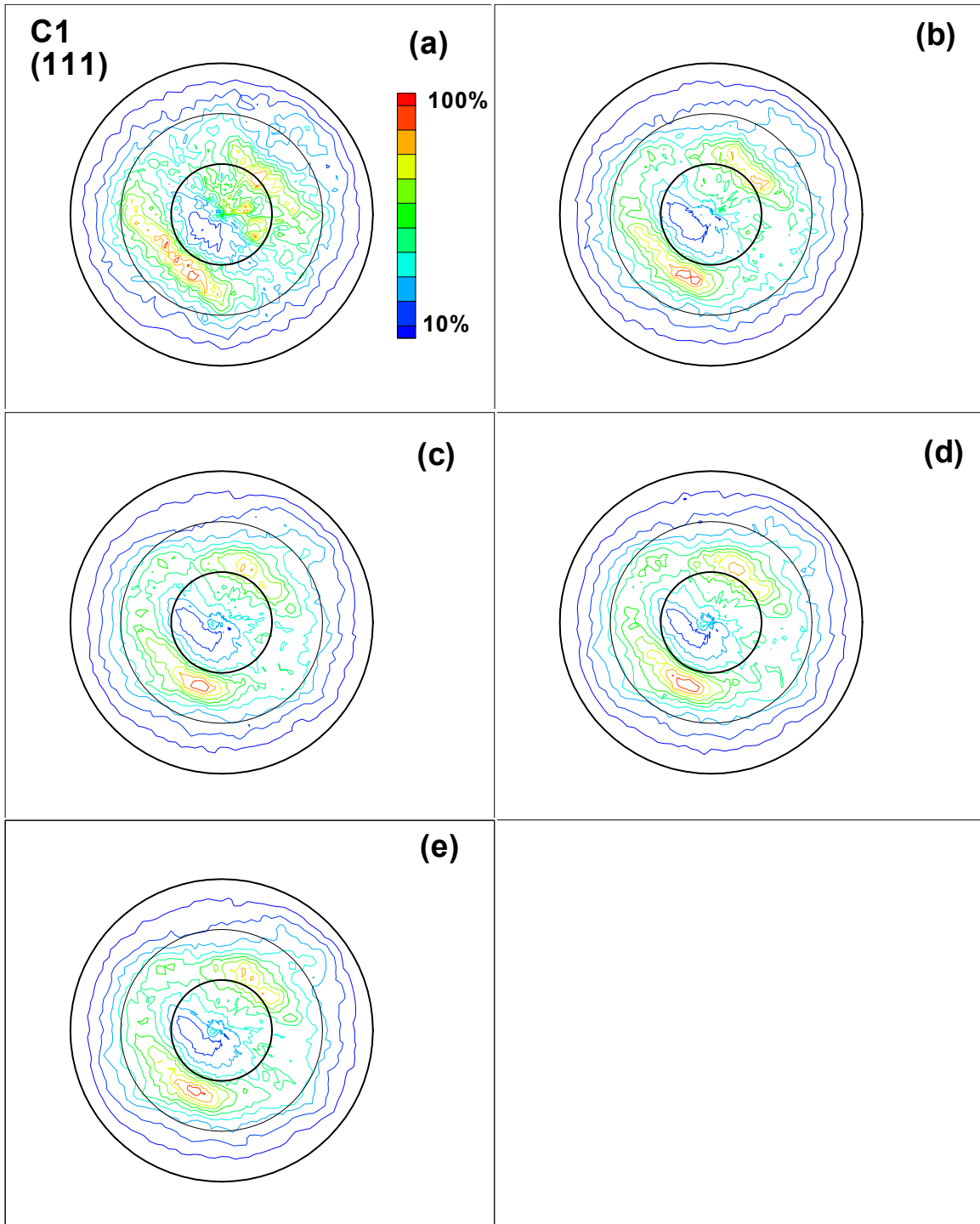


FIGURE B-43. DIRECT (111) POLE FIGURES FOR SPECIMEN C1 AFTER (a) 0, (b) 22,000, (c) 42,000, (d) 62,000 FATIGUE CYCLES, AND (e) AFTER FAILURE

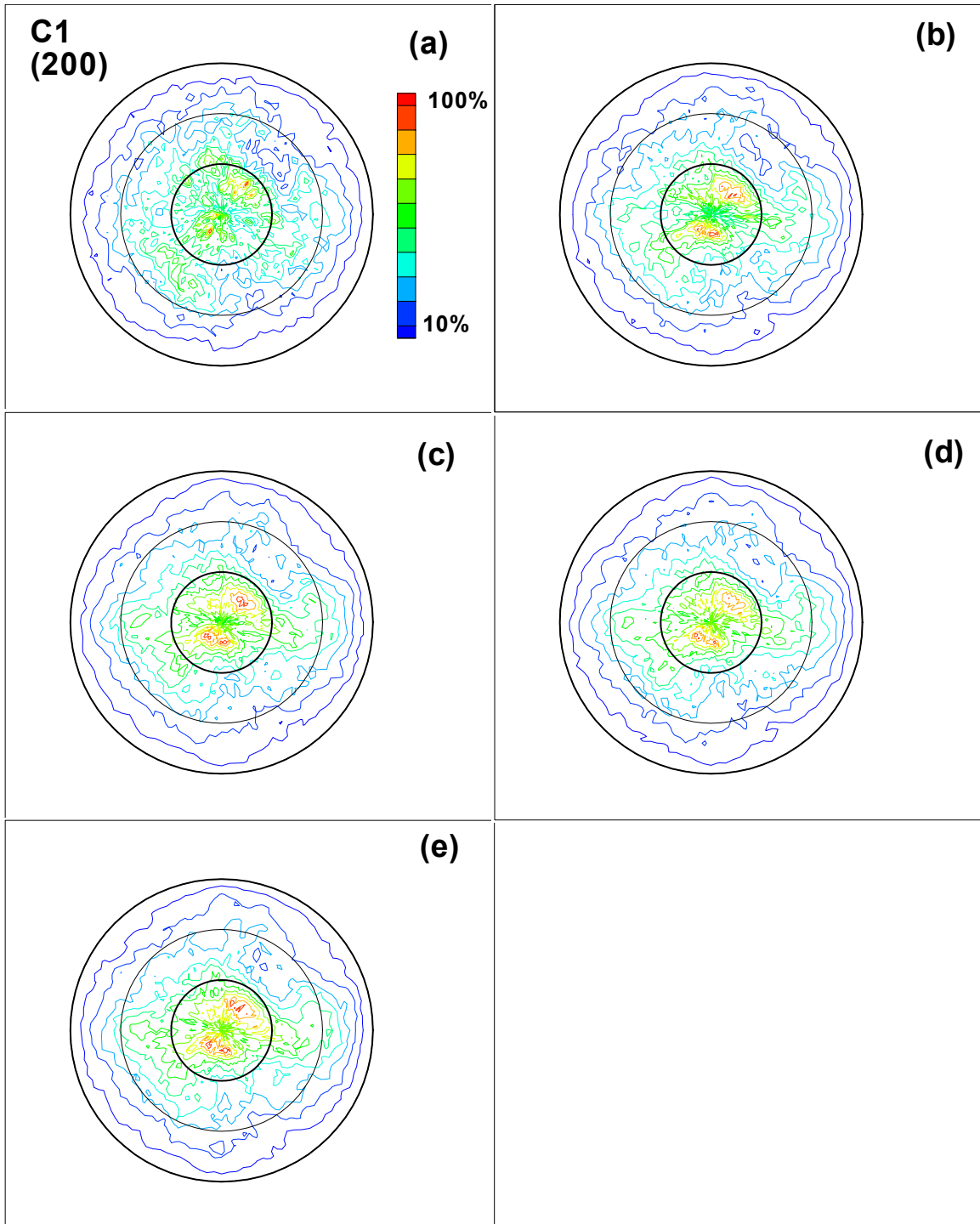


FIGURE B-44. DIRECT (200) POLE FIGURES FOR SPECIMEN C1 AFTER (a) 0, (b) 22,000, (c) 42,000, (d) 62,000 FATIGUE CYCLES, AND (e) AFTER FAILURE

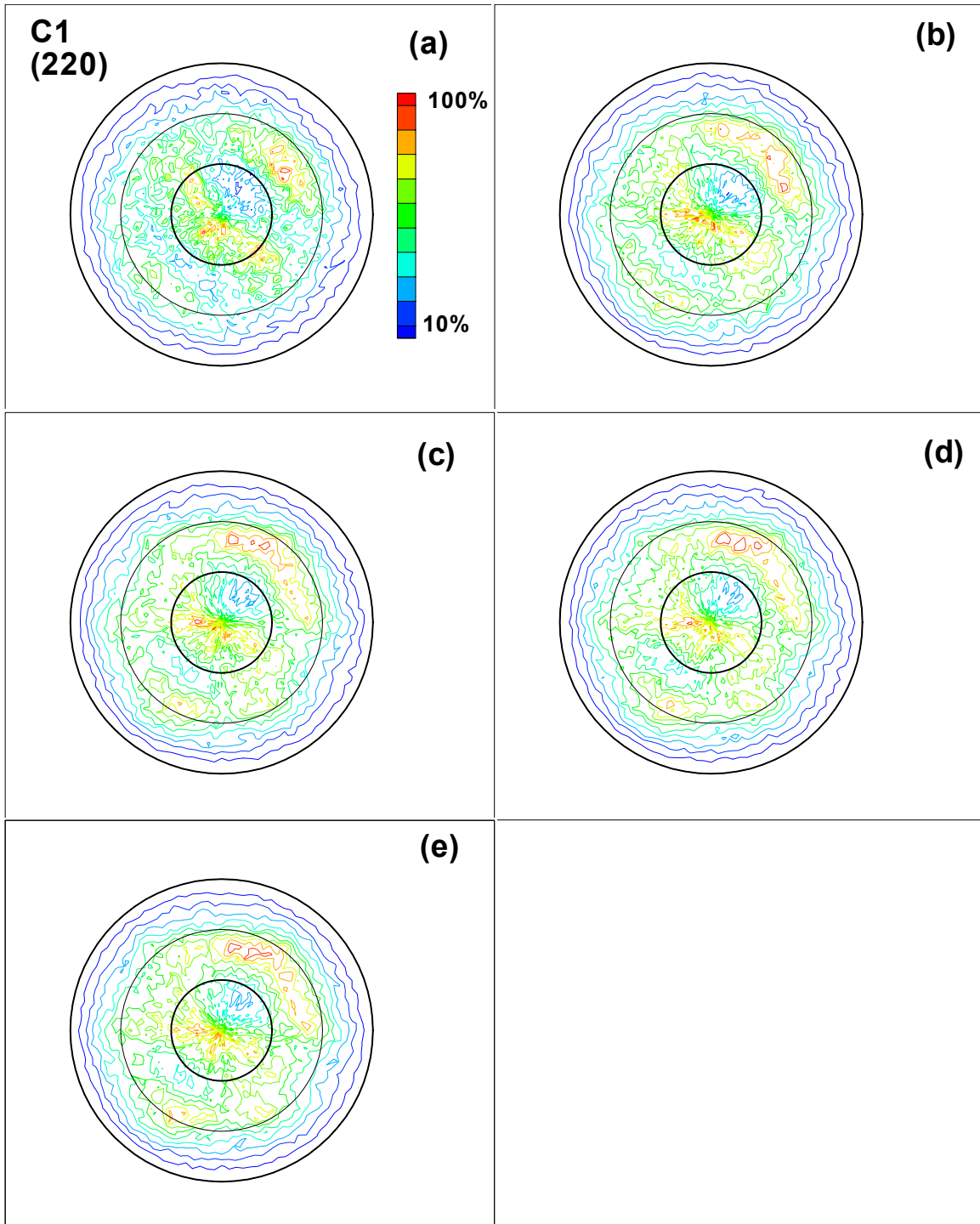


FIGURE B-45. DIRECT (220) POLE FIGURES FOR SPECIMEN C1 AFTER (a) 0, (b) 22,000, (c) 42,000, (d) 62,000 FATIGUE CYCLES, AND (e) AFTER FAILURE

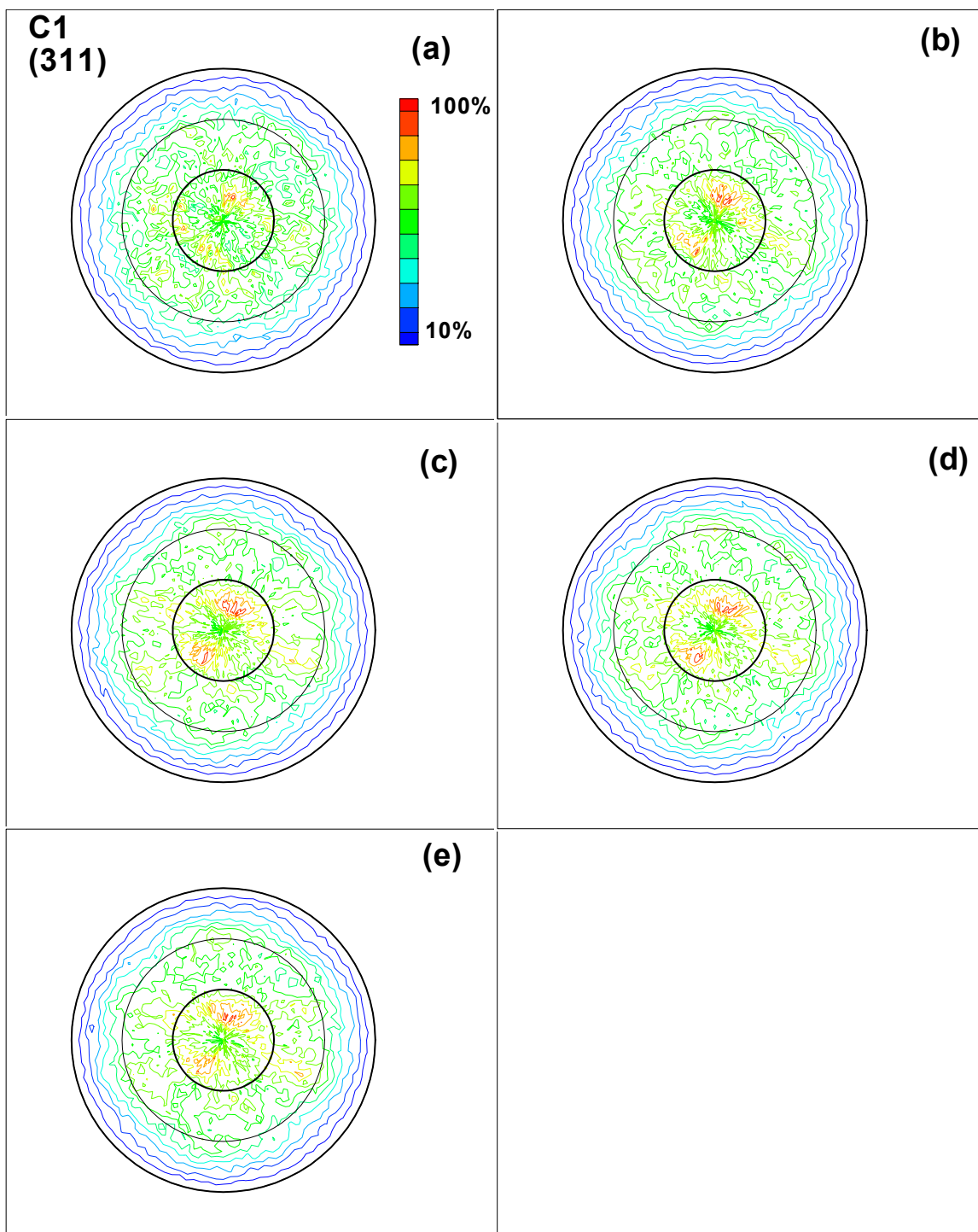


FIGURE B-46. DIRECT (311) POLE FIGURES FOR SPECIMEN C1 AFTER (a) 0, (b) 22,000, (c) 42,000, (d) 62,000 FATIGUE CYCLES, AND (e) AFTER FAILURE

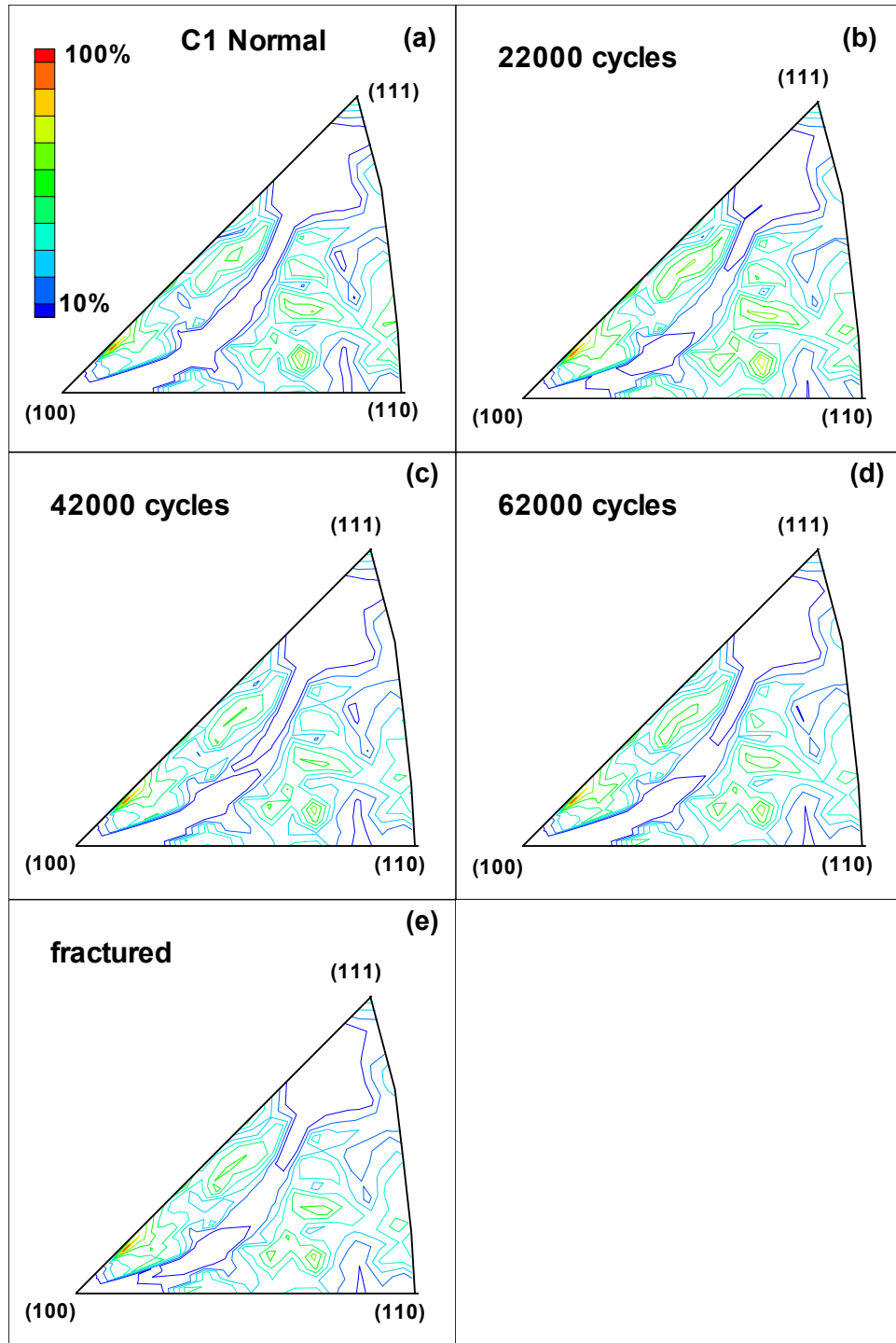


FIGURE B-47. INVERSE POLE FIGURES IN THE NORMAL DIRECTION FOR SPECIMEN C1 AFTER (a) 0, (b) 22,000, (c) 42,000, (d) 62,000 FATIGUE CYCLES, AND (e) AFTER FAILURE

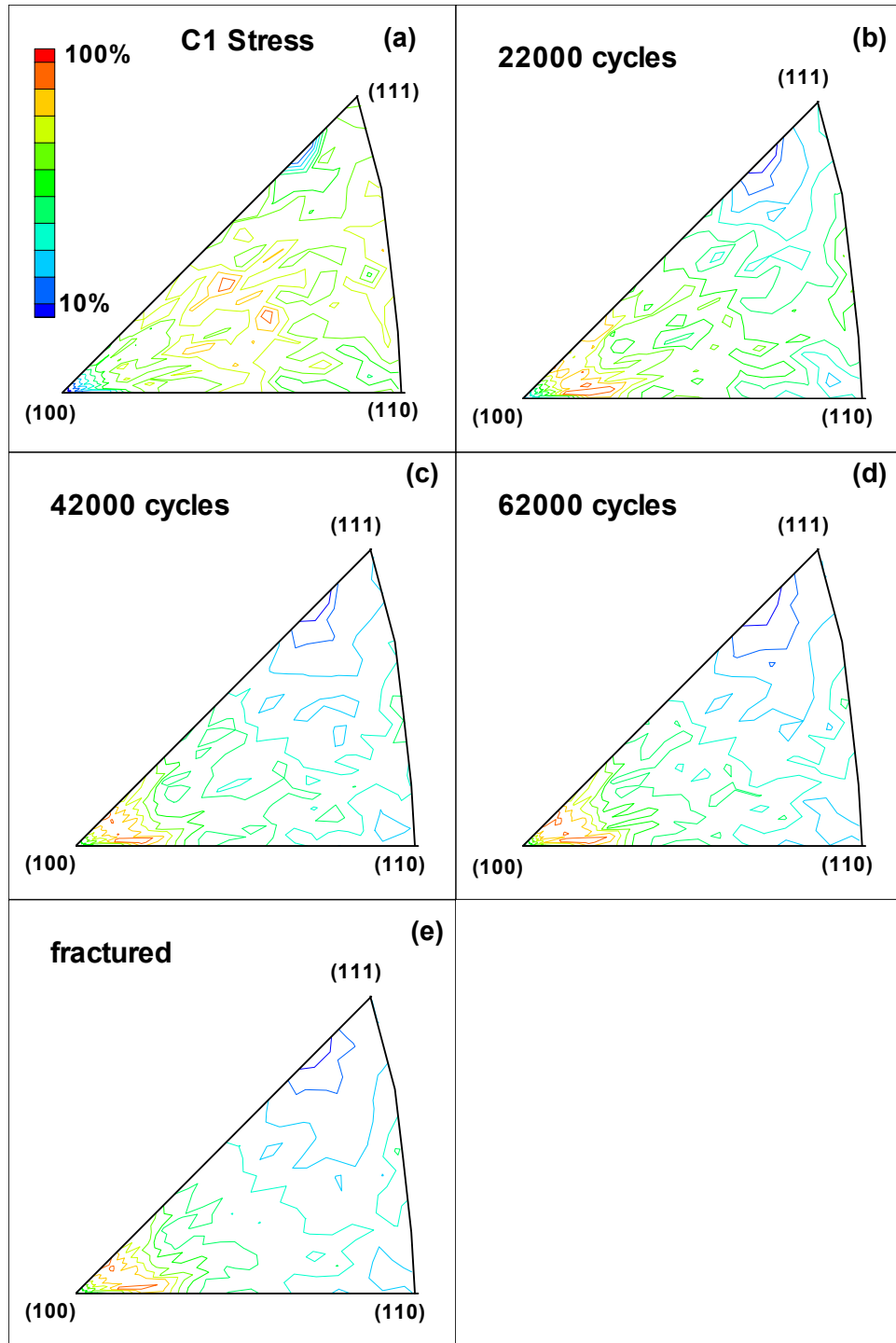


FIGURE B-48. INVERSE POLE FIGURES IN THE STRESS DIRECTION FOR SPECIMEN C1 AFTER (a) 0, (b) 22,000, (c) 42,000, (d) 62,000 FATIGUE CYCLES, AND (e) AFTER FAILURE

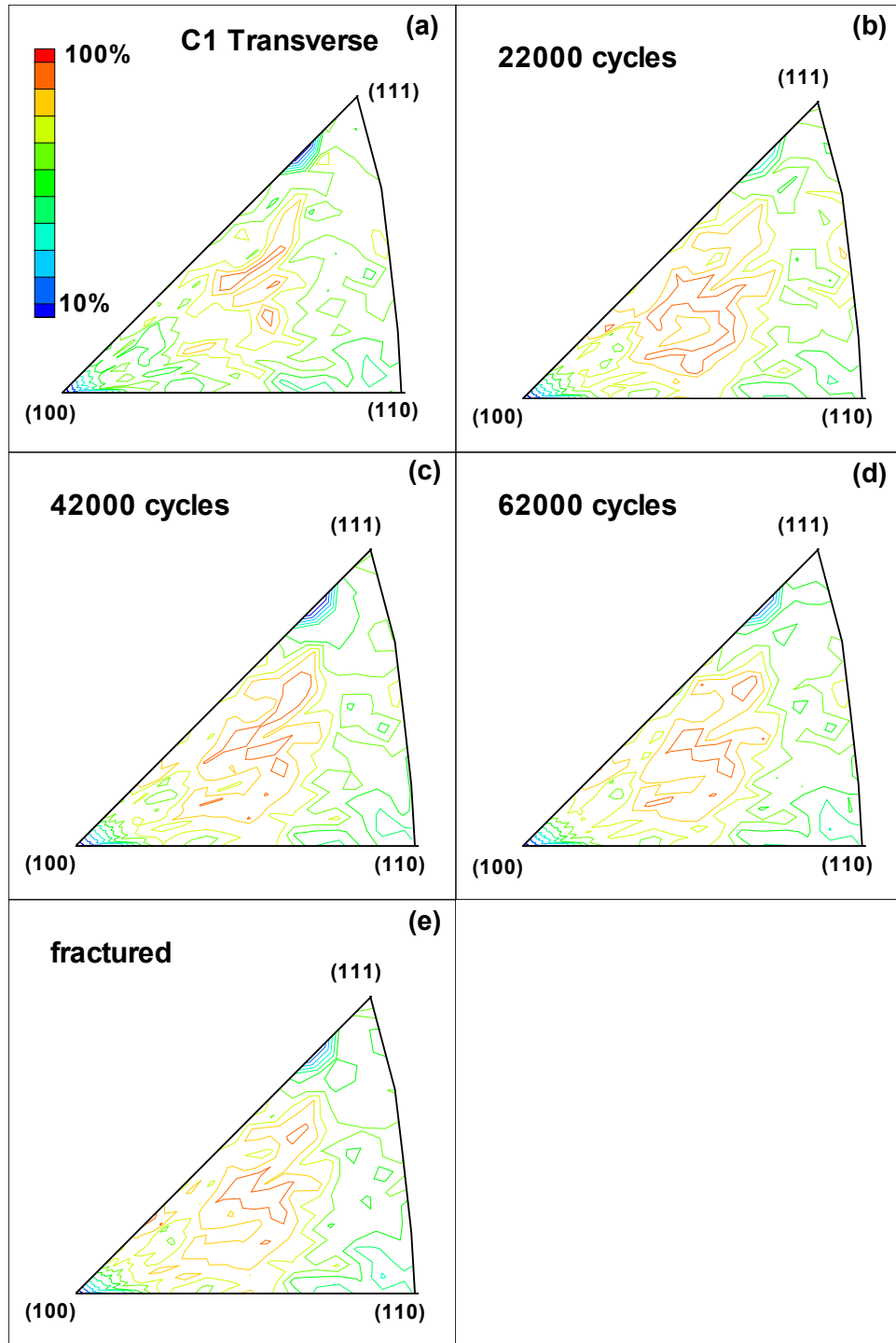


FIGURE B-49. INVERSE POLE FIGURES IN THE TRANSVERSE DIRECTION FOR SPECIMEN C1 AFTER (a) 0, (b) 22,000, (c) 42,000, (d) 62,000 FATIGUE CYCLES, AND (e) AFTER FAILURE

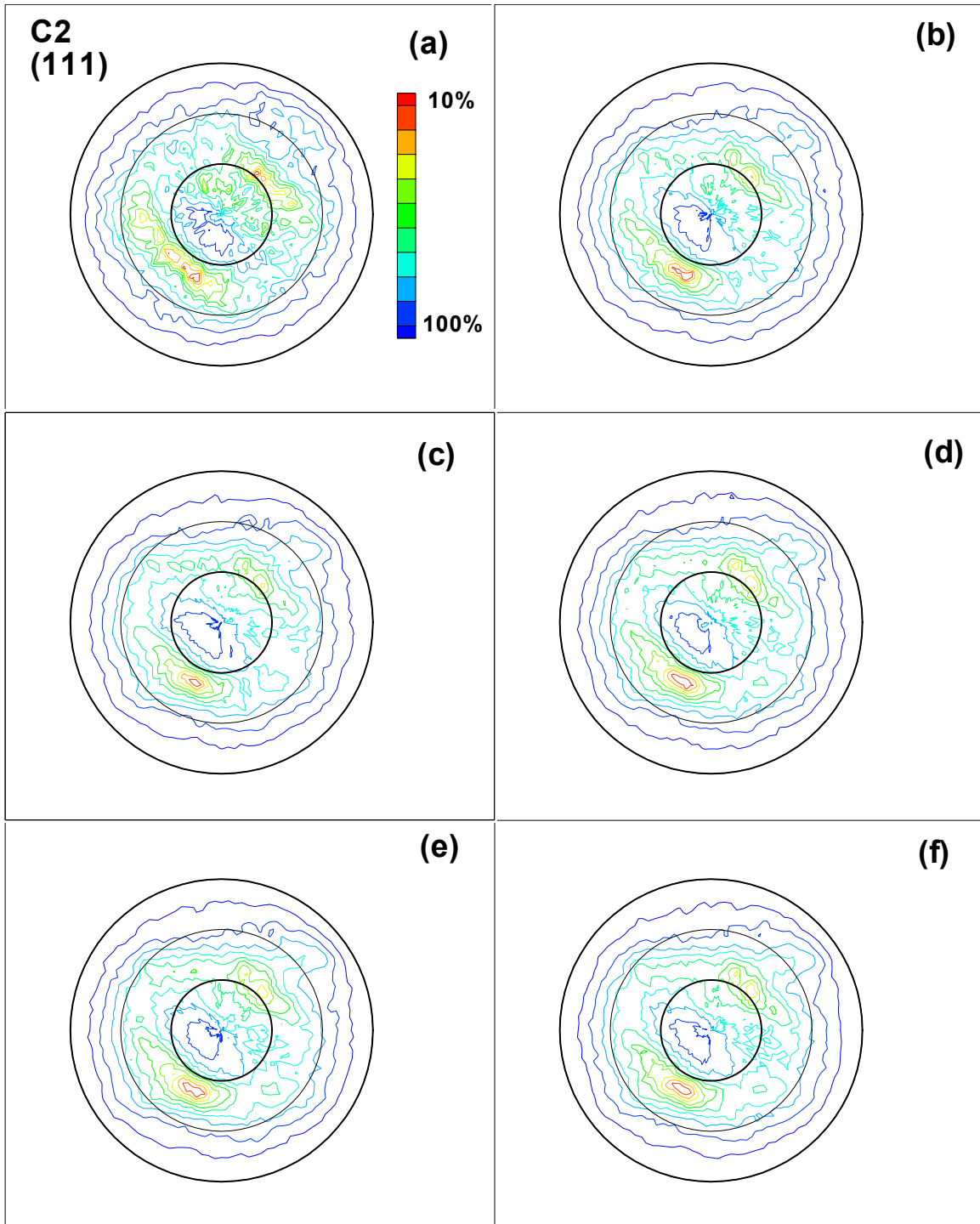


FIGURE B-50. DIRECT (111) POLE FIGURES FOR SPECIMEN C2 AFTER (a) 0, (b) 22,000, (c) 42,000, (d) 62,000, (e) 82,000 FATIGUE CYCLES, AND (f) AFTER FAILURE



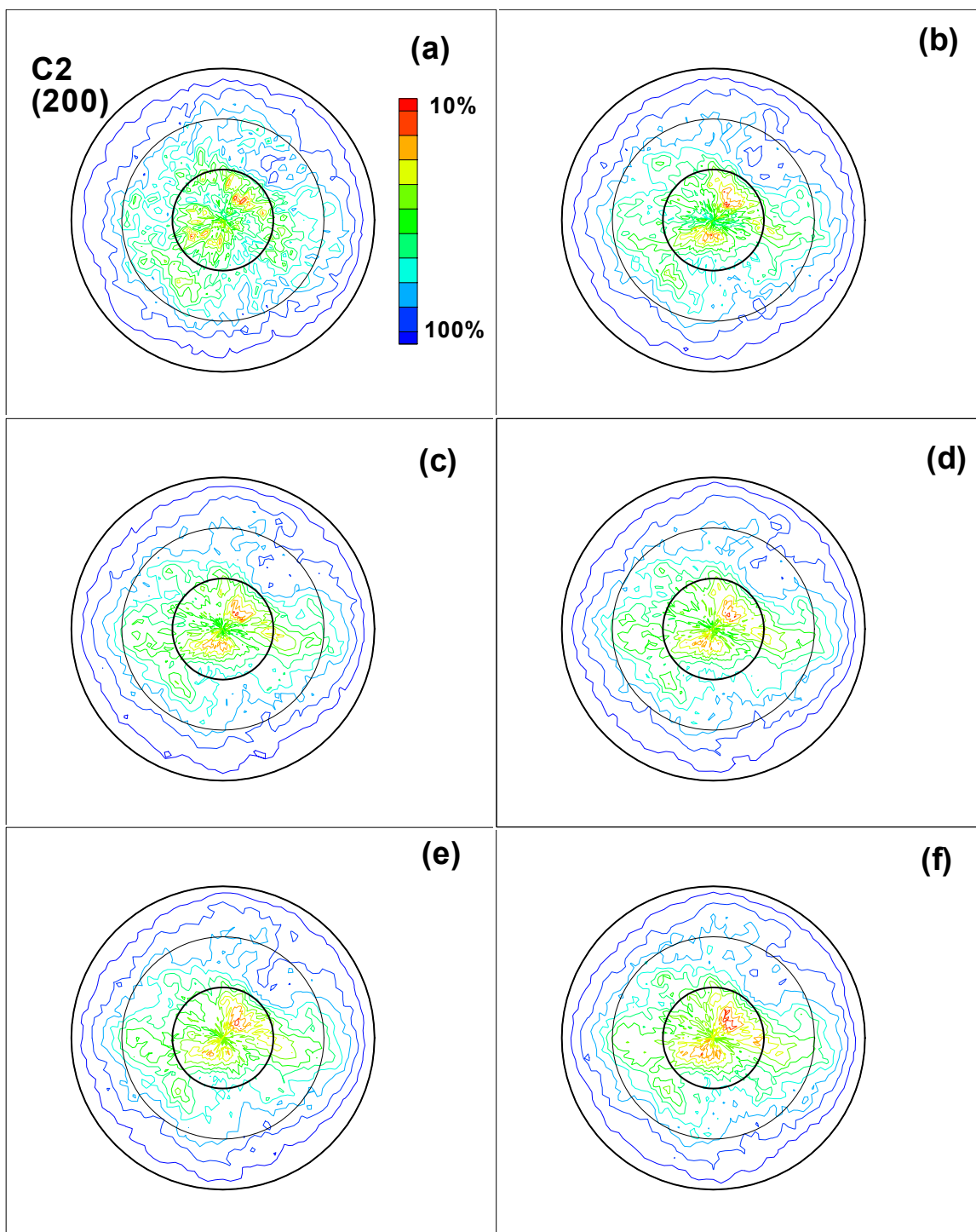


FIGURE B-51. DIRECT (200) POLE FIGURES FOR SPECIMEN C2 AFTER (a) 0, (b) 22,000, (c) 42,000, (d) 62,000, (e) 82,000 FATIGUE CYCLES, AND (f) AFTER FAILURE

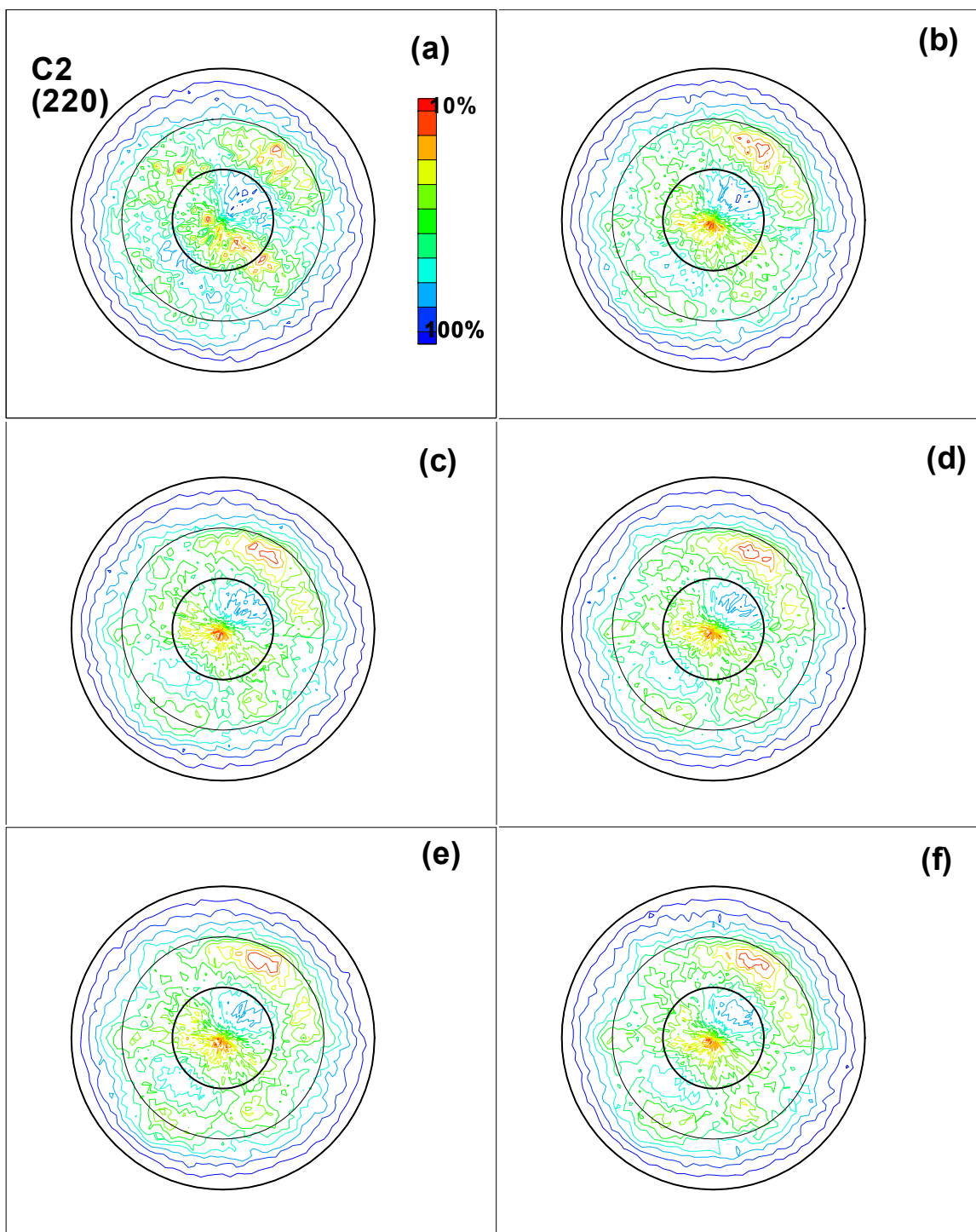


FIGURE B-52. DIRECT (220) POLE FIGURES FOR SPECIMEN C2 AFTER (a) 0, (b) 22,000, (c) 42,000, (d) 62,000, (e) 82,000 FATIGUE CYCLES, AND (f) AFTER FAILURE

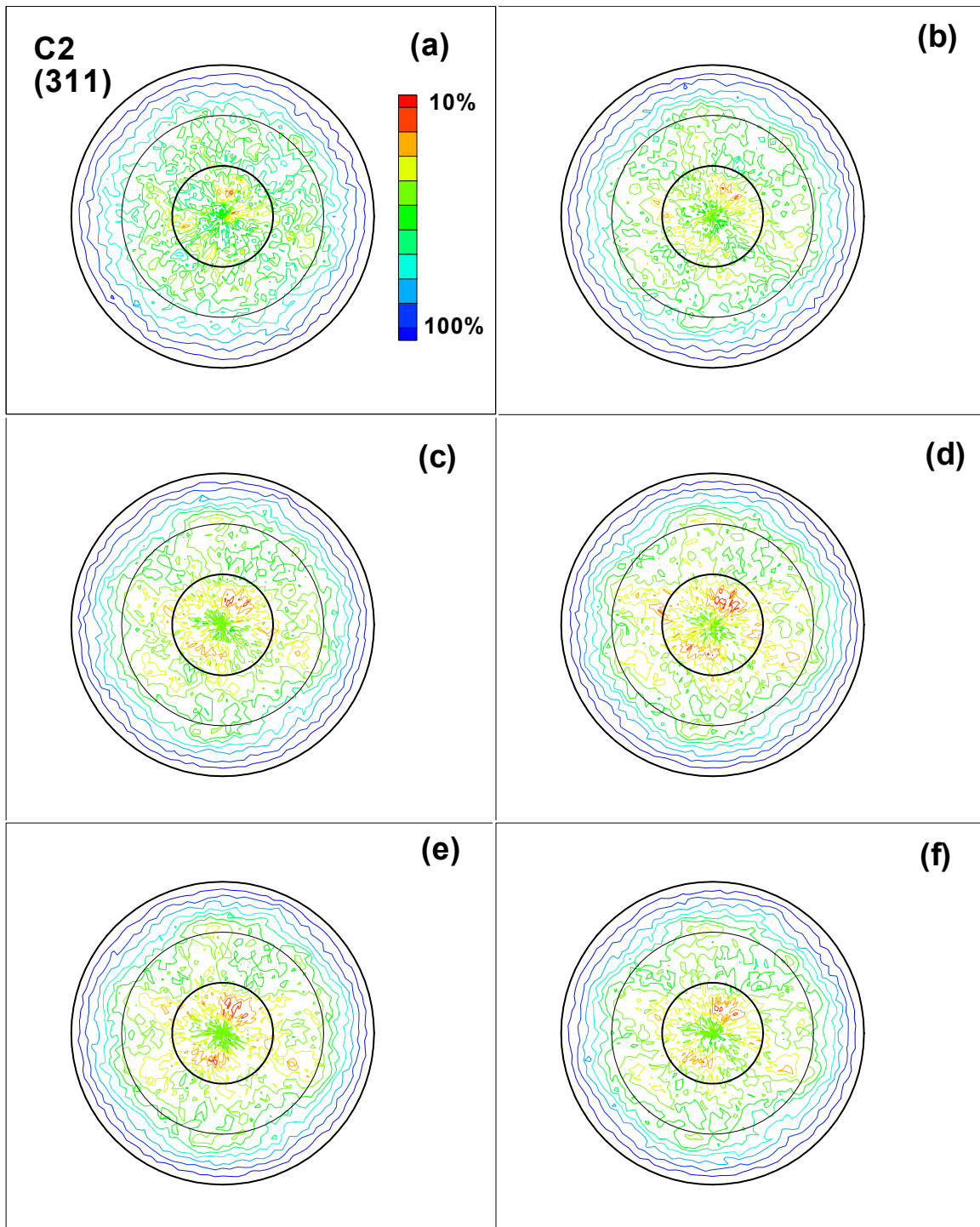


FIGURE B-53. DIRECT (311) POLE FIGURES FOR SPECIMEN C2 AFTER (a) 0, (b) 22,000, (c) 42,000, (d) 62,000, (e) 82,000 FATIGUE CYCLES, AND (f) AFTER FAILURE

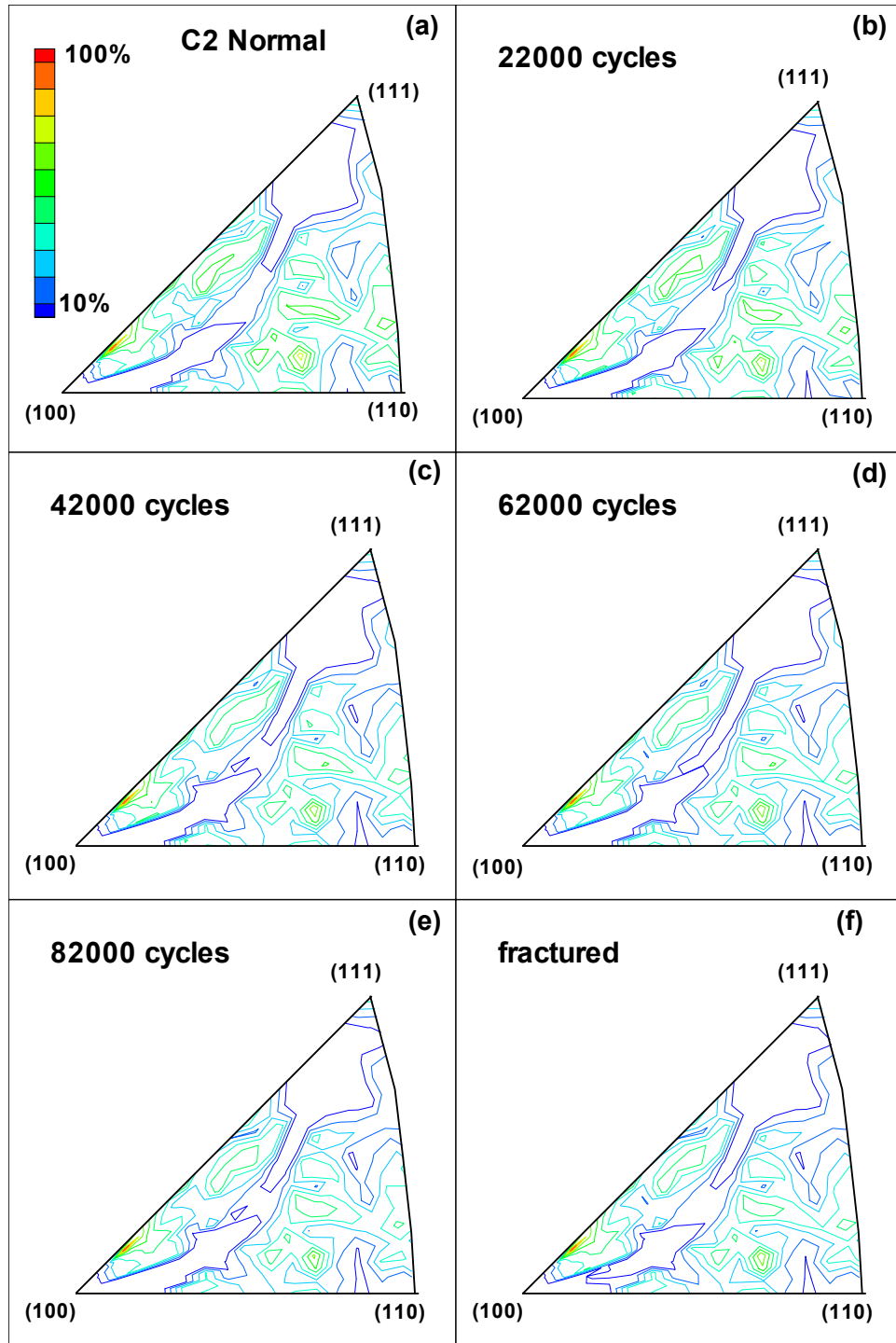


FIGURE B-54. INVERSE POLE FIGURES IN THE NORMAL DIRECTION FOR SPECIMEN C2 AFTER (a) 0, (b) 22,000, (c) 42,000, (d) 62,000, (e) 82,000 FATIGUE CYCLES, AND (f) AFTER FAILURE

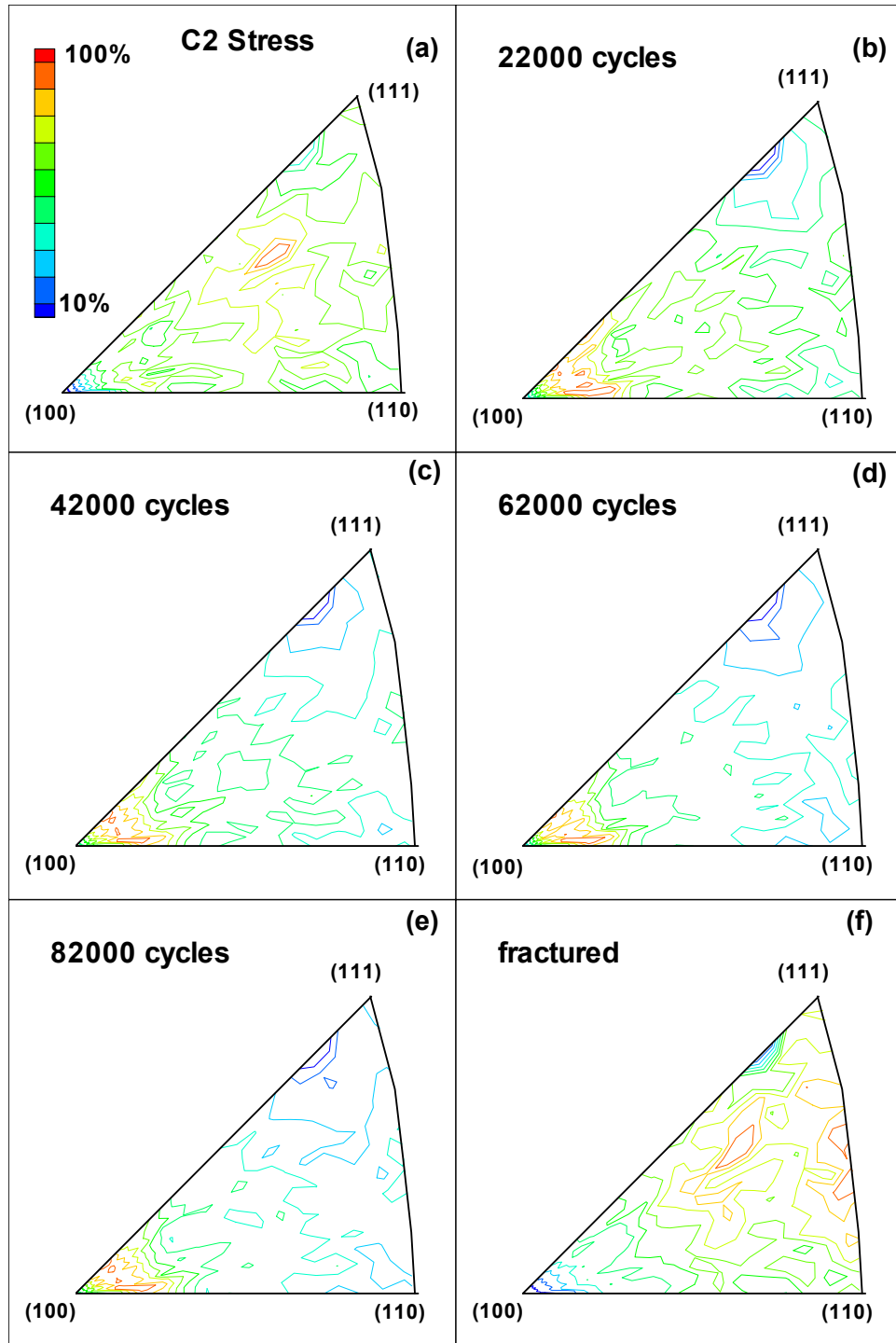


FIGURE B-55. INVERSE POLE FIGURES IN THE STRESS DIRECTION FOR SPECIMEN C2 AFTER (a) 0, (b) 22,000, (c) 42,000, (d) 62,000, (e) 82,000 FATIGUE CYCLES, AND (f) AFTER FAILURE

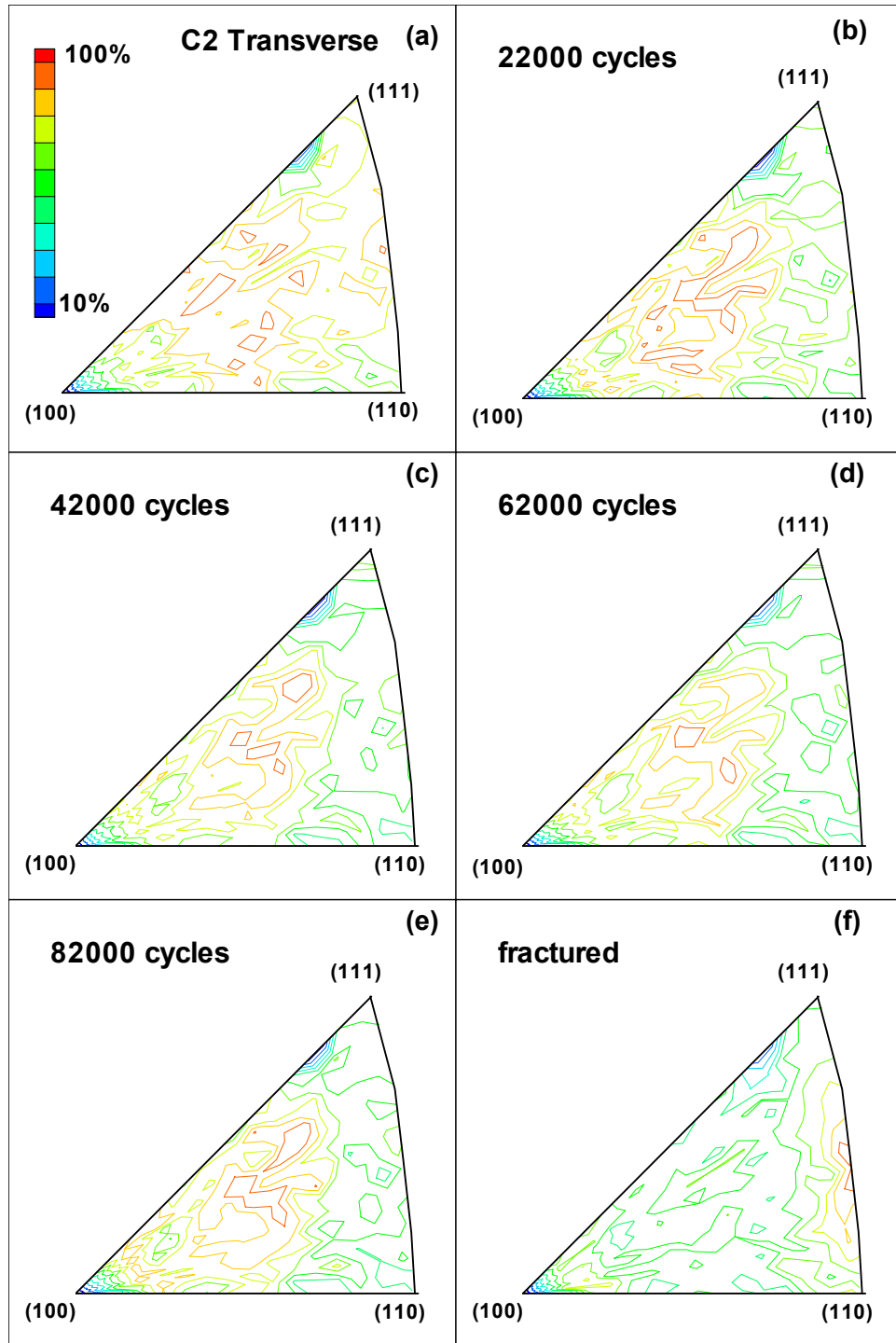


FIGURE B-56. INVERSE POLE FIGURES IN THE TRANSVERSE DIRECTION FOR SPECIMEN C2 AFTER (a) 0, (b) 22,000, (c) 42,000, (d) 62,000, (e) 82,000 FATIGUE CYCLES, AND (f) AFTER FAILURE

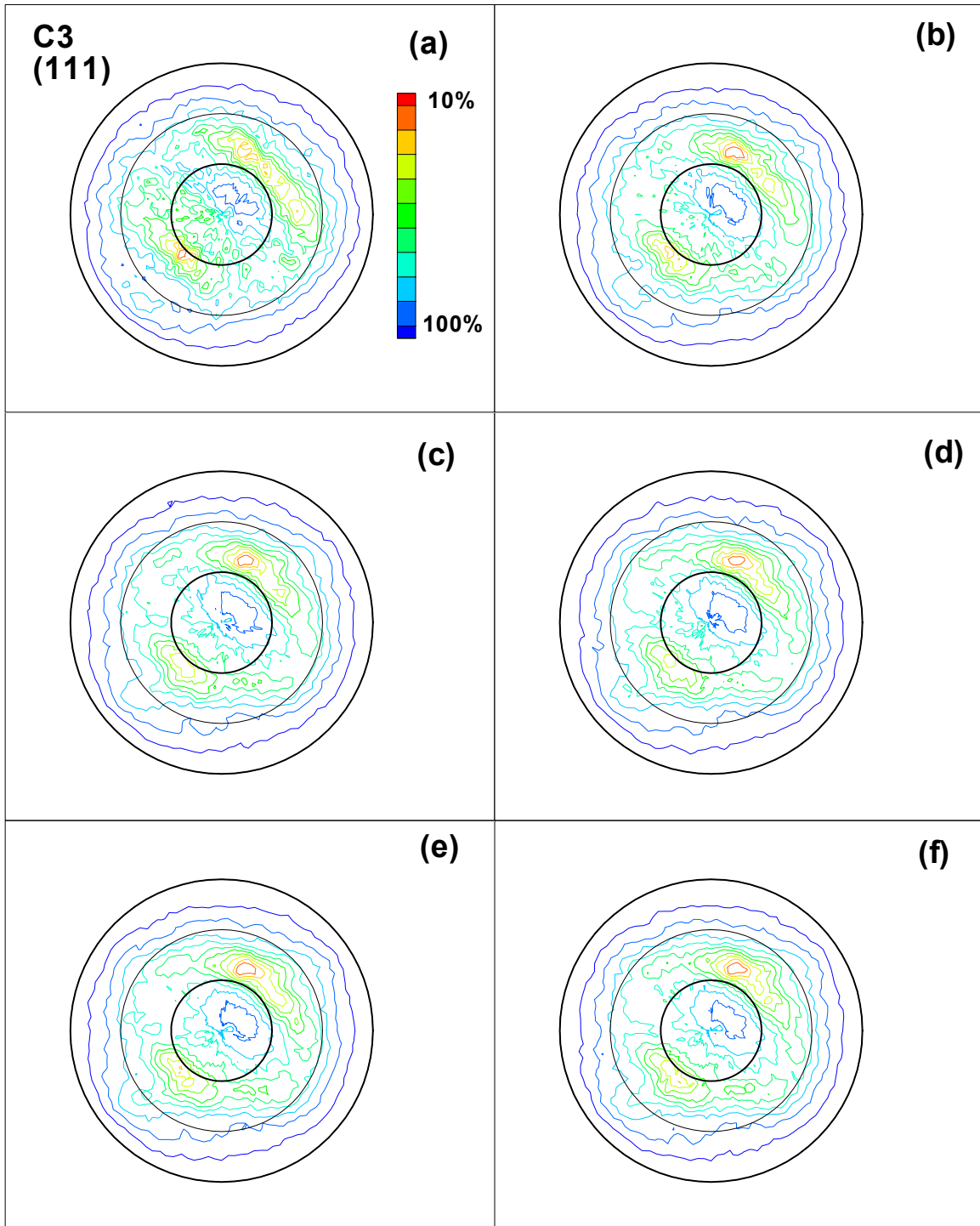


FIGURE B-57. DIRECT (111) POLE FIGURES FOR SPECIMEN C3 AFTER (a) 0, (b) 22,000, (c) 42,000, (d) 62,000, (e) 82,000 FATIGUE CYCLES, AND (f) AFTER FAILURE



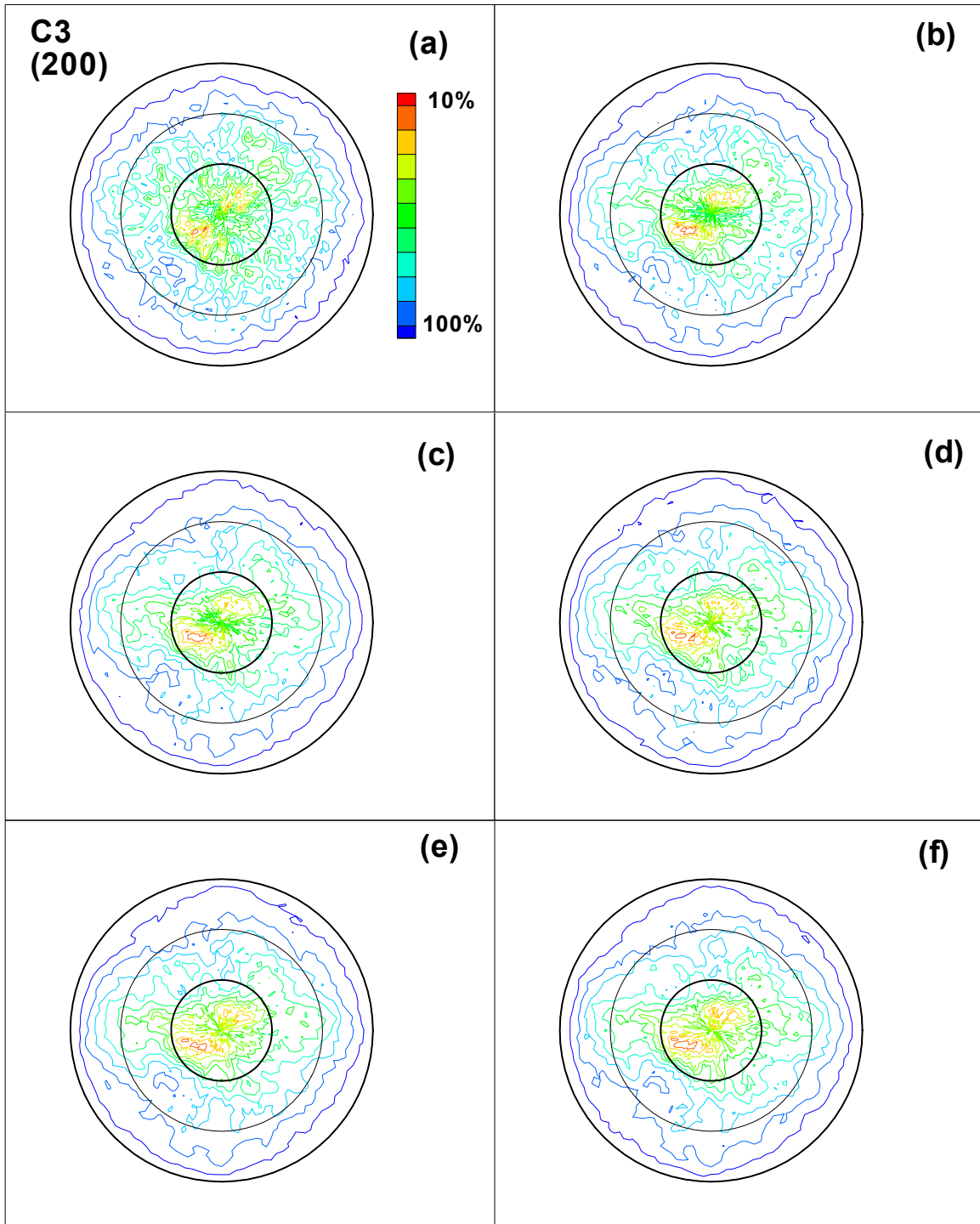


FIGURE B-58. DIRECT (200) POLE FIGURES FOR SPECIMEN C3 AFTER (a) 0, (b) 22,000, (c) 42,000, (d) 62,000, (e) 82,000 FATIGUE CYCLES, AND (f) AFTER FAILURE



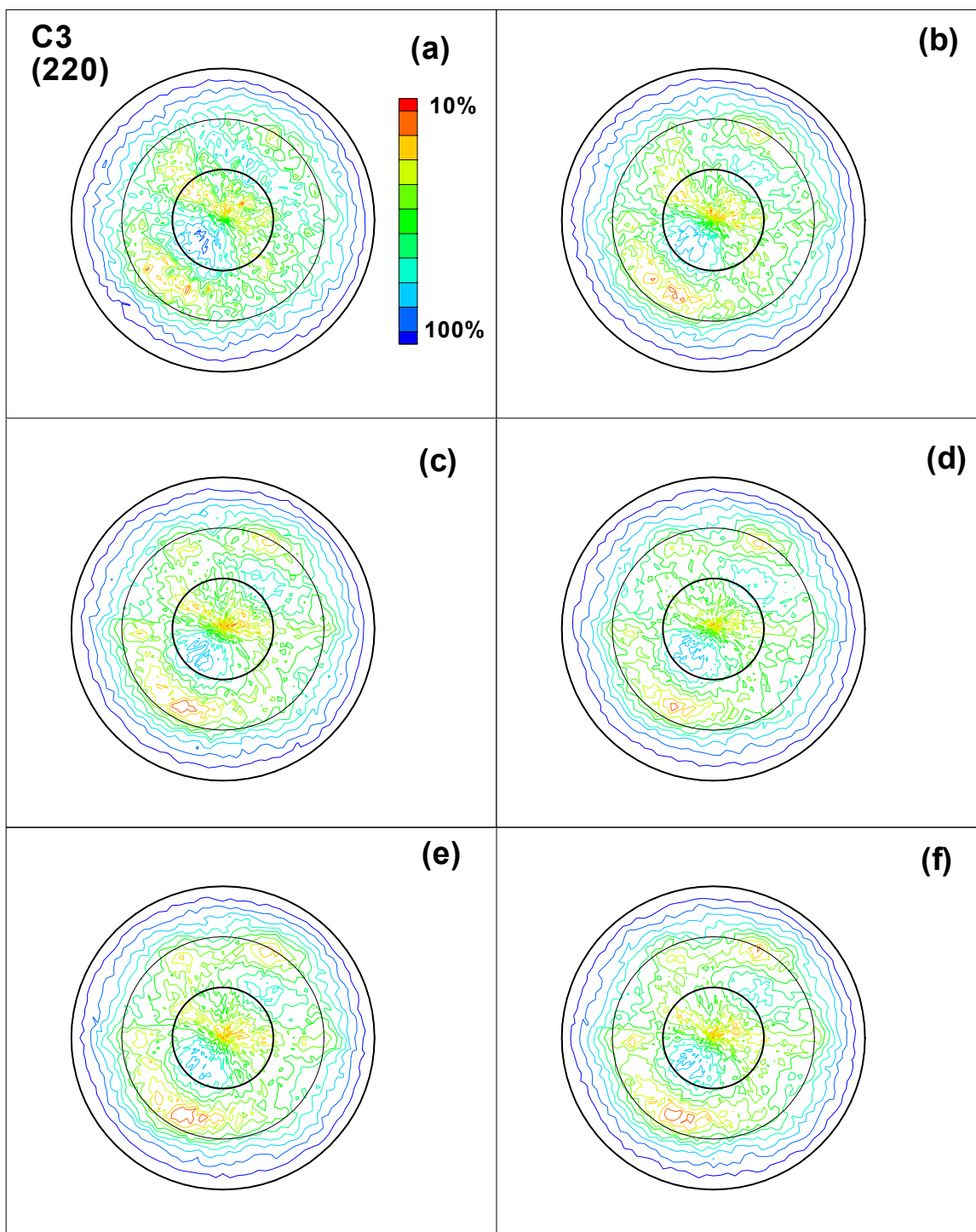


FIGURE B-59. DIRECT (220) POLE FIGURES FOR SPECIMEN C3 AFTER (a) 0, (b) 22,000, (c) 42,000, (d) 62,000, (e) 82,000 FATIGUE CYCLES, AND (f) AFTER FAILURE

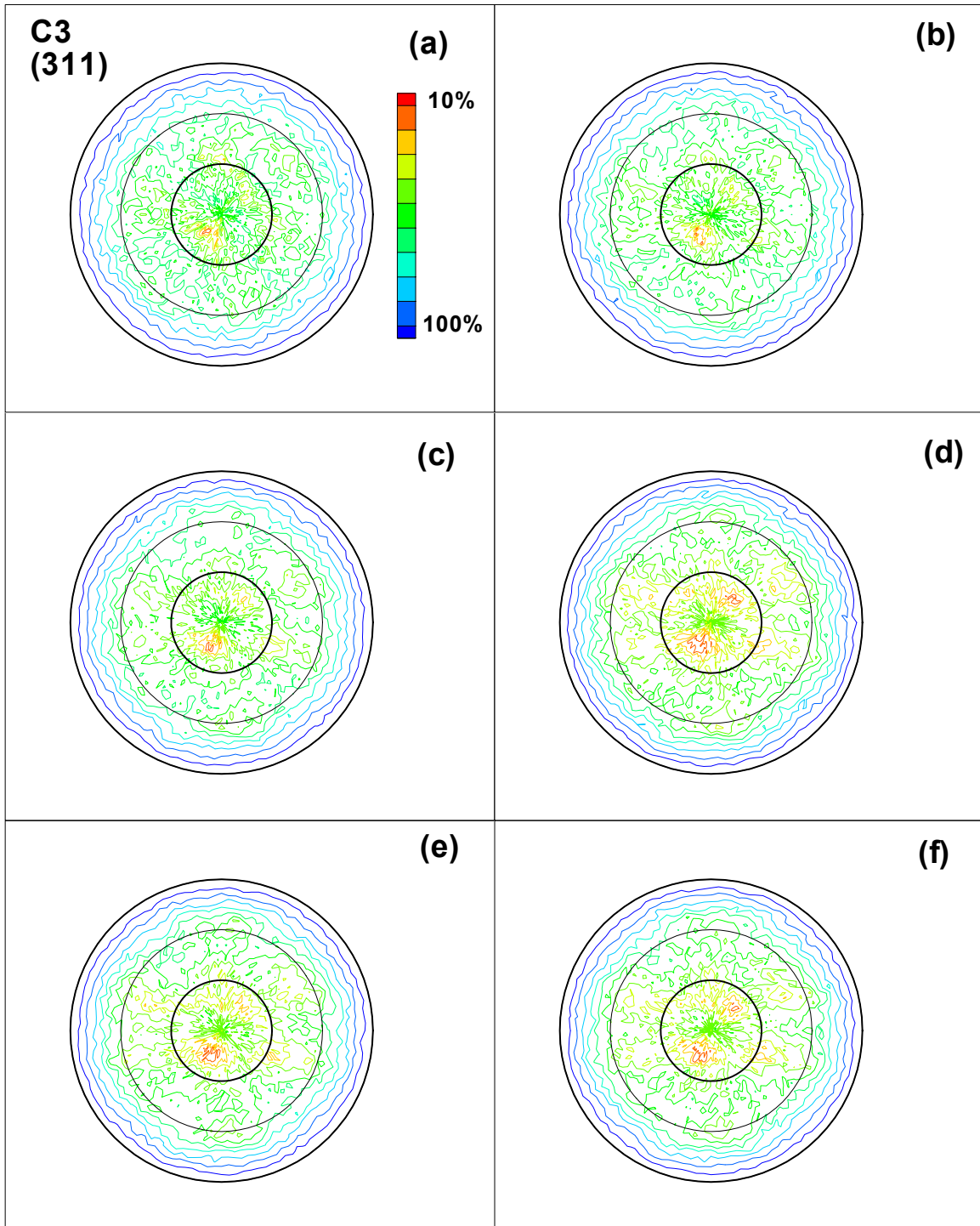


FIGURE B-60. DIRECT (311) POLE FIGURES FOR SPECIMEN C3 AFTER (a) 0, (b) 22,000, (c) 42,000, (d) 62,000, (e) 82,000 FATIGUE CYCLES, AND (f) AFTER FAILURE

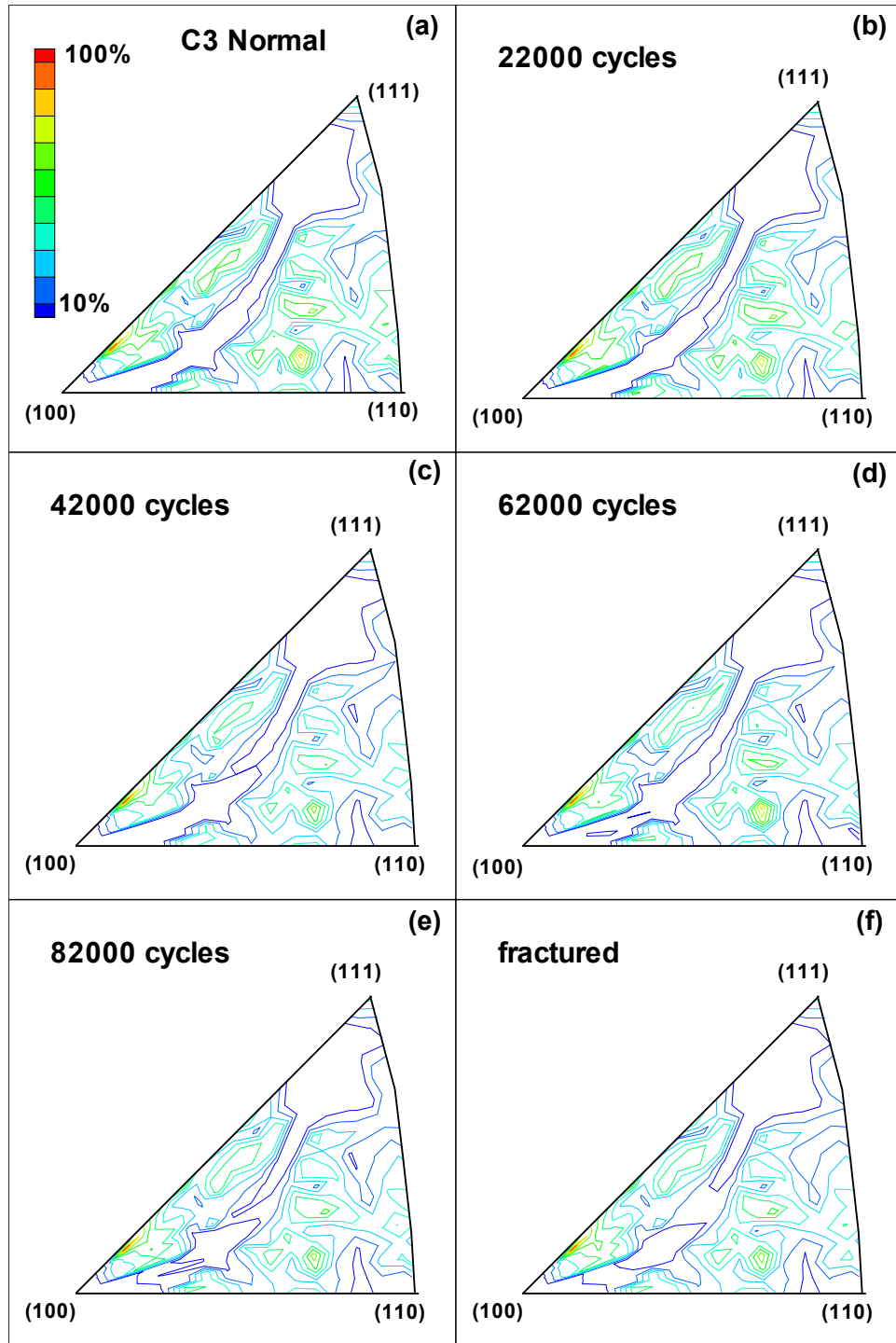


FIGURE B-61. INVERSE POLE FIGURES IN THE NORMAL DIRECTION FOR SPECIMEN C3 AFTER (a) 0, (b) 22,000, (c) 42,000, (d) 62,000, (e) 82,000 FATIGUE CYCLES, AND (f) AFTER FAILURE

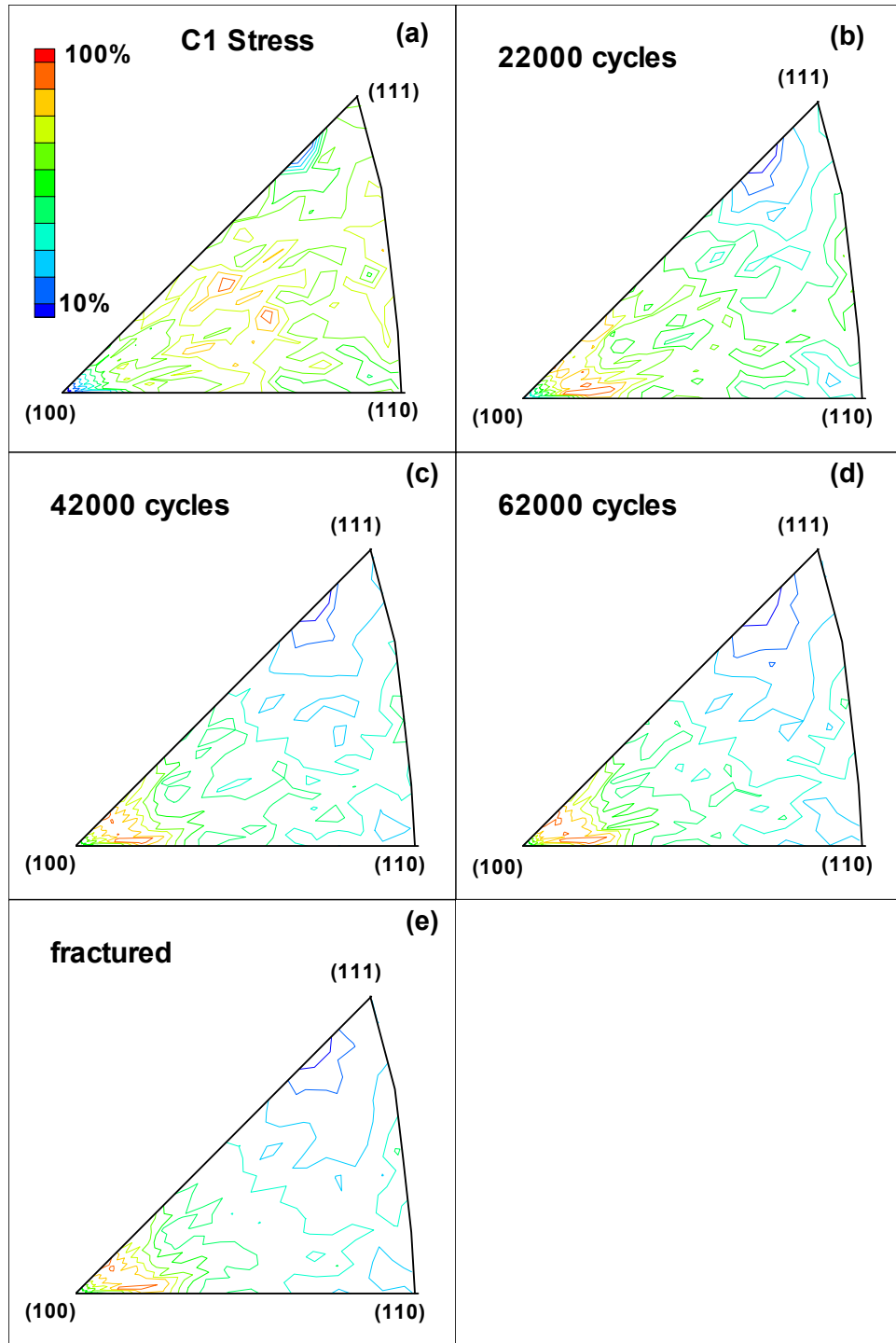


FIGURE B-62. INVERSE POLE FIGURES IN THE STRESS DIRECTION FOR SPECIMEN C3 AFTER (a) 0, (b) 22,000, (c) 42,000, (d) 62,000, AND (e) AFTER FAILURE

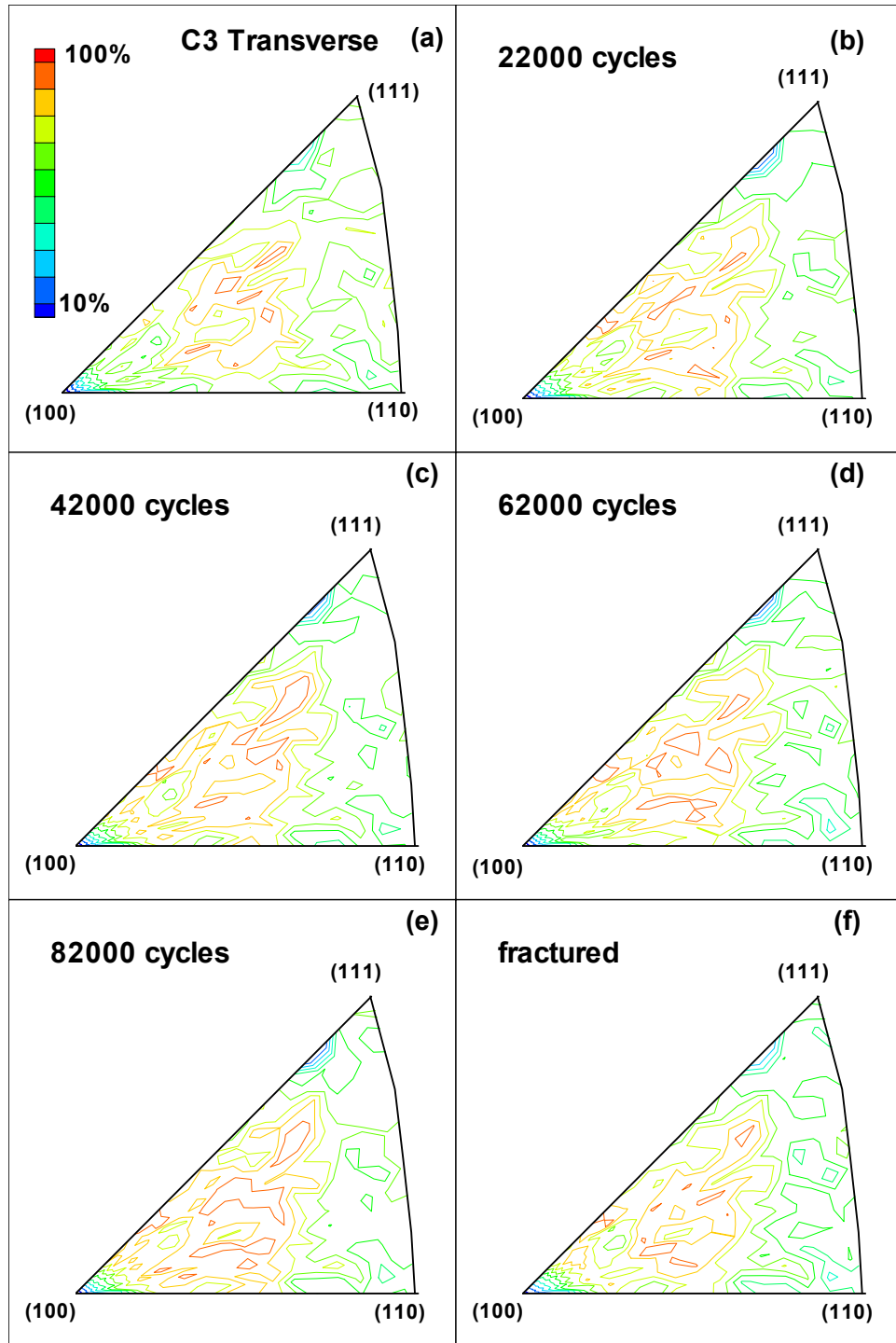


FIGURE B-63. INVERSE POLE FIGURES IN THE TRANSVERSE DIRECTION FOR SPECIMEN C3 AFTER (a) 0, (b) 22,000, (c) 42,000, (d) 62,000, (e) 82,000 FATIGUE CYCLES, AND (f) AFTER FAILURE

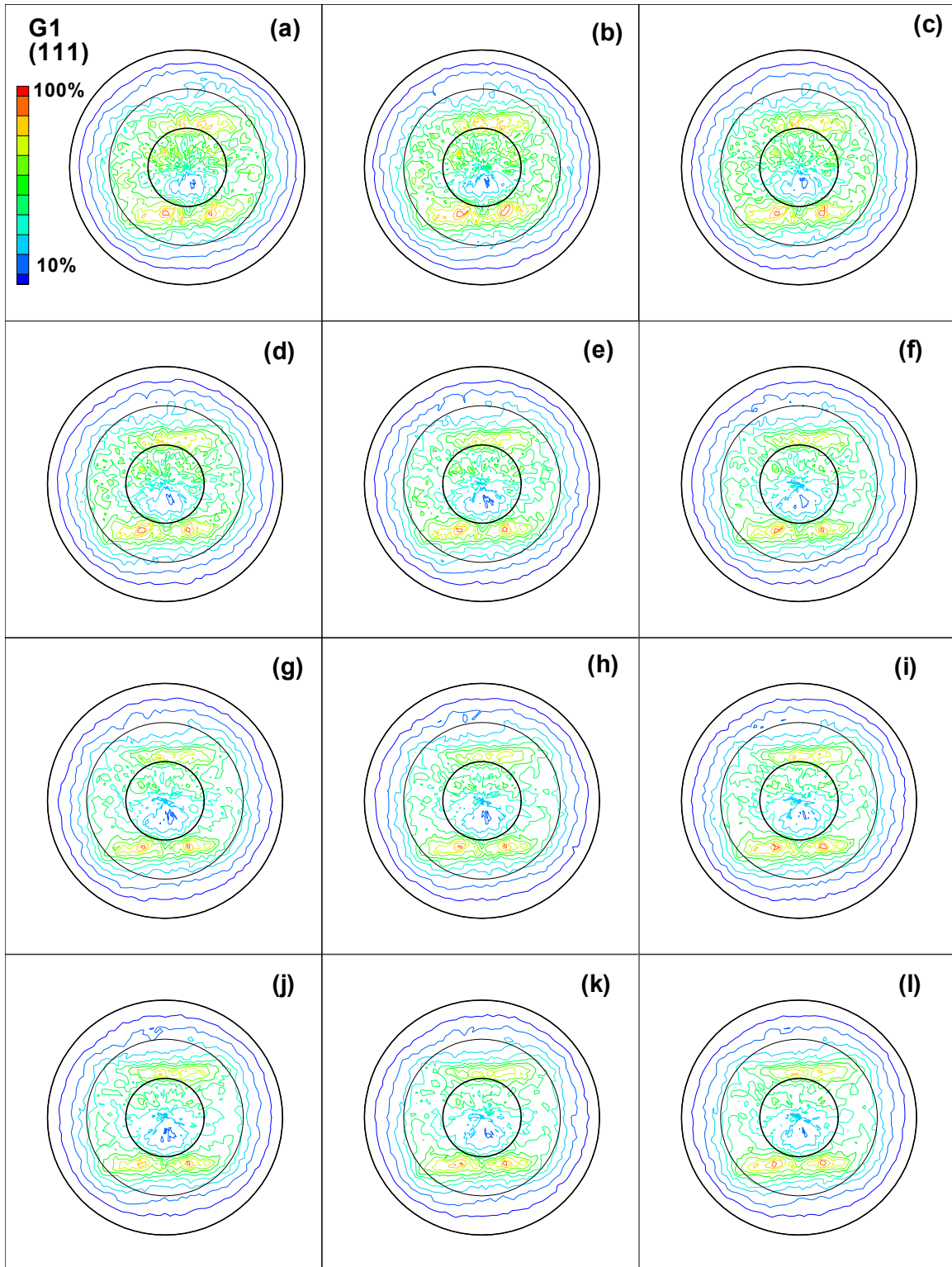


FIGURE B-64. DIRECT (111) POLE FIGURES FOR SPECIMEN G1 AFTER (a) 0, (b) 2,000, (c) 4,000, (d) 6,000, (e) 8,000, (f) 10,000, (g) 12,000, (h) 14,000, (i) 16,000, (j) 18,000, (k) 20,000, AND (l) 22,000 FATIGUE CYCLES



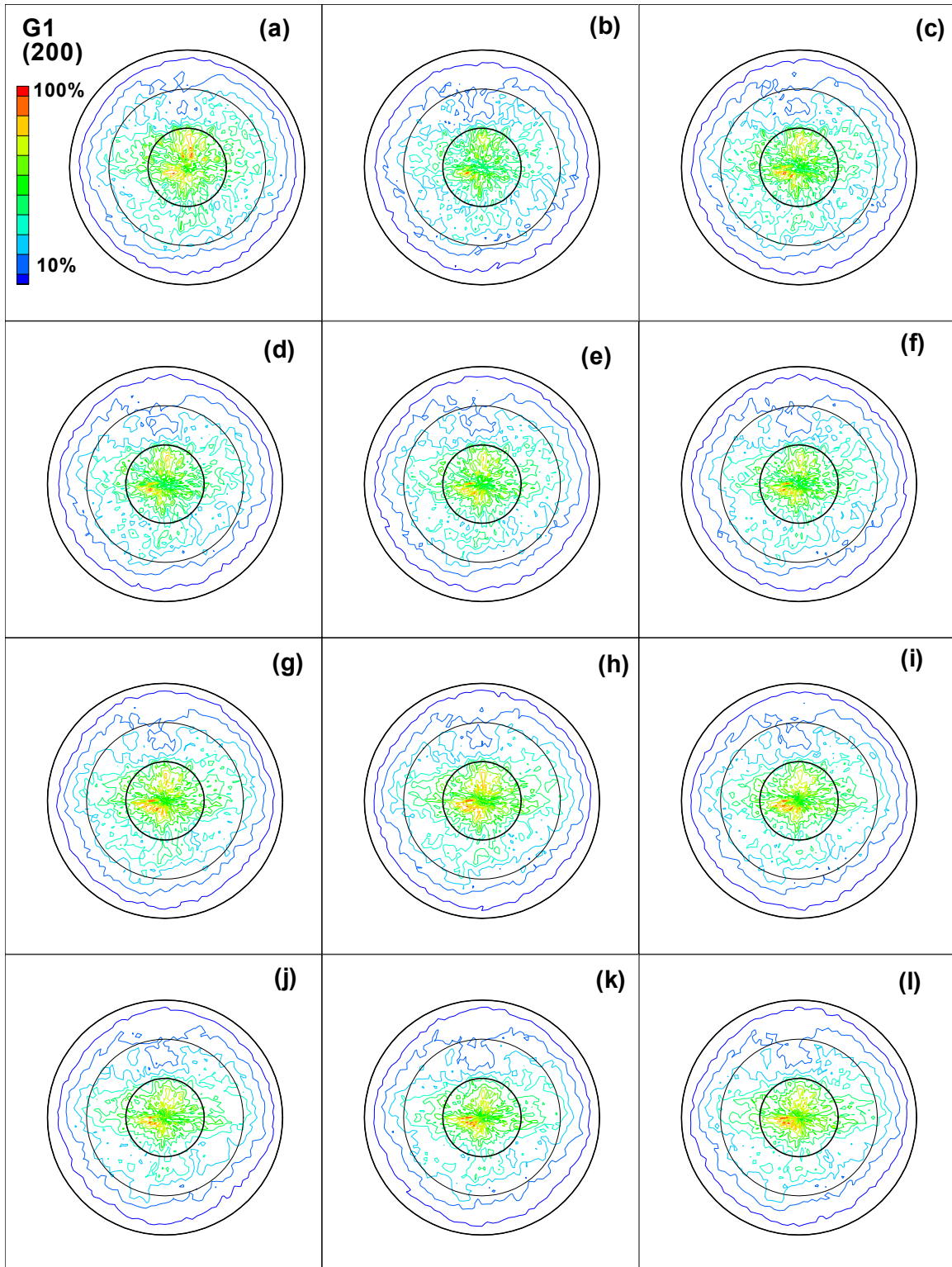


FIGURE B-65. DIRECT (200) POLE FIGURES FOR SPECIMEN G1 AFTER (a) 0, (b) 2,000, (c) 4,000, (d) 6,000, (e) 8,000, (f) 10,000, (g) 12,000, (h) 14,000, (i) 16,000, (j) 18,000, (k) 20,000, AND (l) 22,000 FATIGUE CYCLES

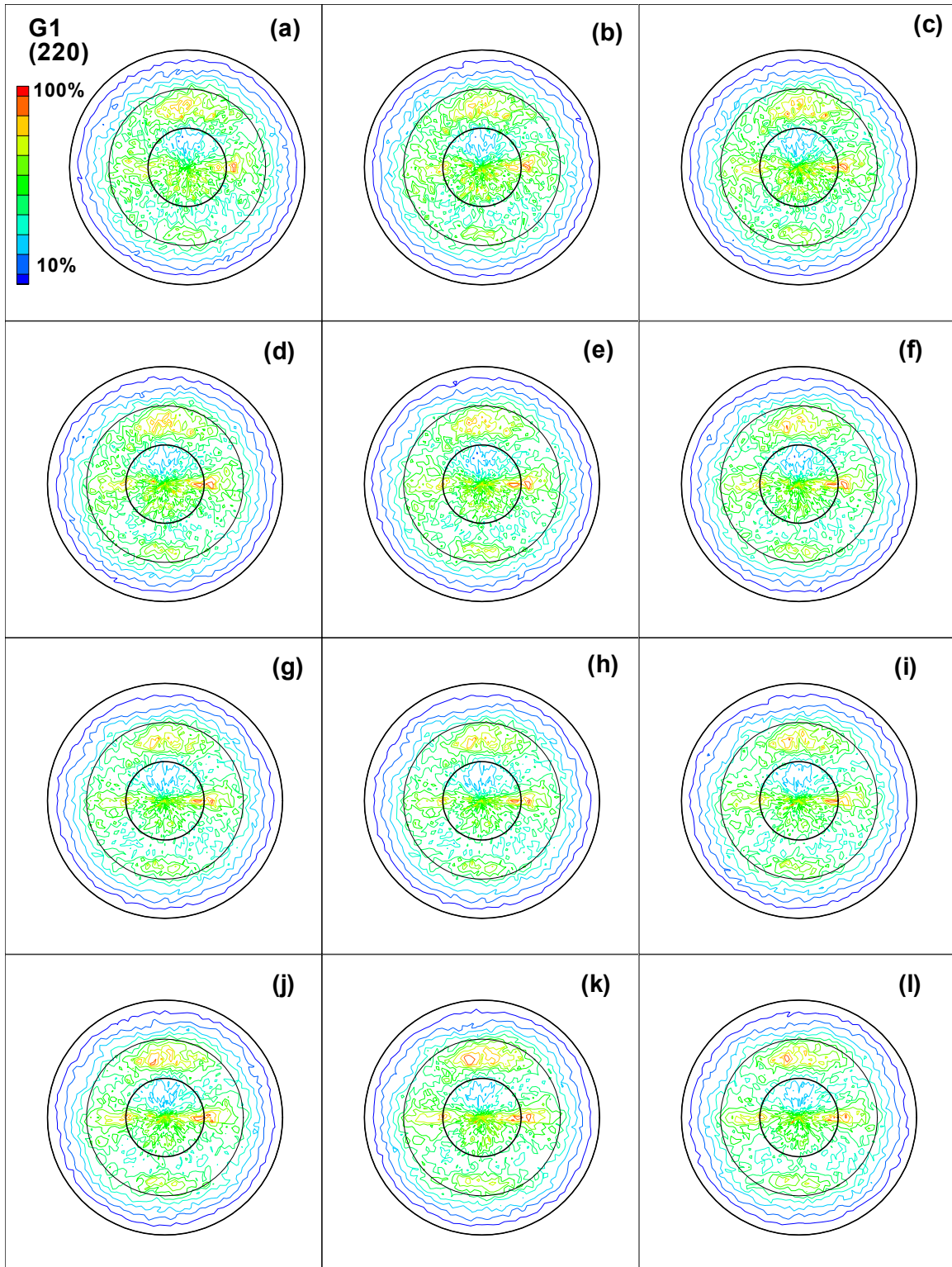


FIGURE B-66. DIRECT (220) POLE FIGURES FOR SPECIMEN G1 AFTER (a) 0, (b) 2,000, (c) 4,000, (d) 6,000, (e) 8,000, (f) 10,000, (g) 12,000, (h) 14,000, (i) 16,000, (j) 18,000, (k) 20,000, AND (l) 22,000 FATIGUE CYCLES



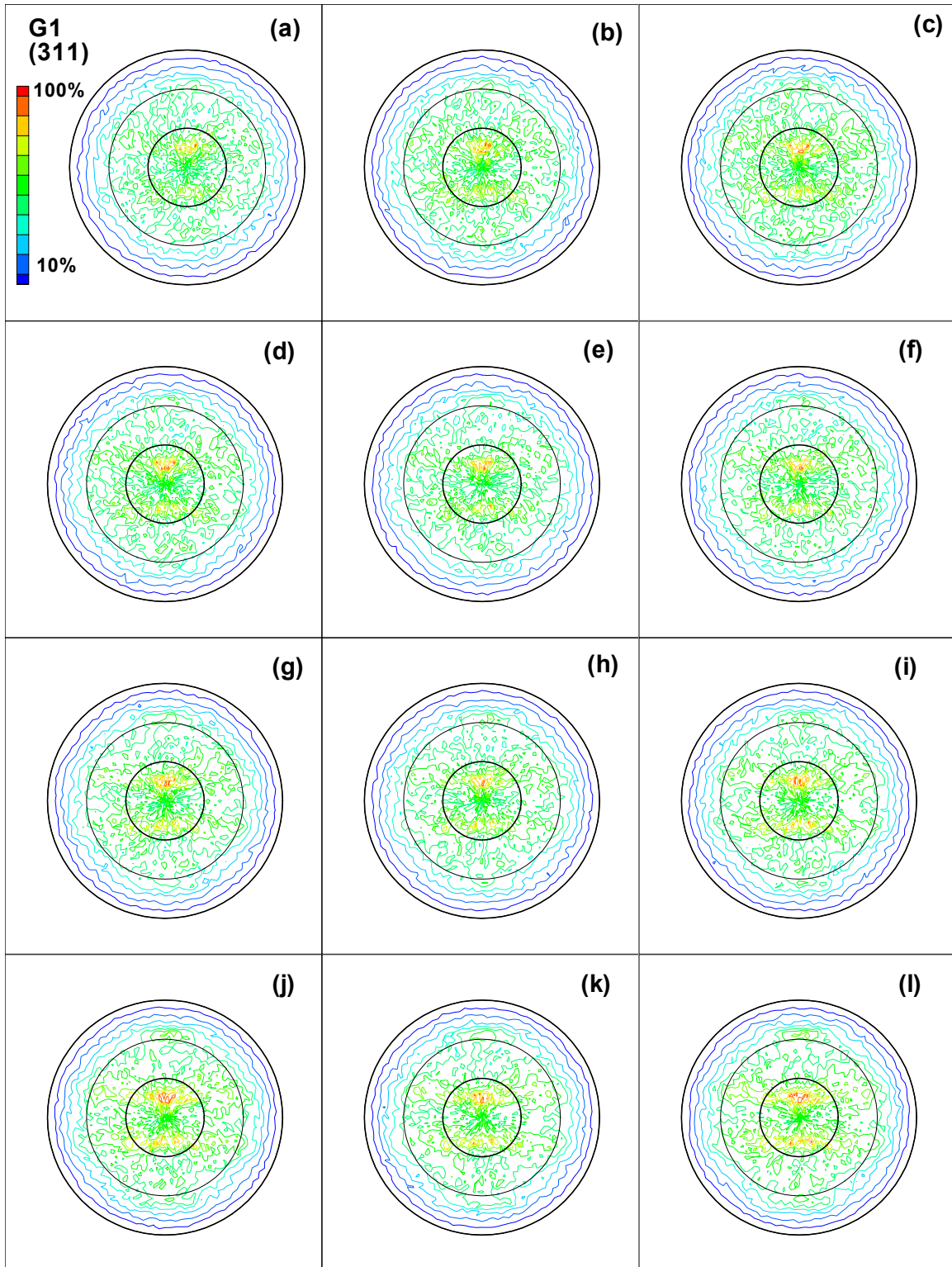


FIGURE B-67. DIRECT (311) POLE FIGURES FOR SPECIMEN G1 AFTER (a) 0, (b) 2,000, (c) 4,000, (d) 6,000, (e) 8,000, (f) 10,000, (g) 12,000, (h) 14,000, (i) 16,000, (j) 18,000, (k) 20,000, AND (l) 22,000 FATIGUE CYCLES

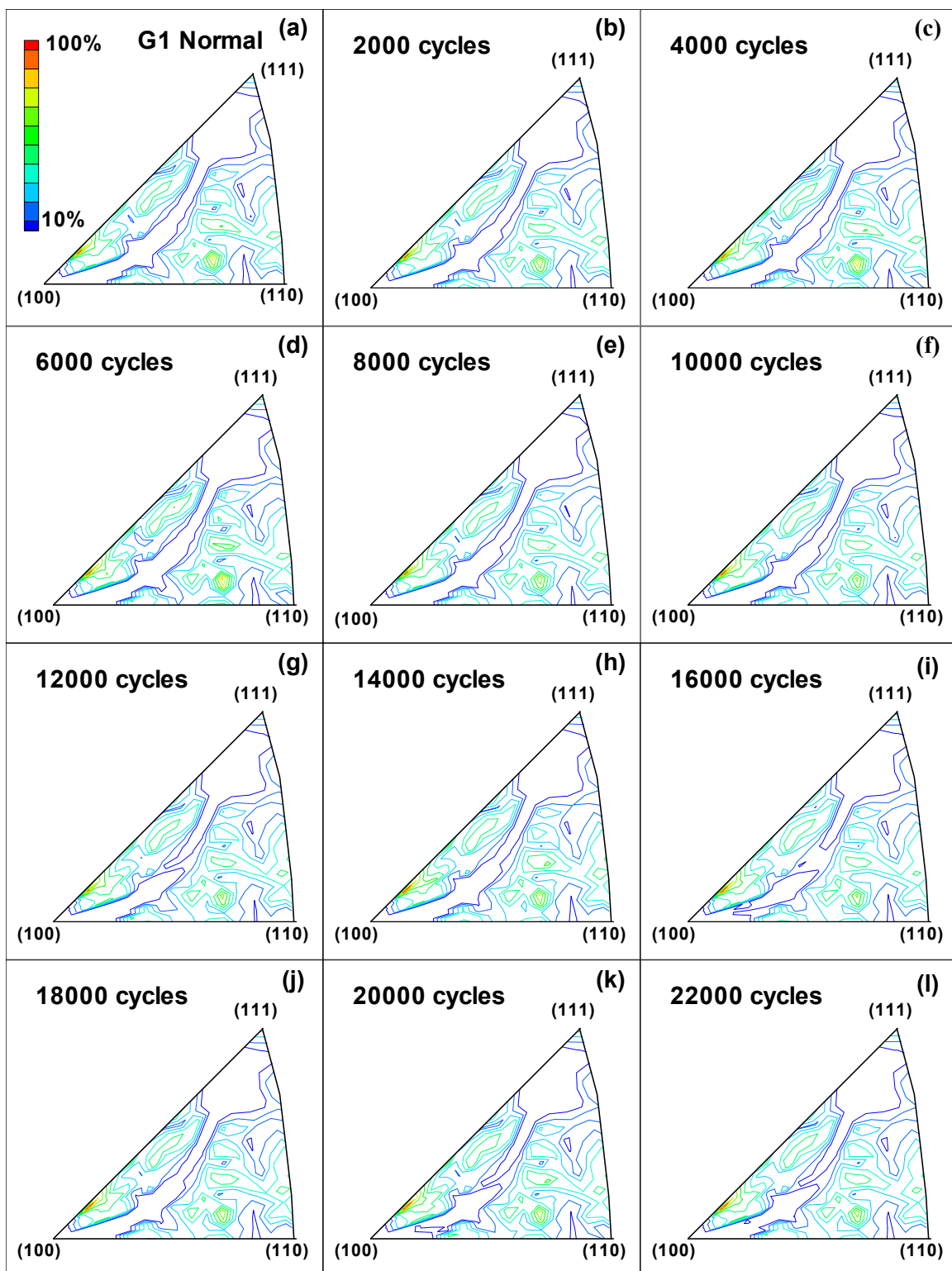


FIGURE B-68. INVERSE POLE FIGURES IN THE NORMAL DIRECTION FOR SPECIMEN G1 AFTER (a) 0, (b) 2,000, (c) 4,000, (d) 6,000, (e) 8,000, (f) 10,000, (g) 12,000, (h) 14,000, (i) 16,000, (j) 18,000, (k) 20,000, AND (l) 22,000 FATIGUE CYCLES

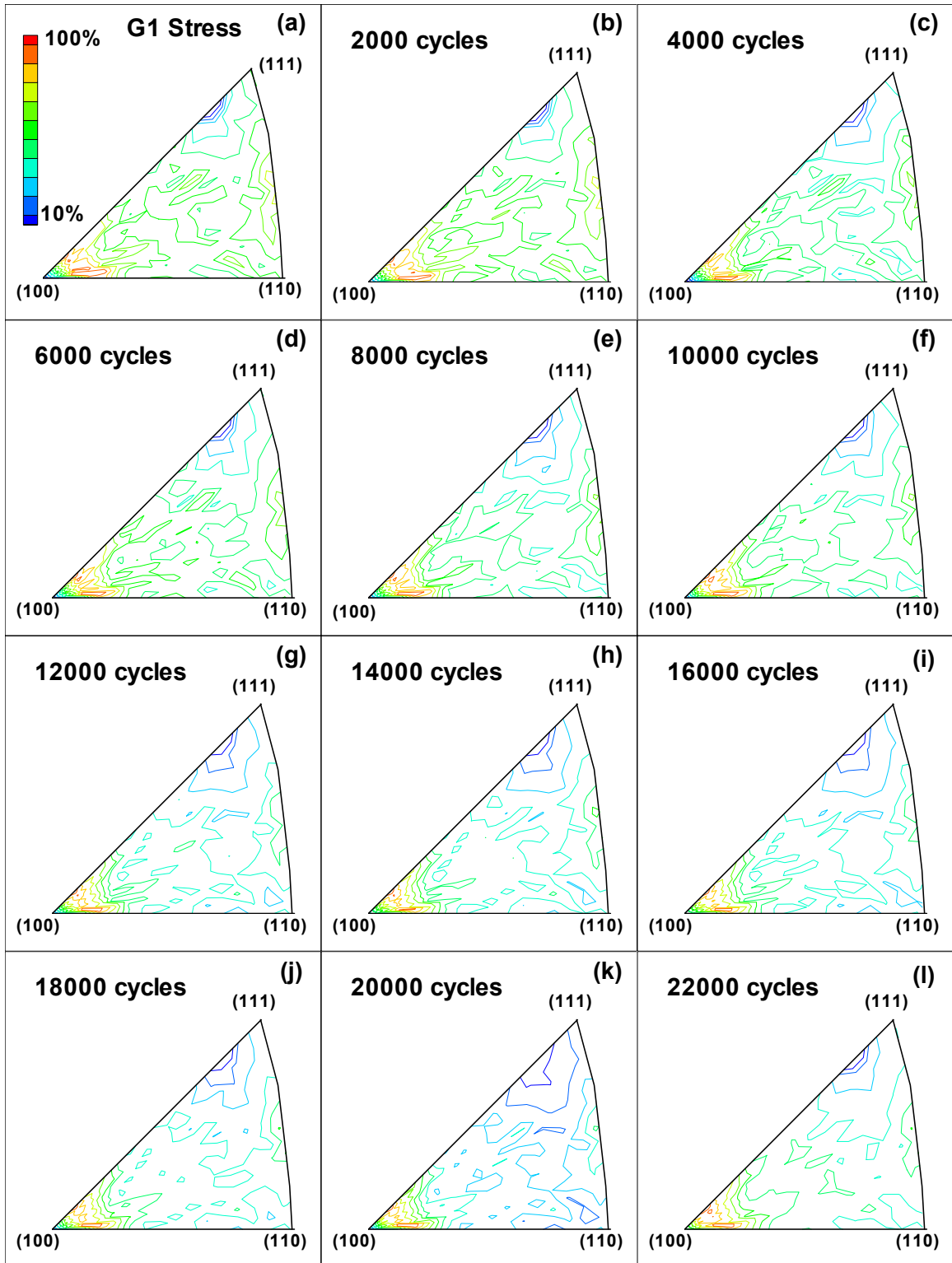


FIGURE B-69. INVERSE POLE FIGURES IN THE STRESS DIRECTION FOR SPECIMEN G1 AFTER (a) 0, (b) 2,000, (c) 4,000, (d) 6,000, (e) 8,000, (f) 10,000, (g) 12,000, (h) 14,000, (i) 16,000, (j) 18,000, (k) 20,000, AND (l) 22,000 FATIGUE CYCLES

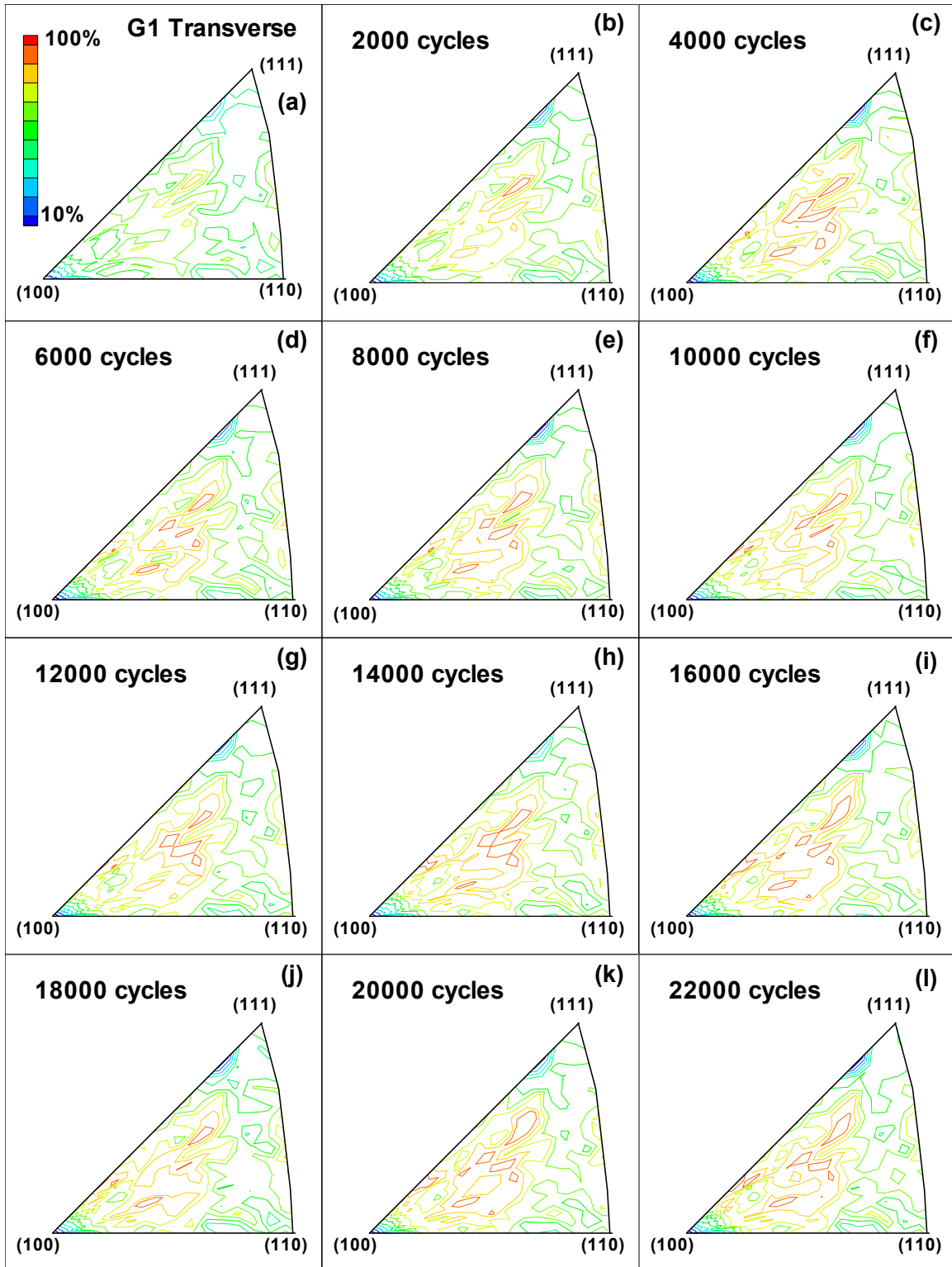


FIGURE B-70. INVERSE POLE FIGURES IN THE TRANSVERSE DIRECTION FOR SPECIMEN G1 AFTER (a) 0, (b) 2,000, (c) 4,000, (d) 6,000, (e) 8,000, (f) 10,000, (g) 12,000, (h) 14,000, (i) 16,000, (j) 18,000, (k) 20,000, AND (l) 22,000 FATIGUE CYCLES

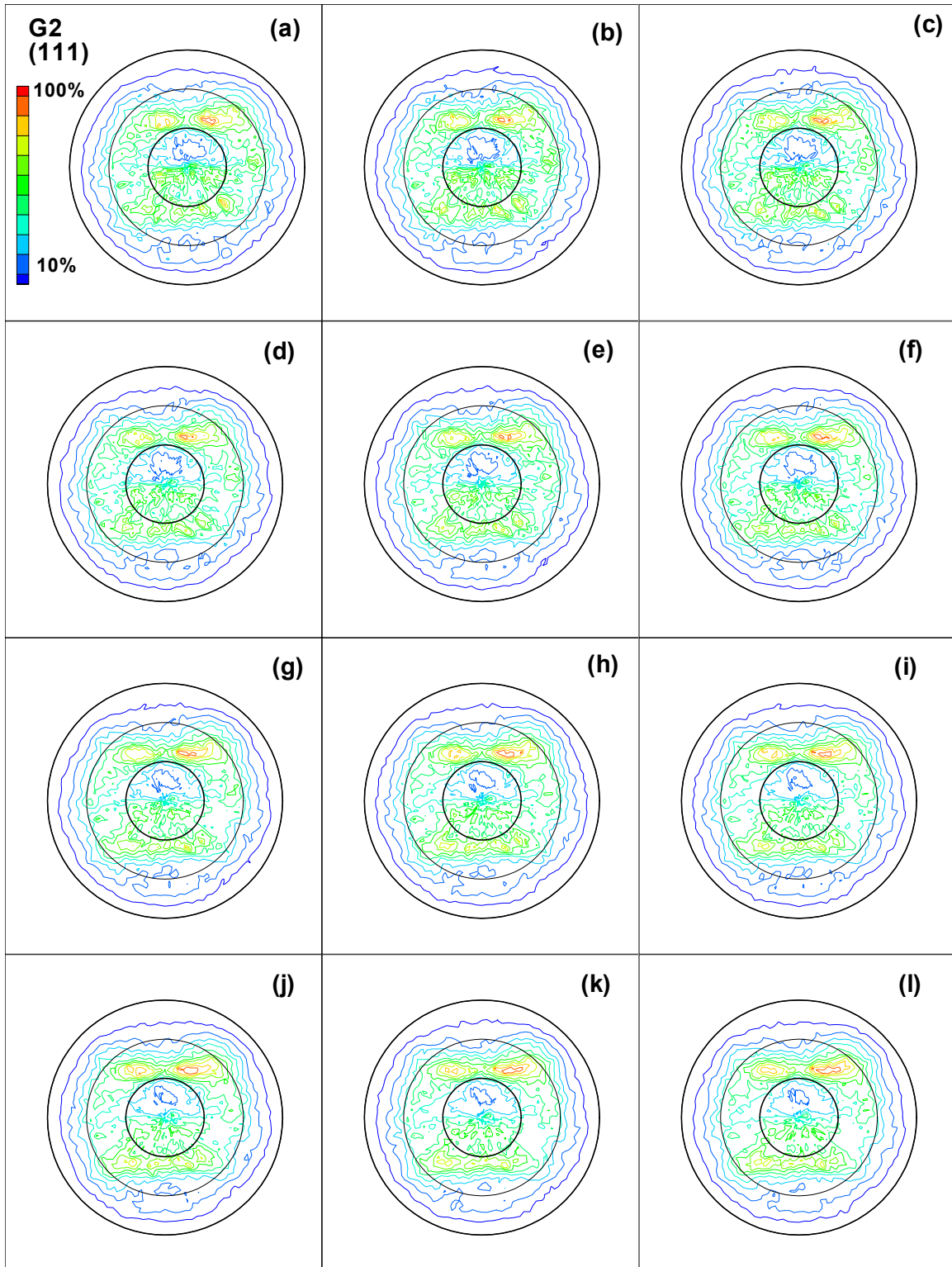


FIGURE B-71. DIRECT (111) POLE FIGURES FOR SPECIMEN G2 AFTER (a) 0, (b) 2,000, (c) 4,000, (d) 6,000, (e) 8,000, (f) 10,000, (g) 12,000, (h) 14,000, (i) 16,000, (j) 18,000, (k) 20,000, AND (l) 22,000 FATIGUE CYCLES



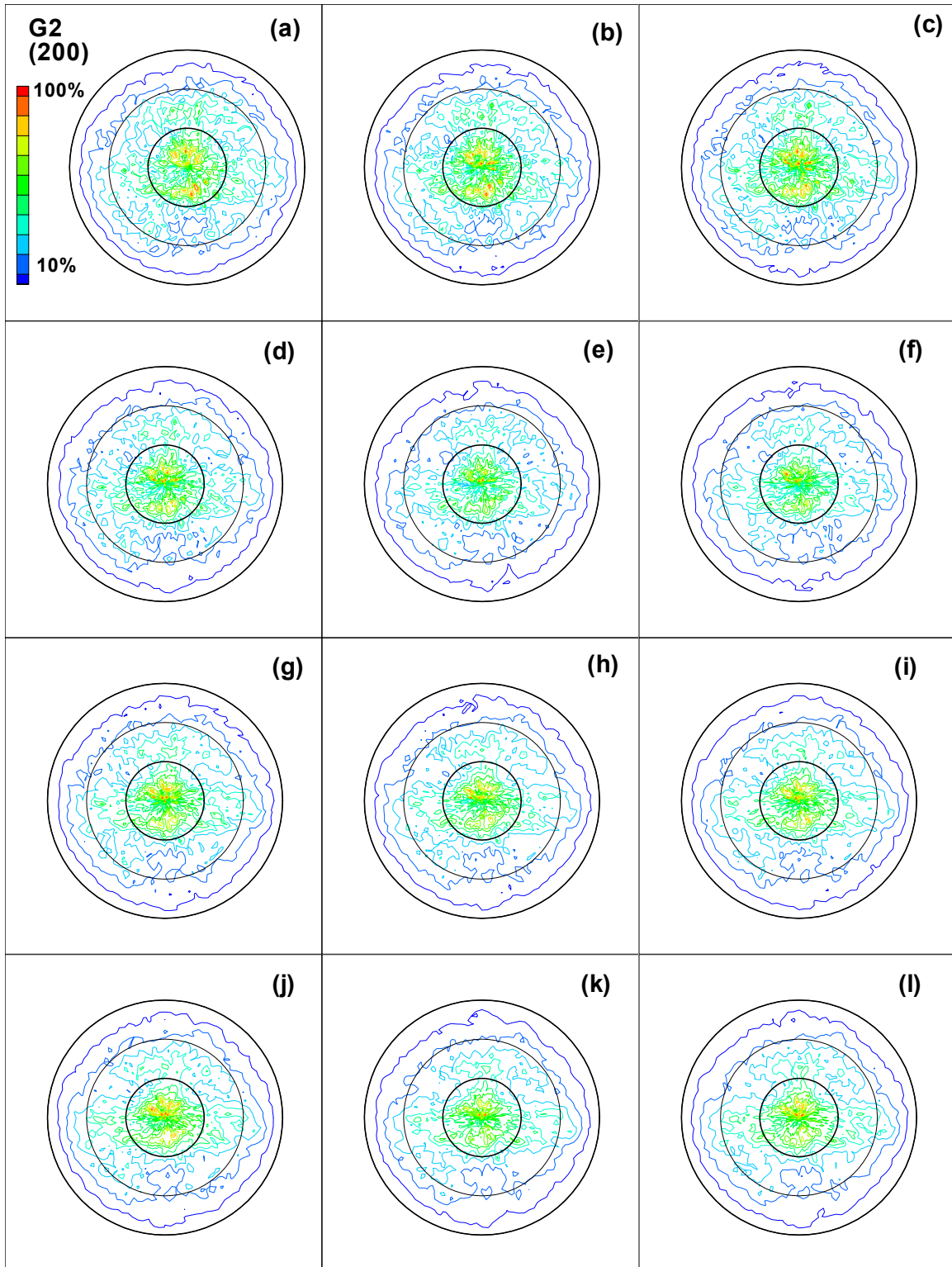


FIGURE B-72. DIRECT (200) POLE FIGURES FOR SPECIMEN G2 AFTER (a) 0, (b) 2,000, (c) 4,000, (d) 6,000, (e) 8,000, (f) 10,000, (g) 12,000, (h) 14,000, (i) 16,000, (j) 18,000, (k) 20,000, AND (l) 22,000 FATIGUE CYCLES

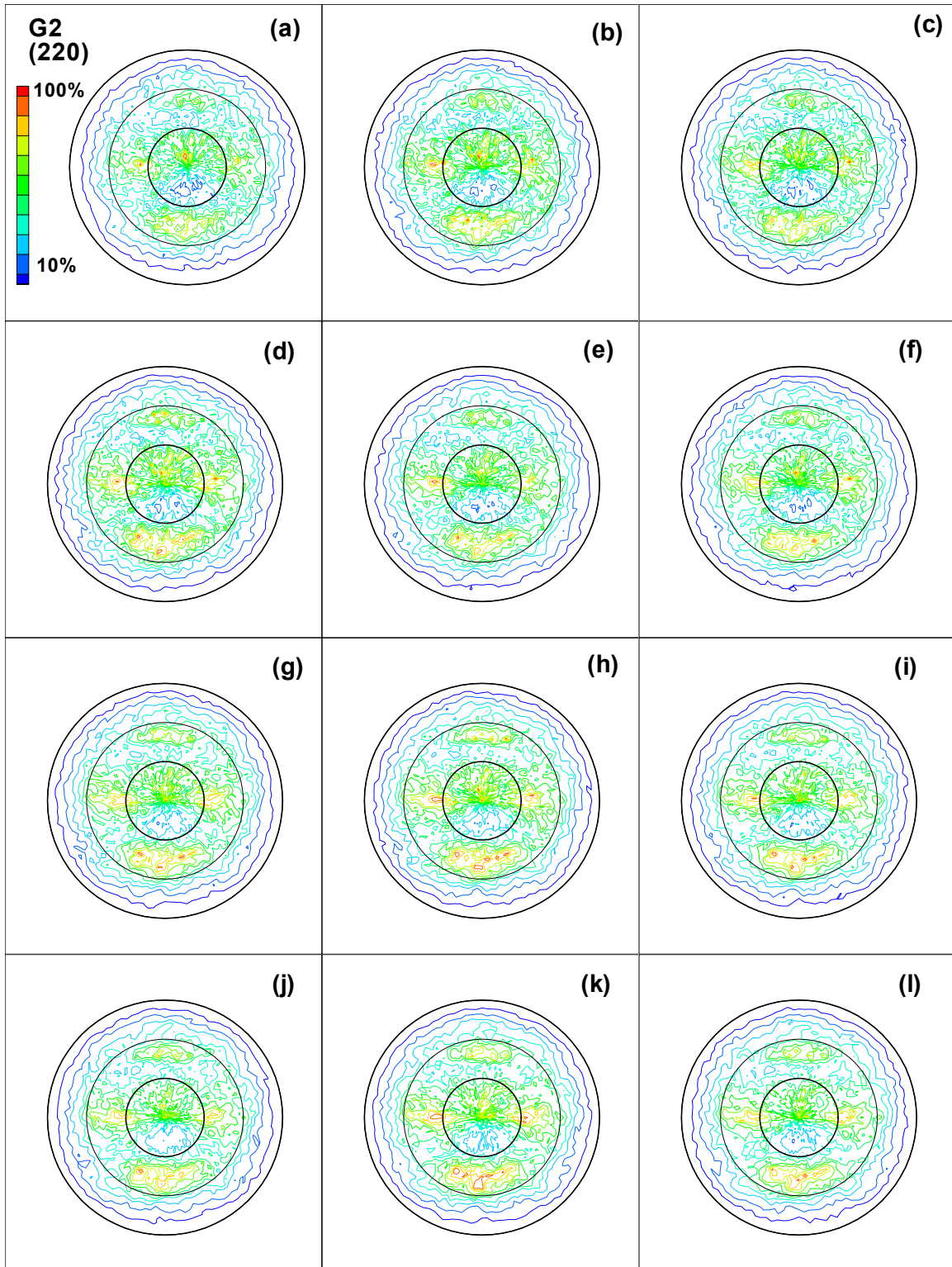


FIGURE B-73. DIRECT (220) POLE FIGURES FOR SPECIMEN G2 AFTER (a) 0, (b) 2,000, (c) 4,000, (d) 6,000, (e) 8,000, (f) 10,000, (g) 12,000, (h) 14,000, (i) 16,000, (j) 18,000, (k) 20,000, AND (l) 22,000 FATIGUE CYCLES

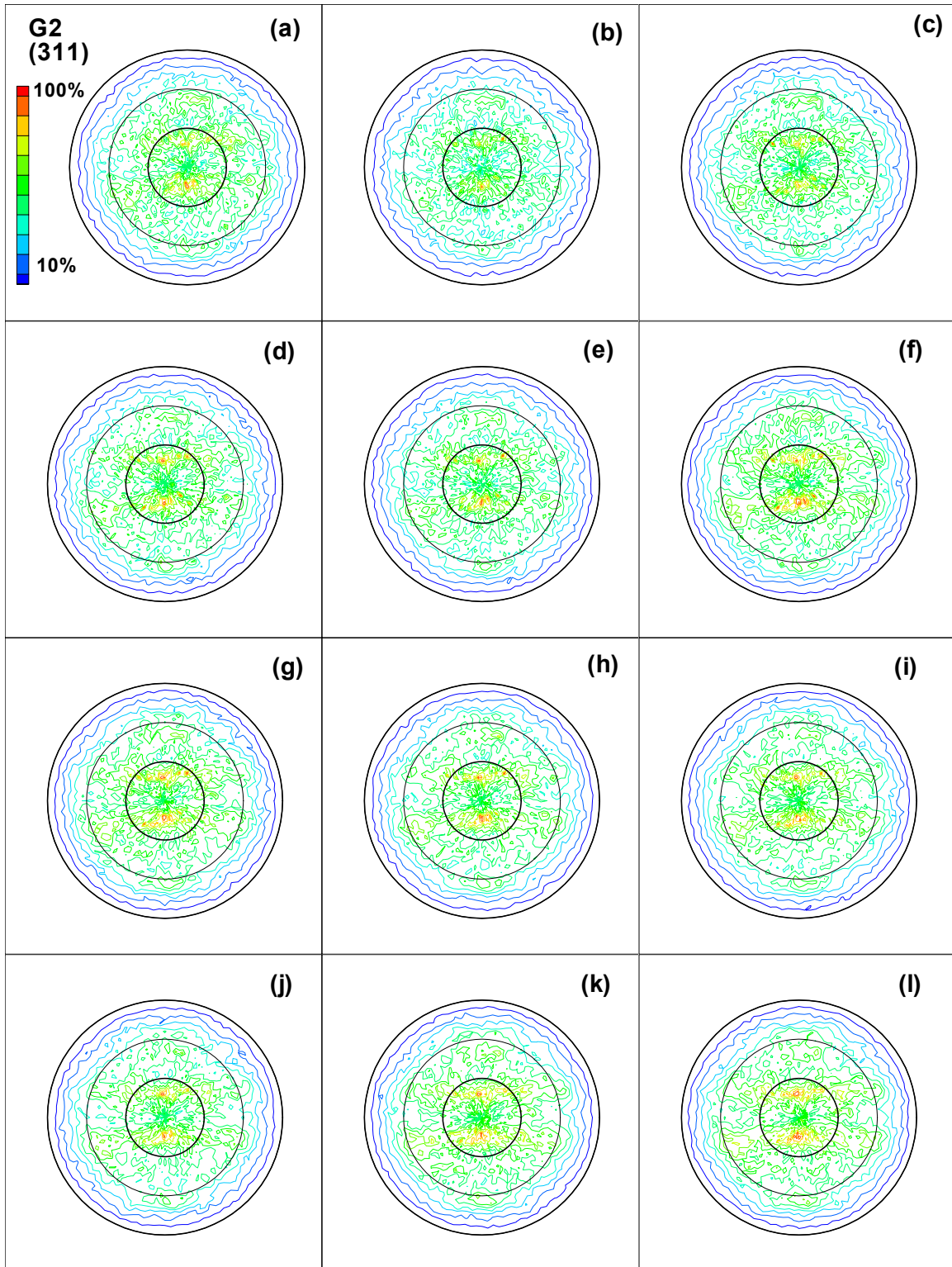


FIGURE B-74. DIRECT (311) POLE FIGURES FOR SPECIMEN G2 AFTER (a) 0, (b) 2,000, (c) 4,000, (d) 6,000, (e) 8,000, (f) 10,000, (g) 12,000, (h) 14,000, (i) 16,000, (j) 18,000, (k) 20,000, AND (l) 22,000 FATIGUE CYCLES



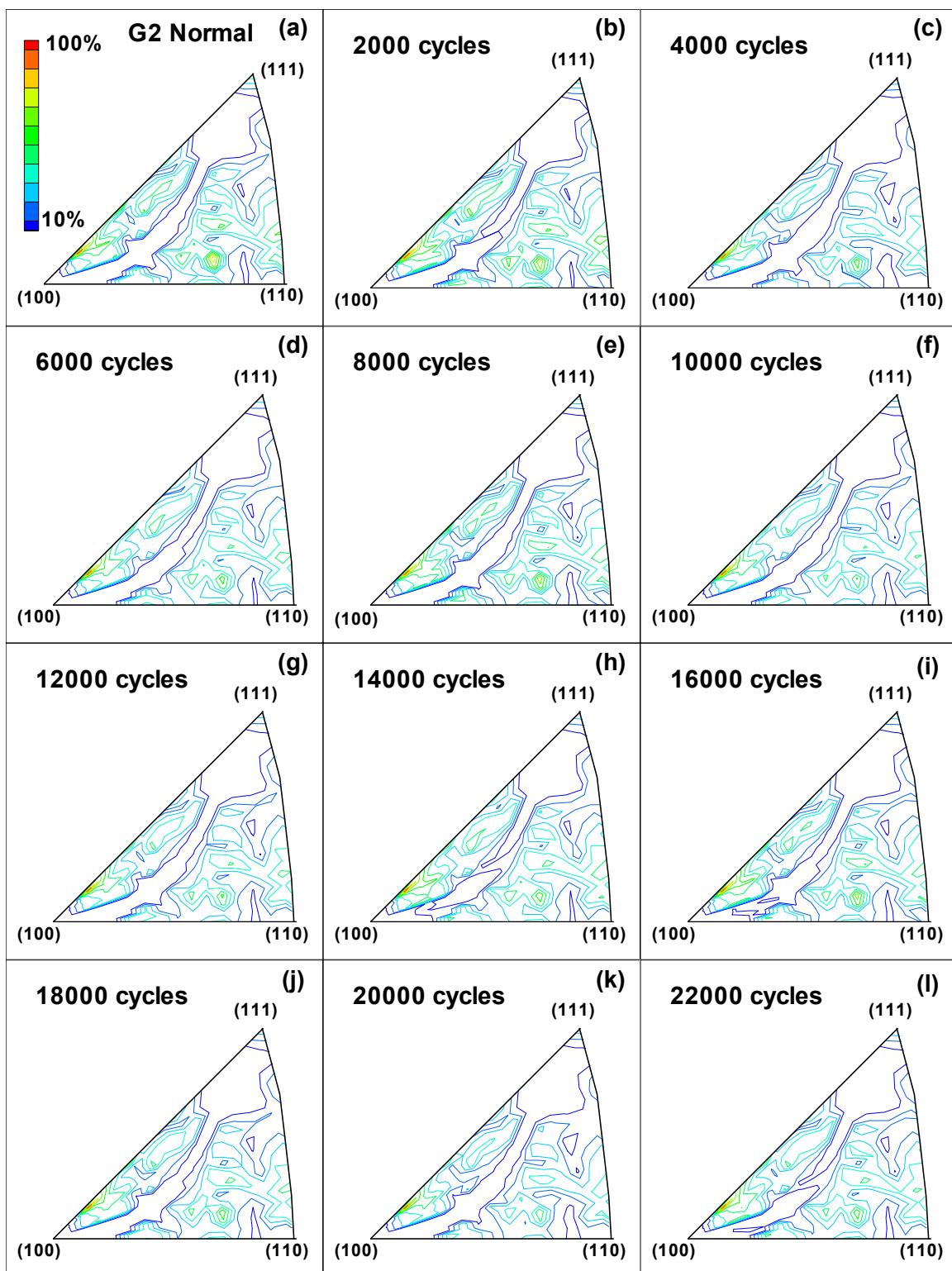


FIGURE B-75. INVERSE POLE FIGURES IN THE NORMAL DIRECTION FOR SPECIMEN G2 AFTER (a) 0, (b) 2,000, (c) 4,000, (d) 6,000, (e) 8,000, (f) 10,000, (g) 12,000, (h) 14,000, (i) 16,000, (j) 18,000, (k) 20,000, AND (l) 22,000 FATIGUE CYCLES

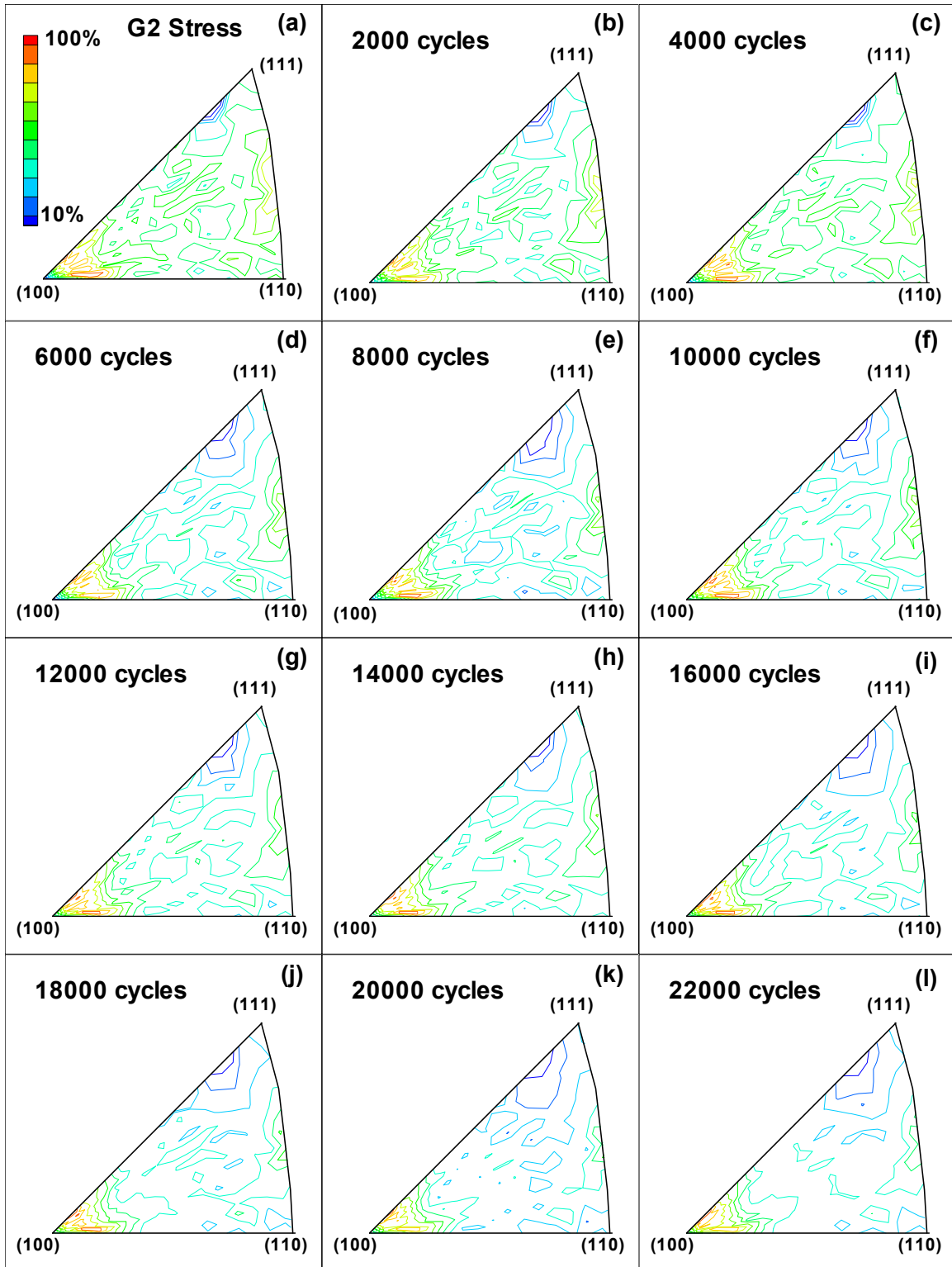


FIGURE B-76. INVERSE POLE FIGURES IN THE STRESS DIRECTION FOR SPECIMEN G2 AFTER (a) 0, (b) 2,000, (c) 4,000, (d) 6,000, (e) 8,000, (f) 10,000, (g) 12,000, (h) 14,000, (i) 16,000, (j) 18,000, (k) 20,000, AND (l) 22,000 FATIGUE CYCLES

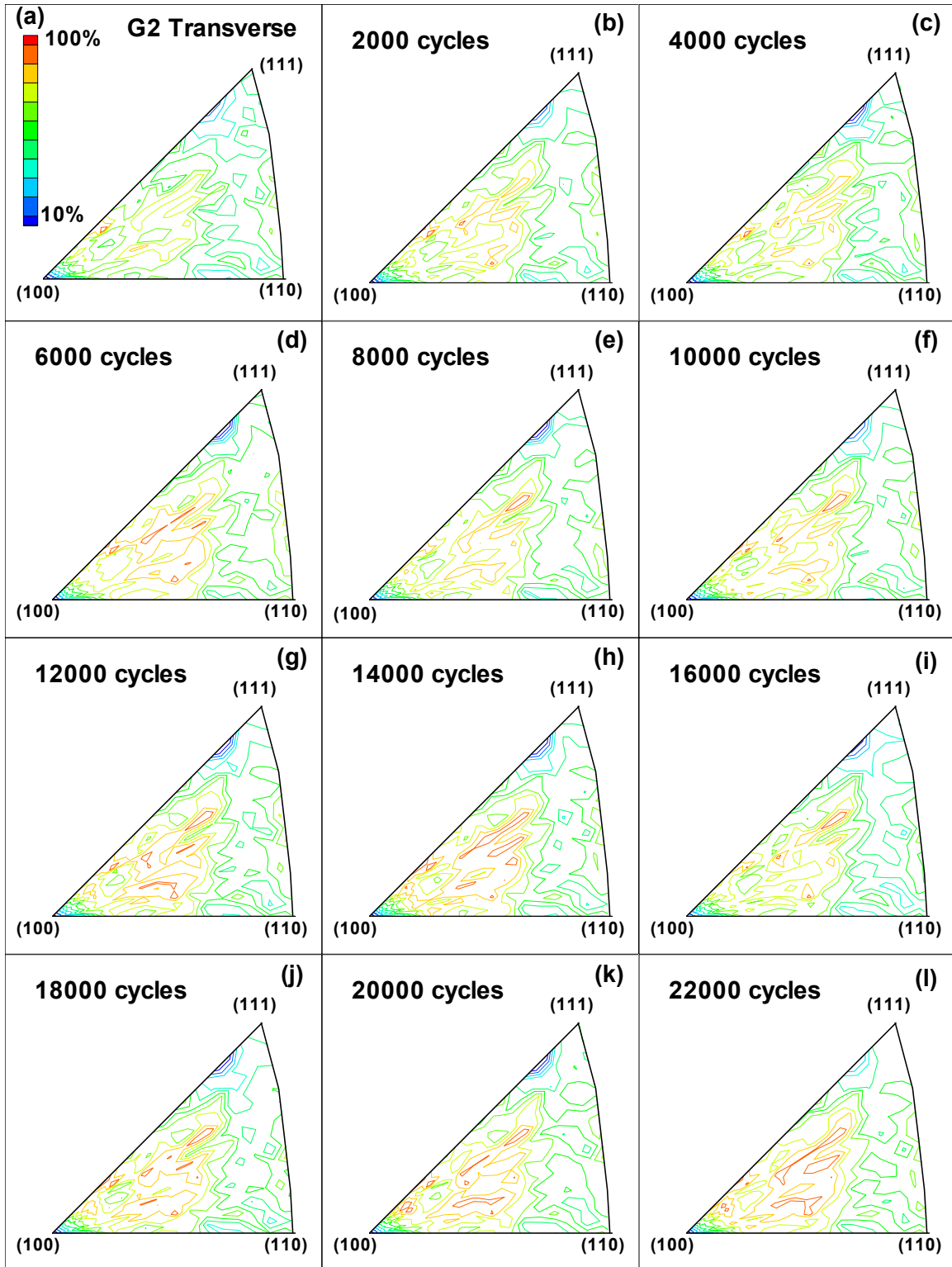


FIGURE B-77. INVERSE POLE FIGURES IN THE TRANSVERSE DIRECTION FOR SPECIMEN G2 AFTER (a) 0, (b) 2,000, (c) 4,000, (d) 6,000, (e) 8,000, (f) 10,000, (g) 12,000, (h) 14,000, (i) 16,000, (j) 18,000, (k) 20,000, AND (l) 22,000 FATIGUE CYCLES

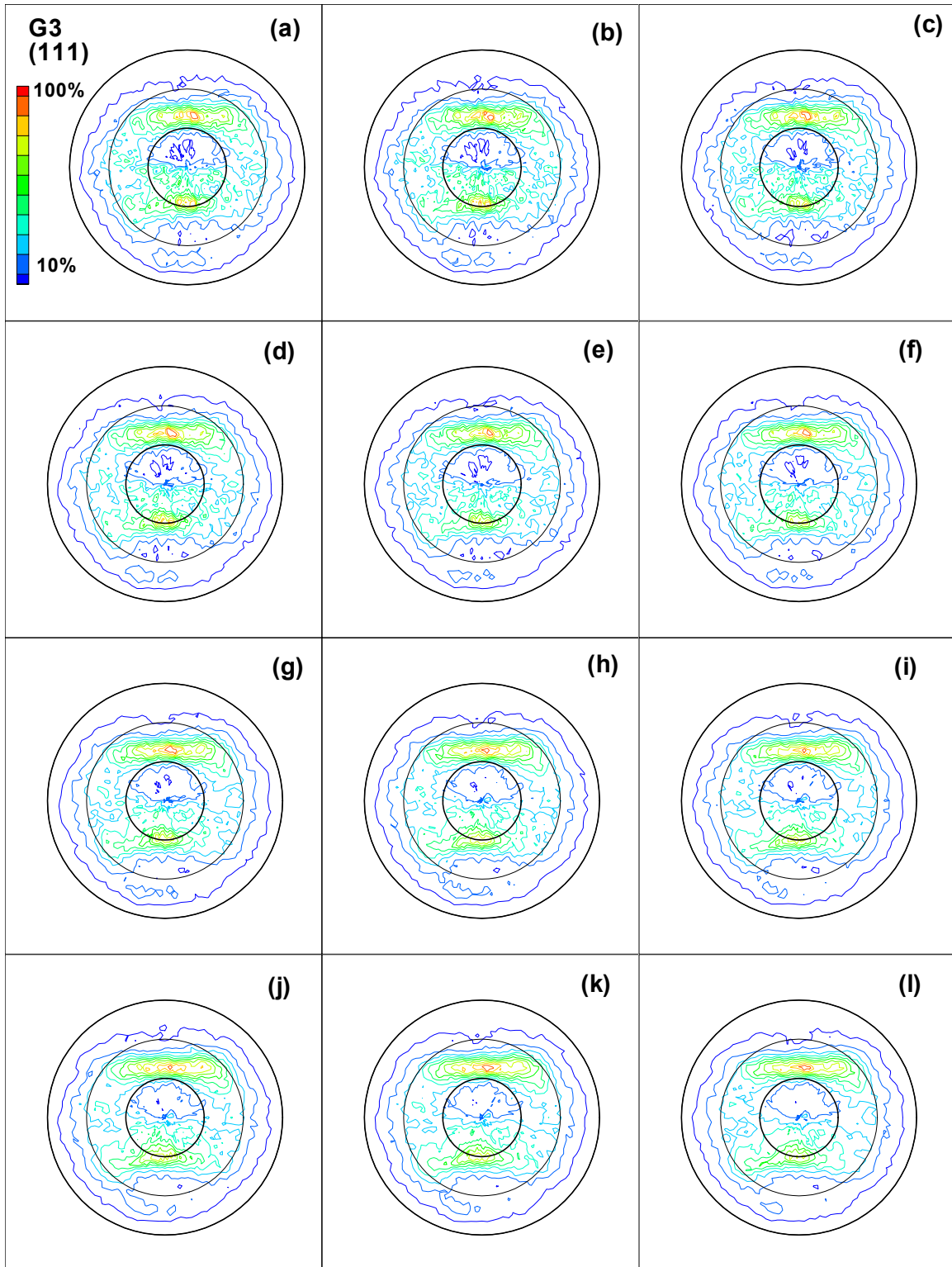


FIGURE B-78. DIRECT (111) POLE FIGURES FOR SPECIMEN G3 AFTER (a) 0, (b) 2,000, (c) 4,000, (d) 6,000, (e) 8,000, (f) 10,000, (g) 12,000, (h) 14,000, (i) 16,000, (j) 18,000, (k) 20,000, AND (l) 22,000 FATIGUE CYCLES

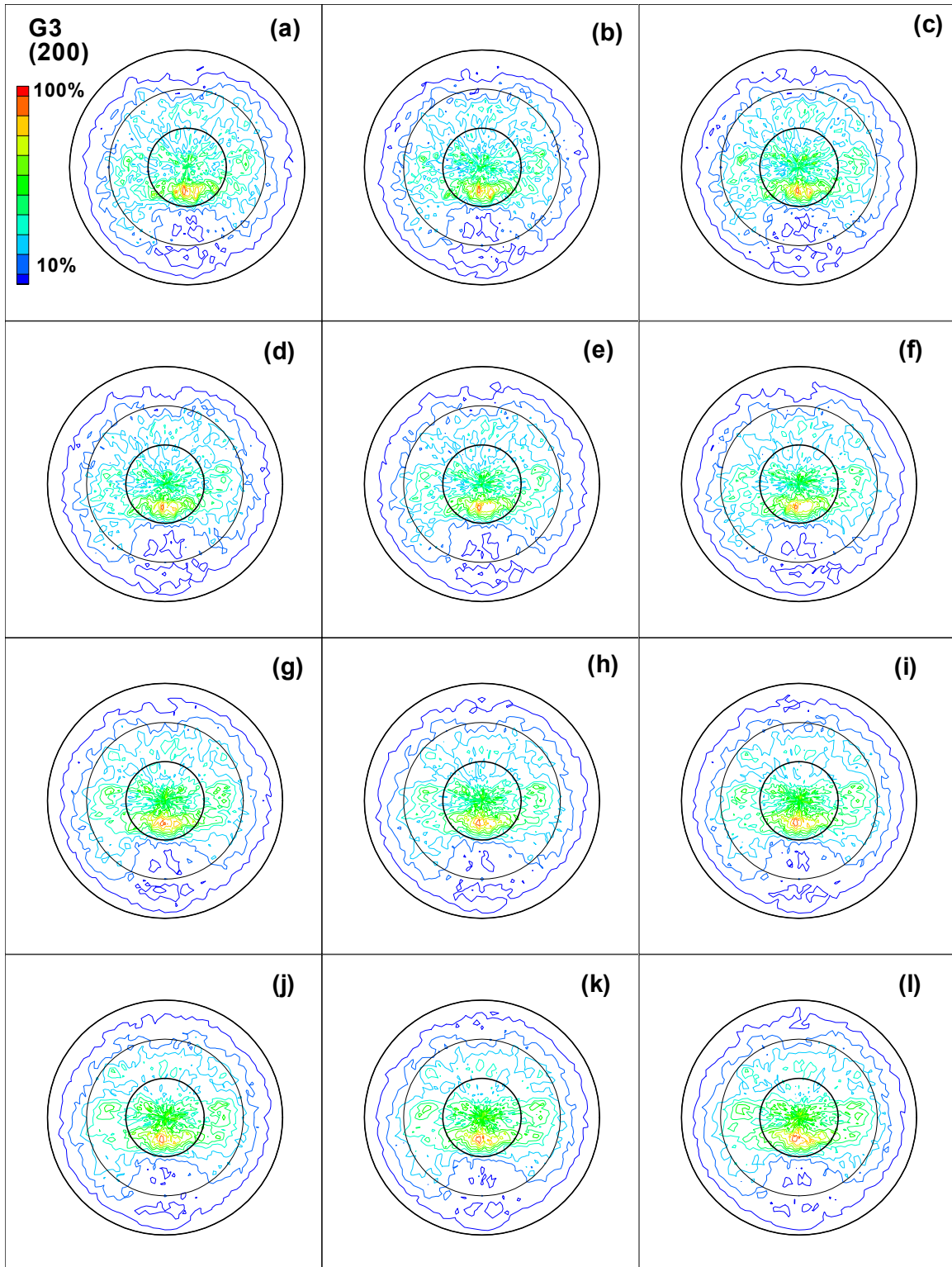


FIGURE B-79. DIRECT (200) POLE FIGURES FOR SPECIMEN G3 AFTER (a) 0, (b) 2,000, (c) 4,000, (d) 6,000, (e) 8,000, (f) 10,000, (g) 12,000, (h) 14,000, (i) 16,000, (j) 18,000, (k) 20,000, AND (l) 22,000 FATIGUE CYCLES



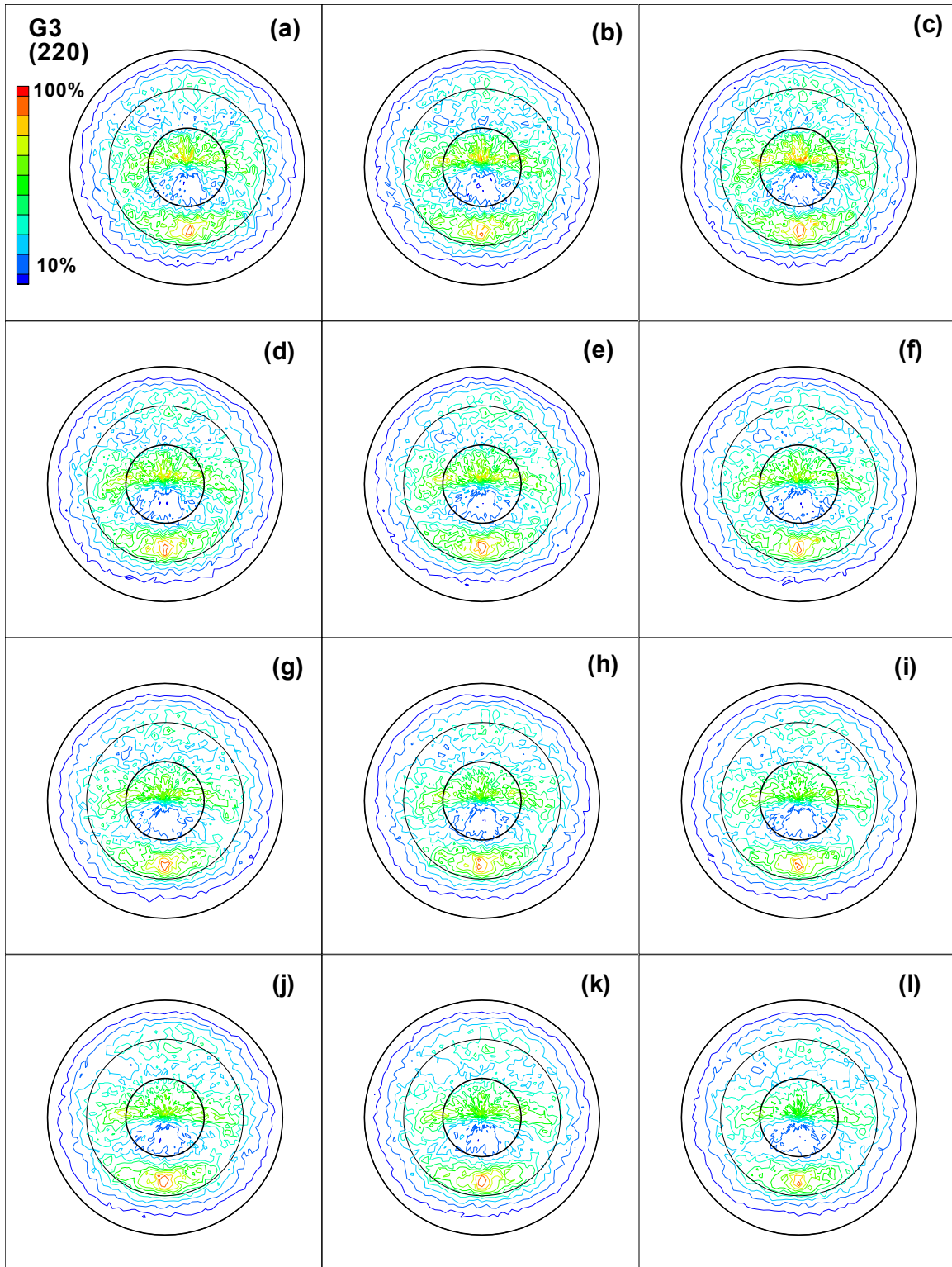


FIGURE B-80. DIRECT (220) POLE FIGURES FOR SPECIMEN G3 AFTER (a) 0, (b) 2,000, (c) 4,000, (d) 6,000, (e) 8,000, (f) 10,000, (g) 12,000, (h) 14,000, (i) 16,000, (j) 18,000, (k) 20,000, AND (l) 22,000 FATIGUE CYCLES

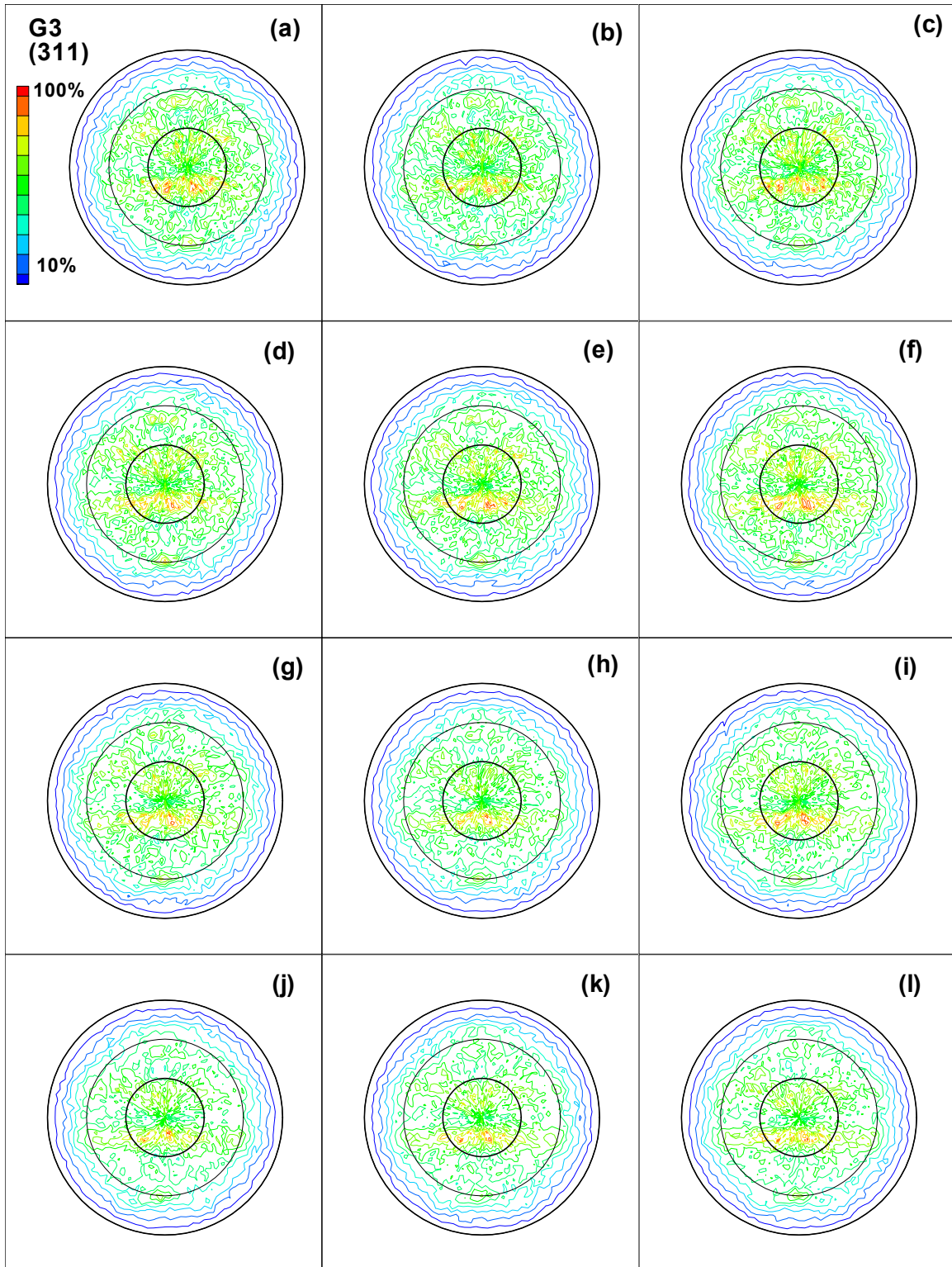


FIGURE B-81. DIRECT (311) POLE FIGURES FOR SPECIMEN G3 AFTER (a) 0, (b) 2,000, (c) 4,000, (d) 6,000, (e) 8,000, (f) 10,000, (g) 12,000, (h) 14,000, (i) 16,000, (j) 18,000, (k) 20,000, AND (l) 22,000 FATIGUE CYCLES

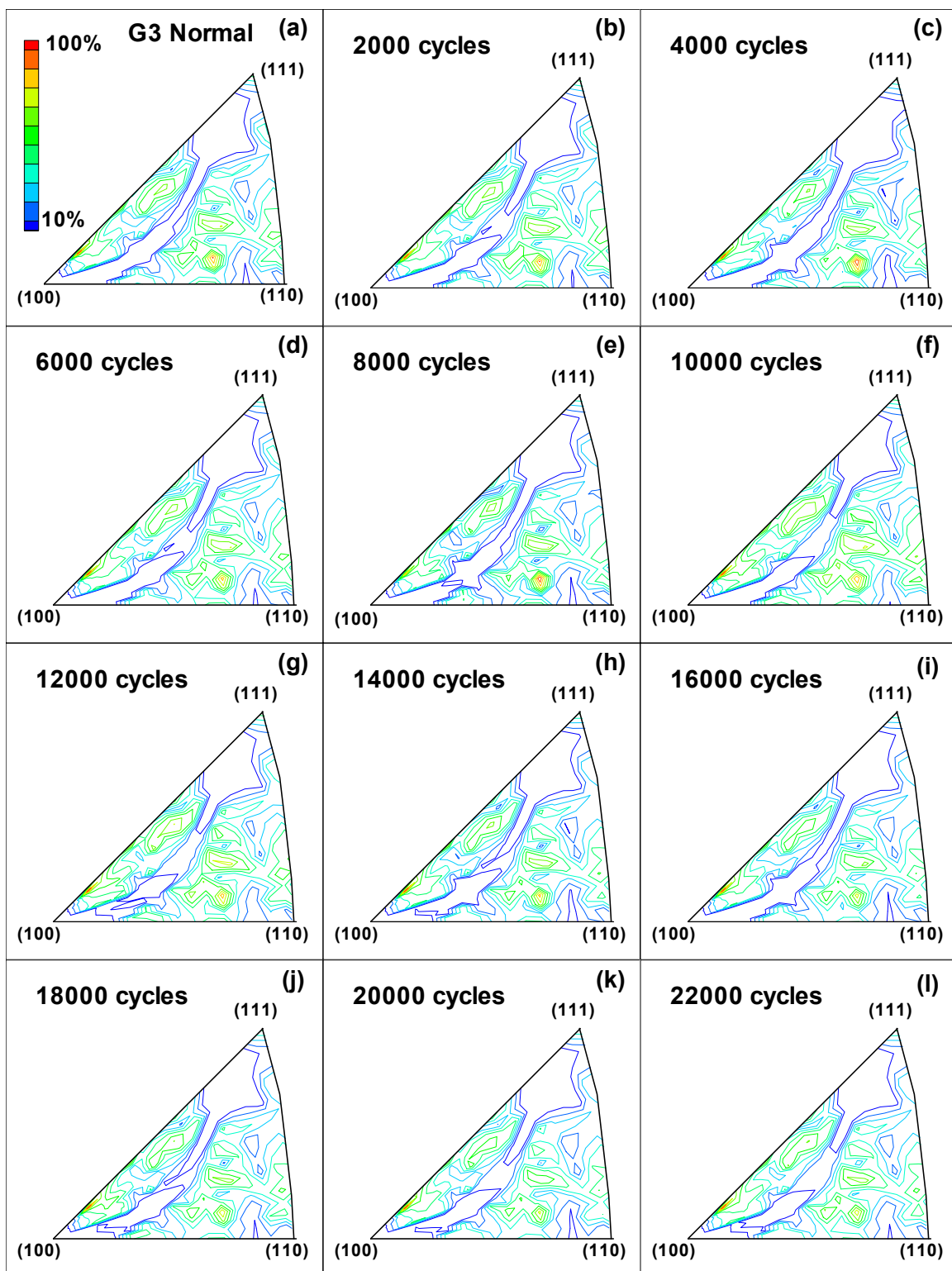


FIGURE B-82. INVERSE POLE FIGURES IN THE NORMAL DIRECTION FOR SPECIMEN G3 AFTER (a) 0, (b) 2,000, (c) 4,000, (d) 6,000, (e) 8,000, (f) 10,000, (g) 12,000, (h) 14,000, (i) 16,000, (j) 18,000, (k) 20,000, AND (l) 22,000 FATIGUE CYCLES



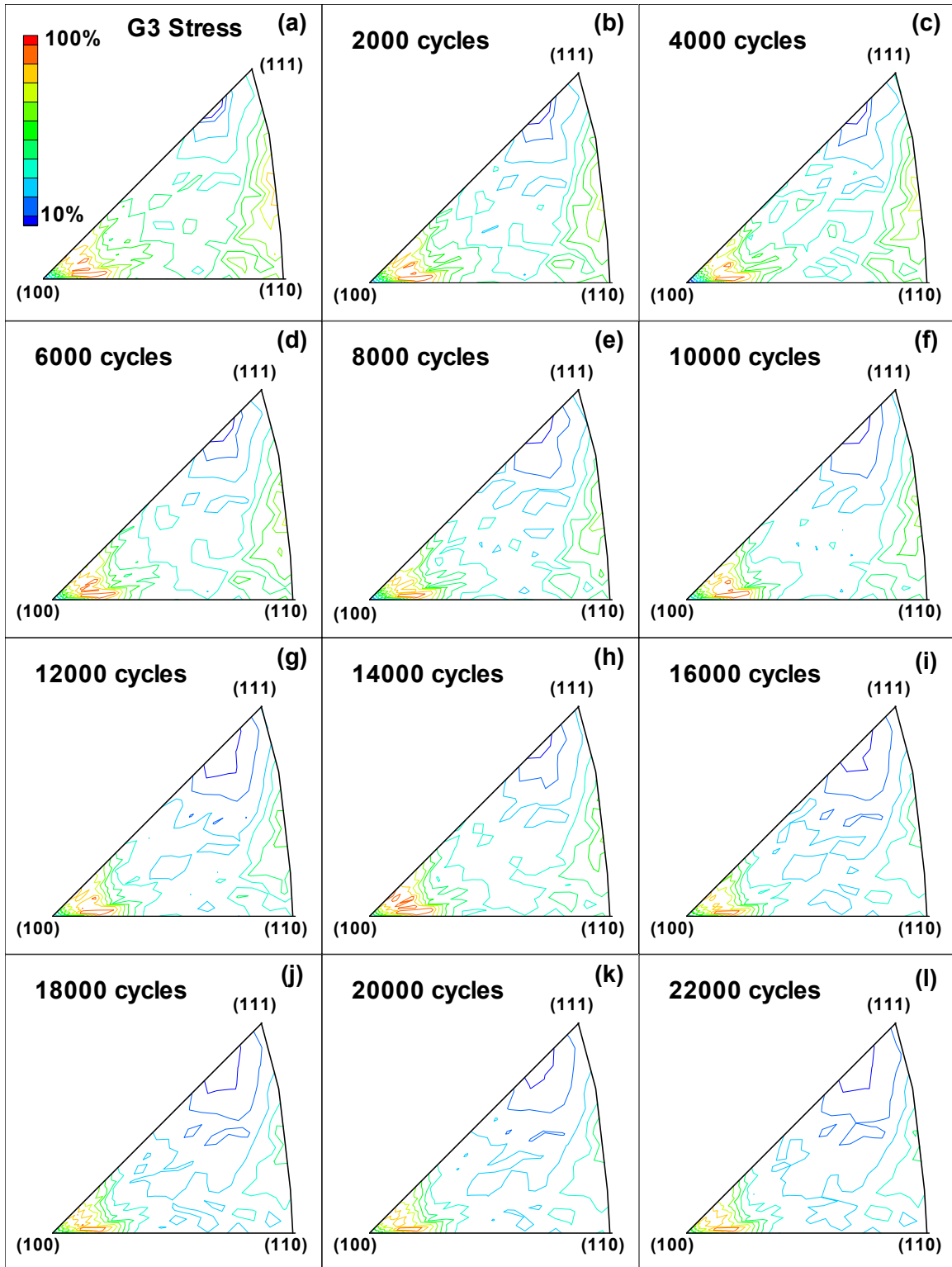


FIGURE B-83. INVERSE POLE FIGURES IN THE STRESS DIRECTION FOR SPECIMEN G3 AFTER (a) 0, (b) 2,000, (c) 4,000, (d) 6,000, (e) 8,000, (f) 10,000, (g) 12,000, (h) 14,000, (i) 16,000, (j) 18,000, (k) 20,000, AND (l) 22,000 FATIGUE CYCLES

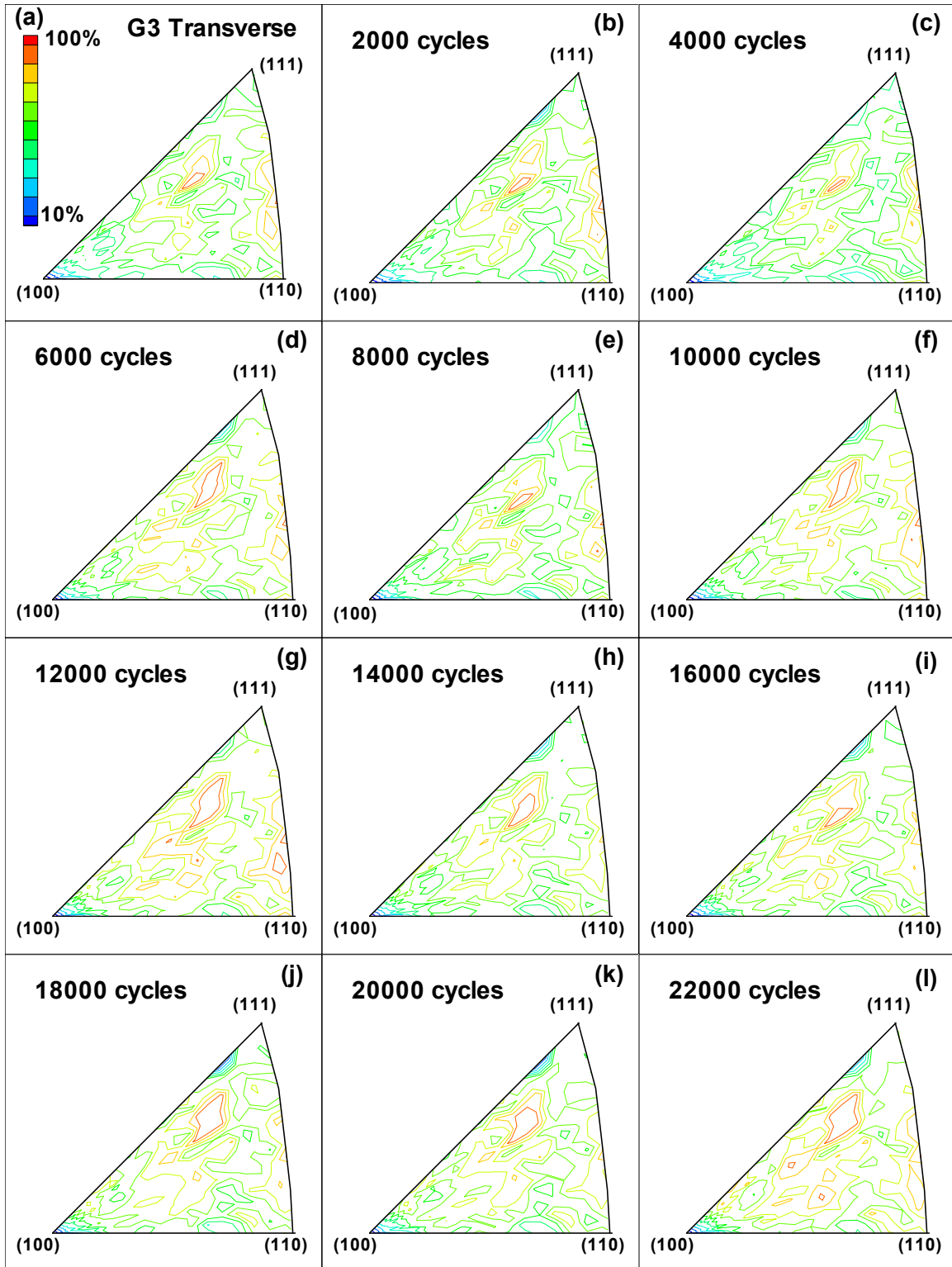


FIGURE B-84. INVERSE POLE FIGURES IN THE TRANSVERSE DIRECTION FOR SPECIMEN G3 AFTER (a) 0, (b) 2,000, (c) 4,000, (d) 6,000, (e) 8,000, (f) 10,000, (g) 12,000, (h) 14,000, (i) 16,000, (j) 18,000, (k) 20,000, AND (l) 22,000 FATIGUE CYCLES

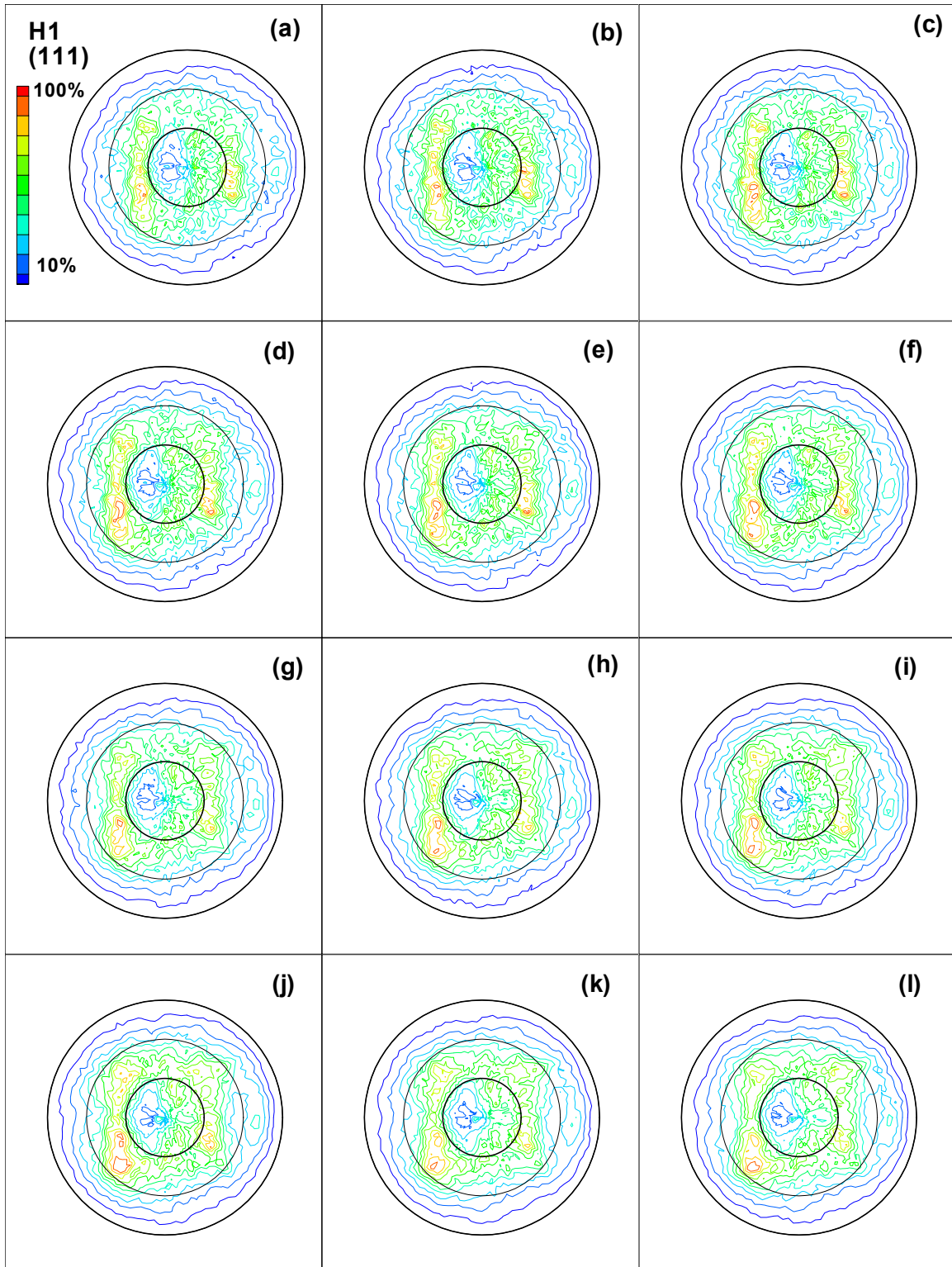


FIGURE B-85. DIRECT (111) POLE FIGURES FOR SPECIMEN H1 AFTER (a) 0, (b) 2,000, (c) 4,000, (d) 6,000, (e) 8,000, (f) 10,000, (g) 12,000, (h) 14,000, (i) 16,000, (j) 18,000, (k) 20,000, AND (l) 22,000 FATIGUE CYCLES

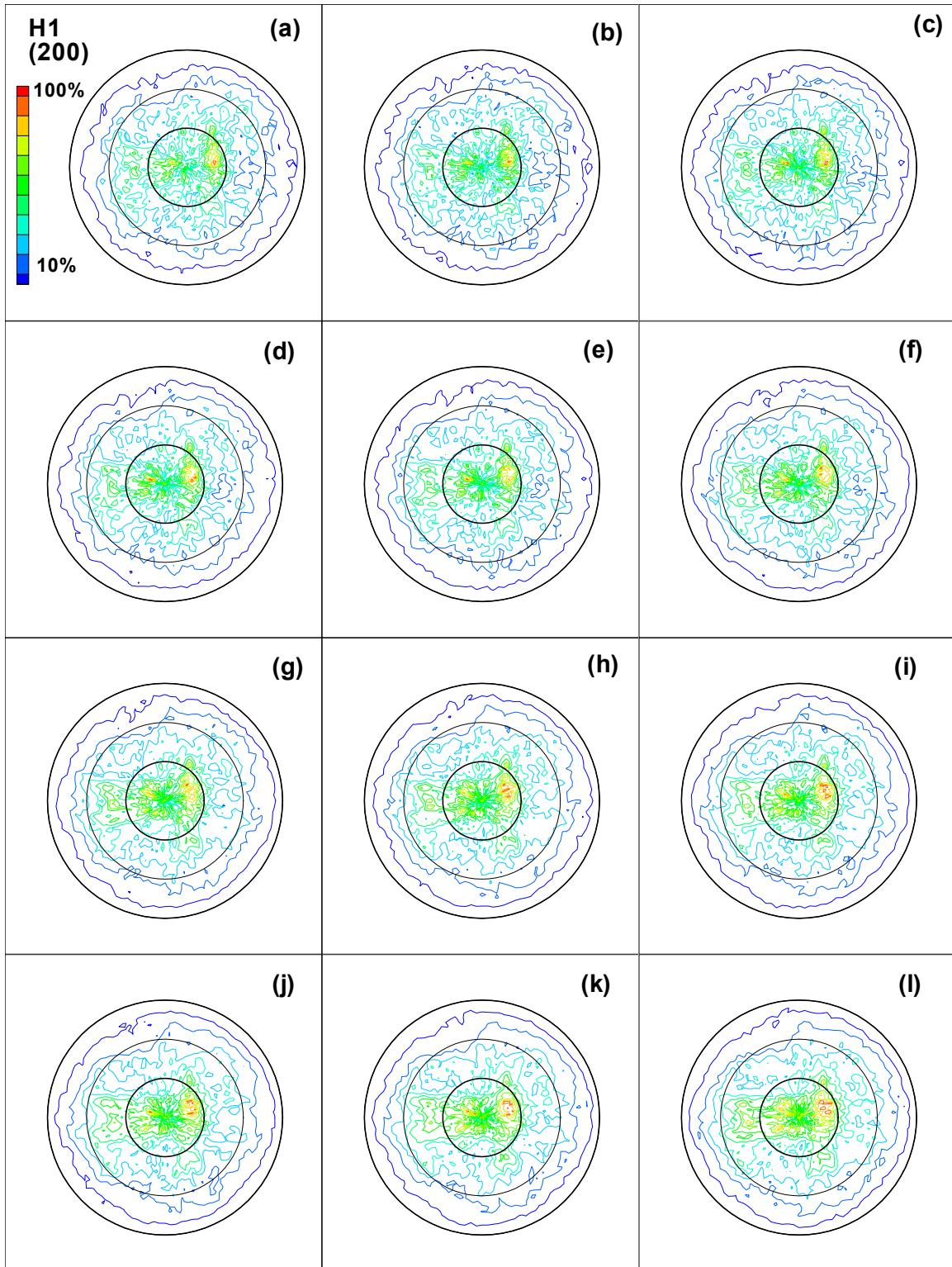


FIGURE B-86. DIRECT (200) POLE FIGURES FOR SPECIMEN H1 AFTER (a) 0, (b) 2,000, (c) 4,000, (d) 6,000, (e) 8,000, (f) 10,000, (g) 12,000, (h) 14,000, (i) 16,000, (j) 18,000, (k) 20,000, AND (l) 22,000 FATIGUE CYCLES

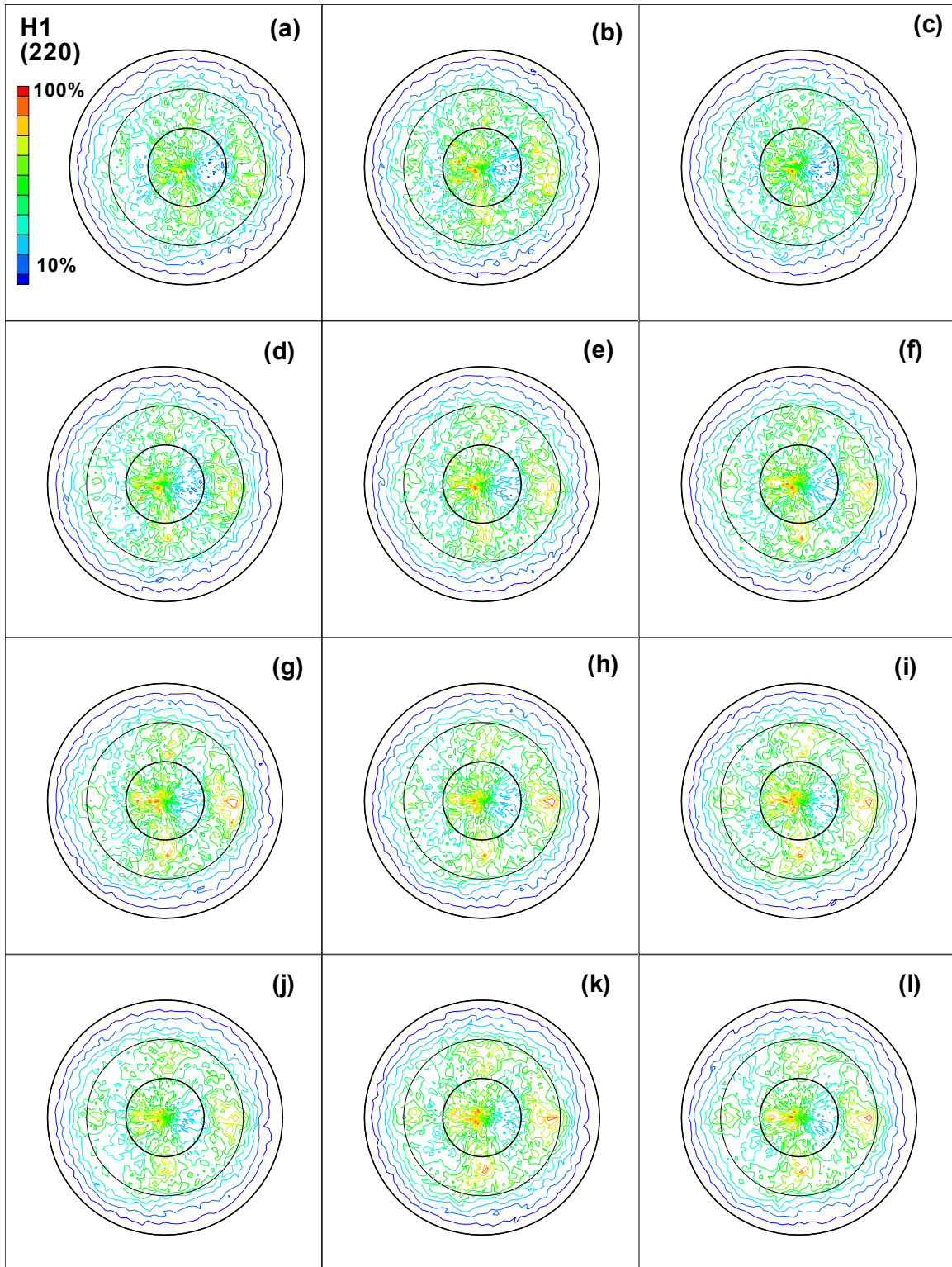


FIGURE B-87. DIRECT (220) POLE FIGURES FOR SPECIMEN H1 AFTER (a) 0, (b) 2,000, (c) 4,000, (d) 6,000, (e) 8,000, (f) 10,000, (g) 12,000, (h) 14,000, (i) 16,000, (j) 18,000, (k) 20,000, AND (l) 22,000 FATIGUE CYCLES



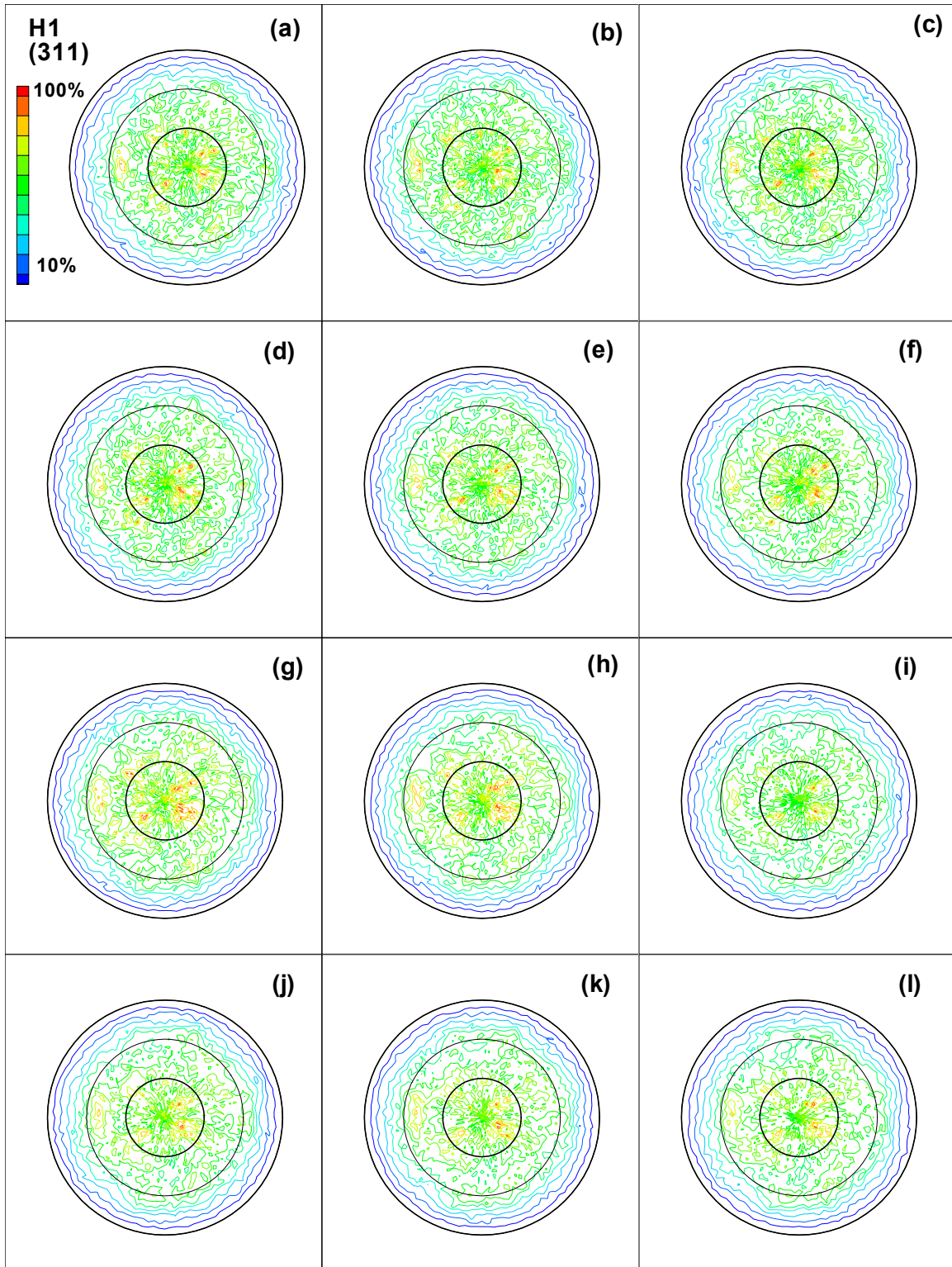


FIGURE B-88. DIRECT (311) POLE FIGURES FOR SPECIMEN H1 AFTER (a) 0, (b) 2,000, (c) 4,000, (d) 6,000, (e) 8,000, (f) 10,000, (g) 12,000, (h) 14,000, (i) 16,000, (j) 18,000, (k) 20,000, AND (l) 22,000 FATIGUE CYCLES

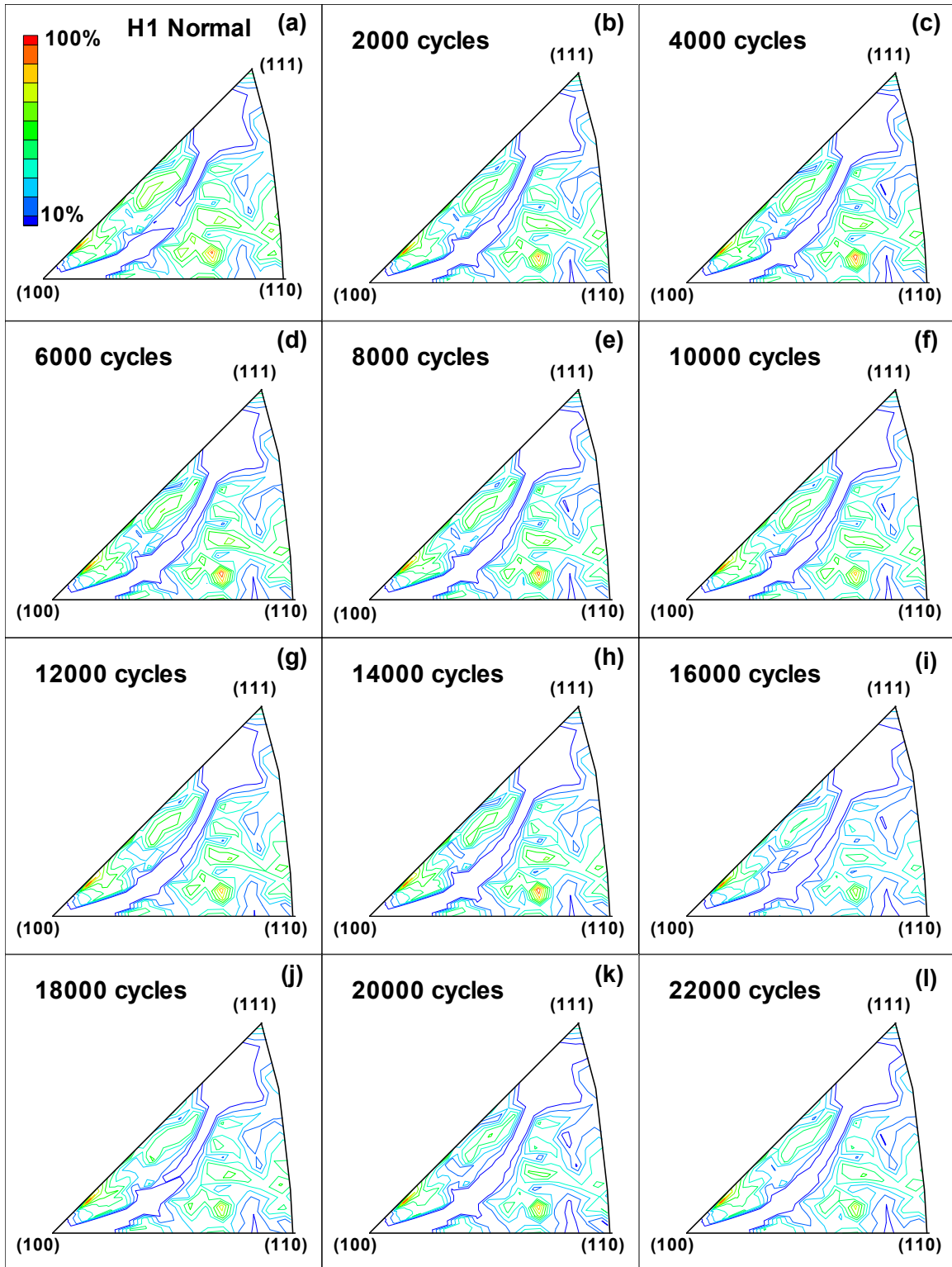


FIGURE B-89. INVERSE POLE FIGURES IN THE NORMAL DIRECTION FOR SPECIMEN H1 AFTER (a) 0, (b) 2,000, (c) 4,000, (d) 6,000, (e) 8,000, (f) 10,000, (g) 12,000, (h) 14,000, (i) 16,000, (j) 18,000, (k) 20,000, AND (l) 22,000 FATIGUE CYCLES



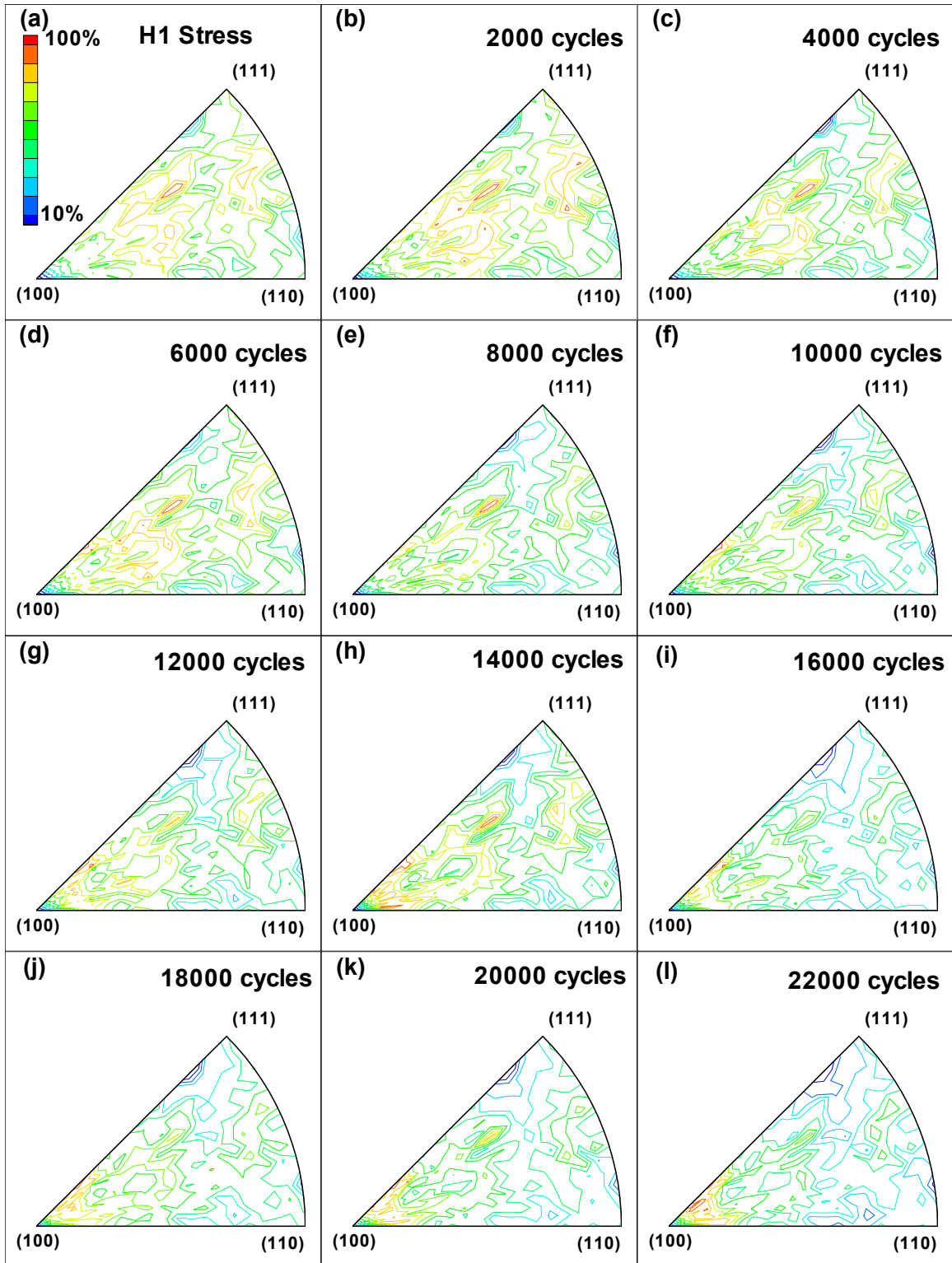


FIGURE B-90. INVERSE POLE FIGURES IN THE STRESS DIRECTION FOR SPECIMEN H1 AFTER (a) 0, (b) 2,000, (c) 4,000, (d) 6,000, (e) 8,000, (f) 10,000, (g) 12,000, (h) 14,000, (i) 16,000, (j) 18,000, (k) 20,000, AND (l) 22,000 FATIGUE CYCLES

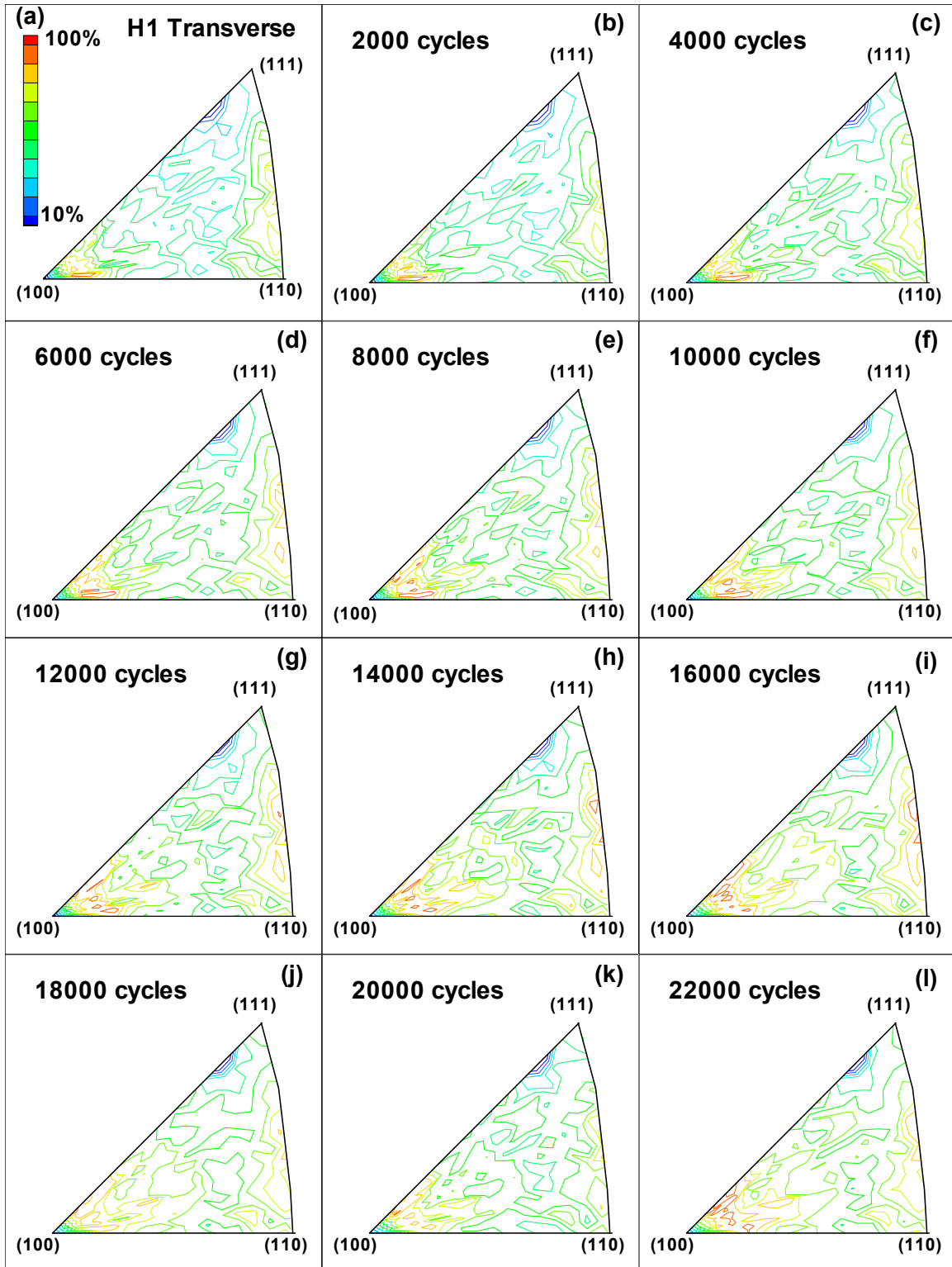


FIGURE B-91. INVERSE POLE FIGURES IN THE TRANSVERSE DIRECTION FOR SPECIMEN H1 AFTER (a) 0, (b) 2,000, (c) 4,000, (d) 6,000, (e) 8,000, (f) 10,000, (g) 12,000, (h) 14,000, (i) 16,000, (j) 18,000, (k) 20,000, AND (l) 22,000 FATIGUE CYCLES

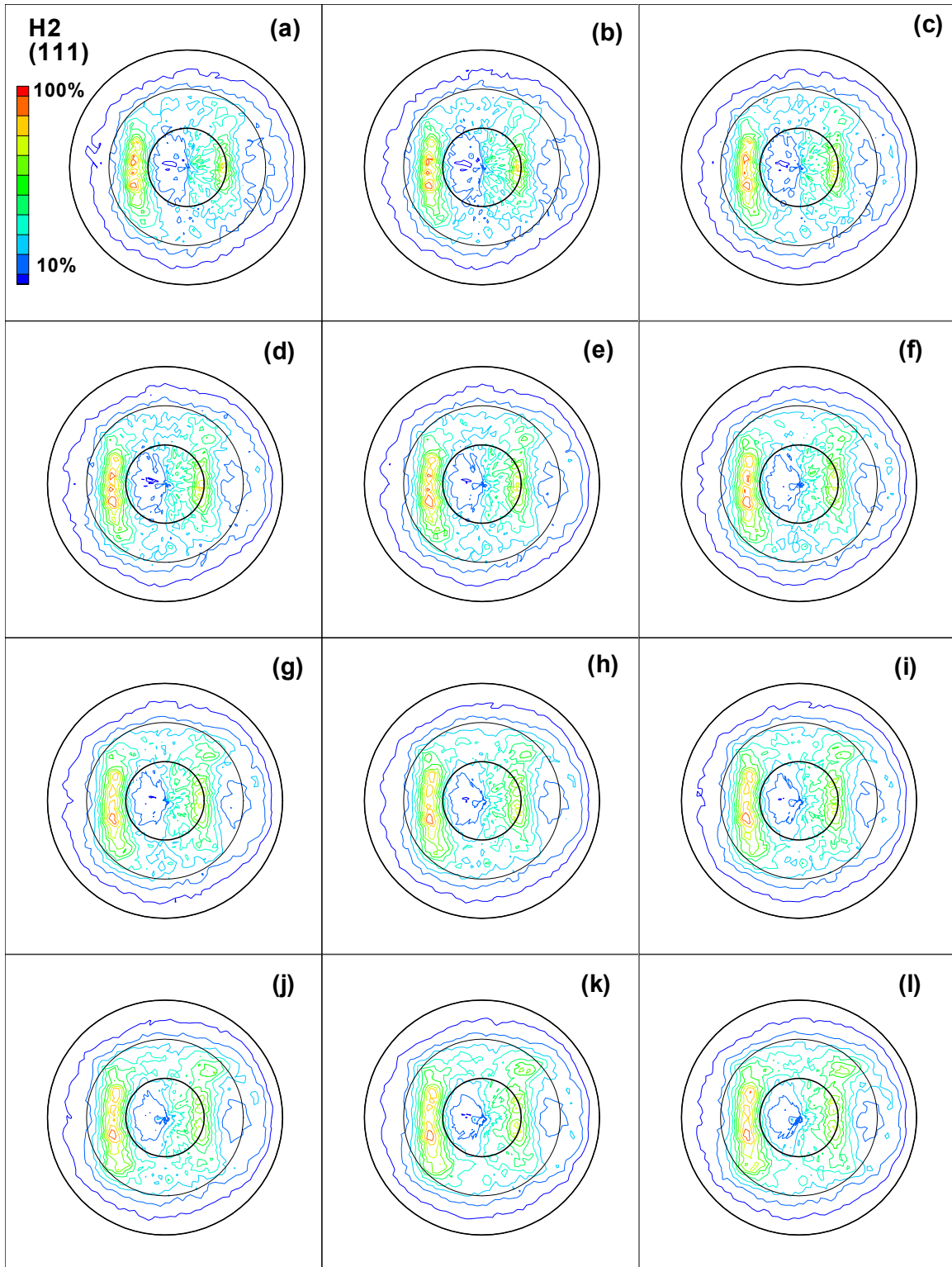


FIGURE B-92. DIRECT (111) POLE FIGURES FOR SPECIMEN H2 AFTER (a) 0, (b) 2,000, (c) 4,000, (d) 6,000, (e) 8,000, (f) 10,000, (g) 12,000, (h) 14,000, (i) 16,000, (j) 18,000, (k) 20,000, AND (l) 22,000 FATIGUE CYCLES

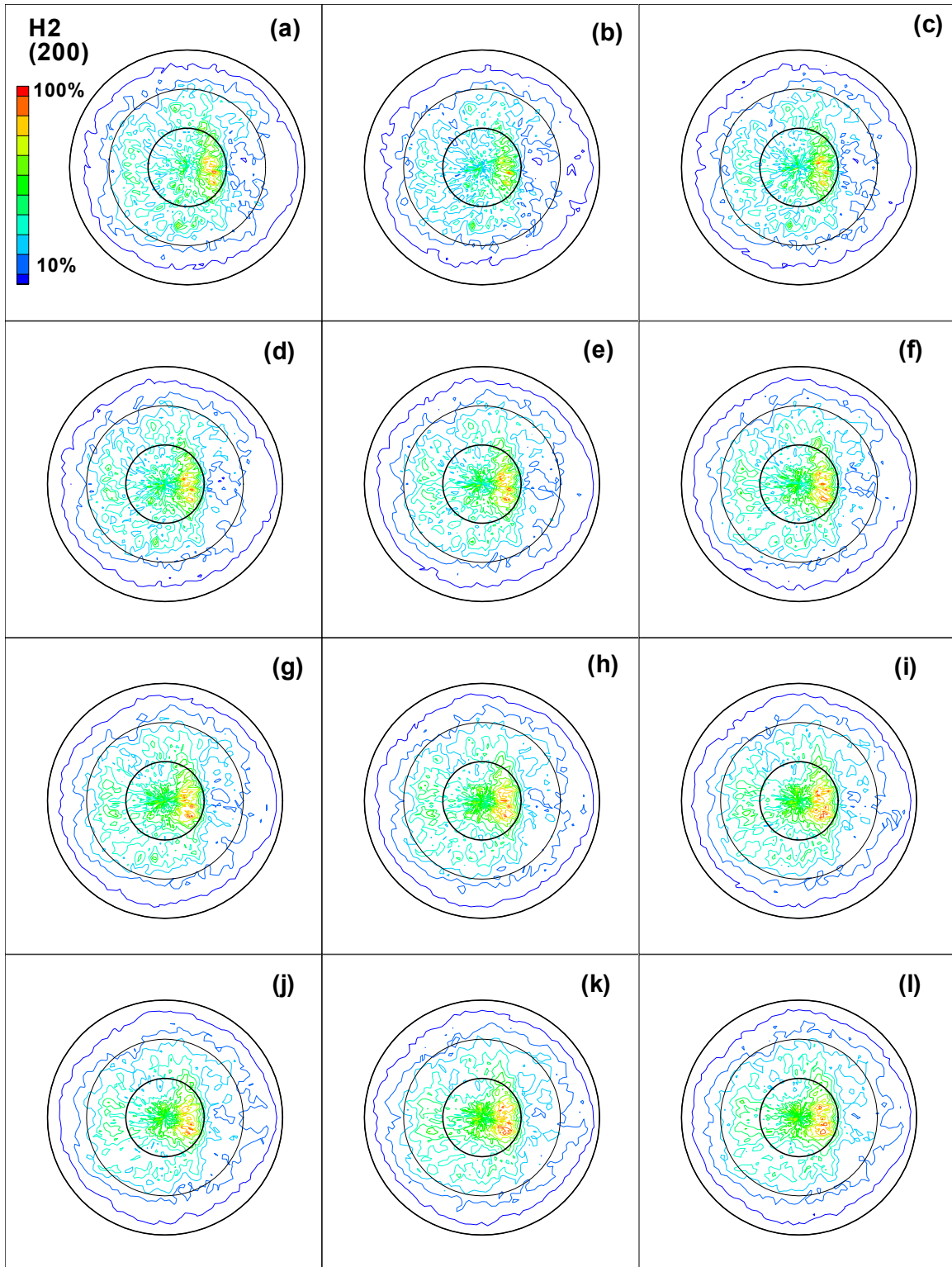


FIGURE B-93. DIRECT (200) POLE FIGURES FOR SPECIMEN H2 AFTER (a) 0, (b) 2,000, (c) 4,000, (d) 6,000, (e) 8,000, (f) 10,000, (g) 12,000, (h) 14,000, (i) 16,000, (j) 18,000, (k) 20,000, AND (l) 22,000 FATIGUE CYCLES

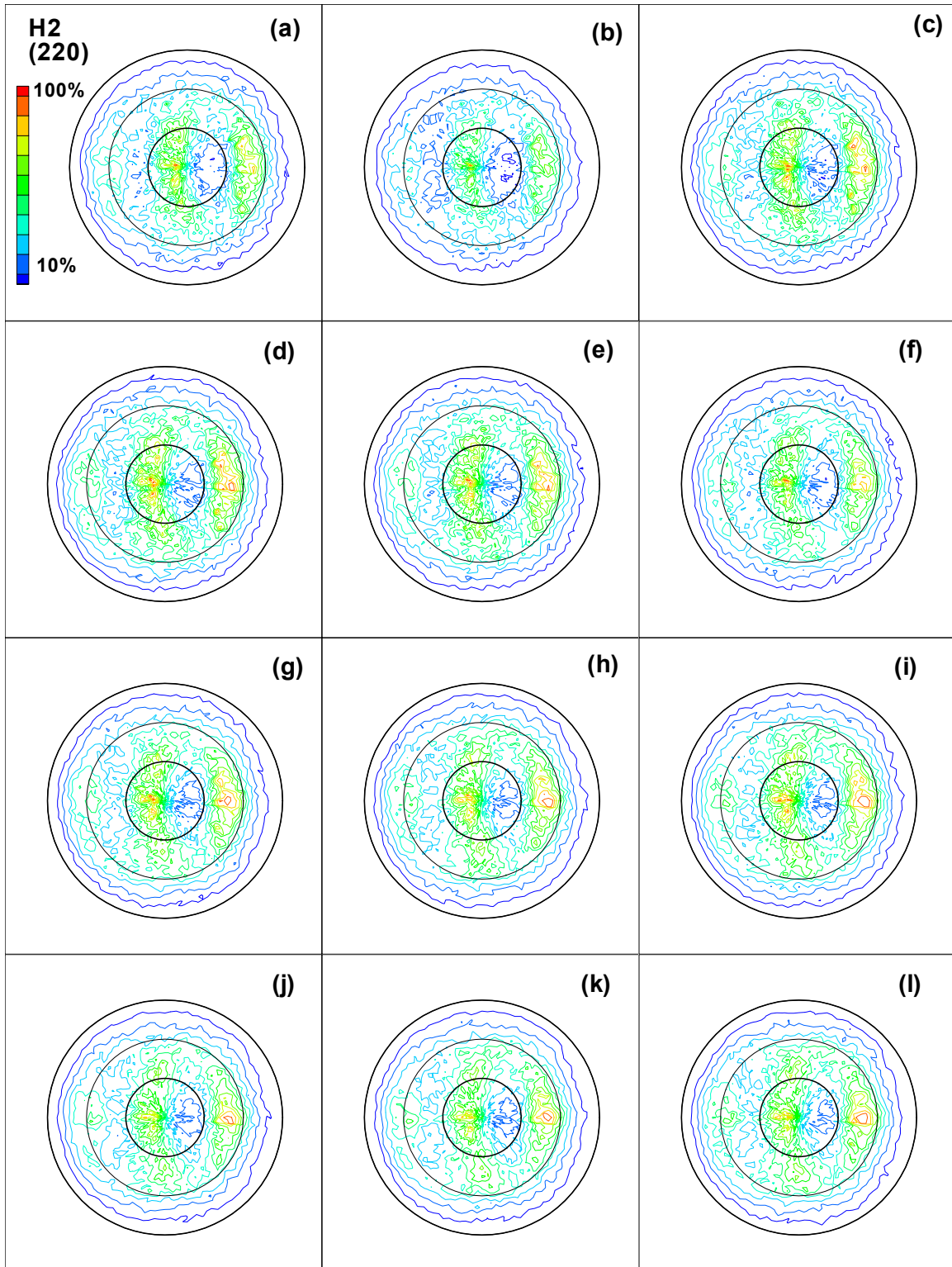


FIGURE B-94. DIRECT (220) POLE FIGURES FOR SPECIMEN H2 AFTER (a) 0, (b) 2,000, (c) 4,000, (d) 6,000, (e) 8,000, (f) 10,000, (g) 12,000, (h) 14,000, (i) 16,000, (j) 18,000, (k) 20,000, AND (l) 22,000 FATIGUE CYCLES



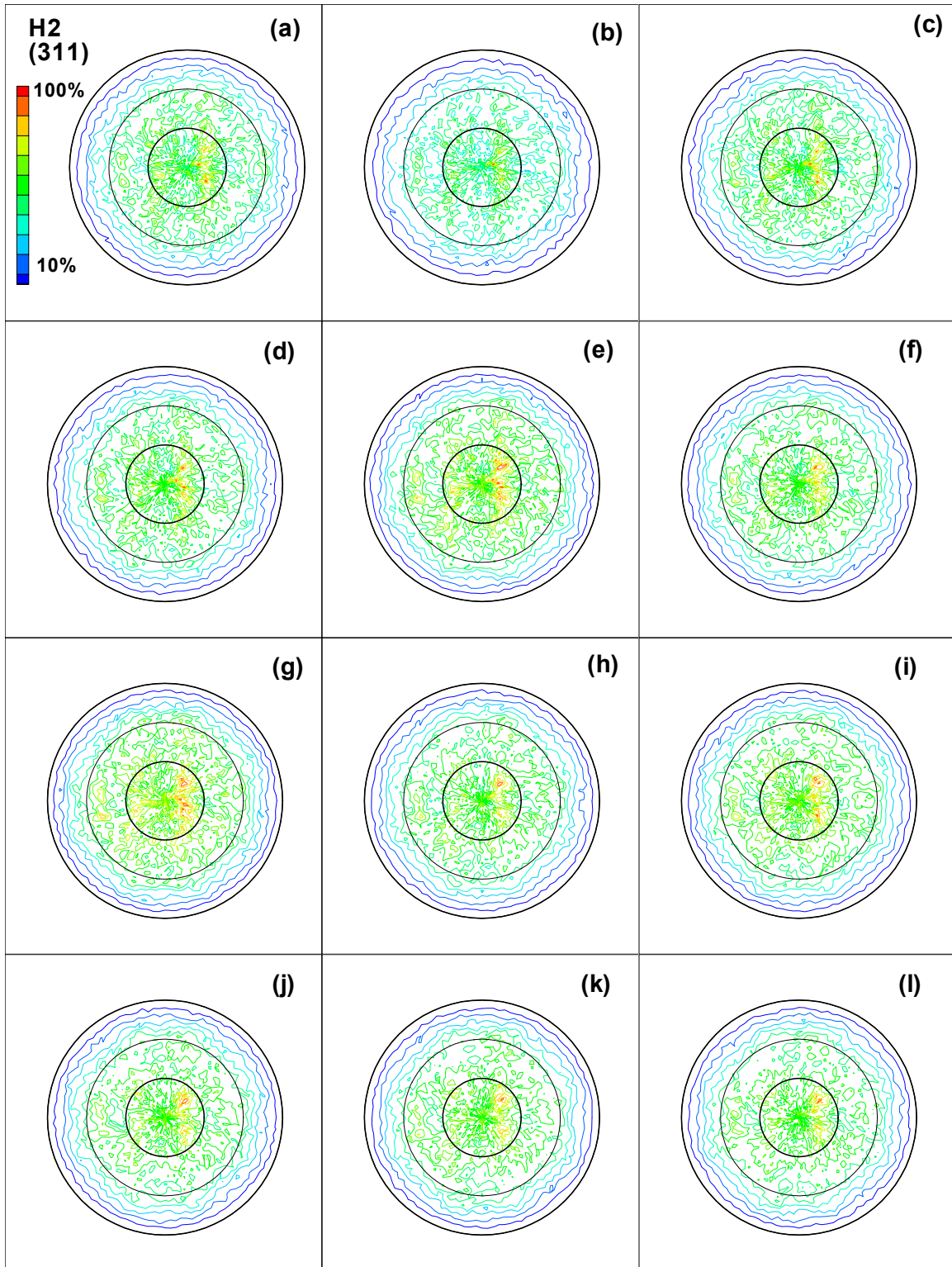


FIGURE B-95. DIRECT (311) POLE FIGURES FOR SPECIMEN H2 AFTER (a) 0, (b) 2,000, (c) 4,000, (d) 6,000, (e) 8,000, (f) 10,000, (g) 12,000, (h) 14,000, (i) 16,000, (j) 18,000, (k) 20,000, AND (l) 22,000 FATIGUE CYCLES

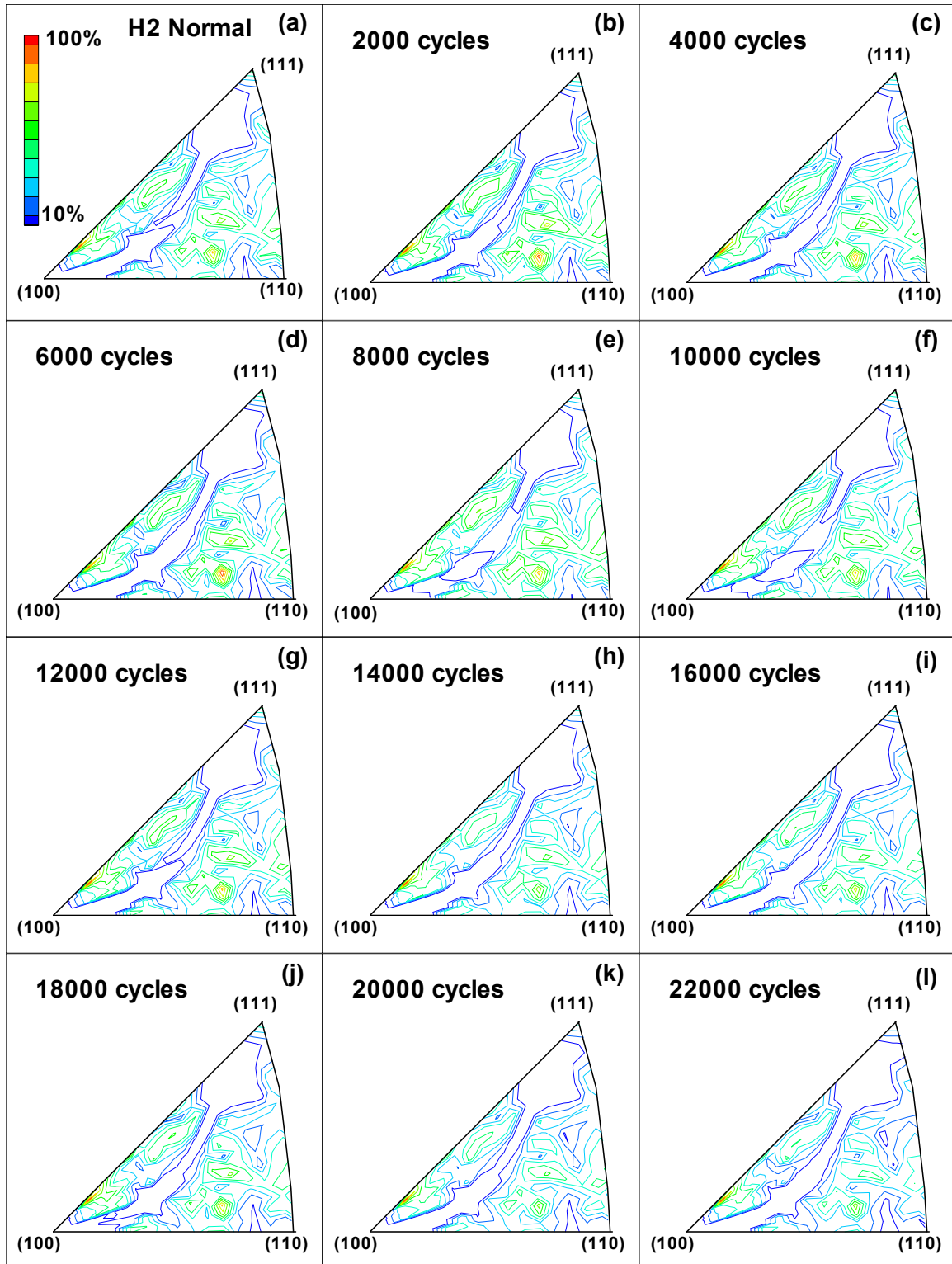


FIGURE B-96. INVERSE POLE FIGURES IN THE NORMAL DIRECTION FOR SPECIMEN H2 AFTER (a) 0, (b) 2,000, (c) 4,000, (d) 6,000, (e) 8,000, (f) 10,000, (g) 12,000, (h) 14,000, (i) 16,000, (j) 18,000, (k) 20,000, AND (l) 22,000 FATIGUE CYCLES



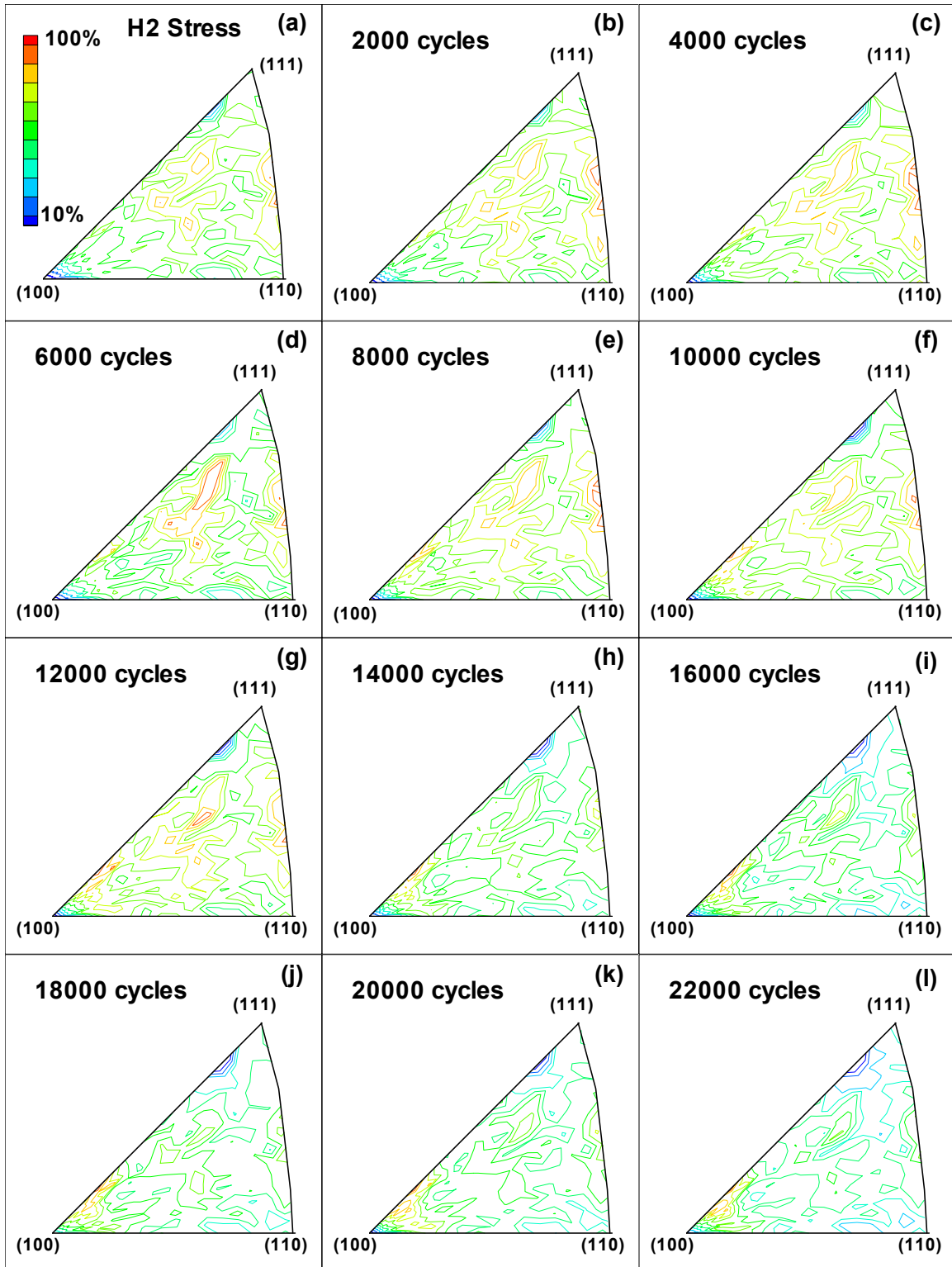


FIGURE B-97. INVERSE POLE FIGURES IN THE STRESS DIRECTION FOR SPECIMEN H2 AFTER (a) 0, (b) 2,000, (c) 4,000, (d) 6,000, (e) 8,000, (f) 10,000, (g) 12,000, (h) 14,000, (i) 16,000, (j) 18,000, (k) 20,000, AND (l) 22,000 FATIGUE CYCLES

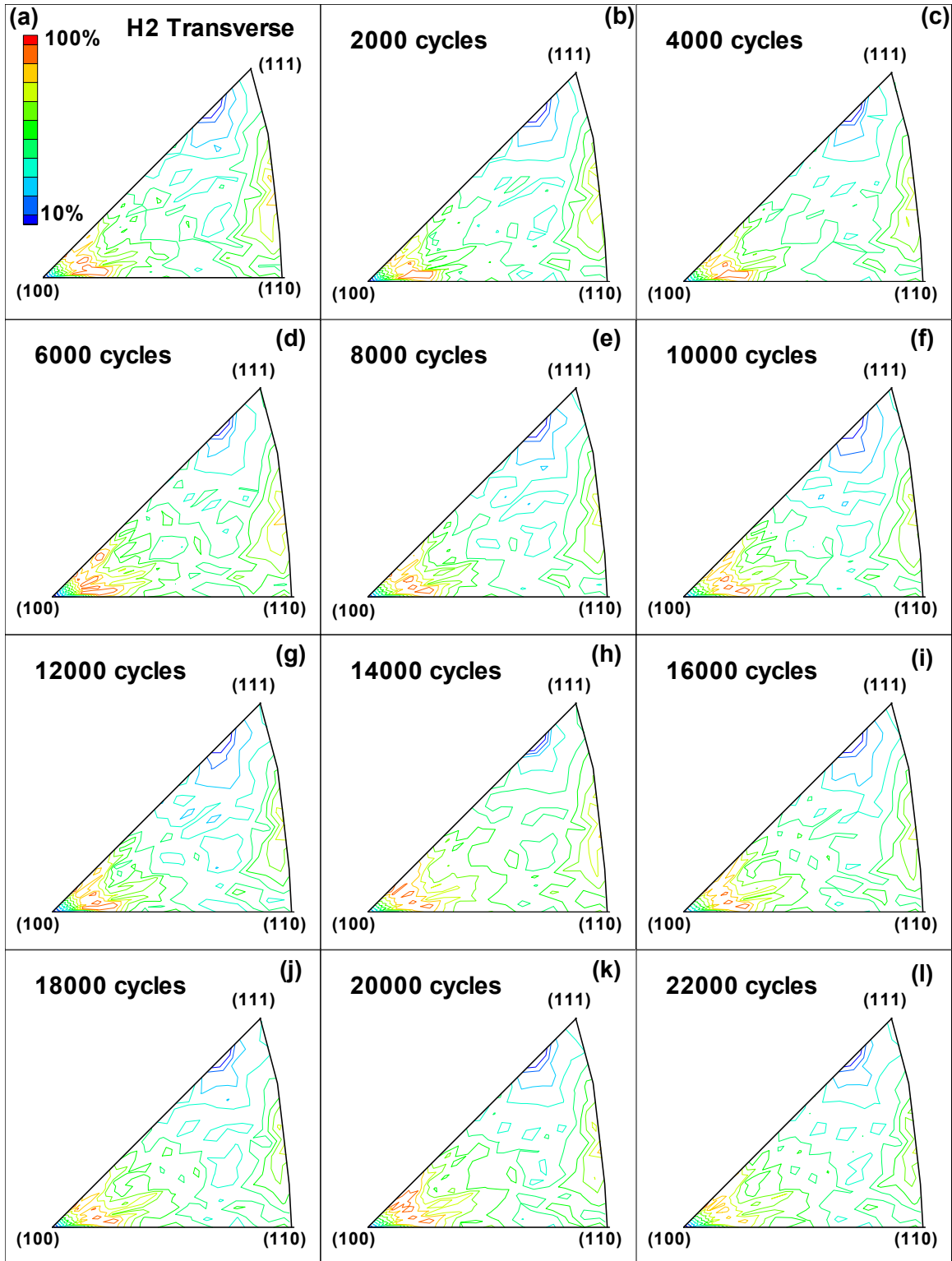


FIGURE B-98. INVERSE POLE FIGURES IN THE TRANSVERSE DIRECTION FOR SPECIMEN H2 AFTER (a) 0, (b) 2,000, (c) 4,000, (d) 6,000, (e) 8,000, (f) 10,000, (g) 12,000, (h) 14,000, (i) 16,000, (j) 18,000, (k) 20,000, AND (l) 22,000 FATIGUE CYCLES

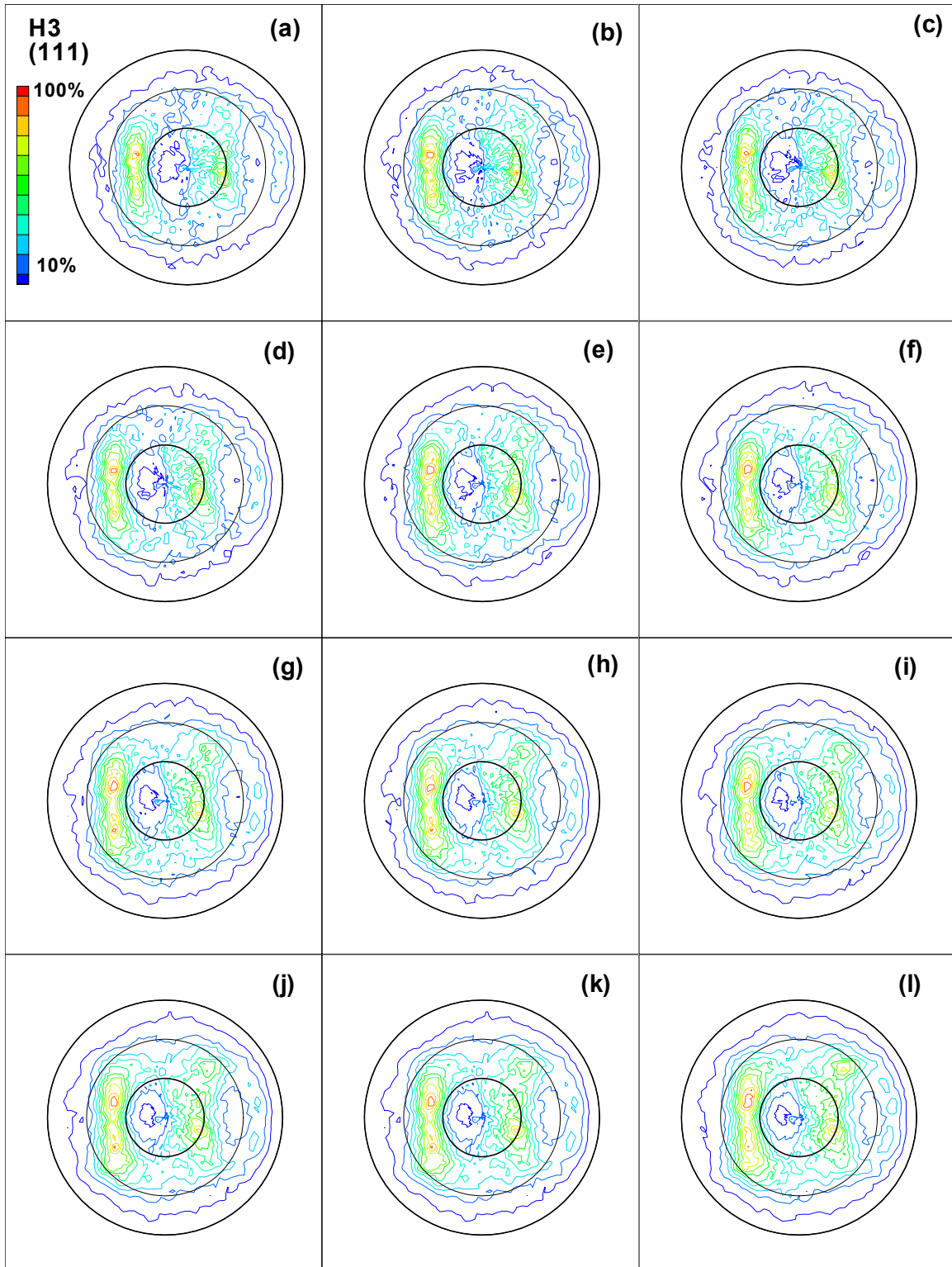


FIGURE B-99. DIRECT (111) POLE FIGURES FOR SPECIMEN H3 AFTER (a) 0, (b) 2,000, (c) 4,000, (d) 6,000, (e) 8,000, (f) 10,000, (g) 12,000, (h) 14,000, (i) 16,000, (j) 18,000, (k) 20,000, AND (l) 22,000 FATIGUE CYCLES

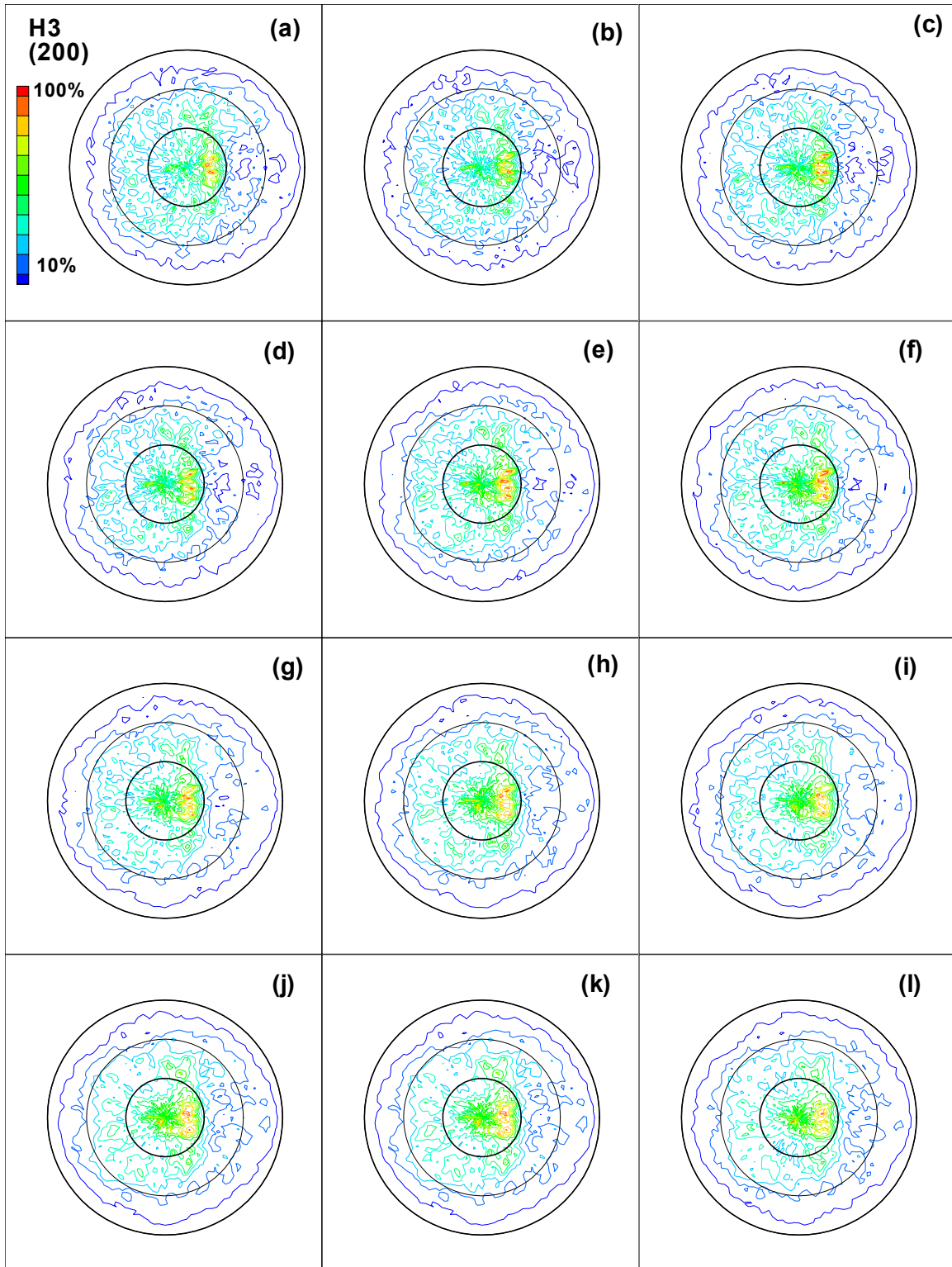


FIGURE B-100. DIRECT (200) POLE FIGURES FOR SPECIMEN H3 AFTER (a) 0, (b) 2,000, (c) 4,000, (d) 6,000, (e) 8,000, (f) 10,000, (g) 12,000, (h) 14,000, (i) 16,000, (j) 18,000, (k) 20,000, AND (l) 22,000 FATIGUE CYCLES

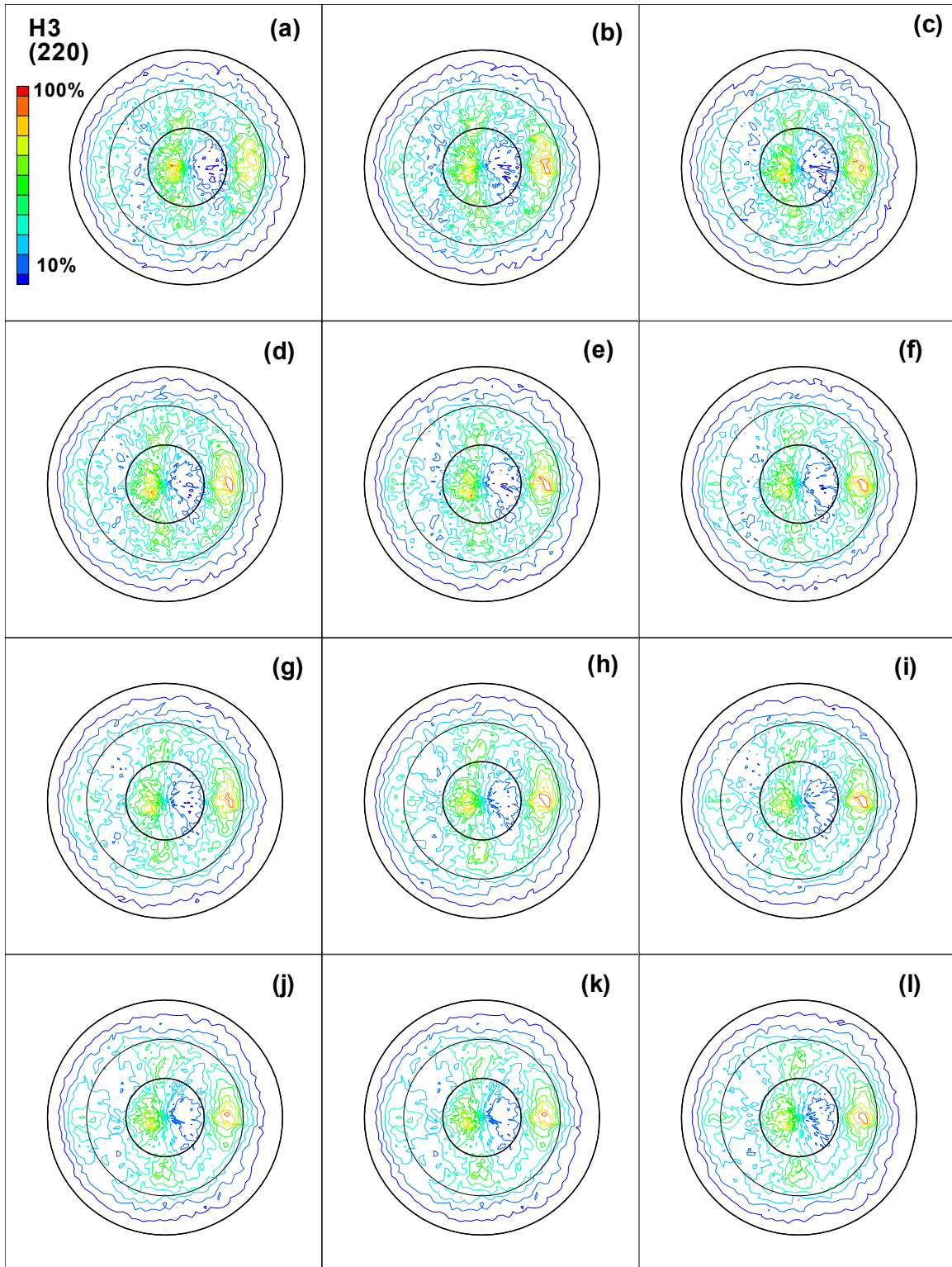


FIGURE B-101. DIRECT (220) POLE FIGURES FOR SPECIMEN H3 AFTER (a) 0, (b) 2,000, (c) 4,000, (d) 6,000, (e) 8,000, (f) 10,000, (g) 12,000, (h) 14,000, (i) 16,000, (j) 18,000, (k) 20,000, AND (l) 22,000 FATIGUE CYCLES



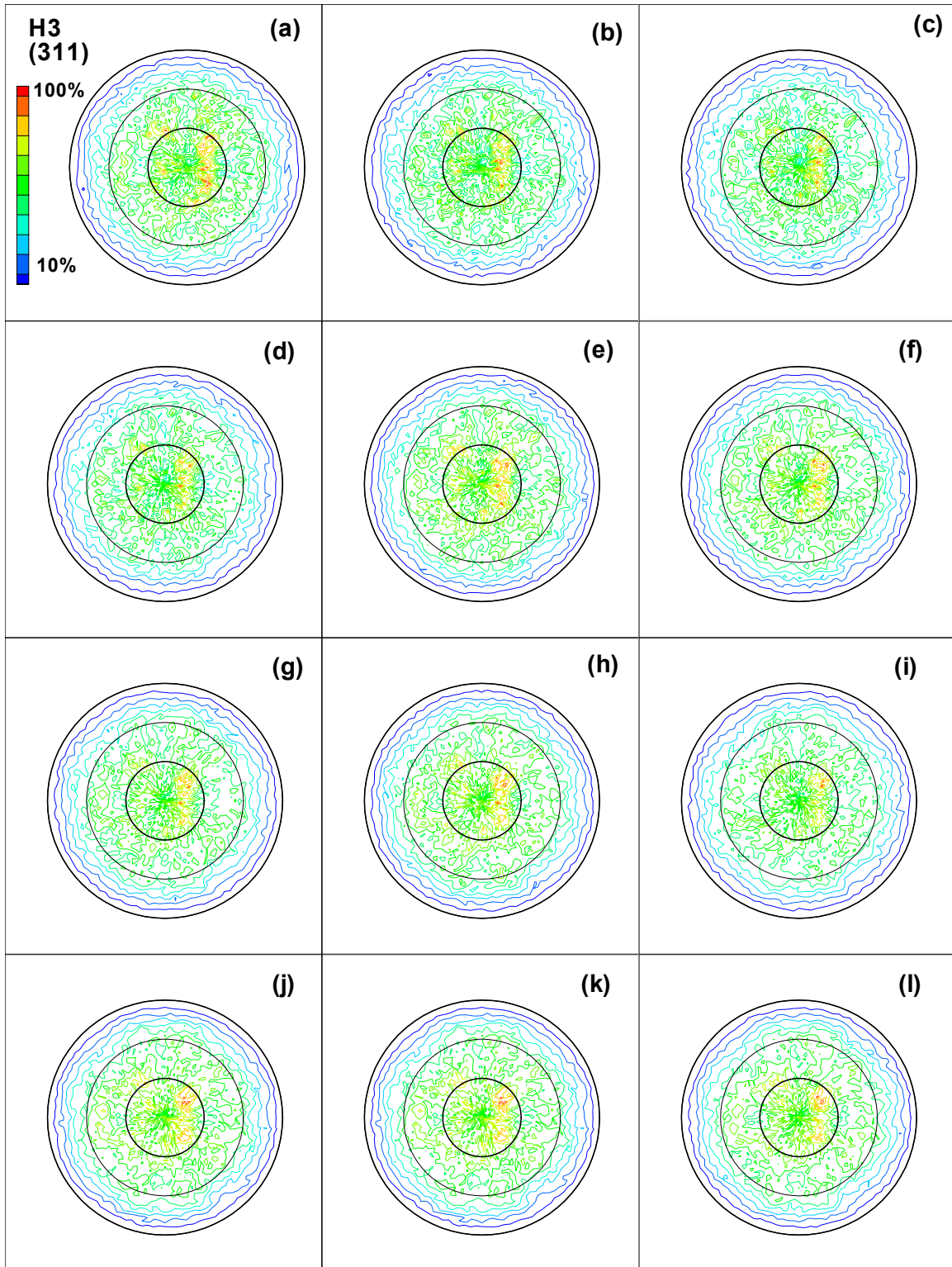


FIGURE B-102. DIRECT (311) POLE FIGURES FOR SPECIMEN H3 AFTER (a) 0, (b) 2,000, (c) 4,000, (d) 6,000, (e) 8,000, (f) 10,000, (g) 12,000, (h) 14,000, (i) 16,000, (j) 18,000, (k) 20,000, AND (l) 22,000 FATIGUE CYCLES

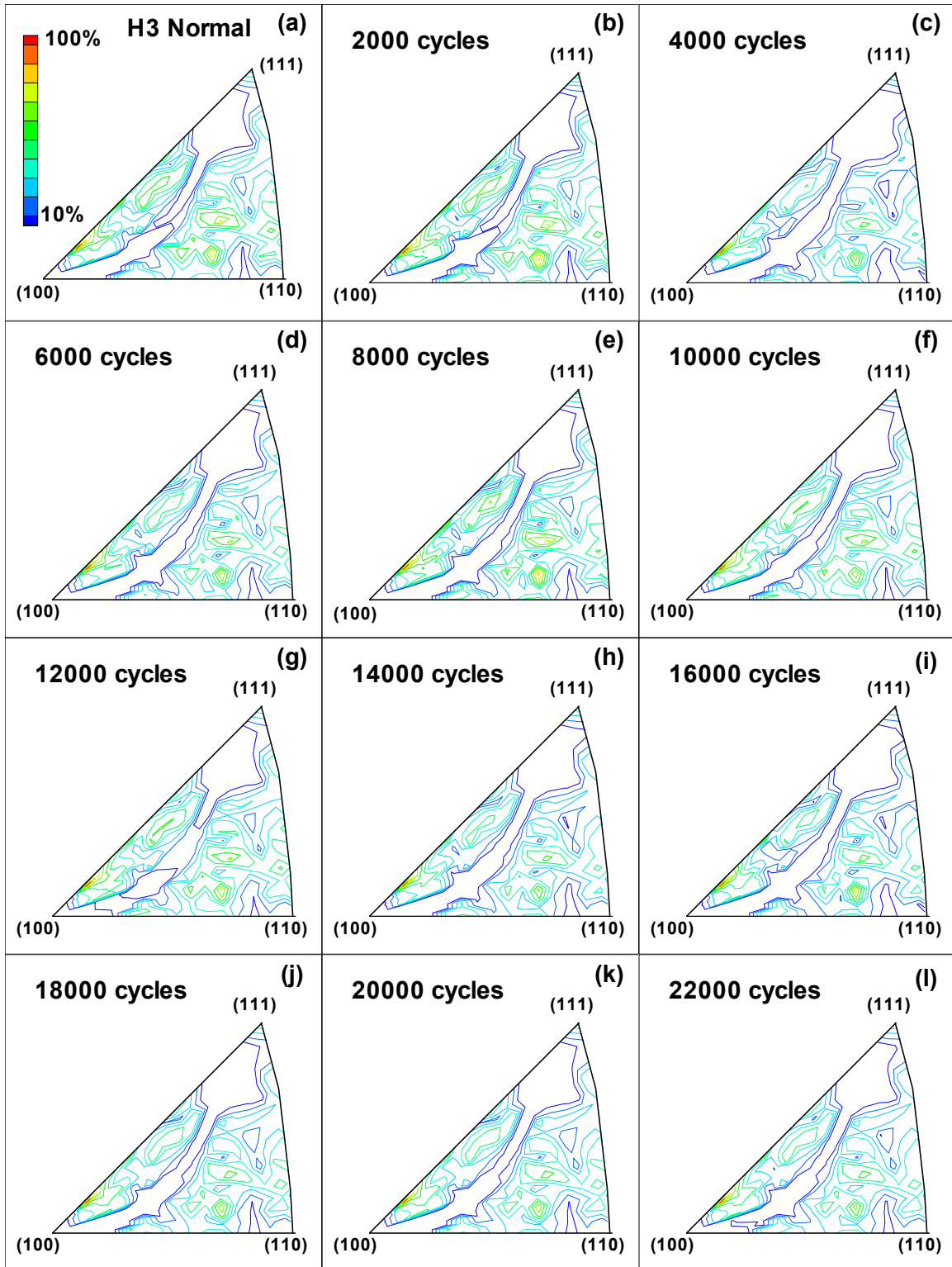


FIGURE B-103. INVERSE POLE FIGURES IN THE NORMAL DIRECTION FOR SPECIMEN H3 AFTER (a) 0, (b) 2,000, (c) 4,000, (d) 6,000, (e) 8,000, (f) 10,000, (g) 12,000, (h) 14,000, (i) 16,000, (j) 18,000, (k) 20,000, AND (l) 22,000 FATIGUE CYCLES



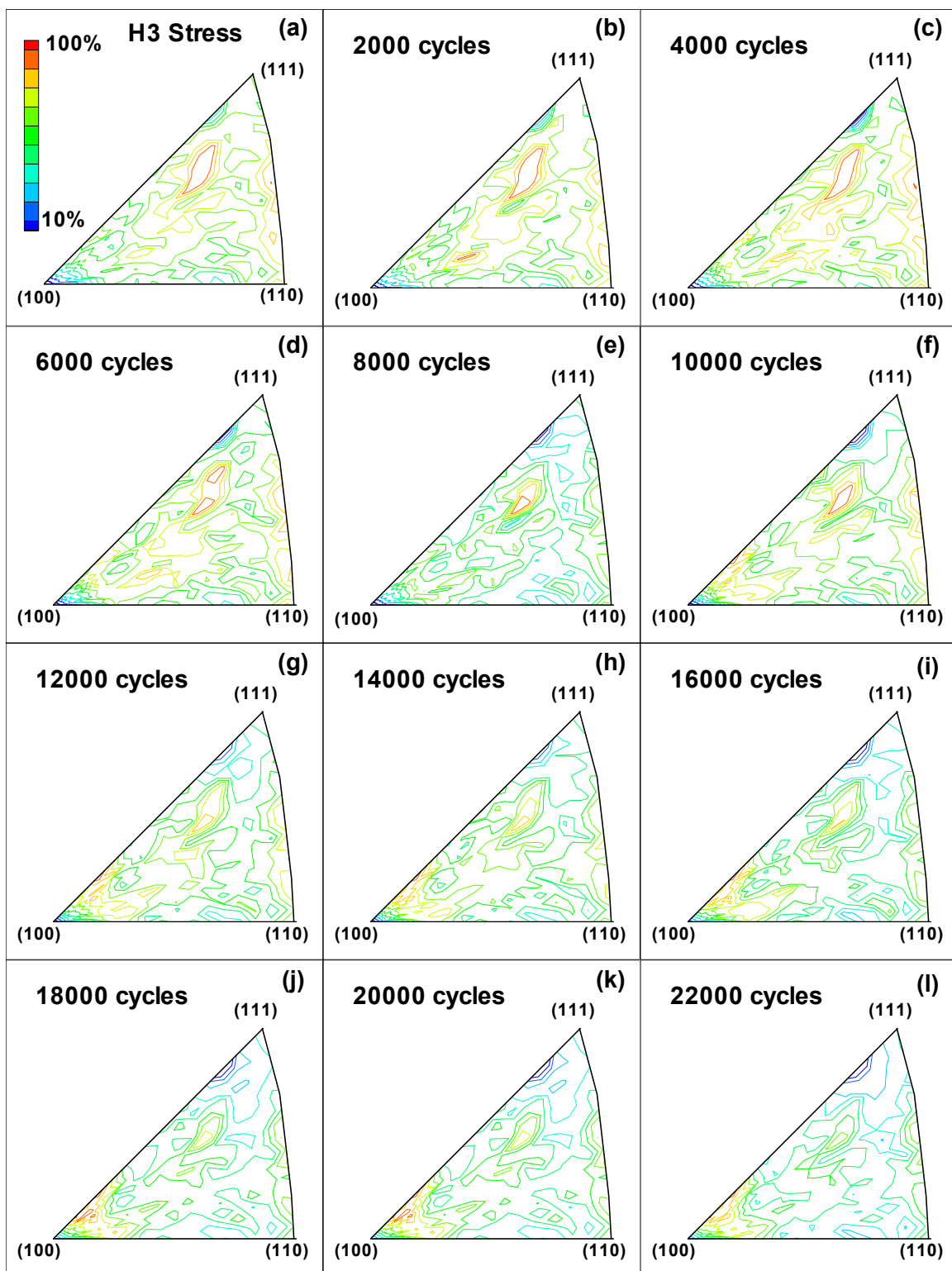


FIGURE B-104. INVERSE POLE FIGURES IN THE STRESS DIRECTION FOR SPECIMEN H3 AFTER (a) 0, (b) 2,000, (c) 4,000, (d) 6,000, (e) 8,000, (f) 10,000, (g) 12,000, (h) 14,000, (i) 16,000, (j) 18,000, (k) 20,000, AND (l) 22,000 FATIGUE CYCLES

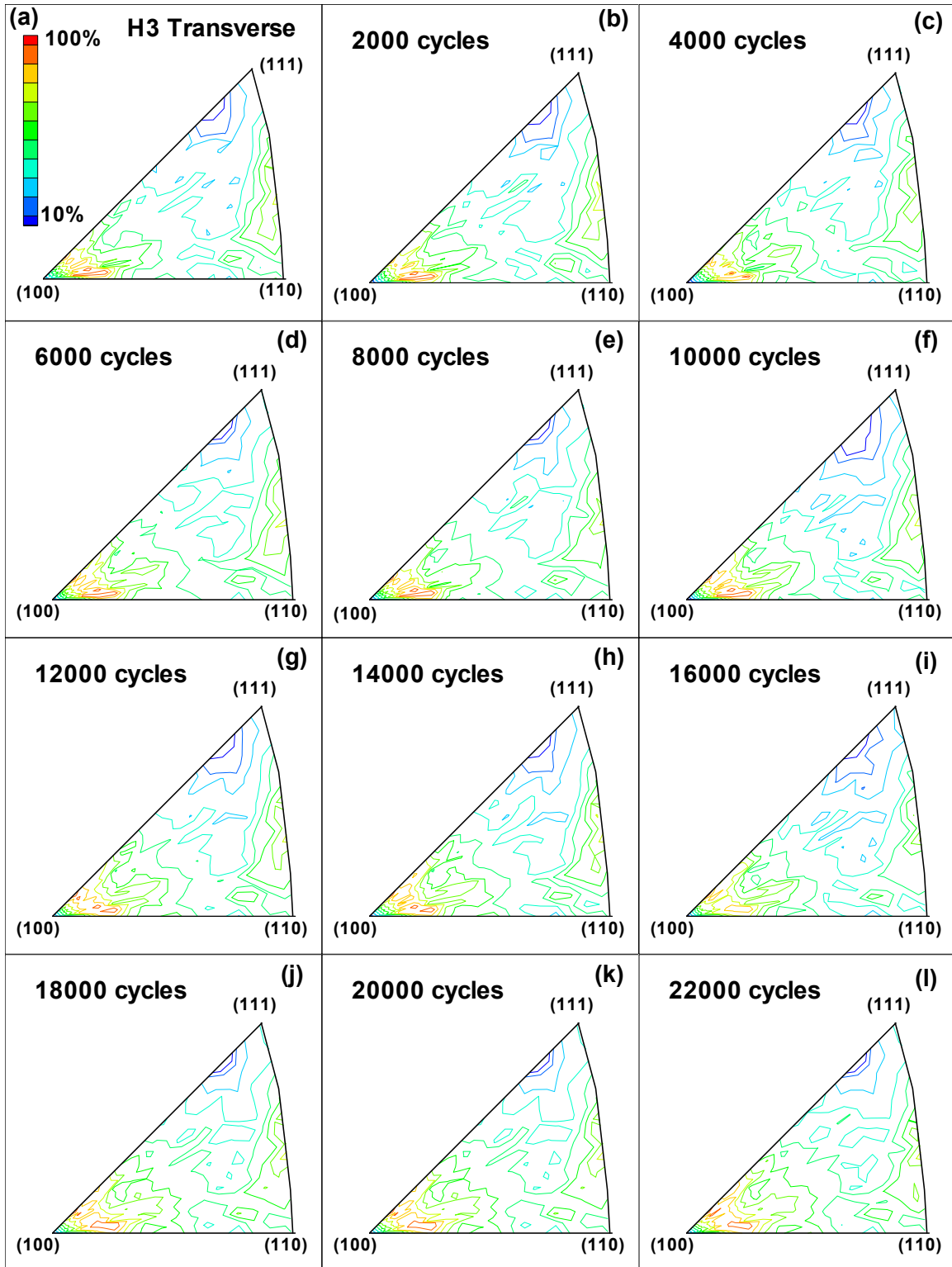


FIGURE B-105. INVERSE POLE FIGURES IN THE TRANSVERSE DIRECTION FOR SPECIMEN H3 AFTER (a) 0, (b) 2,000, (c) 4,000, (d) 6,000, (e) 8,000, (f) 10,000, (g) 12,000, (h) 14,000, (i) 16,000, (j) 18,000, (k) 20,000, AND (l) 22,000 FATIGUE CYCLES

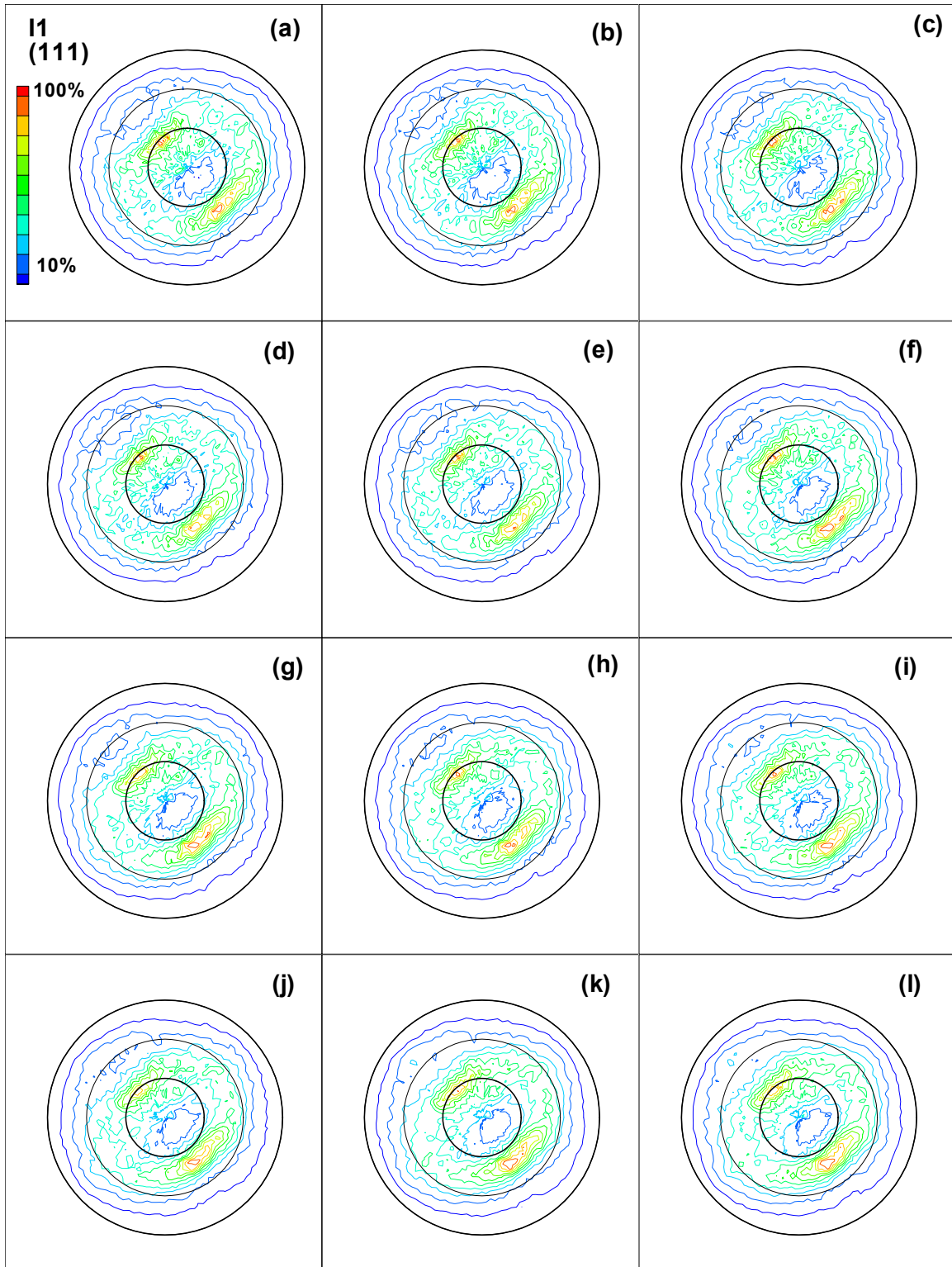


FIGURE B-106. DIRECT (111) POLE FIGURES FOR SPECIMEN I1 AFTER (a) 0, (b) 2,000, (c) 4,000, (d) 6,000, (e) 8,000, (f) 10,000, (g) 12,000, (h) 14,000, (i) 16,000, (j) 18,000, (k) 20,000, AND (l) 22,000 FATIGUE CYCLES

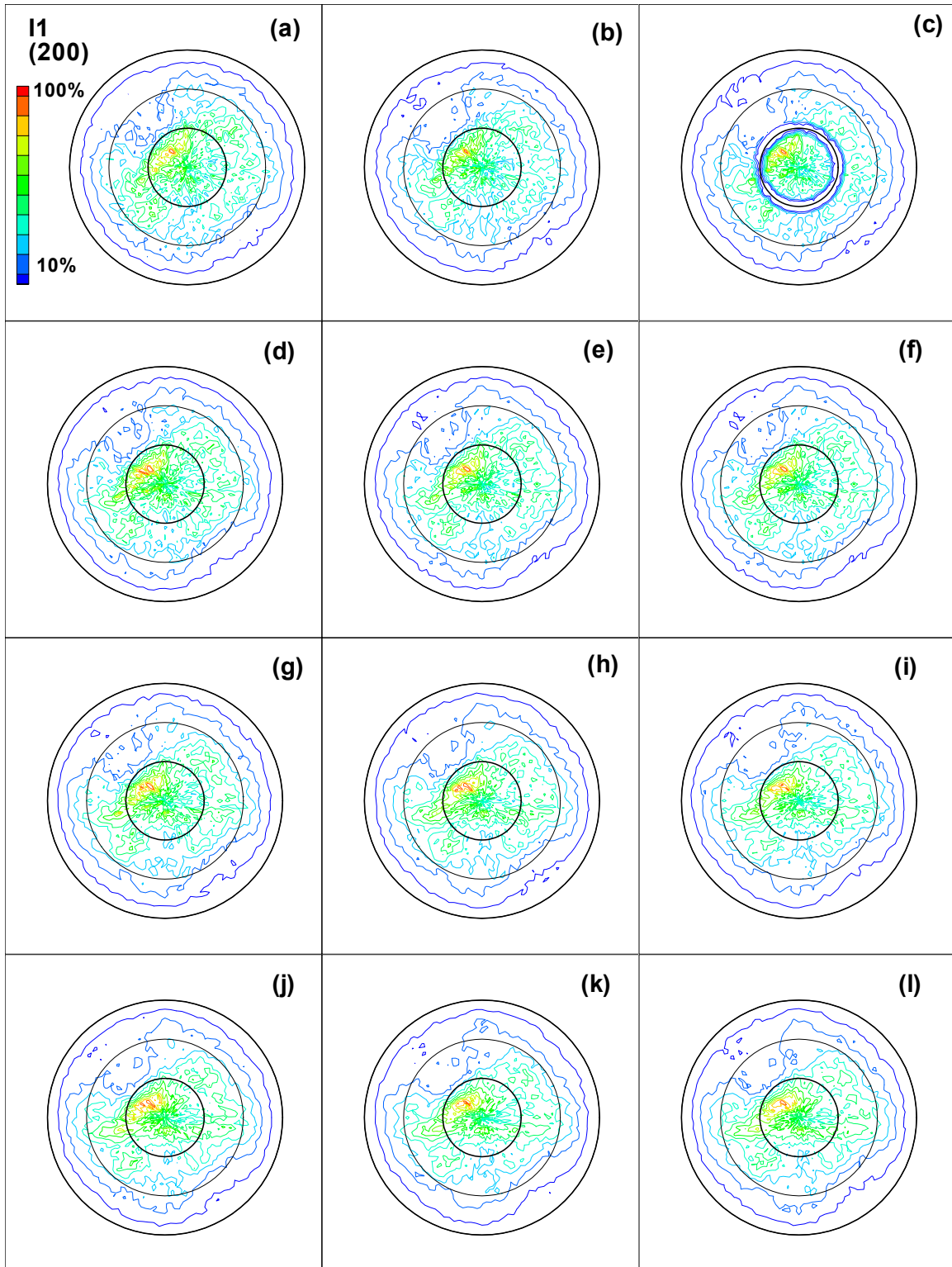


FIGURE B-107. DIRECT (200) POLE FIGURES FOR SPECIMEN I1 AFTER (a) 0, (b) 2,000, (c) 4,000, (d) 6,000, (e) 8,000, (f) 10,000, (g) 12,000, (h) 14,000, (i) 16,000, (j) 18,000, (k) 20,000, AND (l) 22,000 FATIGUE CYCLES

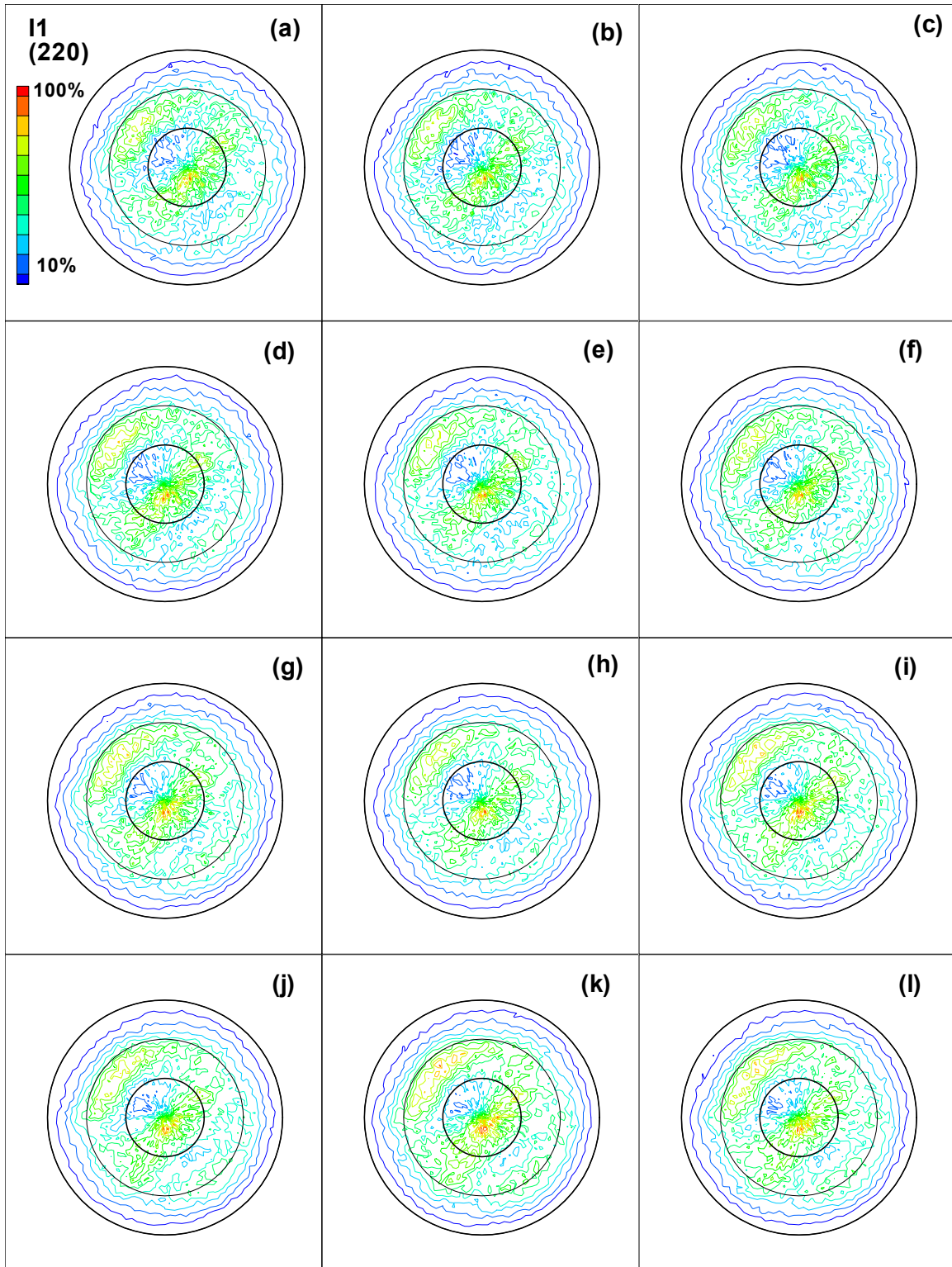


FIGURE B-108. DIRECT (220) POLE FIGURES FOR SPECIMEN I1 AFTER (a) 0, (b) 2,000, (c) 4,000, (d) 6,000, (e) 8,000, (f) 10,000, (g) 12,000, (h) 14,000, (i) 16,000, (j) 18,000, (k) 20,000, AND (l) 22,000 FATIGUE CYCLES



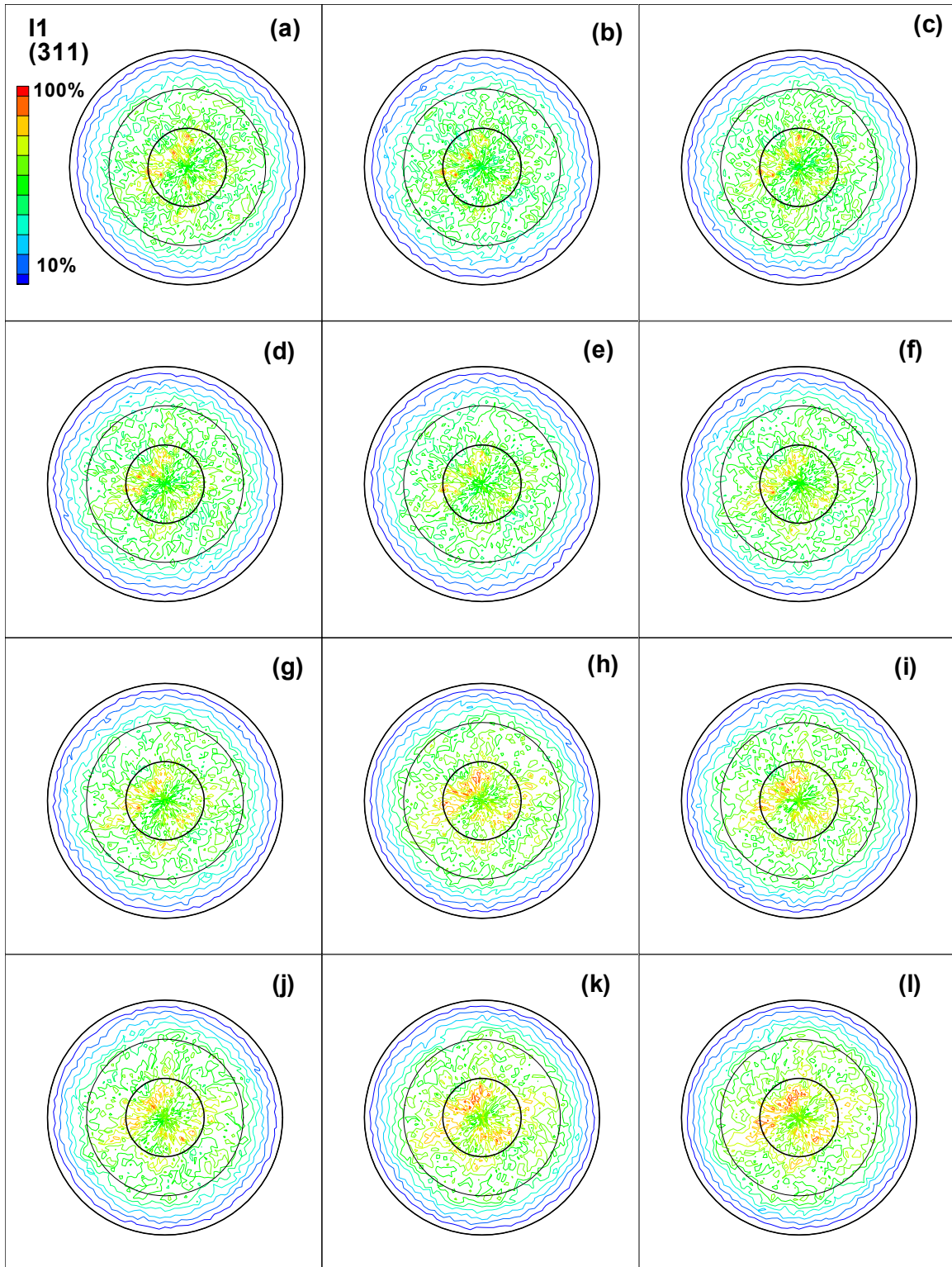


FIGURE B-109. DIRECT (311) POLE FIGURES FOR SPECIMEN I1 AFTER (a) 0, (b) 2,000, (c) 4,000, (d) 6,000, (e) 8,000, (f) 10,000, (g) 12,000, (h) 14,000, (i) 16,000, (j) 18,000, (k) 20,000, AND (l) 22,000 FATIGUE CYCLES

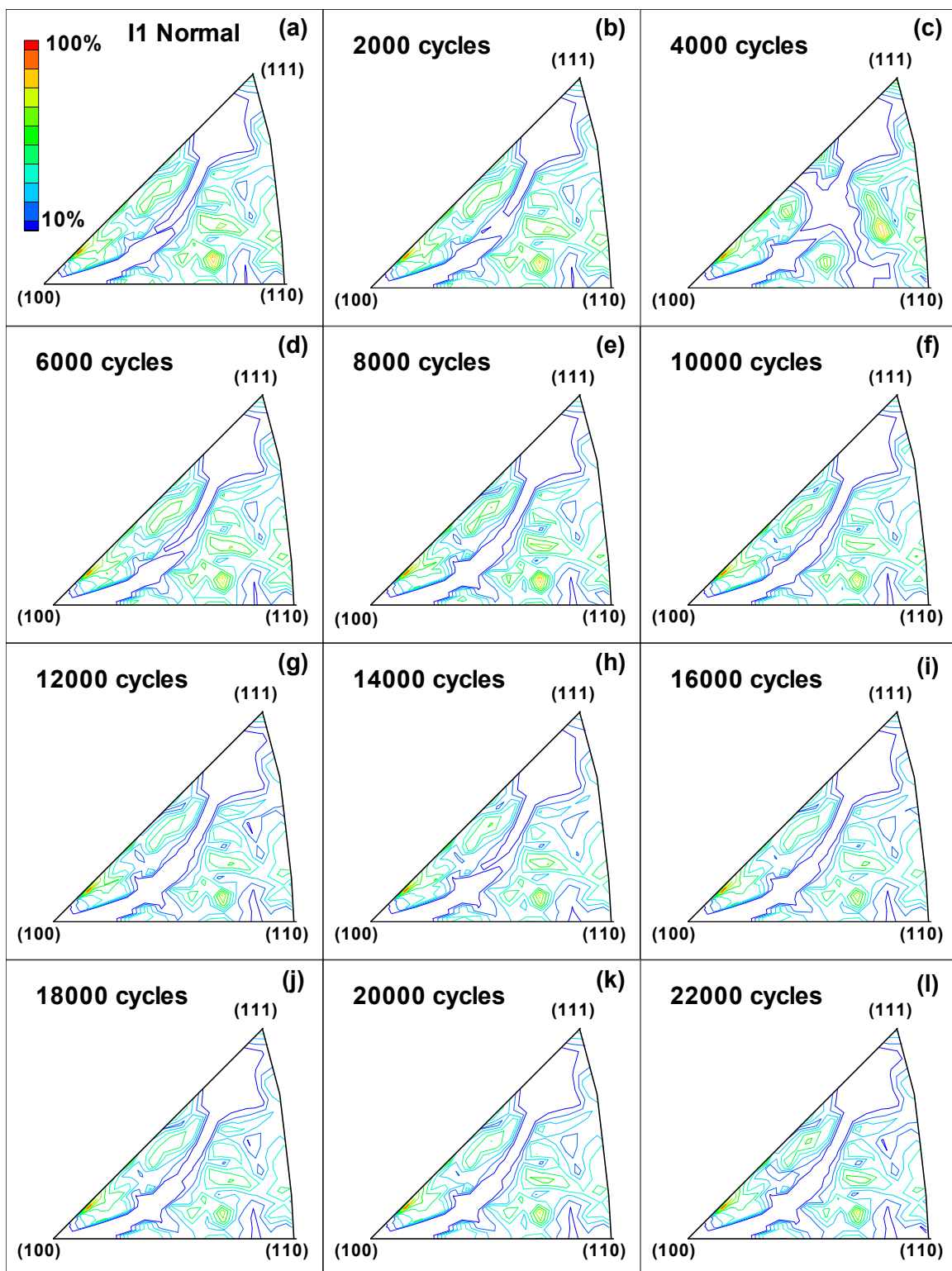


FIGURE B-110. INVERSE POLE FIGURES IN THE NORMAL DIRECTION FOR SPECIMEN I1 AFTER (a) 0, (b) 2,000, (c) 4,000, (d) 6,000, (e) 8,000, (f) 10,000, (g) 12,000, (h) 14,000, (i) 16,000, (j) 18,000, (k) 20,000, AND (l) 22,000 FATIGUE CYCLES



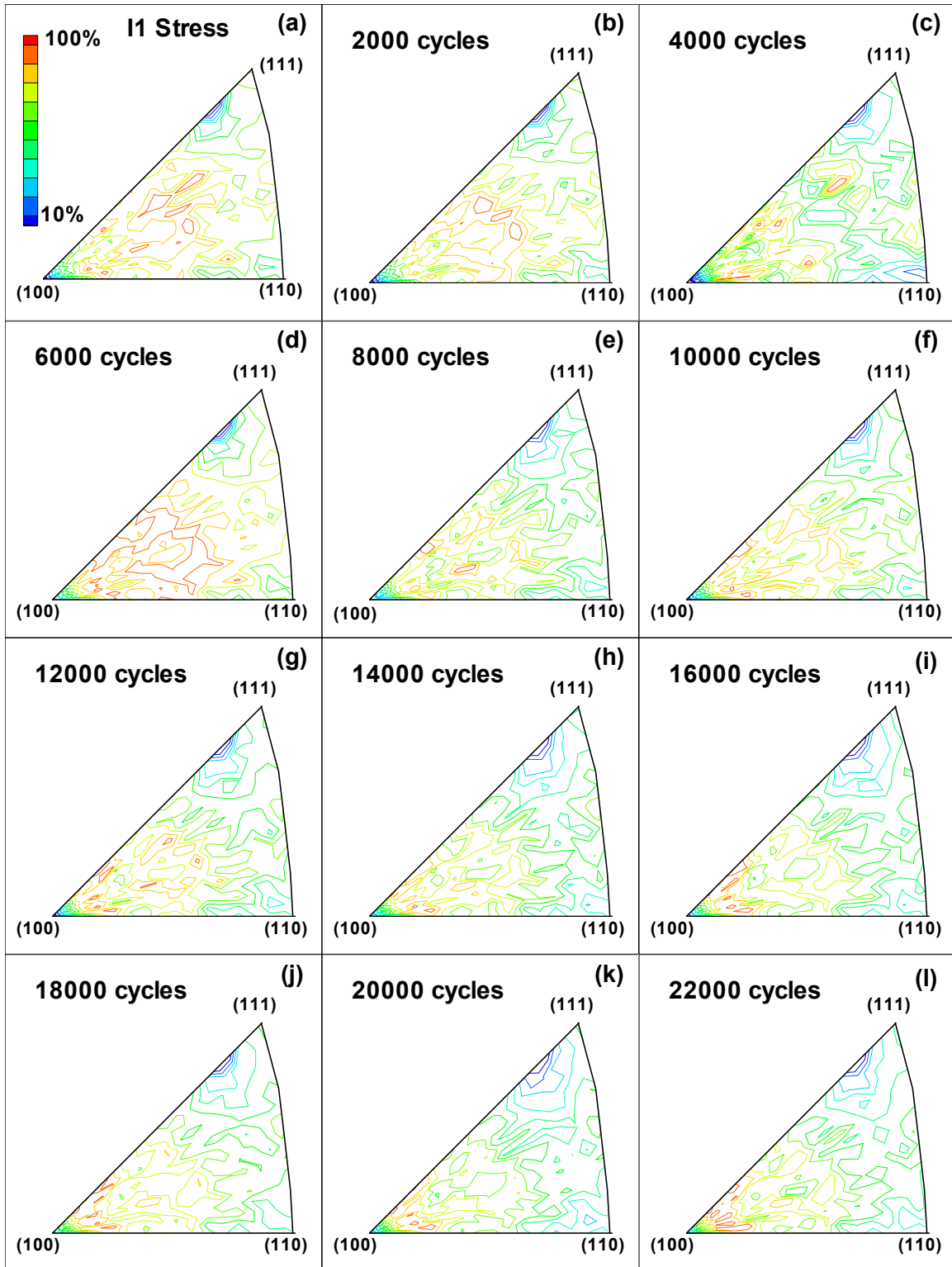


FIGURE B-111. INVERSE POLE FIGURES IN THE STRESS DIRECTION FOR SPECIMEN I1 AFTER (a) 0, (b) 2,000, (c) 4,000, (d) 6,000, (e) 8,000, (f) 10,000, (g) 12,000, (h) 14,000, (i) 16,000, (j) 18,000, (k) 20,000, AND (l) 22,000 FATIGUE CYCLES

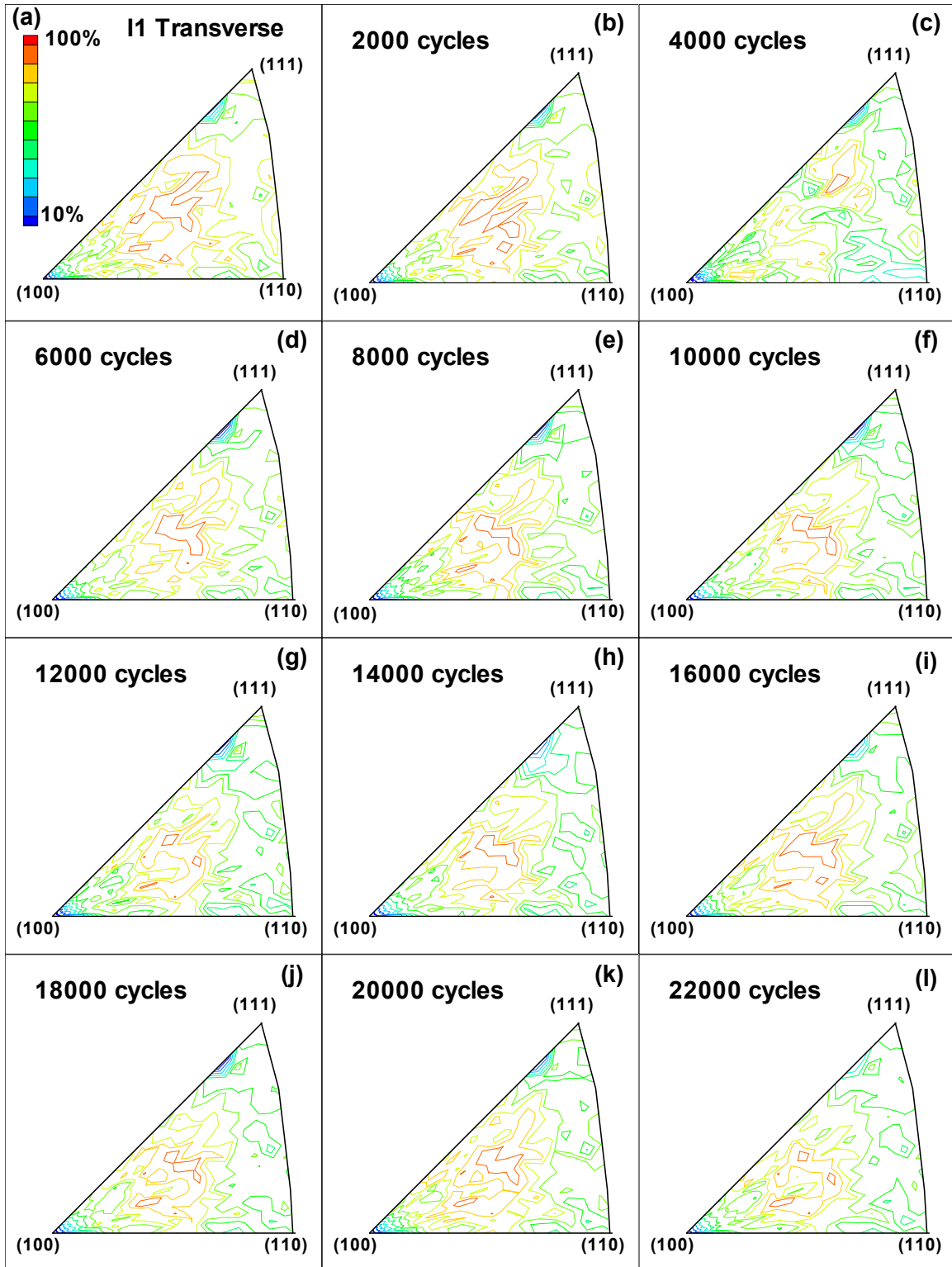


FIGURE B-112. INVERSE POLE FIGURES IN THE TRANSVERSE DIRECTION FOR SPECIMEN I1 AFTER (a) 0, (b) 2,000, (c) 4,000, (d) 6,000, (e) 8,000, (f) 10,000, (g) 12,000, (h) 14,000, (i) 16,000, (j) 18,000, (k) 20,000, AND (l) 22,000 FATIGUE CYCLES

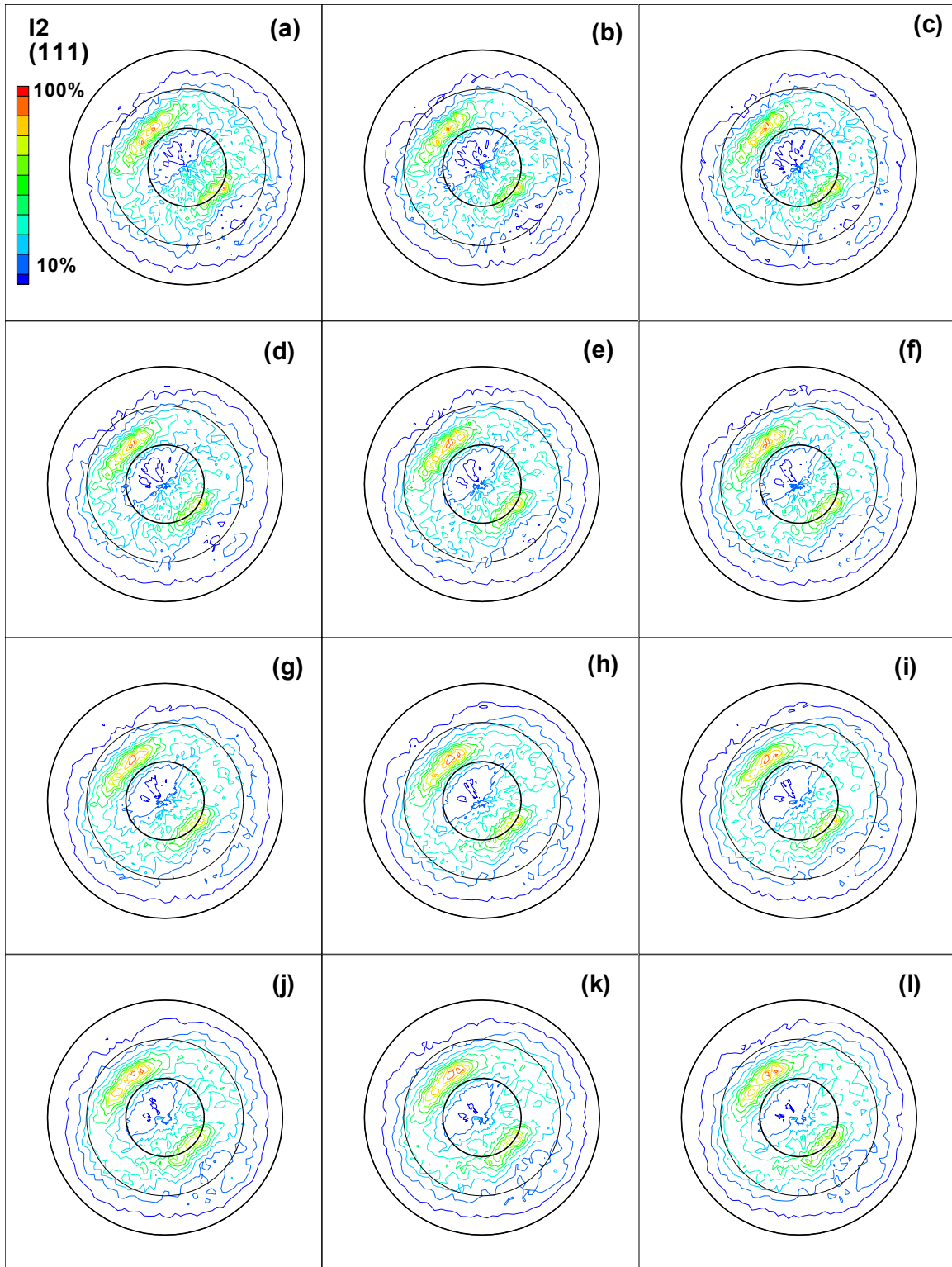


FIGURE B-113. DIRECT (111) POLE FIGURES FOR SPECIMEN I2 AFTER (a) 0, (b) 2,000, (c) 4,000, (d) 6,000, (e) 8,000, (f) 10,000, (g) 12,000, (h) 14,000, (i) 16,000, (j) 18,000, (k) 20,000, AND (l) 22,000 FATIGUE CYCLES

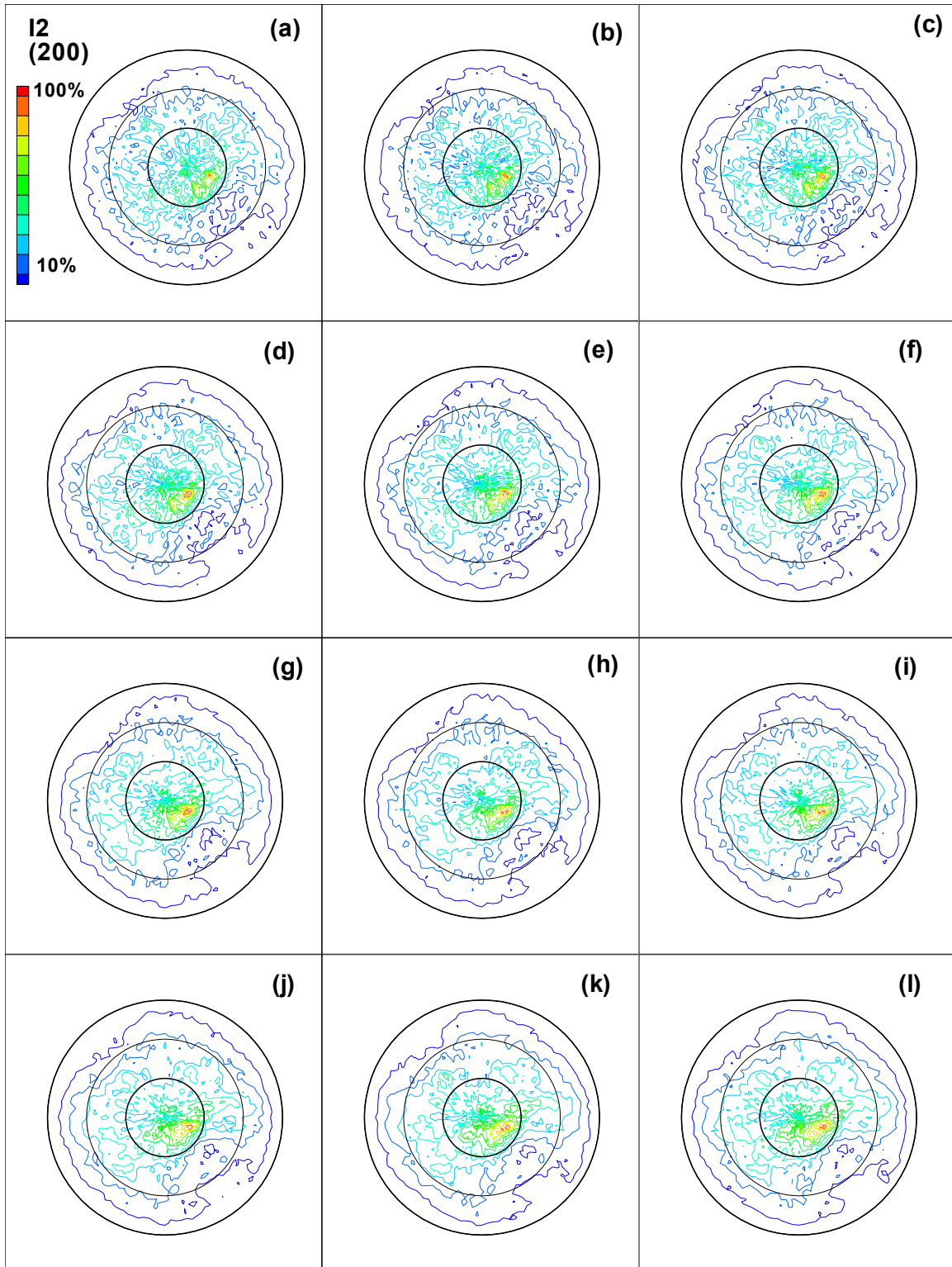


FIGURE B-114. DIRECT (200) POLE FIGURES FOR SPECIMEN I2 AFTER (a) 0, (b) 2,000, (c) 4,000, (d) 6,000, (e) 8,000, (f) 10,000, (g) 12,000, (h) 14,000, (i) 16,000, (j) 18,000, (k) 20,000, AND (l) 22,000 FATIGUE CYCLES

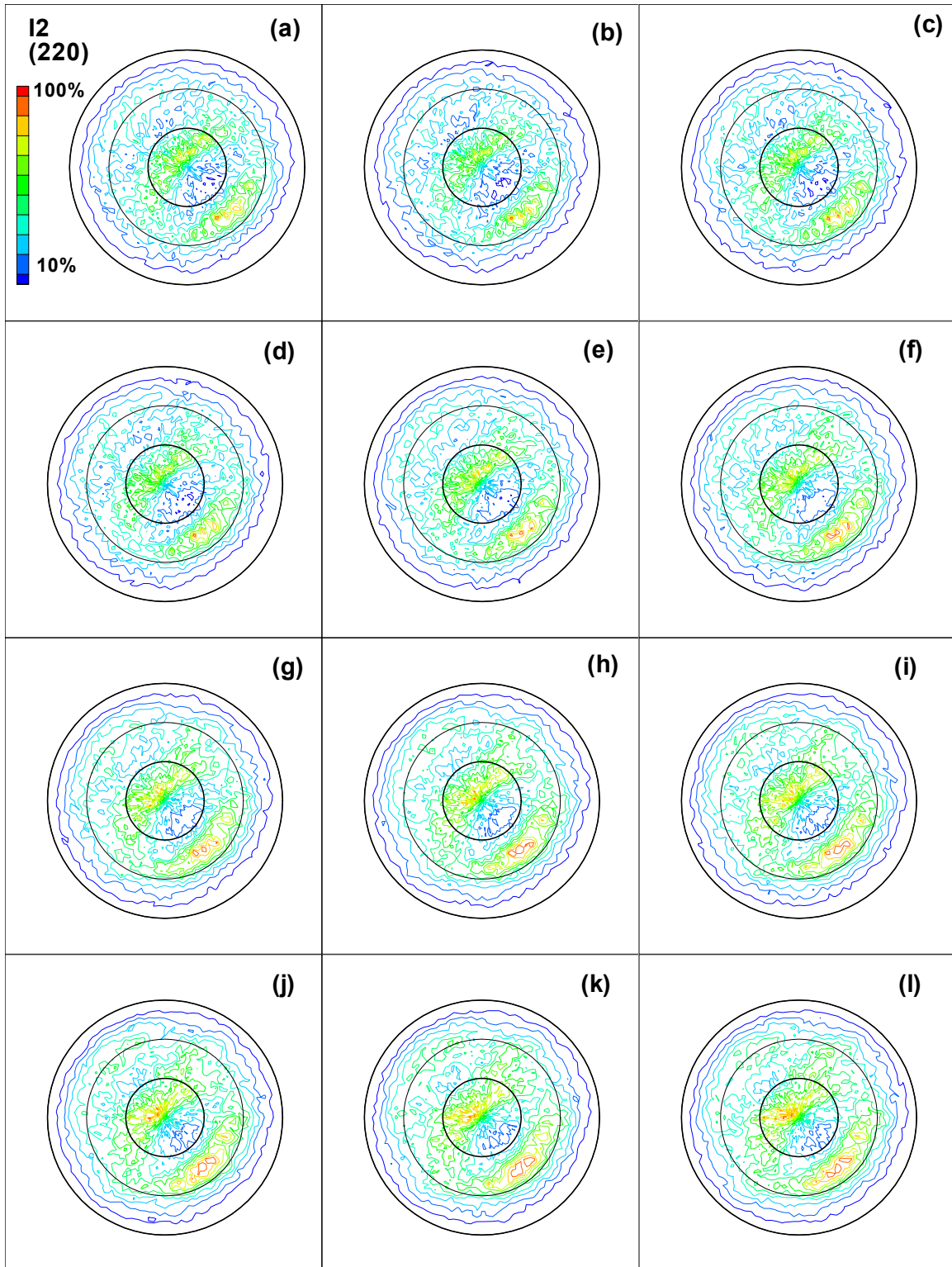


FIGURE B-115. DIRECT (220) POLE FIGURES FOR SPECIMEN I2 AFTER (a) 0, (b) 2,000, (c) 4,000, (d) 6,000, (e) 8,000, (f) 10,000, (g) 12,000, (h) 14,000, (i) 16,000, (j) 18,000, (k) 20,000, AND (l) 22,000 FATIGUE CYCLES



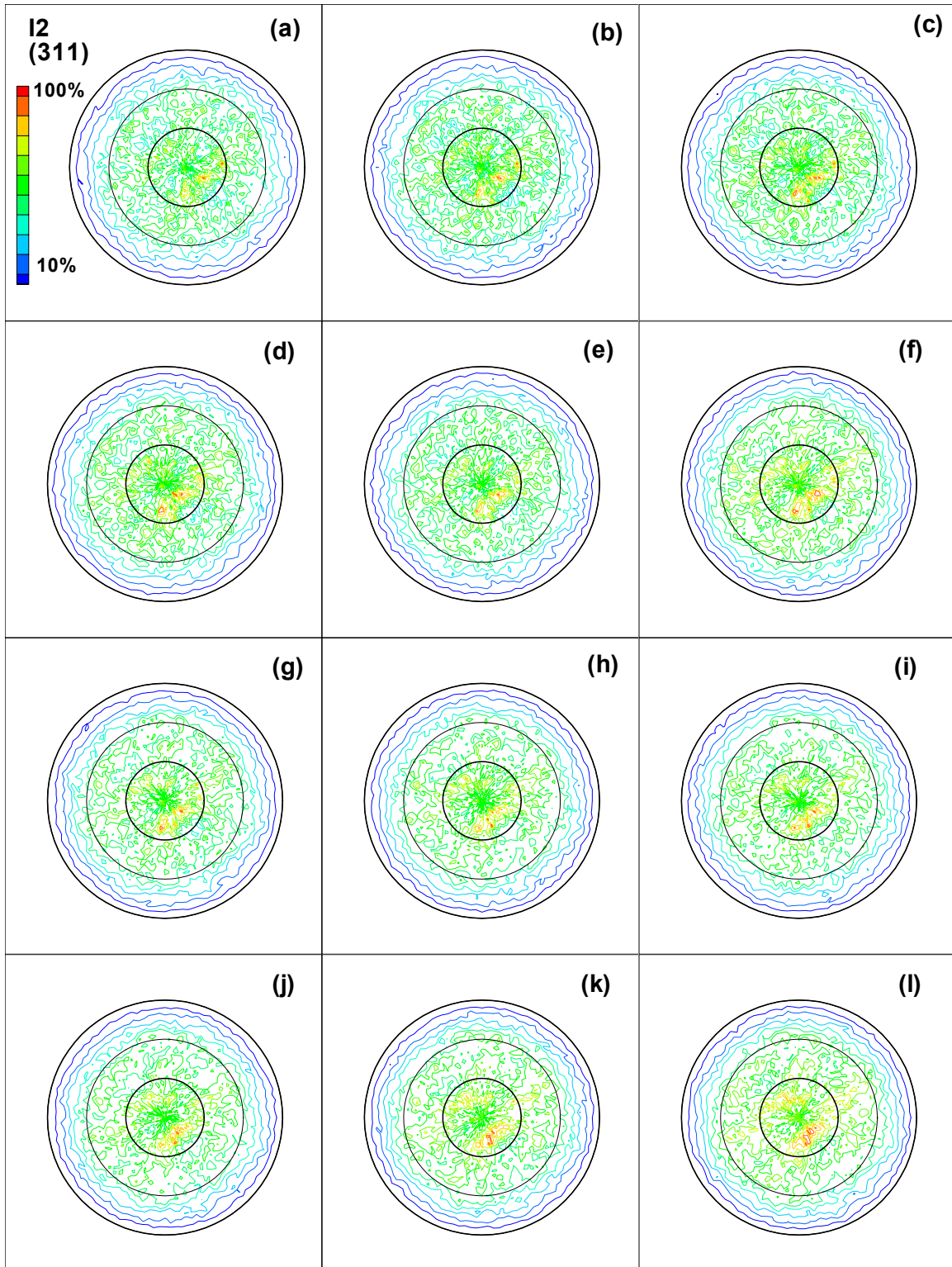


FIGURE B-116. DIRECT (311) POLE FIGURES FOR SPECIMEN I2 AFTER (a) 0, (b) 2,000, (c) 4,000, (d) 6,000, (e) 8,000, (f) 10,000, (g) 12,000, (h) 14,000, (i) 16,000, (j) 18,000, (k) 20,000, AND (l) 22,000 FATIGUE CYCLES

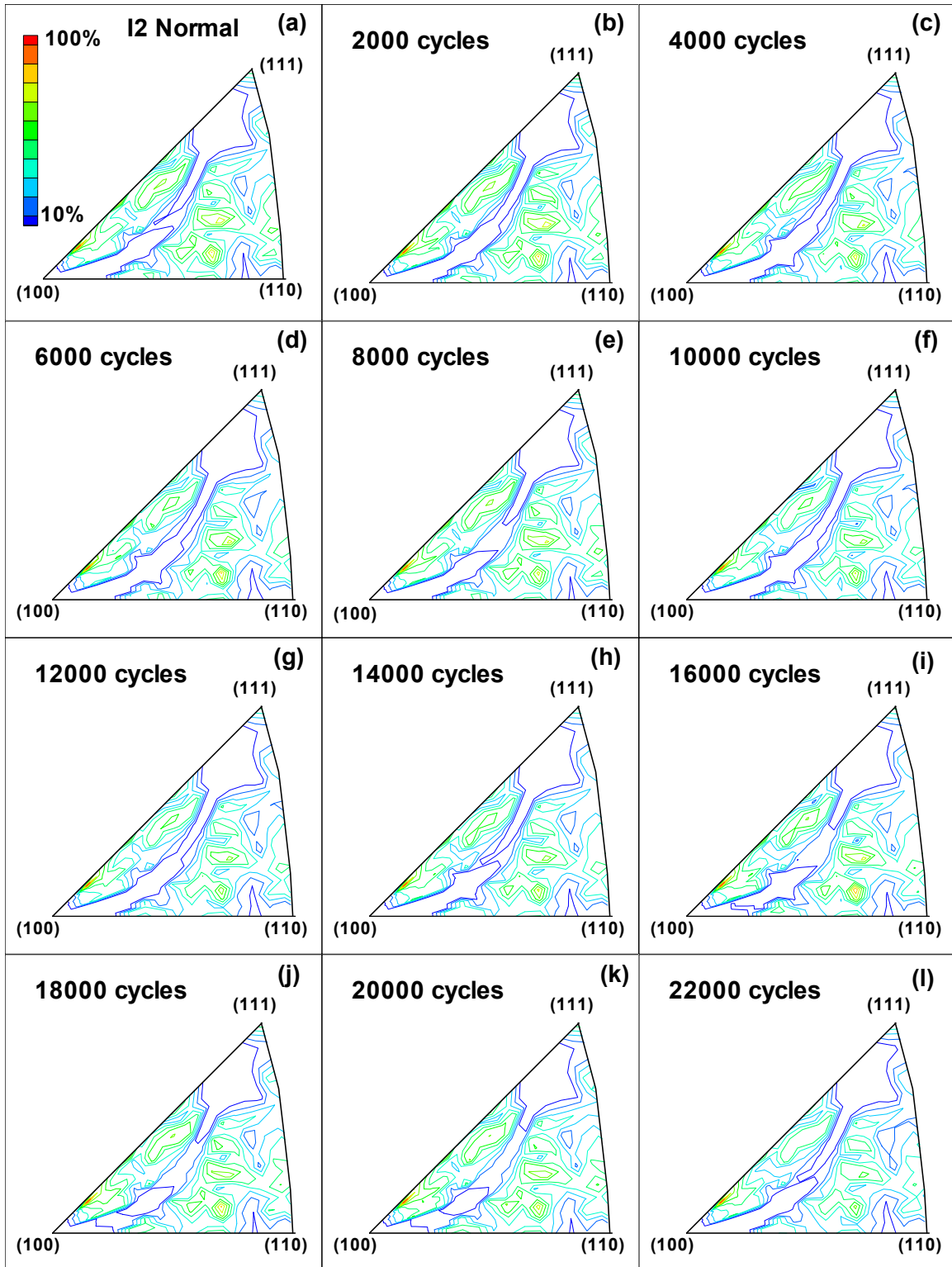


FIGURE B-117. INVERSE POLE FIGURES IN THE NORMAL DIRECTION FOR SPECIMEN I2 AFTER (a) 0, (b) 2,000, (c) 4,000, (d) 6,000, (e) 8,000, (f) 10,000, (g) 12,000, (h) 14,000, (i) 16,000, (j) 18,000, (k) 20,000, AND (l) 22,000 FATIGUE CYCLES



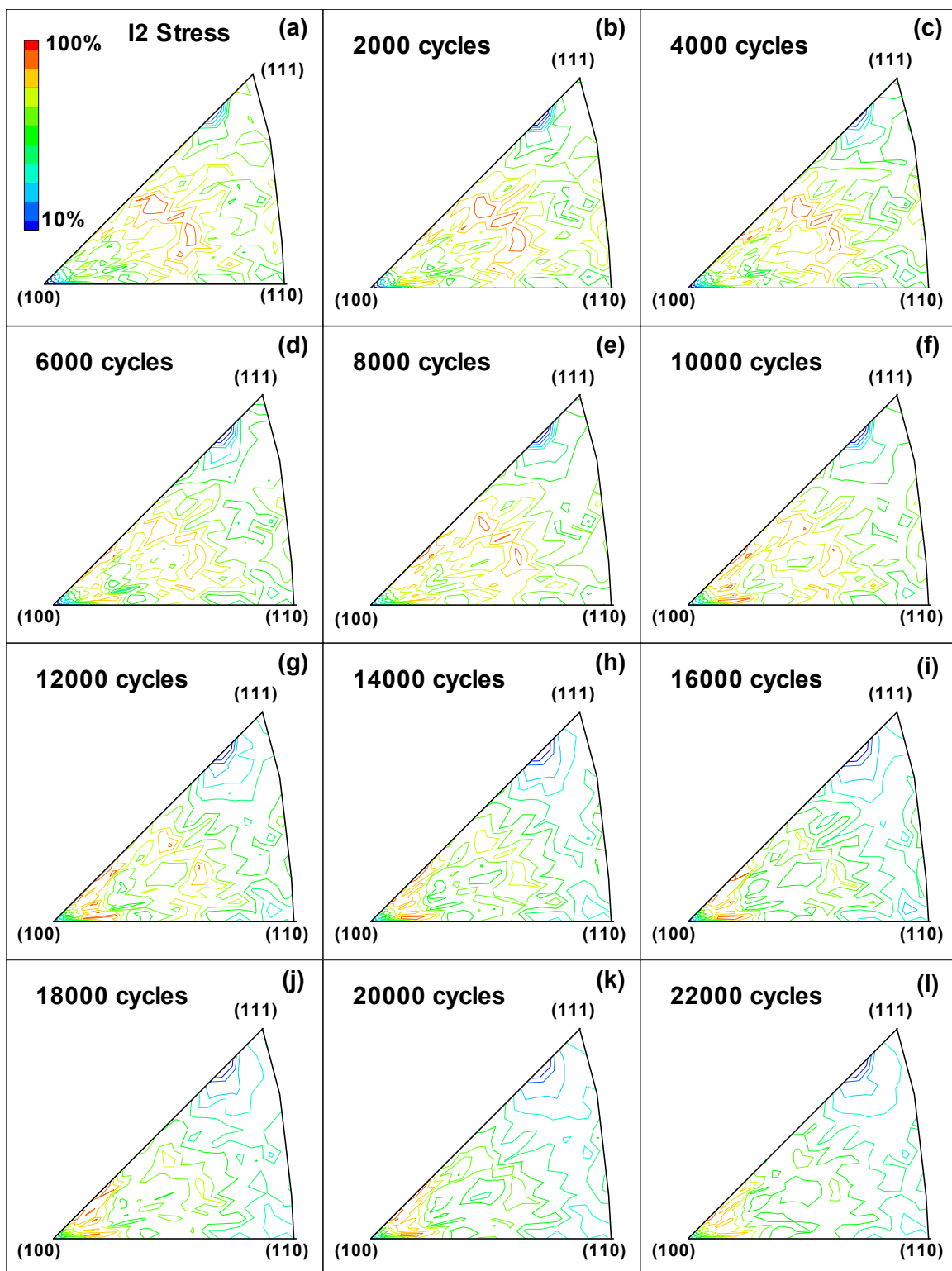


FIGURE B-118. INVERSE POLE FIGURES IN THE STRESS DIRECTION FOR SPECIMEN I2 AFTER (a) 0, (b) 2,000, (c) 4,000, (d) 6,000, (e) 8,000, (f) 10,000, (g) 12,000, (h) 14,000, (i) 16,000, (j) 18,000, (k) 20,000, AND (l) 22,000 FATIGUE CYCLES

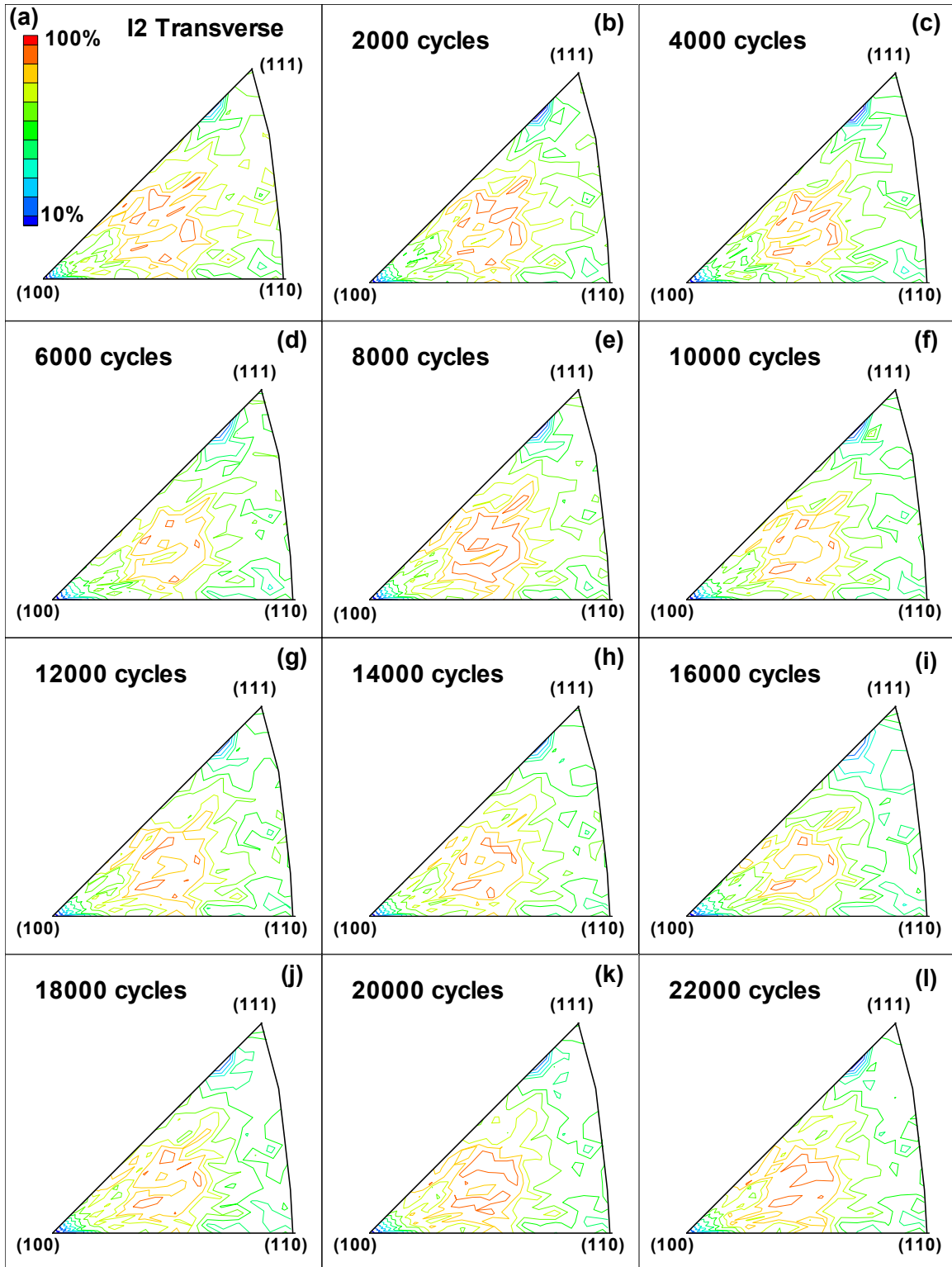


FIGURE B-119. INVERSE POLE FIGURES IN THE TRANSVERSE DIRECTION FOR SPECIMEN I2 AFTER (a) 0, (b) 2,000, (c) 4,000, (d) 6,000, (e) 8,000, (f) 10,000, (g) 12,000, (h) 14,000, (i) 16,000, (j) 18,000, (k) 20,000, AND (l) 22,000 FATIGUE CYCLES

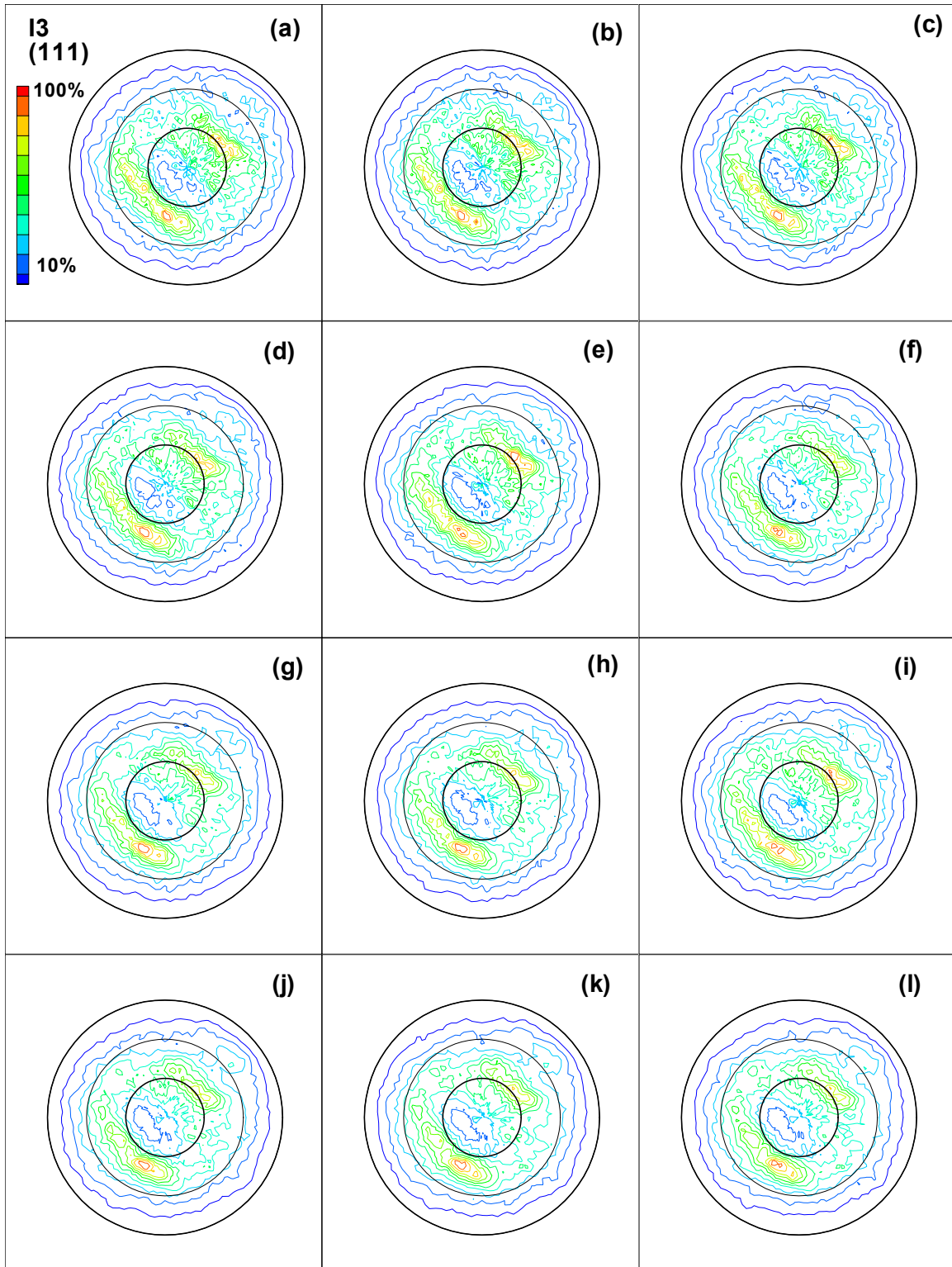


FIGURE B-120. DIRECT (111) POLE FIGURES FOR SPECIMEN I3 AFTER (a) 0, (b) 2,000, (c) 4,000, (d) 6,000, (e) 8,000, (f) 10,000, (g) 12,000, (h) 14,000, (i) 16,000, (j) 18,000, (k) 20,000, AND (l) 22,000 FATIGUE CYCLES

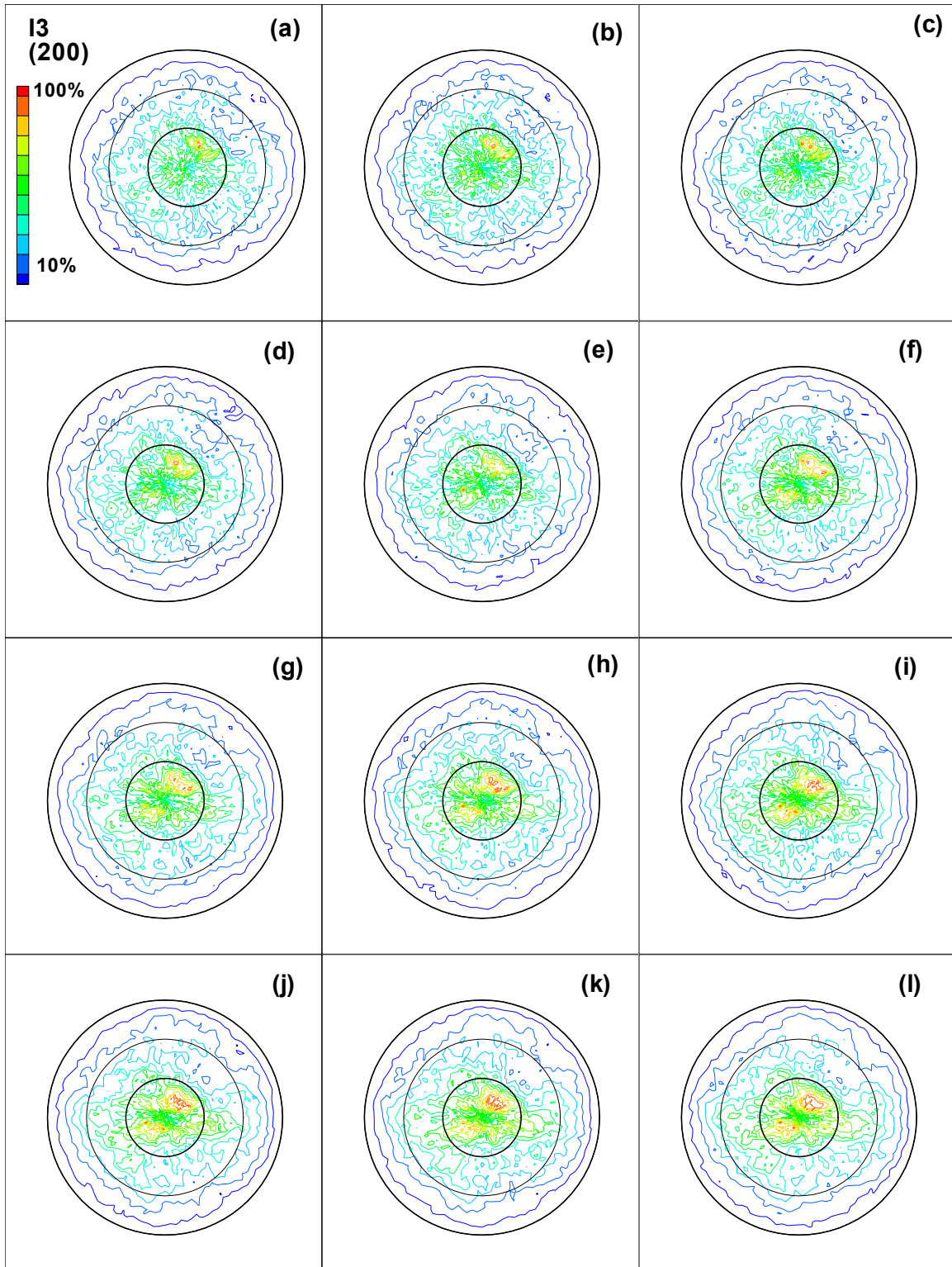


FIGURE B-121. DIRECT (200) POLE FIGURES FOR SPECIMEN I3 AFTER (a) 0, (b) 2,000, (c) 4,000, (d) 6,000, (e) 8,000, (f) 10,000, (g) 12,000, (h) 14,000, (i) 16,000, (j) 18,000, (k) 20,000, AND (l) 22,000 FATIGUE CYCLES

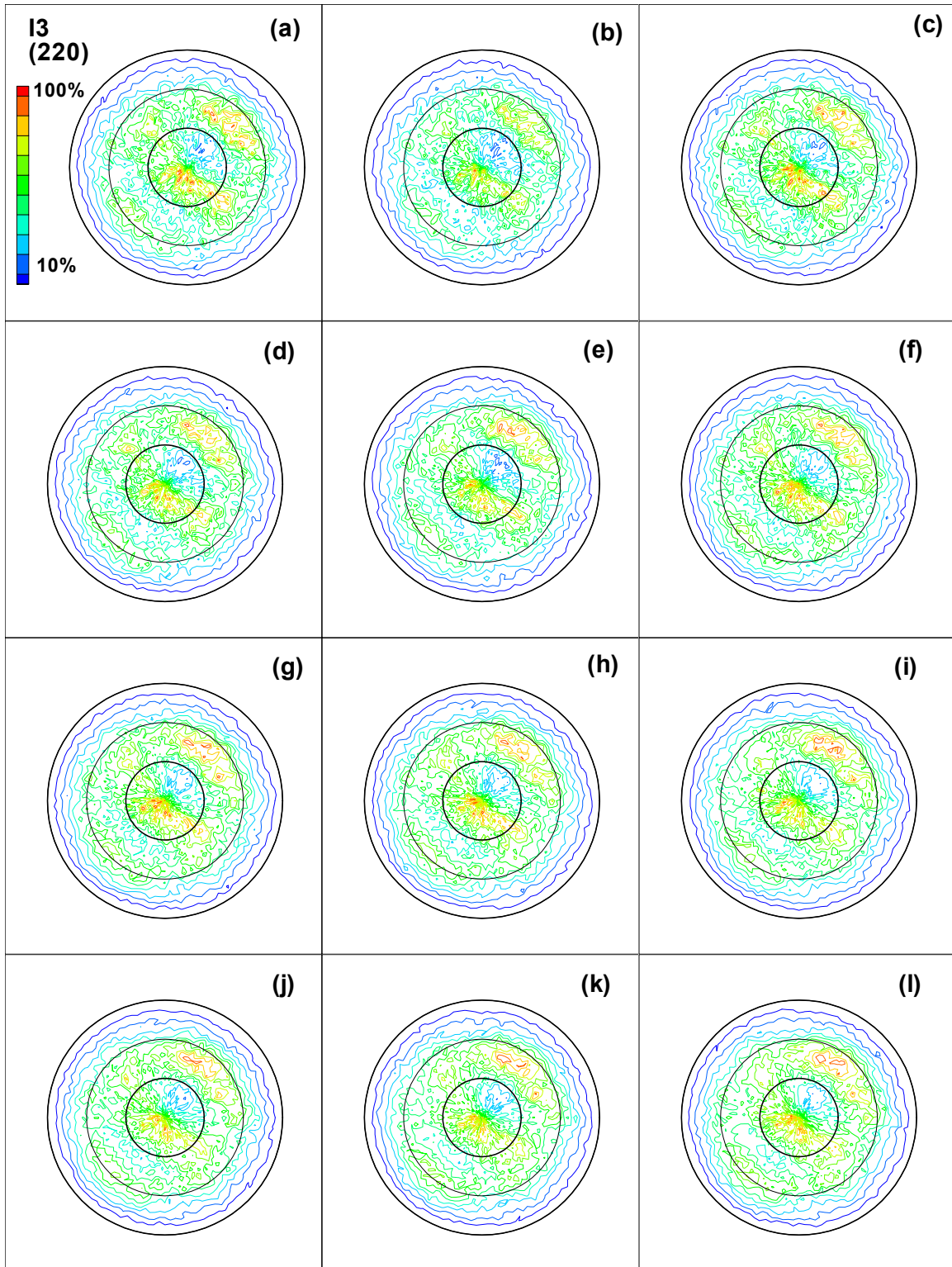


FIGURE B-122. DIRECT (220) POLE FIGURES FOR SPECIMEN I3 AFTER (a) 0, (b) 2,000, (c) 4,000, (d) 6,000, (e) 8,000, (f) 10,000, (g) 12,000, (h) 14,000, (i) 16,000, (j) 18,000, (k) 20,000, AND (l) 22,000 FATIGUE CYCLES



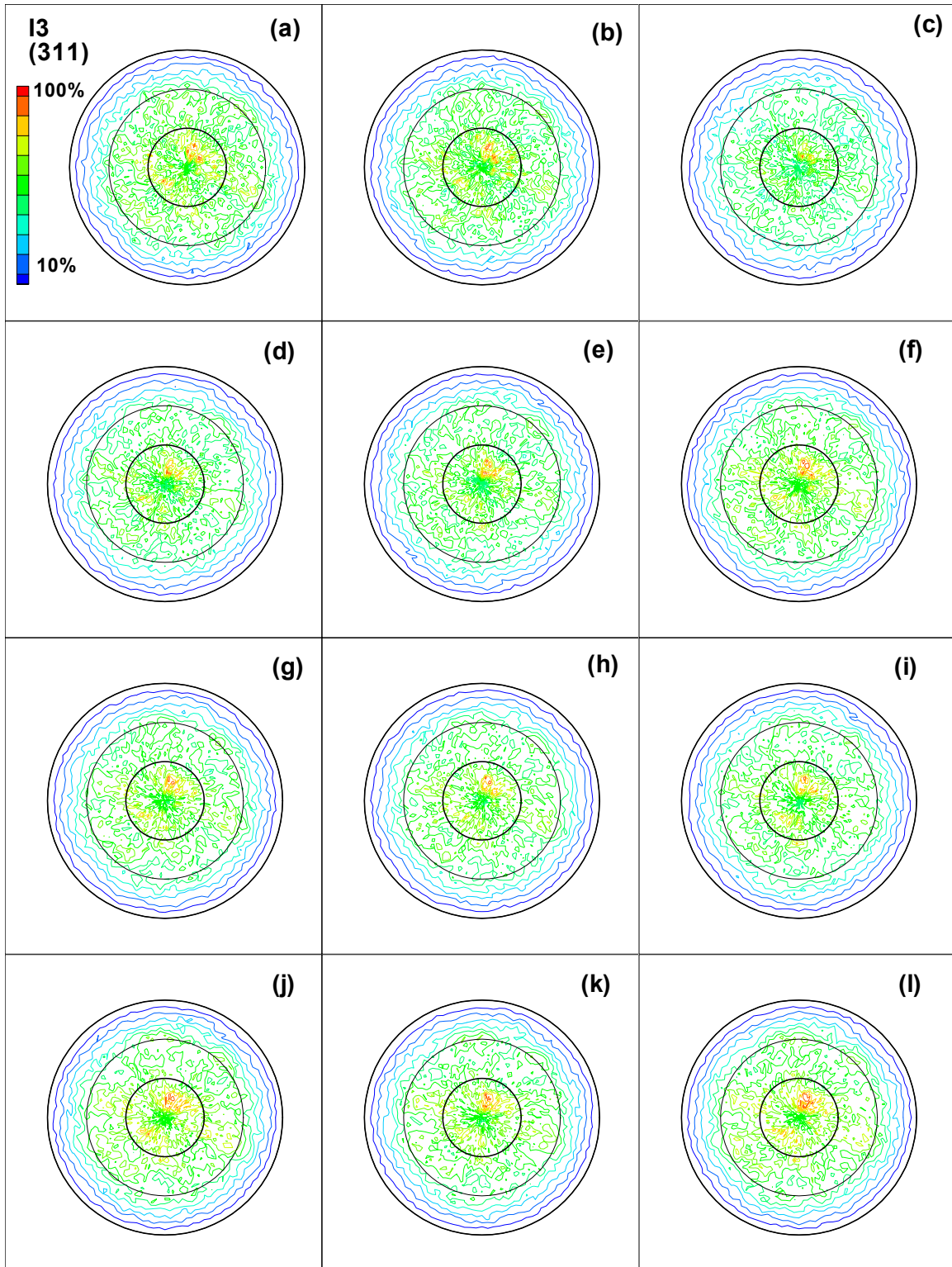


FIGURE B-123. DIRECT (311) POLE FIGURES FOR SPECIMEN I3 AFTER (a) 0, (b) 2,000, (c) 4,000, (d) 6,000, (e) 8,000, (f) 10,000, (g) 12,000, (h) 14,000, (i) 16,000, (j) 18,000, (k) 20,000, AND (l) 22,000 FATIGUE CYCLES

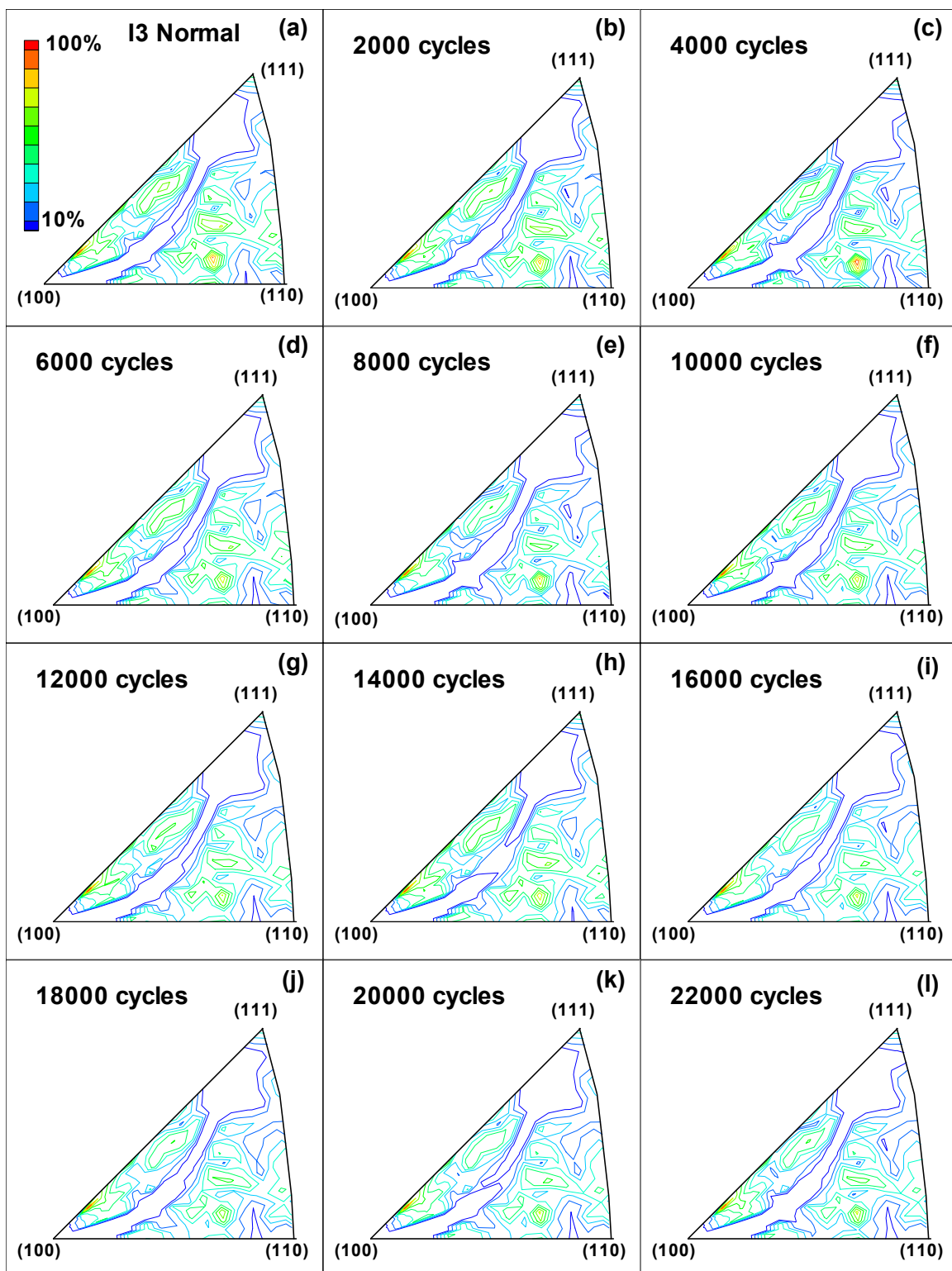


FIGURE B-124. INVERSE POLE FIGURES IN THE NORMAL DIRECTION FOR SPECIMEN I3 AFTER (a) 0, (b) 2,000, (c) 4,000, (d) 6,000, (e) 8,000, (f) 10,000, (g) 12,000, (h) 14,000, (i) 16,000, (j) 18,000, (k) 20,000, AND (l) 22,000 FATIGUE CYCLES



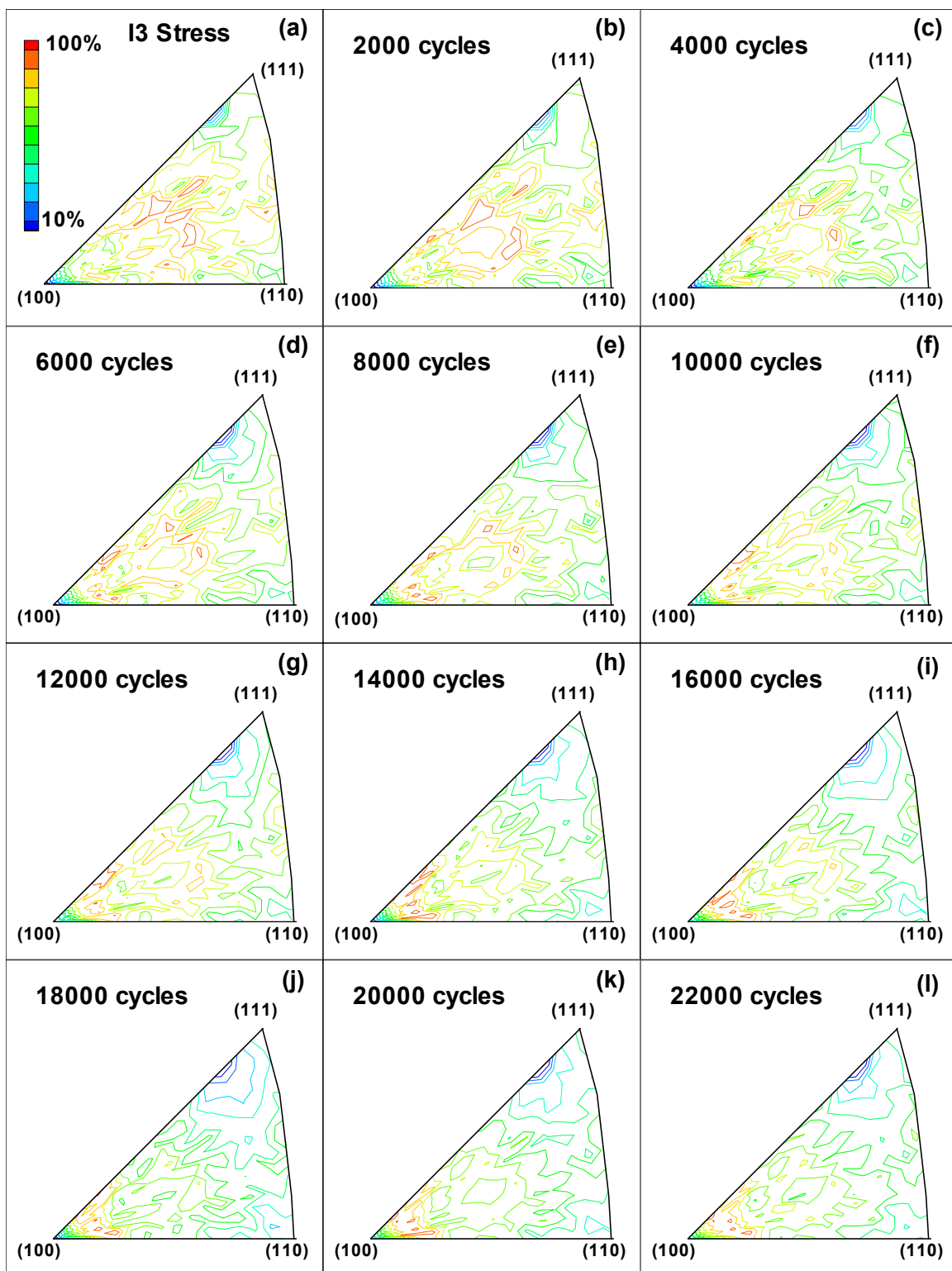


FIGURE B-125. INVERSE POLE FIGURES IN THE STRESS DIRECTION FOR SPECIMEN I3 AFTER (a) 0, (b) 2,000, (c) 4,000, (d) 6,000, (e) 8,000, (f) 10,000, (g) 12,000, (h) 14,000, (i) 16,000, (j) 18,000, (k) 20,000, AND (l) 22,000 FATIGUE CYCLES

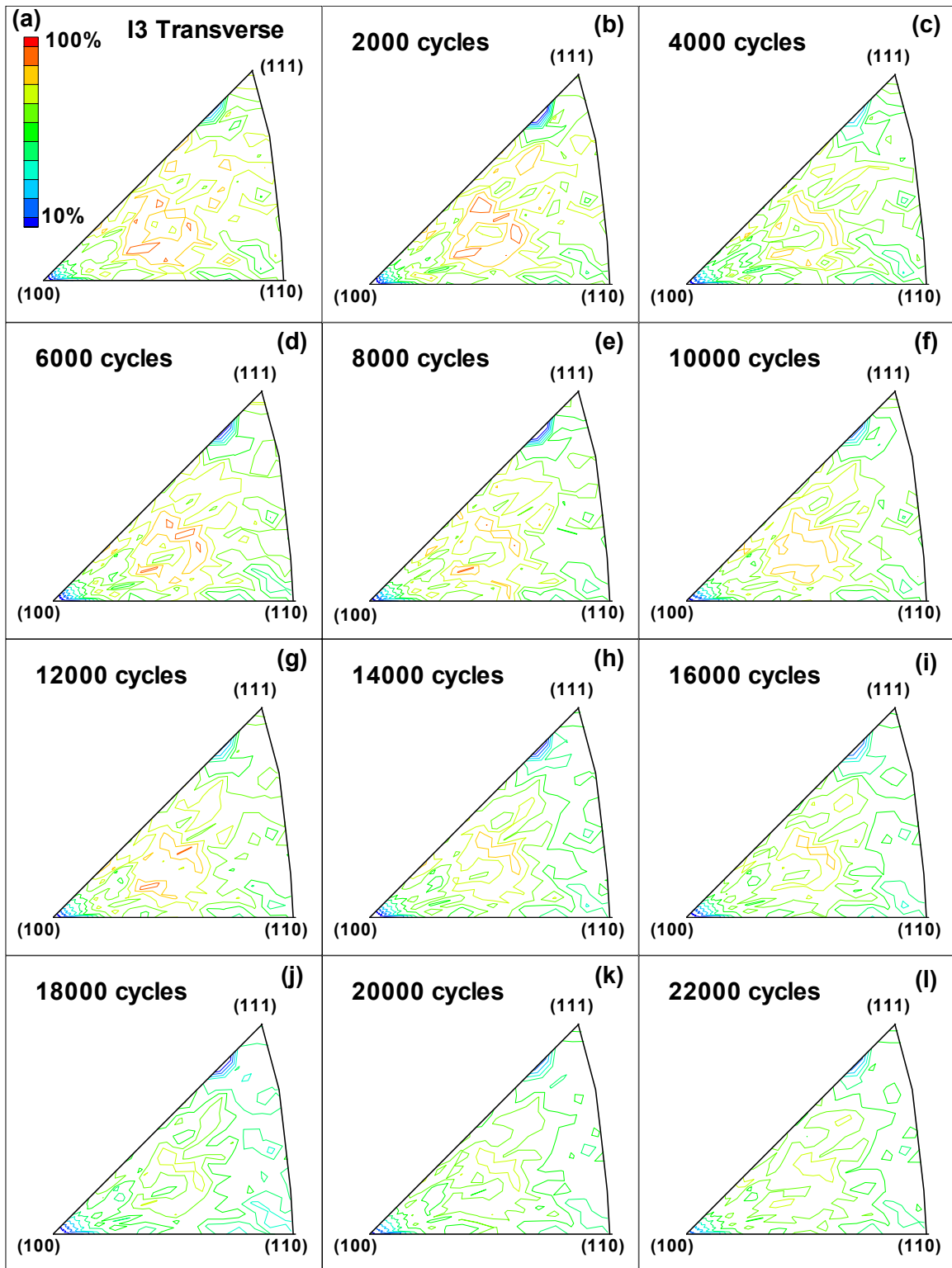


FIGURE B-126. INVERSE POLE FIGURES IN THE TRANSVERSE DIRECTION FOR SPECIMEN I3 AFTER (a) 0, (b) 2,000, (c) 4,000, (d) 6,000, (e) 8,000, (f) 10,000, (g) 12,000, (h) 14,000, (i) 16,000, (j) 18,000, (k) 20,000, AND (l) 22,000 FATIGUE CYCLES

## APPENDIX C—SCANNING ELECTRON MICROSCOPE SURFACE INVESTIGATION AS A FUNCTION OF FATIGUE

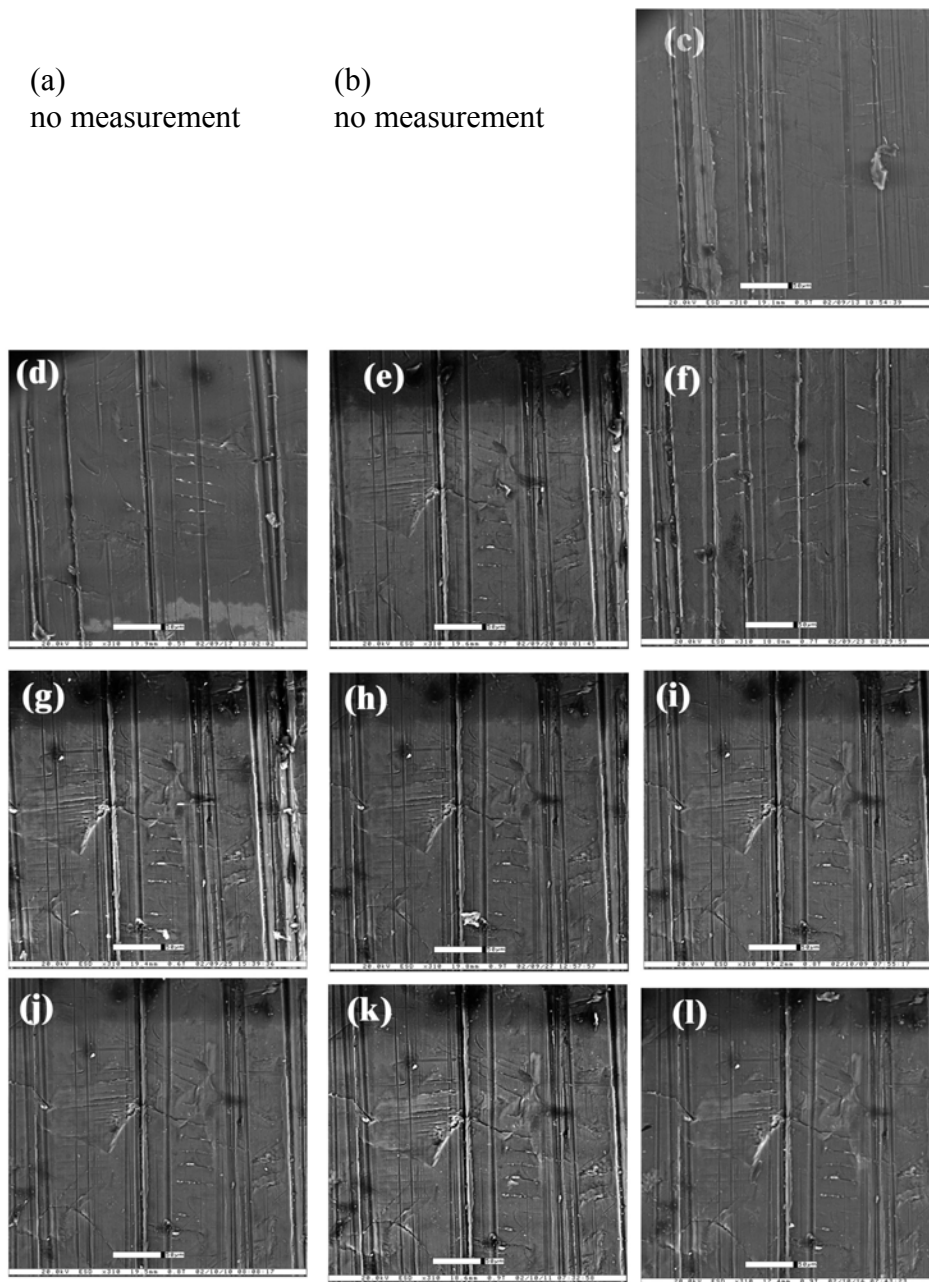


FIGURE C-1. SEM IMAGES OF SAMPLE G4 AS A FUNCTION OF THE NUMBER OF FATIGUE CYCLES (The onset of cracking occurs near 6,000 cycles. The vertical lines on each specimen were introduced during the machining process. The scale bar for each figure is 50  $\mu\text{m}$ . No measurement was made for (a) the virgin sample or (b) after 2,000 cycles. The remaining figures are after (c) 4,000, (d) 6,000, (e) 8,000, (f) 10,000, (g) 12,000, (h) 14,000, (i) 16,000, (j) 18,000, (k) 20,000, and (l) 22,000 fatigue cycles.)

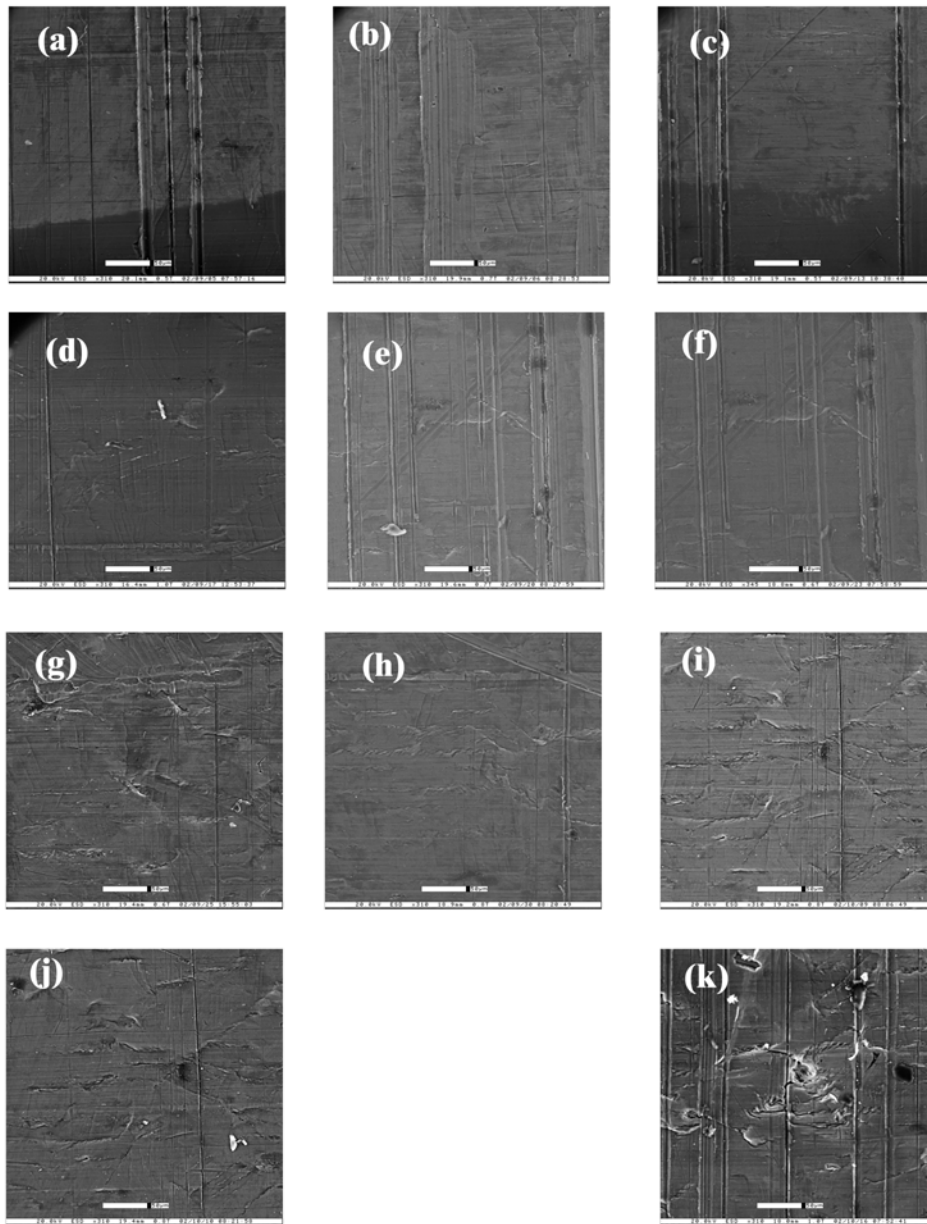


FIGURE C-2. SEM IMAGES OF SAMPLE H4 AS A FUNCTION OF THE NUMBER OF FATIGUE CYCLES (The onset of cracking occurs near 4,000 cycles. The vertical lines on each specimen were introduced during the machining process. The scale bar for each figure is 50  $\mu\text{m}$ . The figures are for (a) the virgin sample and then after (b) 2,000, (c) 4,000, (d) 6,000, (e) 8,000, (f) 10,000, (g) 12,000, (h) 14,000, (i) 16,000, (j) 18,000, (k) 22,000 fatigue cycles. The image taken at 20,000 samples could not be reloaded.)

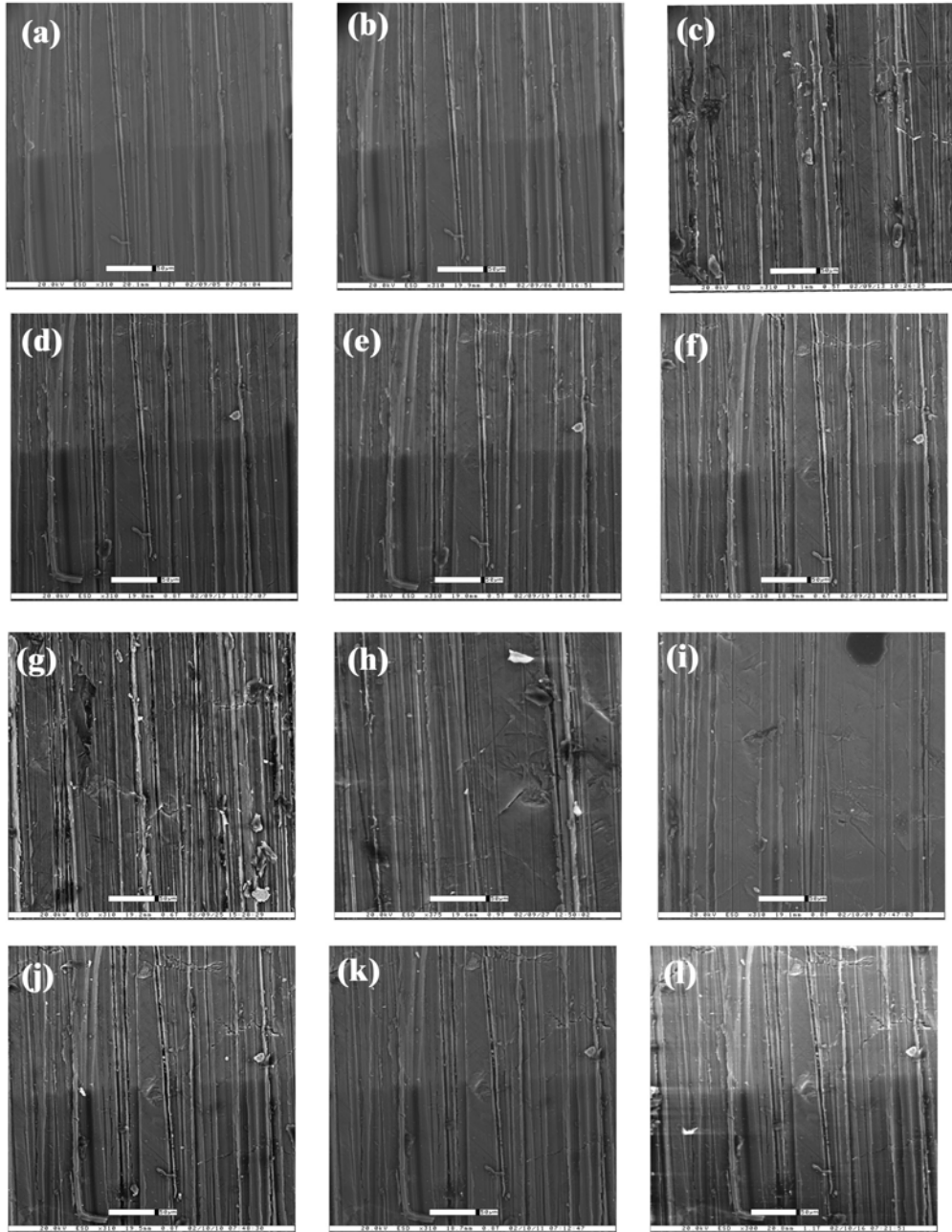


FIGURE C-3. SEM IMAGES OF SAMPLE I4 AS A FUNCTION OF THE NUMBER OF FATIGUE CYCLES (The onset of cracking occurs near 4,000 cycles. The vertical lines on each specimen were introduced during the machining process. The scale bar for each figure is 50  $\mu\text{m}$ . The figures are for (a) the virgin sample and then after (b) 2,000, (c) 4,000, (d) 6,000, (e) 8,000, (f) 10,000, (g) 12,000, (h) 14,000, (i) 16,000, (j) 18,000, (k) 20,000, and (l) 22,000 fatigue cycles.)

## APPENDIX D—LITERATURE REVIEW

.....

---

# Effects of Texture on Crack Initiation During Cyclic Fatigue

*Literature Review*



Dr. Patricia Stampe  
Ms. Natanette Craig  
Dr. Robin Kennedy  
Dr. William Tucker

Department of Physics  
Florida A&M University  
Tallahassee, FL 32307

January 15, 2002



# Effects of Texture on Crack Initiation During Cyclic Fatigue

## *Literature Review*

### **Abstract**

The detection of fatigue cracks before catastrophic failure is of great concern to the aerospace industry. This document provides a review of literature on the effects of texture on fatigue in polycrystalline materials, with the purpose of investigating crack initiation during cyclic fatigue. These topics will be reviewed as three principal issues. Firstly, the effects of texture on materials properties will be reviewed. Secondly, the evolution of texture in polycrystalline materials as a response to thermal and mechanical conditions will be investigated. Finally the practicality of using x-ray diffraction as a test for changes in texture leading to crack initiation will be discussed.

## Table of Contents

<b>Abstract .....</b>	<b>5</b>
<b>1. Introduction.....</b>	<b>7</b>
1.1 Motivation .....	7
1.2 Definition of Crystalline Texture .....	7
<b>2. Causes of Fatigue Failure .....</b>	<b>9</b>
2.1 Mechanisms for Intergranular Crack Initiation.....	9
2.2 Mechanisms of Transgranular Crack Initiation .....	10
2.3 Evidence for the Influence of Texture on Mechanical Properties and Fatigue.....	12
2.3.1 Residual Stress and Texture .....	12
2.3.2 Yield Strength and Fatigue Lifetime .....	13
2.3.3 Microstructural Studies .....	15
2.4 Property Determination by X-ray Texture Measurement.....	16
<b>3. Texture Development in Polycrystals .....</b>	<b>16</b>
3.1 Alloy Preparation and Machining.....	17
3.2 Deformation .....	17
3.3 Cyclic fatigue .....	18
<b>4. Conclusion .....</b>	<b>19</b>
<b>References .....</b>	<b>20</b>

## **1. Introduction**

### **1.1 Motivation**

Objects subjected to repetitive stresses are liable to fracture even when these stresses are lower than the tensile strength of the material. This is due to a process known as fatigue. Fatigue is caused by gradual microscopic changes in the material, which lead to the formation of dislocations and eventually the initiation of microcracks. These microcracks then propagate through the material on successive stress cycles and coalesce into larger cracks, eventually causing failure of the object. This phenomenon is a cause for concern in the aerospace industry, since failures of aircraft parts during flight have catastrophic consequences. In order to provide preventative maintenance, it is thus necessary to find a non-destructive mechanism for testing a material's likelihood for crack initiation.

The propagation of cracks through materials has been shown to depend on a number of factors, including the crystalline texture of the material. This texture is known to be sensitive to thermal and mechanical processing during part preparation[1]. It has been suggested that texture may also evolve during cyclic fatigue of a material[2]. Since texture is readily measured by x-ray diffraction, it should be relatively straightforward to determine whether texture development could be used as a benchmark to test for the proximity of a material to crack initiation.

This document is a review of the relevant literature on texture and fatigue in polycrystalline materials. Its purpose is to review the effects of texture on fatigue failure, the evolution of texture during cyclic stress, the practicality of x-ray diffraction as a test for proximity to crack initiation.

### **1.2 Definition of Crystalline Texture**

Before beginning this document, it is useful to define crystalline texture and specify how it is measured and quantified. Most metals used in manufacturing are 'polycrystalline'; that is, they are formed of an aggregate of small grains of metal[3]. Each grain is a small crystal of the material, with its atoms arranged on planes forming a uniform crystal lattice. Crystalline 'texture' refers to the orientation of the crystal lattices of each of these grains within the material. If there is 'no' texture or 'random' texture in the metal, the grains are oriented randomly with respect to each other. This means that there is equal probability of finding a grain with a given orientation, for example (111), in any direction in space. Here (111) denotes the Miller indices of the crystal plane[3]. When a randomly textured material is subjected to thermal or mechanical conditioning, some grain rotation may occur, causing particular grain orientations to become preferred. This process is said to introduce texture to the material. A material that is completely textured would

resemble the texture of a single crystal. All grains would have exactly the same orientation.

Diffraction techniques are used to measure and quantify the degree of texturing within a material. Bulk diffraction methods, such as x-ray and neutron diffraction, measure a relatively large volume, encompassing many grains. Electron back scattering methods on the other hand, due to the microscopic size of the electron beam, measure only one grain of the material at a time. These techniques can be used to produce a map of the probability distribution of a given set of planes occurring over three-dimensional space, called a 'pole figure'. To obtain a pole figure, the detector is set at a fixed angle, so as to detect reflections from only one set of lattice planes, as determined by Bragg's Law,  $n\lambda = 2d\sin\theta$ . The specimen is rotated  $360^\circ$  about its surface normal, then tilted so that the surface normal is a few degrees out of the diffraction plane, and rotated once more through  $360^\circ$ . This procedure is repeated until the sample has been rotated through all possible orientations in three-dimensional space. The intensity distribution recorded in this manner is then plotted as shown in Figure 1, with the tilt angle varying from zero to ninety degrees radially, and the  $360^\circ$  degree rotation plotted azimuthally. To fully understand the texture of a material it is necessary to collect a number of pole figures for various important sets of lattice planes. In a cubic material these are commonly the  $\{111\}$ ,  $\{100\}$  and  $\{110\}$  planes. These data sets can then be numerically combined to produce an Orientation Distribution Function (ODF) that quantitatively describes the probability of a grain having a particular orientation[4].

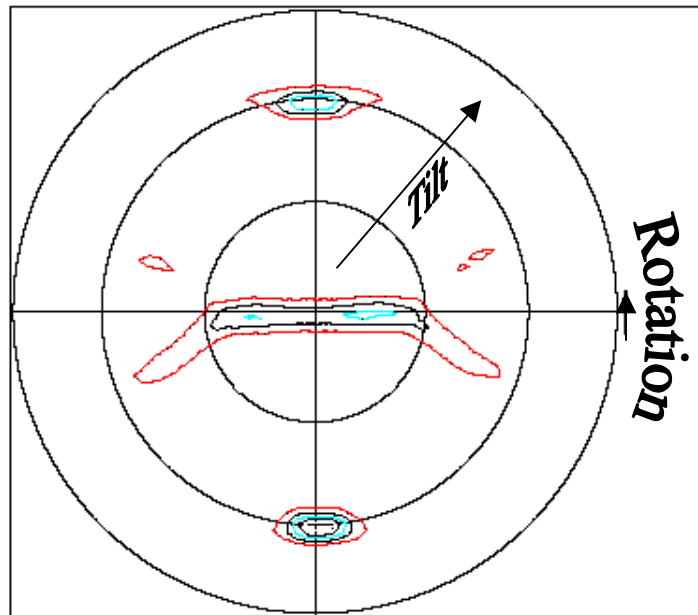


*Figure 1: Pole figure of the  $\{110\}$  reflections of an elastically deformed aluminum plate. The presence of localized regions of intensity indicate that the texture of this plate is not random. With random texture, the intensity would be uniform over the entire figure.*

Recently it has become possible to determine the orientation of individual grains using techniques such as Electron Backscattering Diffraction (EBSD) or Orientation Imaging Microscopy (OIM). With these techniques, powerful electron beams with extremely fine spatial resolution (from either electron microscopes or synchrotron sources[5, 6]) are focussed on individual grains and the resulting diffraction pattern is analyzed to obtain the orientation of the crystal planes within that grain. By scanning the beam over the surface in a controlled manner, this technique can be used to find the orientation of the surface grains in a small region of the material. This can be useful for example, in examining the grain orientation along a crack edge. It is limited, however, in its ability to address the texture of a bulk part of the specimen, particularly since the electron beam does not penetrate nearly as far into the sample as an x-ray beam. Thus bulk diffraction can be combined with these localized techniques to give a good picture of the crystalline texture of a material at both macroscopic and microscopic scales.

## **2. Causes of Fatigue Failure**

On the microstructural level, a crack forms when the local stress exceeds the local strength of the material. During cyclic fatigue, however, the applied stress is lower than the tensile strength of the bulk material. This suggests that no cracks will be initiated unless residual stresses are formed within the material as a result of the cyclic stress. These residual stresses can be caused by structures created during the manufacture of the part and by the ordinary cycling processes that the part is subjected to during its lifetime. Such residual stresses generally are not bulk phenomena, but rather occur at certain locations within the part, commonly referred to as stress concentrators. The stress concentrator may be a machined structure, for example a rivet hole or weld, or some local microstructure such as precipitates, grain boundaries and dislocations. The local strength near this stress concentrator depends on both the strength of the adjacent grain boundaries and the tensile and shear strength of the local grain. These will vary throughout the material. If the tensile stress exceeds the strength of the grain boundaries, the material will crack along the grain boundary, forming an ‘intergranular’ crack. If the shear or tensile stress exceeds the strength of the grain, the material will split across the grain, forming a ‘transgranular’ crack. Sections 2.1 and 2.2 will briefly discuss the rationale behind the dependence of these two crack mechanisms on crystalline texture. Section 2.3 will list detailed examples of the dependence of failure on texture from the literature.

### **2.1 Mechanisms for Intergranular Crack Initiation**

Intergranular cracks propagate via the splitting of adjacent grains along the grain boundary between them. There are a number of factors that can affect the probability of cracking along a grain boundary.

Chemical or corrosion fatigue occurs when the grain boundary has been weakened by corrosion or by the presence of particulates in the material. Corrosion, like etching, can be direction dependant, since, in general, chemical etchants will attack high energy portions of the material preferentially. These can be grain boundaries or densely

occupied lattice planes. This study, however, focuses on mechanical fatigue, and as such chemical fatigue will not be discussed in detail. A good review of this subject can be found in Reference 1.

Another cause of intergranular cracking is when the grain boundary acts as a strong concentrator of residual stress, for example at twin boundaries. Twin boundaries abound in face centered cubic (f.c.c.) materials such as aluminum alloys. Many researchers have found [7, and references therein] that these boundaries act as very effective sites for crack nucleation. In fact, intergranular failure in a number of different f.c.c. materials has been shown to occur predominantly along twin boundaries. Peralta et al [7] present a model proving that twin boundaries will act as stress concentrators whenever the tensile axis of the applied stress is neither in nor perpendicular to the twin plane. Further, the model predicts that the stress concentration due to a twin boundary is a maximum when the tensile axis is applied along the twin axis (the  $\langle 111 \rangle$  direction). This shows that the texture of the material is extremely important to fatigue, since the orientation of the grains within the material determines the orientation of twin boundaries with respect to the tensile axis.

A third factor affecting crack growth along grain boundaries is the misorientation angle between adjacent grains[8]. While the misorientation angle between individual grains can not be determined directly from measurements of the bulk texture of the material, the distribution of misorientation angles between the grains can be measured directly using localized diffraction techniques such as EBSD. From this a misorientation distribution function (MODF) can be calculated and correlated to crack initiation rates within a material. Blochwitz et al [8] use data from nickel and austenitic steel to calculate the probability of crack formation as a function of misorientation between grains. Again, the misorientation between grains will change as the texture of the material changes, suggesting that again texture is important in crack formation processes.

## **2.2 Mechanisms of Transgranular Crack Initiation**

Transgranular or intragranular cracking occurs when the tensile or shear strength of an individual grain is less than the local stress. As mentioned in the introduction, a grain is essentially a single crystal of a material, and will be treated as such in this discussion. The tensile strength of a crystal varies with direction in the crystal lattice, although for cubic materials this anisotropy is not usually pronounced. The anisotropy of the shear strength with direction is stronger, and as such is more important for crack formation than the anisotropy of the tensile strength. Figure 2 shows a schematic diagram of tensile and shear deformation mechanism. Tensile fracture is a simple splitting apart of the crystal planes(Figure 2(a)) involving the simultaneous breaking of bonds between all atoms on the separating planes. Shearing involves the slipping of crystal planes over each other in the material(Figure 2(b)), and is more complex.

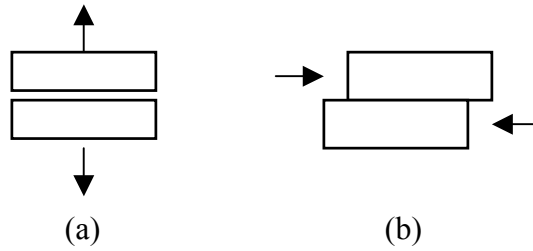
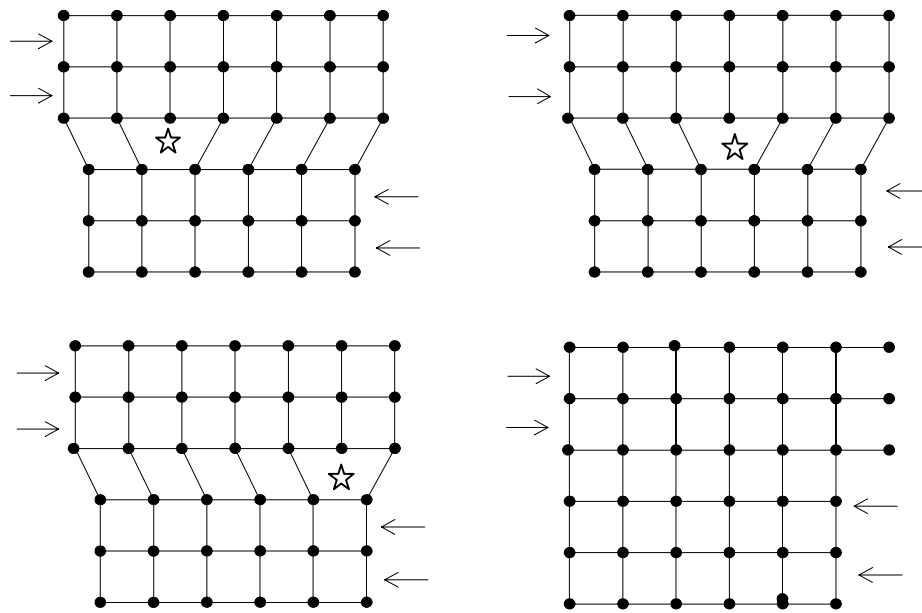


Figure 2: (a) Tensile versus (b) shear fracture.

It has been known for many years [3] that when a material is deformed, microscopic examination shows evidence of shearing having occurred along many parallel planes within a grain. These slip planes [3 pg. 35, and references therein] are those crystal lattice planes which have the highest density of atoms. Within these planes, slip occurs along the direction containing the most closely packed atoms. In a face centered cubic material these planes are the  $\{111\}$  planes, which slip along the  $\langle 110 \rangle$  directions. This means that grains oriented with their  $\langle 111 \rangle$  planes parallel or close to parallel to the maximum shear stress will be more likely to encounter slip. Thus the probability of slip occurring is strongly dependent on the orientation of the individual grains, i.e. the texture of the material.

When visualizing the role of slip on crack formation, it should be recalled that slip does not occur across the entire length of the plane at once, but rather along a dislocation front[1] as shown below in Figure 3. As the material is cycled, this dislocation front moves through the grain, causing a net atomic lattice spacing slip when it reaches the grain boundary. As several dislocations propagate in a complex manner through the material they can interact, forming pinning sites (known as dislocation walls) and microvoids. These defects in turn act as stress concentrators and can cause crack initiation in a weak part of the material. These defects can also result in a hardening of the material's response to applied stress, due to the pinning of dislocations at these sites making the material more brittle.





*Figure 3. Propagation of slip due to cyclic shearing. The dislocation (☆) moves progressively across the sample with each cycle. When it reaches the edge of the crystal a unit slip is formed.*

## 2.3 Evidence for the Influence of Texture on Mechanical Properties and Fatigue

Sections 2.1 and 2.2 summarized the main causes of cracking and rationalized the dependence of mechanical properties on the crystalline texture of the material. There is a considerable body of evidence to this effect, in addition to that listed in the above sections. Literature reports include data for materials with a wide range of crystal structures including hexagonal, body centered cubic and face centered cubic single crystals and polycrystals. This review will be limited to polycrystalline f.c.c. materials such as the aluminum alloys on which this project concentrates.

### 2.3.1 Residual Stress and Texture

Stress build up during cycling can cause crack initiation when the local residual stress exceeds the local strength. Even single deformations can cause significant residual stress build up if the applied stress is close to the plastic threshold for the material. Pang et al[9,10] subjected different f.c.c. materials (309H Stainless Steel, and Aluminum Alloy AA7050) to uniaxial loading close to the plastic deformation threshold. They measured the residual stress in the specimens by neutron diffraction after the load was released, and discovered that the amount of residual stress depended on grain size and orientation, i.e. texture. Some of the grains were stretched plastically, and did not return to their original

shape after the stress was released. Other grains, which were oriented in different directions to the tensile stress axis, were strained only elastically, and consequently returned to their original shape. This difference in response between adjacent grains strained plastically and elastically resulted in a large amount of stress build-up along the grain boundaries between them, causing crack initiation sites. The strain difference also resulted in a net grain rotation as determined by the net change in the crystalline texture measured before and after deformation[9].

Peralta et al[11] reviewed the effects of cyclic stress on residual stress build up and cyclic hardening in polycrystalline f.c.c. metals. They make reference to numerous conflicting reports on the fatigue properties of nominally identical materials. It is suggested that these discrepancies are due to the fact that for many studies *both* the grain size and the texture change from specimen to specimen. In general, an increase in grain size will cause a decrease in the fatigue lifetime. This is because the larger the grain size, the longer are the slip planes and the grain boundaries. Since both slip planes and grain boundaries act as crack initiation sites, the number of cycles to crack initiation is reduced with increased grain size[12]. Without a systematic study of the effect of texture on fatigue, it is impossible to determine from previous results whether it is the grain size or the texture that is the cause of the discrepancies noted by various groups.

Consequently, Peralta et al[11] examined the hardening rate of copper polycrystals, i.e. the number of cycles required for the strength of the material to be substantially altered by the formation of dislocation walls. By looking at copper polycrystals with the same grain size but different textures, they were able to determine conclusively that the texture had an effect on the number of cycles to hardening since it determines the rate at which slip occurs in these crystals. Luoh and Chang[13] also found that crystalline texture had an effect on the hardening due to dislocation buildup in copper polycrystals. They report, however, that the amount of texture dependence was a function of the magnitude of the applied strain. At low strain, they found little difference in hardening rates between crystals with different textures. They also report that the hardening was more pronounced in materials with small grain size due to microstructural changes. This microstructure will be discussed in more detail in section 2.3.3. It is important to remember that these results are reported for pure copper polycrystals. These materials have many less impurity sites than commercial aluminum alloys, and their response to applied stress may be qualitatively different.

### 2.3.2 Yield Strength and Fatigue Lifetime

The mechanical properties of numerous materials have been found to depend on crystalline texture. Measurements of the yield strength and fatigue lifetime have been made as a function of texture for a number of aluminum alloys. In AA2195 the yield strength was found to correlate directly to the grain orientation and morphology[14]. Microscopic studies after tensile testing found that the type of damage (i.e. slip/intergranular cracks) was related to the orientation of the damaged grain with respect to the tensile stress direction. Spriano et al [15] investigated the effects of rolling induced texture on the yield strength of an aluminum-lithium 8090-T851 plate. They found that

specimens that had a high proportion of grains with  $\{100\}$  planes parallel to the surface were softer than specimens with predominantly  $\{110\}$  planes parallel to the surface. In a detailed study on AA2195, Chen and Chaturvedi [16] investigated both the yield strength and the fatigue properties for a number of stress ratios. Their specimens were cut at various angles to the rolling direction of the aluminum alloy plate, so as to obtain a variation in grain orientation with respect to the strain axis. Again they found that both the tensile strength and the amount of fatigue damage depended on the orientation of the grains with respect to the applied stress.

Similar results were during the cyclic fatigue of nickel alloys and stainless steels. D.J. Morrison[17] studied the influence of grain size and texture on the cyclic response of nickel. As was found for copper polycrystals, the fatigue properties of nickel alloys and steels were shown to depend on the strain amplitude. When large strains were applied there was a significant difference in response between specimens with different orientation and morphology. For small amounts of strain little difference in fatigue properties was noted. These results appear to confirm those found for copper. It is important, however, to note that since both the texture and grain size differed in Morrison's nickel plates it is not possible to state conclusively whether it is the crystalline texture and not the grain size which is affecting the fatigue response. In the nickel-based alloy PM1000 a large difference in the number of cycles to failure was found for materials with different textures[18], again confirming the fact that texture is important to the mechanical properties of a material.

In a careful study on 316L austenitic stainless steel, Mineur et al [12] studied the effects of texture on the cyclic behavior, surface damage and fatigue lifetime of specimens with identical grain sizes. Samples were cut from a plate at various angles, so as to vary the alignment of the applied uniaxial strain axis with respect to the orientation of the grains in the material. These experiments were carried out both in air and in vacuum so as to determine environmental effects on the cracking rate as well. The specimens were sorted into two groups, those with 'hard texture' (primarily  $\langle 111 \rangle$  and  $\langle 100 \rangle$  directions) and those with 'soft texture', consisting of  $\langle 110 \rangle$  and other directions. The fatigue lifetime was found to be almost independent of the texture of the sample, however the fatigue damage was significantly different for the hard and soft textures. It was found that the hard specimens did not form localized stress concentrators, but rather the residual stress was spread out homogeneously. This reduces the probability of crack initiation, compared to the soft orientations for which single slip behavior predominates, causing larger surface deformation. In both air and vacuum, the samples with hard texture had significantly fewer cracks than those with soft texture. It is hypothesized that the fewer cracks in the hard materials propagate faster than the many cracks in the soft material, yielding essentially the same number of total cycles to failure in the two orientations.

From the data, it can be concluded that the mechanical properties of a material depend strongly on its texture. There is conflicting evidence as to whether the fatigue lifetime depends on texture, however it has been conclusively shown that the number of cycles to crack initiation is a function of the texture of the material. It is clear that in order to investigate this more closely, one must be careful to eliminate concerns of grain size and microstructure of the material to focus only on differences due to texture changes.

### 2.3.3 Microstructural Studies

In determining the role of texture on crack initiation, it is important to study the microstructure of fatigued specimens before and after damage. This microstructure can be examined using both microscopic examination of the surface structures in the damaged region as well as localized diffraction studies of the orientation of grains in the vicinity of the crack. In this section we summarize some of the results of microscopic examination of crack initiation sites in terms of grain boundary effects or transgranular effects.

As discussed briefly in section 2.1, Peralta et al [7] predicted that crack initiation along grain boundaries should depend on the misorientation angle between adjacent grains, and was largest for twin boundaries. Considerable microstructural evidence of this exists in addition to that of Reference 7. SEM micrographs of nickel and austenitic steel surfaces after growth showed that the frequency of crack growth was strongly dependent on the angle between adjacent grains[8]. In fact, it was found that the crack frequency was maximum for a misorientation angle of  $60^\circ$ , which corresponds to the misorientation angle between annealing twins. Peralta's theoretical prediction of twin boundaries being preferential sites for crack initiation was thus confirmed. Examination of aluminum alloys showed similar results. In AA7010, for example, Patton et al found that the local microstructure strongly influenced crack propagation rates[19].

Transgranular cracking was also identified microscopically. Polycrystalline copper has been examined extensively, since it has no impurities or precipitates to complicate analysis. An excellent review of data on copper was compiled by Pedersen in 1990[20]. By comparison of data from many publications, Pedersen concluded that in polycrystalline copper the formation of slip bands was related to the texture of the material. In fact, he found the same relationship between 'hard' and 'soft' orientations in copper as was described for stainless steel in section 2.3.2. This meant that those crystals with  $\langle 111 \rangle$  and  $\langle 100 \rangle$  components had fewer slip bands than those with  $\langle 110 \rangle$  components. Crooks et al found in AA8090-T851[14] that slip bands were found primarily in grains oriented with particular directions to the applied stress. Studies of the fracture surfaces in this material showed that failure occurred due to delamination fracture caused by these planar slip bands. There are some conflicting reports, however, such as that of Lopes et al [21] who claim to find no dependence of crack initiation on grain orientation in stainless steel. They suggest that crack initiation depends only on grain boundary properties and not the orientation of the individual grains. Despite a few such claims to the contrary, there appears to be a general consensus that grain orientation is important for crack initiation. The agreement between a simple material such as copper and more complex steel and aluminum alloys shows that these conclusions are general and can be applied to most polycrystalline materials.

Electron backscattering diffraction used to examine the microstructure in the vicinity of cracks is also revealing. It has been shown that the orientation of all of the grains along cracks in AA2090 was nearly identical to each other[6], strongly suggesting that cracks grow along certain crystal directions. Furthermore, the microtexture found in individual

grains could be linked to the macrotexture, or bulk texture measured using either x-ray or neutron diffraction.

Other microstructural factors affecting crack initiation and growth rate should be mentioned briefly. In complex alloys, such as steels and aluminum alloys, precipitates are often formed. These precipitates often have beneficial effects on the mechanical properties of the material, as is true in steels and composite materials. However they can also form ideal stress concentrators in the material, and can act as crack initiation sites. Patton et al[19] found for example that when such precipitates were present in grains of certain texture they acted as preferential damage sites in AA7010. Grain size also affects cracking, as was mentioned briefly above. Large grains may increase the size of slip planes and the probability of transgranular fracture. Luoh and Chang[13] found that small grained specimens had a higher frequency of crack initiation along grain boundaries, due to the presence of more twin boundaries than in a larger grained specimen of the same material. This is in contrast to the earlier statement (Section 2.3.1) that large grain sizes reduce strength due to the presence of longer grain boundaries. This suggests that the dependence of material strength on grain size is complex, and emphasizes the importance of using specimens with uniform microstructure to investigate the effects of texture on fatigue.

## **2.4 Property Determination by X-ray Texture Measurement**

Sections 2.1-2.3 showed clearly the dependence of a range of materials properties on the orientation of grains within a polycrystalline material. If one can determine the crystalline texture of the material, the one should be able to predict the material's strength and fatigue properties. The best method to characterize the average orientation of grains within the material is to obtain the orientation distribution function for the material using x-ray diffraction. Although EBSD can also determine texture, its uncertainty is larger than x-ray methods since it measures a much smaller volume of the material as opposed to a bulk method such as x-ray diffraction or neutron diffraction. As well, electron diffraction examines only grains at the surface of the material, which can have different textures to those in the bulk due to mechanical treatment during the preparation of the material. Neutron diffraction, while similar to x-ray diffraction in sampled volume, can only be done at neutron sources, making it a less practical method than x-ray diffraction which can be made portable.

## **3. Texture Development in Polycrystals**

In order to be able to use the crystalline texture as a gauge of proximity to crack initiation, it must be shown that the texture can be changed as a result of cyclic fatigue. In this section, the various mechanisms of altering the texture of a polycrystalline metal will be discussed in addition to existing evidence for texture development during cycling.

### 3.1 Alloy Preparation and Machining

It has been known for many years that heat treatment and machining have enormous effects on the crystalline texture of a polycrystalline material. In fact, heat treatment and mechanical surface treatments such as shot peening have been used for many years to improve particular mechanical properties of a material, due to the changes in texture and residual stress these methods produce. The effects of heat treatment and machining are explained in great detail in chapter 12 of reference 22. Only a brief discussion will be given here.

When a material is heated to an elevated temperature, the grains within the material begin to grow. This grain growth depends on the energetics of the material. As well, recrystallization occurs during which the orientation of an individual grain can change due to anisotropic properties of the material. Thus it is not surprising that, due perhaps to internal stresses, grains with certain orientations grow faster than other grains and dominate the material. This becomes even more likely in a material which already has some non-random texture. Such behavior was observed in a detailed study of the texture changes in cold-rolled steel, as well as tantalum, molybdenum and tungsten metals during annealing [23]. These authors found that by investigating the dependence of Young's modulus on crystal direction, they could predict the recrystallization rotation, and thus predict the change in texture after annealing. This result, while interesting in showing the nature of texture change, is not relevant to fatigue fracture, unless the cycling is performed at temperatures on the order of hundreds of degrees Celsius.

Fabrication processes such as extrusion and rolling also cause major changes in the texture. This is principally due to the presence of preferential slip planes in the material. When put under tensile stress, a grain will rotate so as to bring its principal slip direction parallel to the tensile axis. When under compression, the slip direction will rotate to lie in the compression plane. Rolling consists of two complementary stresses: compression normal to the rolling plane and tension in the rolling plane. In f.c.c. materials such as aluminum, grains will preferentially rotate to form the  $\{110\}[112]$  texture, with the  $\{110\}$  plane parallel to the rolling plane and the  $[112]$  direction parallel to the rolling direction. Due to the massive amount of research on this topic, we will simply refer the reader to reference 22 for a review of the work.

### 3.2 Deformation

Similar changes in texture can occur during ordinary tensile testing of materials in the laboratory environment. The application of a tensile strain in one direction will cause grain rotation as described above and thus a change in texture. Significant changes in texture have been found in metals which have been plastically deformed [9, 24-26]. As might be expected, the amount of texture development has been found to depend on the strain rate and the original texture of the material[25,26]. Again, a large body of

literature exists on this subject. The basic conclusion is the same: that applying a tensile or compressive stress on a material causes the net rotation of grains, i.e. texture changes.

### 3.3 Cyclic fatigue

Little research has been done on the effects of cyclic fatigue on texture. It seems reasonable to expect, however, that if texture develops under uniaxial tensile deformation, as discussed in section 3.2 above, repetitive cyclic tensile stress should also induce texture changes. Since the stress applied during cyclic fatigue is much smaller than that used for plastic deformation, one would expect the texture development to be smaller per cycle. However, as the material is subjected to many cycles, an observable change in texture would be expected. Such a change has been observed by Packer and Coyle[2]. They examined the change in texture of soft aluminum foils by monitoring the intensity of a particular x-ray reflection as a function of fatigue cycles. The intensity of this reflection was found to change with the number of fatigue cycles. Tirschler et al[27] investigated the stability of the texture in nickel polycrystals under cyclic fatigue at low strain rate. They examined the texture using EBSD of selected grains. They report a very small change in some components of the texture. These changes were within the uncertainty of their measurements, which is large due to the limited number of individual grains which can be observed. They also concluded that the macrotexture measured by neutron diffraction showed no changes. However closer examination of their data shows there are small changes in the ODF's presented, although they may be within the uncertainty of the measurement. As well, they reported the occurrence of unexplained rotations of grains about an axis at an angle to the specimen normal. These rotations *are* nothing less than a manifestation of texture change. This make it difficult to understand their report of no texture change, as their results seem to suggest otherwise. From these few results, one can conclude that although changes in texture under cyclic fatigue may be small, they should occur. Such changes in texture can then be used to examine the proximity of the material to crack initiation.



#### **4. Conclusion**

As this review has shown, there is a definite correlation between the crystalline texture of a polycrystalline metal and the processes of crack initiation and propagation within the material. This is due to both the orientation of crystal planes within the grains with respect to the applied stress and the misorientation angle between adjacent grains. We have also found a considerable body of work showing evidence of the effects of tensile and compressive strains on the texture of a material. Despite a lack of a large body of concrete evidence linking texture evolution to fatigue, we conclude that cyclic fatigue will cause the development of some change in crystalline texture within a material, although the actual texture change may be small. This suggests that the use of crystalline texture as a gauge of fatigue damage, as suggested by Packer and Coyles[2], is practical. As discussed in section 2.4, x-ray diffraction is the most practical method of obtaining a measurement of the average texture of a bulk part of the fatigued specimen. We believe that careful measurements of the crystalline texture of polycrystalline metals during cyclic fatigue will reveal firstly that fatigue causes changes in the macrotexture of the specimen. Secondly, careful examination of these data in comparison with microstructural studies, should show a link between texture development and crack initiation.

## References

- [1] Donald J. Wulpi, Understanding How Components Fail, Second Edition, 1999 (ASM International, Materials Park, OH).
- [2] M.E. Packer and R.A. Coyle, “Modification of Texture by Fatigue and its Application to Fatigue Metering”, *Metal Science* **12** (1978) 421.
- [3] P.J.E. Forsyth, The Physical Basis of Metal Fatigue, 1969 (American Elsevier Publishing Company, Inc , New York).
- [4] H.J. Bunge, *Zeitschrift fur Metallkunde* **56** (1965) 872; R.J. Roe, *J. Appl. Phys.* **36** (1965) 2024.
- [5] Stuart I Wright, David P. Field, “Recent Studies of Local Texture and Its Influence on Failure”, *Mat. Sci. Eng. A* **257** (1998) 165.
- [6] J.D. Haase, A. Guvenilir, J.R. Witt and S.R. Stock, “X-ray Microbeam Mapping of Microtexture Related to Fatigue Crack Asperities in Al/Li 2090”, *Acta. Mater.* **46** (1998) 4791.
- [7] P. Peralta, L. Llanes, J. Bassani and C. Laird, “Deformation from Twin-Boundary Stresses and the Role of Texture: Application to Fatigue”, *Phil. Mag. A* **70** (1994) 219.
- [8] C. Blochwitz, R. Richter, W. Tirschler and K. Obrtlík, “The Effect of Local Textures on Microcrack Propagation in Fatigued F.C.C. Materials”, *Mat. Sci. Eng. A* **234-236** (1997) 563.
- [9] J.W.L. Pang, T.M. Holden, J.S. Wright and T.E. Mason, “The Generation of Intergranular Strains in 309H Stainless Steel under Uniaxial Loading”, *Acta Mater.* **48** (2000) 1131.
- [10] J.W.L. Pang, T.M. Holden and T. E. Mason, “In Situ Generation of Intergranular Strains in an Al7050 Alloy”, *Acta Mater.* **46** (1998) 1503.
- [11] P. Peralta, A. Czapka, K. Obergfell, L. Llanes, C. Laird, and T.E. Mitchell, “Effect of Texture and Testing Conditions on Strain Localization during Cyclic Deformation of Copper Polycrystals”, *Mat. Sci. Eng. A* **270** (1999) 349.
- [12] M. Mineur, P. Villechaise and J. Mendez, “Influence of the Crystalline Texture on the Fatigue Behavior of a 316L austenitic stainless steel”, *Mat. Sci. Eng. A* **286** (2000) 257.
- [13] T. Luoh and C.P. Chang, “Effect of Grain size/texture on the cyclic stress-strain behavior of polycrystalline copper”, *Mat. Sci. Eng. A* **256** (1998) 18.

- [14] R. Crooks, Z. Wang, V.I. Levit and R.N. Shenoy, "Microtexture, Microstructure and Plastic Anisotropy of AA2195", *Mat. Sci. Eng. A* **257** (1998) 145.
- [15] S. Spriano, R. Doglione and M. Baricco, "Texture, Hardening and Mechanical Anisotropy in AA 8090-T851 plate", *Mat. Sci. Eng. A* **257** (1998) 134.
- [16] D.L. Chen and M.C. Chaturvedi, "Near-Threshold Fatigue Crack Growth Behavior of 2195 Aluminum-Lithium-Alloy-Prediction of Crack Propagation Direction and Influence of Stress Ratio", *Mett. Mat. Trans. A* **31A** (2000) 1531.
- [17] D.J. Morrison, "Influence of Grain Size and Texture on the Cyclic Stress-Strain Response of Nickel", *Mat. Sci. Eng. A* **187** (1994) 11.
- [18] F.E.H. Müller, M. Heilmeier and L. Schultz, "The Influence of Texture and Grain Structure on the High T Low-Cycle Fatigue Behavior of the ODS Nickel-Based Superalloy PM 1000", *Mat. Sci. Eng. A* **234-236** (1997) 509.
- [19] G. Patton, C. Rinaldi, Y. Bréchet, G. Lormand and R. Fougères, "Study of Fatigue Damage in 7010 Aluminum Alloy", *Mat. Sci. Eng. A* **254** (1998) 207.
- [20] O.B. Pedersen, "Overview No. 89: Mechanism Maps for Cyclic Plasticity and Fatigue of Single Phase Materials". *Acta Metall. Mater.* **38** (1990) 1221.
- [21] L.C.R. Lopes, C.B. Thomson and V. Randle, "Correlation Between Grain Boundary Structure and Cyclic Plastic Strain Below Yield Stress", Low Cycle Fatigue and Elasto-Plastic Behavior of Materials, 1998 (Elsevier, Netherlands) pp 327-32.
- [22] R.W.K. Honeycombe, The Plastic Deformation of Metals, 1984 (Edward Arnold Publishers, London). Chapter 12.
- [23] Y.B. Park, D.N. Lee and G. Gottstein, "A Model of the Development of Recrystallization Textures in Body Centered Cubic Metals", *Mat. Sci. Eng. A* **257** (1998) 178.
- [24] H.C. Fu, J.C. Huang, T.D. Wang and C.C. Bampton, "Evolution of Microstructure and Superplastic Deformation Mechanism in Super  $\alpha_2$ Ti<sub>3</sub>Al Base Alloys", *Acta Mater.* **46** (1998) 465.
- [25] H. Takuda, S. Kikuchi, T. Tsukada, K. Kubota and N. Hatta, "Effect of Strain Rate on Deformation Behaviour of a Mg-8.5Li-1Zn alloy sheet at Room Temperature", *Mat. Sci. Eng. A* **271** (1999) 251.
- [26] Tanja Pettersen and Erik Nes, "Hot Deformation to High Strains; Microstructure, Texture and Flow Stress Behavior", *Mater. Sci. Forum* **331-337** (2000) 601.
- [27] W. Tirschler, R. Tamm, C. Blochwitz, W. Skrotzki, "Texture Stability of Nickel During Cyclic Deformation at Room Temperature", *Mat. Sci. Eng. A* **254** (1998) 311.